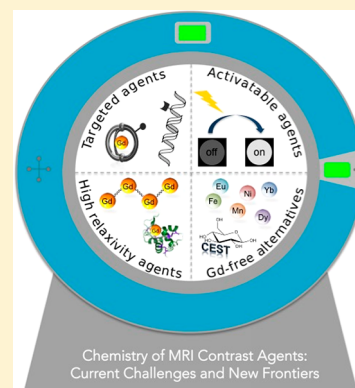# CHEMICAL REVIEWS

Chemistry of MRI Contrast Agents: Current Challenges and New Frontiers

Jessica Wahsner,[†] Eric M. Gale,[†] Aurora Rodríguez-Rodríguez, and Peter Caravan*

Athinoula A. Martinos Center for Biomedical Imaging and the Institute for Innovation in Imaging, Department of Radiology, Massachusetts General Hospital and Harvard Medical School, Charlestown, Massachusetts 02129, United States

ABSTRACT: Tens of millions of contrast-enhanced magnetic resonance imaging (MRI) exams are performed annually around the world. The contrast agents, which improve diagnostic accuracy, are almost exclusively small, hydrophilic gadolinium(III) based chelates. In recent years concerns have arisen surrounding the long-term safety of these compounds, and this has spurred research into alternatives. There has also been a push to develop new molecularly targeted contrast agents or agents that can sense pathological changes in the local environment. This comprehensive review describes the state of the art of clinically approved contrast agents, their mechanism of action, and factors influencing their safety. From there we describe different mechanisms of generating MR image contrast such as relaxation, chemical exchange saturation transfer, and direct detection and the types of molecules that are effective for these purposes. Next we describe efforts to make safer contrast agents either by increasing relaxivity, increasing resistance to metal ion release, or by moving to gadolinium(III)-free alternatives. Finally we survey approaches to make contrast agents more specific for pathology either by direct biochemical targeting or by the design of responsive or activatable contrast agents.

Chemistry of MRI Contrast Agents: Current Challenges and New Frontiers

CONTENTS

1. INTRODUCTION

Gadolinium(III)-based contrast agents (GBCAs), as a class, are one of the most successful examples of inorganic drugs, along with the platinum anticancer compounds and the technetium-99m radiopharmaceuticals used for cardiac and bone imaging. This success comes from the diagnostic and prognostic information that these agents provide, as well as their very favorable safety profile when compared to other imaging agents or drugs. GBCAs are used in about 40% of all magnetic resonance imaging (MRI) exams and in about 60% of neuro MRI exams. This represents about 40 million administrations of GBCAs worldwide.[1]

The growth of MRI and contrast-enhanced MRI has been remarkable. When one of us reviewed the field in 1999 we noted that since the approval of Gd-DTPA in 1988, about 30 tons of gadolinium metal ion had been cumulatively administered to patients worldwide over that 11 year period.[2] Now almost 50 tons of gadolinium are administered annually. The market for GBCAs is over one billion dollars per year. What has driven this growth?

GBCAs have been so successful because they provide essential diagnostic information that often cannot be obtained with other noninvasive techniques. A prime example is using GBCAs to detect blood brain barrier (BBB) disruption. GBCAs do not cross the BBB, so contrast enhancement of the brain can arise from pathologies such as multiple sclerosis, primary or metastatic cancer, or stroke. The absence of contrast enhancement can also enable a differential diagnosis when other symptoms are considered. GBCAs also detect increased vascular permeability associated with lesions outside the brain as well, for example in breast cancer detection and staging. GBCAs are also widely used to image the blood vessels to detect blockages or aneurysms, or to guide surgical interventions. One can also exploit the kinetics of contrast enhancement after injection, for example to measure regional perfusion of the heart.[3]

Another factor in the success of GBCAs is that their effect is immediate. Unlike in nuclear medicine where the patient receives the radiopharmaceutical and then waits a period before imaging, in MRI, the contrast agent is administered while the patient is in the scanner and diagnostic images appear within minutes. This practical aspect allows more patient throughput and facilitates workflow in radiology practice. Unlike radioactive tracers used in nuclear medicine, GBCAs are shelf-stable and do not need to be synthesized on demand. Moreover there is no ionizing radiation associated with GBCAs or MRI in general. A further factor is that GBCAs shorten the T_1 of protons, and this allows for faster imaging (higher throughput) and for imaging that is less sensitive to artifacts from motion (better quality images).

Gadolinium is not the only element that can be used to generate MR image contrast. Iron oxide nanoparticles and a manganese(II) complex have been approved for imaging the liver, although these were not commercially successful. In our 1999 review, we focused solely on gadolinium(III) complexes as contrast agents. At that time it was clear that the Gd(III) complexes would dominate the field. In this current review, we focus more broadly. In the intervening time, a number of changes have occurred to cause us to cast a wider net.

For 18 years following GBCA approval for human use, these compounds were considered to be among the safest pharmaceuticals. Indeed the rate of immediate adverse events is very low (<1 per thousand injections) and usually mild with severe adverse events occurring at about once per 40000 injections.[4] However, in 2006 GBCAs were associated with a devastating and potentially fatal condition called nephrogenic systemic fibrosis (NSF).[5,6] NSF occurs in patients with poor

kidney function, and its onset can occur months after the last GBCA administration. More recently it has been recognized that some fraction of the injected gadolinium can remain in the body for long periods, although the chemical form of Gd(III) and its whole body distribution is still not well-understood. Repeat usage of GBCAs can result in a buildup of residual Gd(III) to the point where it can be detectable by MRI or other methods.[7] Together, these findings have led to renewed interest in finding alternatives to using gadolinium(III) for MR contrast.

New techniques for contrast agent detection have also emerged or been improved. In a seminal 2000 paper, Ward and Balaban proposed generating image contrast by saturating exchangeable hydrogen resonances (e.g., N−H protons) which then chemically transfer this saturation to bulk water resulting in signal loss.[8] There have been a number of clever approaches to exploit this mechanism involving small molecules, metal chelates, and nanoparticles. Direct detection of nuclei such as C-13 or F-19 had been limited because of very low sensitivity when compared with imaging water. However, gains in hyperpolarization technology have enabled imaging of hyper-polarized C-13 labeled molecules in humans.[9] Pyruvate can be hyperpolarized, injected into the body, and then quantified, along with its metabolic transformation into alanine and lactate. Imaging pyruvate metabolism may be useful in staging cancers. Fluorine-19 in the form of perfluorocarbon emulsions can be used to label cells, and ^{19}F MRI can be used to image the location and concentration of these cell therapies once they are injected into the body.[10]

The ability of GBCAs to delineate pathology is based mainly on nonspecific distribution. Most GBCAs have an extracellular distribution and are eliminated via the kidneys. Pathology is detected because of altered anatomy (e.g., a narrowed blood vessel) or physiology (e.g., leaky blood brain barrier). GBCAs that distribute to the liver can detect liver lesions that do not take up the contrast agent. However, there is a great potential to move beyond passive distribution and create contrast agents that are biochemically targeted and potentially more specific to disease.

Contrast agents are detected indirectly by their effect on bulk water molecules. The magnitude of this effect is strongly influenced by the chemical properties of the contrast agent and can be potentially modulated to produce a stronger signal in certain environments. Activatable contrast agents, whose signal is altered by pH, enzymatic activity, temperature change, or ion flux, represent an exciting and growing area of research.

The goals of this review are to provide an overview of the state of the art approved MRI contrast agents, their applications, and the risks associated with them; to provide an understanding of the molecular mechanisms that give rise to MR contrast from relaxation and exchange; to review the coordination chemistry of these agents and the factors responsible for designing an agent safe for human use. We then move from this foundation to review new gadolinium-(III)- and nongadolinium(III)-based contrast agents, molecu-larly targeted agents, and activatable agents. The review should provide the reader with an understanding of the state of the art MRI contrast agents, the current challenges in the field, and the strategies employed to overcome these challenges.

We start with a description of contrast agents that have been approved for human use. Since these are so well-studied, they also form the basis of descriptions of the mechanism of action as well as stability and safety. The field of MRI contrast agents

has grown tremendously in the last decades. It has not been possible to cover all of the outstanding chemistry reported. For reasons of scope, we focus primarily on discrete molecular entities (small molecules, metal chelates). While there is some discussion of nanoparticle-based agents, this is limited to formulations that have been studied in humans and some exemplary representatives of targeting and/or high relaxivity. We also focus on contrast agents, molecules that generate image contrast in MRI, and provide only a brief overview of agents that are directly detected like hyperpolarized nuclei or perfluorocarbon emulsions.

2. STANDARD OF CARE AND NEW FRONTIERS

2.1. Applications

MR contrast agents are an absolutely integral component of modern radiology. The first MR contrast agent was made available in 1988 for imaging blood-brain barrier abnormalities, and since then, contrast enhanced MRI has played an increasingly important role is diagnostic medicine.[11] Today, there have been a dozen FDA-approved MR contrast agents and 8 of these agents are still commercially available in the United States. Contrast-enhanced MRI is now routinely used for imaging lesions in the central nervous system, breast, and abdomen, for angiographic imaging, cardiac imaging, and articular imaging, among numerous additional applications. Tens of millions of contrast-enhanced examinations are ordered annually worldwide.

All 8 of the MR contrast agents commercially available in the United Stated are small molecule Gd(III) complexes. Seven of the commercially available agents received their primary indication for imaging lesions of the central nervous system (CNS), but one agent (Gd-EOB-DTPA) received FDA approval for liver imaging applications. There are four MR contrast agents that have FDA approval but are no longer currently marketed. The Gd(III)-complex MS-325 was approved for angiographic (blood vessel) imaging. A Mn(II) complex (Mn-DPDP) and a superparamagnetic iron-oxide nanoparticle (SPION) formulation (ferumoxide) were ap-proved for liver imaging, and an oral SPION formulation was approved for gastrointestinal imaging (ferumoxsil).

The seven commercially available Gd(III)-based MRI contrast agents with indications for CNS lesions are administered as an intravenous bolus. These contrast agents are classified as extracellular fluid (ECF) contrast agents. They rapidly extravasate from the bloodstream into the tissue interstitial, extracellular spaces and are rapidly eliminated from the systemic circulation via filtration through the kidneys. Two of these agents are partially excreted through the liver and into the bile and feces.

The contrast enhancement observed after injection reflects the distribution of the exogenously administered agent, and extracellular agents can be ideal for identifying pathologic tissue. For example, tumors are typically characterized by hyper-vascularity, compromised endothelium, and/or an underdeveloped lymphatic drainage system and thus tempo-rarily retain greater concentrations of the contrast agent than healthy tissue and for longer periods of time. The contrast agent thus provides conspicuous contrast enhancement of the tumor in the minutes after injection. Important information about the tumor vascularity and perfusion can be learned by acquiring scans during the contrast agents first pass through the arteries or by dynamically monitoring accumulation and

clearance of the contrast agent from the tumor. In the seconds immediately following bolus injection, extracellular MRI contrast agents can also provide high-resolution imaging of the blood vessels to detect vascular pathologies such as stenoses, occlusions, and aneurisms. Contrast agents that are partially eliminated via the hepatobiliary system provide strong contrast enhancement of liver parenchyma as the agent transits the liver in the minutes after the blood signal has largely returned to baseline. This contrast is useful for differential diagnosis of liver malignancies which are devoid of normal hepatocytes.

2.2. New Directions

2.2.1. Contrast Agents with Biochemical Specificity. The clinically available ECF agents are specifically designed to passively move through patients with little or no interactions with proteins or cells.[12] The signal observed is strictly reflective of the agent's distribution. ECF agents provide superb contrast to differentiate anatomical structures or to characterize pathophysiology but do so in a nonspecific manner. However, new contrast agents with the capability to detect or quantify pathologic biomarkers could revolutionize the specificity with which MRI can be used to detect, characterize, and quantify pathologic tissue.

There are two general approaches to increased biochemical specificity. The first is to couple the contrast agent to a targeting vector to localize the agent to a specific protein or cell type. However, the concentration of a monomeric contrast agent needed for detection is at least in the micromolar range. Thus, abundant targets need to be selected, large assemblies of the imaging reporter must be used, or some other mechanism of target accumulation must be exploited. The second approach is to modulate the contrast generating signal in response to some stimulus. For example the hydration state of the contrast agent may change with pH, resulting in increased or decreased signal. Or the contrast agent may be chemically transformed by the action of a specific enzyme, resulting in a change in signal. Sections 5 and 6 will highlight innovate approaches toward biochemically specific targeted and activatable MRI contrast agents, respectively.

3. BACKGROUND AND THEORY

3.1. Classification of Contrast Agents: Biodistribution and Applications

MR contrast agents can be administered either (1) intravenously, (2) orally, or (3) by inhalation. Intravenous MR contrast agents may be categorized in 3 types: (a) extracellular fluid (ECF), (b) blood pool, and (c) target/organ-specific agents (Figure 1).

3.1.1. Intravenous MRI Contrast Agents. (a) Extracellular fluid (ECF) agents are distributed between the intravascular and cellular space. ECF agents are low molecular weight chelates, and after intravenous injection, they travel to the heart and then out to the systemic arteries, leaking into the extravascular, extracellular space. They are rapidly eliminated from the body through the renal pathway (see Figure 2). ECF agents are the most commonly used contrast agents and represent >98% of all contrast agents sold in the United States.[13] They are generally employed to image arterial abnormalities and to detect altered tissue endothelium (e.g., disrupted blood brain barrier). ECF agents approved for clinical use all consist of a nine-coordinate Gd(III) ion chelated by an octadentate polyaminocarboxylate ligand with a
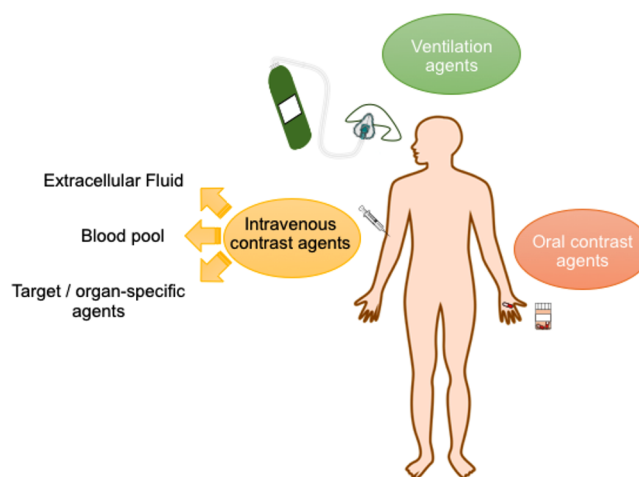
Figure 1. Route of administration of MRI contrast agents.
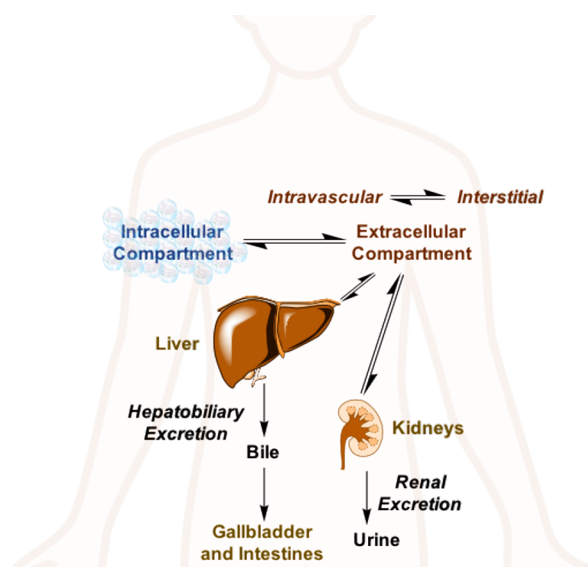
Figure 2. Main distribution sites and excretion pathways for intravenously administered soluble metal complexes.[15]

water coligand (Figure 3). The ECF agents approved for human use are listed in Table 1. Like all drugs, contrast agents have a commercial name like "Dotarem®" and a generic name, in this case, gadoterate meglumine. There is also a chemical abbreviation and, in this case, $[Gd(DOTA)(H_2O)]^-$ or Gd-DOTA. In the literature, the reference to the commercial name can be confusing. In the past, the ECF agents were dominantly sold by a single supplier such that gadoterate meglumine = Dotarem. But now there are increasing numbers of generic products. For example GE Healthcare now sells its own version of gadoterate meglumine which is marketed as "Clariscan®" which has the same Gd-DOTA chelate that is used in Dotarem. Clariscan was also the name given to an iron oxide nanoparticle formulation NC100150 that underwent clinical trials in the 1990s but was never approved for commercial use. In general, it is best to avoid the use of commercial names to avoid confusion over the compound involved and to avoid product promotion for a particular commercial entity.

(b) Blood pool agents are compounds that are, after injection, restricted to the intravascular space and which provide high contrast for imaging the arteries and veins. In the
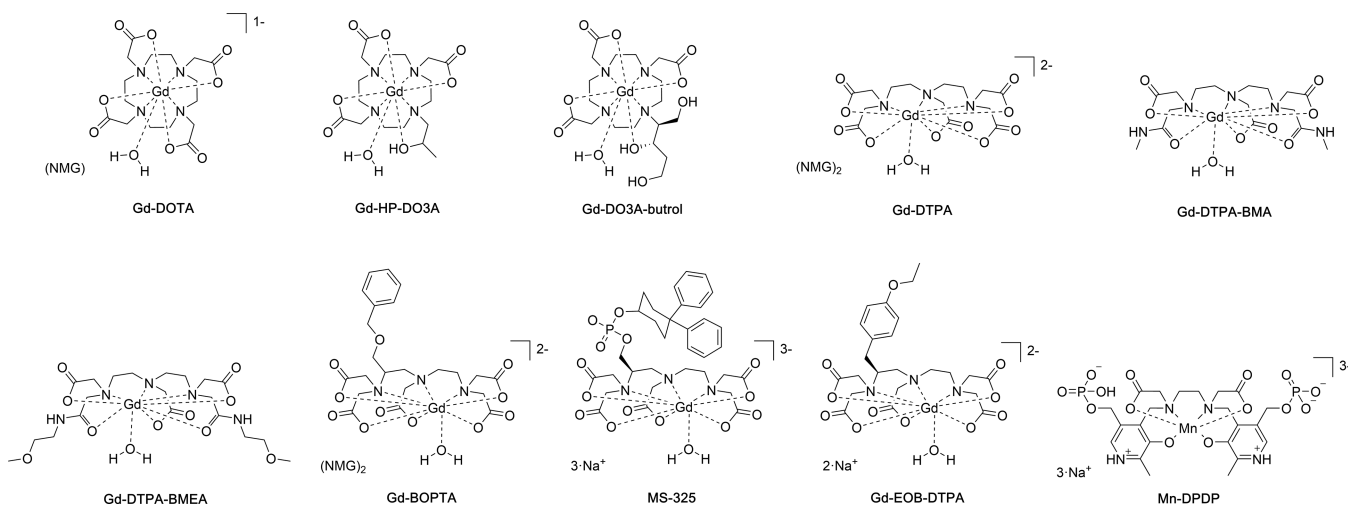
Figure 3. Commercially approved T_1 contrast agents (NMG = meglumine).

Table 1. ECF MRI Contrast Agents That Have Been Used in the Clinic

ECF agent (trade name)	ECF agent (chemical code)	ECF agent (generic name)	approval date
Dotarem, Clariscan	Gd-DOTA	gadoterate meglumine	1989 (Europe)
			2013 (United States)
ProHance	Gd-HPDO3A	gadoteridol	1992
Gadovist (Europe)	Gd-DO3A-butrol	gadobutrol	1998 (Europe)
Gadavist (United States)			2011 (United States)
Magnevist[a]	Gd-DTPA	gadopentetate dimeglumine	1988
Omniscan[a]	Gd-DTPA-BMA	gadodiamide	1993
Optimark[a]	Gd-DTPA-BMEA	gadoversetamide	1999
Multihance[b,c]	Gd-BOPTA	gadobenate dimeglumine	2004

[a]Agents suspended by the European Medicines Agency in 2017. [b]Agent available for limited, liver-specific indications in the EU. [c]Multipurpose agent that is also suitable for liver imaging.[14]
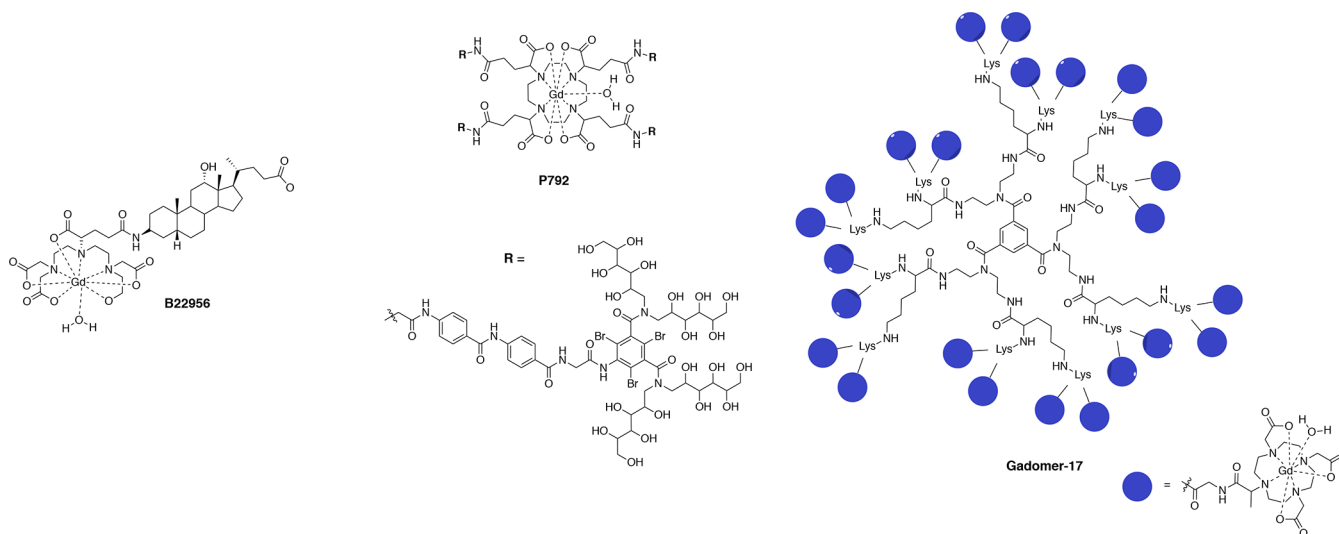
Figure 4. Chemical structures of the Gd(III)-based blood pool contrast agents (charges and counterions are omitted for simplicity).

1990s, there were many blood pool agents under development. There were three main strategies employed, all of which resulted in compounds that underwent human clinical trials: (1) low molecular weight compounds that bind noncovalently to human serum albumin upon intravenous injection, which restricts distribution to the intravascular space. An example is MS-325 (gadofosveset trisodium which had commercial names of Angiomark, Vasovist, and Ablavar) (Figure 3). MS-325 was

80−90% bound to HSA but the unbound fraction could be eliminated through the kidneys.[16−21] MS-325 was approved for commercial use but is no longer commercially available. The compound B22956 (Figure 4) was another albumin-binding Gd-DTPA based agent that progressed to phase 2 clinical trials.[22−26] (2) Large discrete Gd(III)-based compounds that were too large to rapidly extravasate across the endothelial barrier but still small enough to be filtered by the kidney. The

Table 2. Examples of Blood Pool Contrast Agents That Have Been Used in Human Clinical Trials

blood pool agent (trade name)	blood pool agent (chemical code)	blood pool agent (generic name)	approval date
	approved for use as an iron replacement therapy; not approved but used off-label for MRA		
Feraheme		ferumoxytol (USPIO)	2009 (United States); 2013 (Europe)
	approved for MRA but no longer commercially available		
Ablavar (formerly, Vasovist, Angiomark)	MS-325	gadofosveset trisodium	2005 (Europe); 2008 (United States)
	used in clinical trials but clinical development of the agents has been discontinued		
	B22956	Gadocoletic acid	–
Gadomer	SH L 643A	Gadomer-17	–
Vistarem	P792	Gadomelitol	–
Clariscan	NC-100150	PEG-feron (USPIO)	–
	VSOP-C184		–
Sinerem/Combidex	AMI-227	ferumoxtran-10 (USPIO)	–

Table 3. Organ-Specific MRI Contrast Agents That Have Been Used Clinically or Received Approval for Clinical Trials

organ-specific agent (trade name)	organ-specific agent (short name)	organ-specific agent (generic name)	approval date	applications
	approved and commercially available			
Primovist (Europe); Eovist (United States)	Gd-EOB-DTPA	disodium gadoxetic acid	2005 (Europe); 2008 (United States)	liver
Multihance[a]	Gd-BOPTA	gadobenate dimeglumine	1998 (Europe); 2004 (United States)	liver
	approved for use as an iron replacement therapy; not approved but used off-label for MRA			
Feraheme		ferumoxytol (USPIO)	2009 (United States); 2013 (Europe)	brain lesions, liver, lymph nodes, blood vessels
	agent withdrawn from one or all major markets			
Teslascan	Mn-DPDP	mangafodipir trisodium	1997	liver, myocardium
Feridex (United States); Endorem (Europe)	AMI-25	ferumoxides (SPIO)	1996 (United States)	liver
Resovist	SH U 555 A	ferucarbotran (SPIO)	2001 (Europe)	liver
	used in clinical trials but clinical development of the agents has been discontinued			
	Dy-DTPA-BMA	sprodiamde	–	myocardium, brain perfusions
Sinerem/Combidex	AMI-227	ferumoxtran-10 (USPIO)	–	metastatic lymph nodes, macrophage imaging

[a]Gd-BOPTA is predominantly used as an ECF agent but does provide some hepatobiliary enhancement and can be used for liver imaging.

dendrimer Gadomer (aka Gadomer-17) (Figure 4) was a 17 kDa dendrimer with 24 macrocyclic Gd(III)-chelates that advanced to phase 2 clinical trials.[27−30] Gadomer combined increased size with a high Gd(III) payload for high relaxivity. The compound P792 (Figure 4) was a single Gd-DOTA derivative with the chelate at the barycenter and 4 large hydrophilic branches to increase the hydrodynamic radius.[31−34] This compound was also used in phase 2 clinical trials. (3) Small iron oxide nanoparticles that had a high T_1 relaxivity. These compounds are truly intravascular and have long blood circulation times. The nanoparticles are not cleared from the body, rather they eventually accumulate in the liver and spleen and the iron is incorporated into the body's pool of iron. Iron oxide particles that underwent phase 2 and/or phase 3 angiography clinical trials were NC100150,[35,36] VSOP-C184,[37,38] and AMI-227.[39−43] None of these was ultimately approved for human use. The SPION ferumoxytol was approved for use as an intravenous iron replacement therapy in anemic patients. Ferumoxytol has excellent T_1 relaxivity and has been used off-label at some institutions as a blood pool agent in humans. Off-label means that the compound is not being used for its approved packaging label (in this case to treat anemia).

The lack of approved and commercially available blood pool agents is driven by market demand. In the 1990s, when most of these agents were being developed, the MR scanner performance was insufficient to support dynamic contrast enhanced MR angiography (MRA). Dynamic MRA involves very rapid injection of a contrast agent and rapid imaging to get an image of the contrast agent as it traversed the systemic arteries after injection but before it arrived in the venous circulation. However, power injectors (for reproducible rapid injection) and higher performing scanners with faster gradients (for faster imaging) enabled contrast-enhanced MRA to be routinely performed with ECF agents, and there is now much lower demand for dedicated blood pool agents (Table 2).

(c) Organ-specific agents are capable of targeting specific organs or tissues, for example the liver, spleen, or lymph nodes. ECF agents are eliminated via the kidneys. Altering the elimination pathway to include the liver can enable liver-specific imaging. Table 3 lists examples of contrast agents that are approved for commercial use or were studied in human clinical trials. For instance, the approved MRI contrast agent gadoxetic acid is rapidly taken up by hepatocytes and can therefore be used to image the liver and biliary system.[44] Gadobenate can also be used for liver imaging, but its hepatocyte uptake is much lower than that of gadoxetic acid.[45] A Mn(II)-based example is the agent mangafodipir (Mn-DPDP)[46] that dissociates after injection to the free Mn(II) ion. The Mn(II) is then rapidly taken up by hepatocytes,

Table 4. Oral Contrast (OC) Agents That Are Approved for Clinical Application

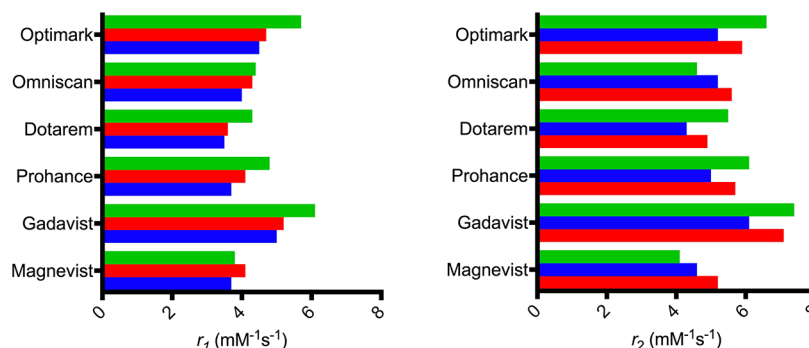| OC agent (trade name)	OC agent (short name)	OC agent (generic name)	approval date
Lumirem/GastroMARK	AMI-121	ferumoxsil (MPIO)	1996
Ferriseltz	–	ferric ammonium citrate	1992
LumenHance	–	manganese chloride	1997

Figure 5. Longitudinal (left) and transverse (right) relaxivities ($mM^{-1}\ s^{-1}$) of some commercial gadolinium(III)-based contrast agents at different magnetic fields (green = 0.47 T, red = 1.5 T, and blue = 3 T) in human plasma at 37 °C.[59]

cardiomyocytes, and pancreatic cells and can be employed to image the liver, myocardium, or pancreas. Organ-specific agents that are based on iron oxide particles exhibit a different distribution. SPIONs are imported into the cells of the reticuloendothelial system through phagocytosis, which enables selective access to the liver, spleen, lymph nodes, tumor associated macrophages, and bone marrow.[47] Depending on the SPION size and coating, different tissues can be targeted. For instance ferumoxide[48] and ferucarbotran[49] were both rapidly taken up by the Kuppfer cells in the liver and enabled liver-specific imaging. Ferumoxtran-10 has a longer circulating time and can be used for blood pool imaging but, with time, also significantly accumulates in lymph nodes which enables cancer staging applications.[50] None of the approved SPIONs, nor mangafodipir are commercially available anymore, and to the best of our knowledge, clinical development has been discontinued.

3.1.2. Oral Contrast Agents. Oral contrast agents are orally administered and are suitable for imaging the gastrointestinal tract (GI) imaging. Gd(III)- and Mn(II)-based agents, SPIOs, barium sulfate suspensions as well as fruit juice rich in manganese (e.g., blueberry or pineapple juice) have been investigated as oral contrast agents.[51−56] The following Table 4 summarizes the oral contrast agents that are currently available for clinical application. These are not widely used.

3.1.3. Ventilation Agents. Ventilation agents are contrast agents that are inhaled to improve the diagnostic value of MRI for the lungs. Gadolinium(III)-based aerosols and oxygen gas are paramagnetic and after inhalation they can be used to estimate ventilation in the lungs by its effect on lung water T_1. Direct detection is also used with hyperpolarized gases (^{3}He, ^{129}Xe) and with inert perfluorinated gases such as SF_6.[57]

3.2. Classification of Contrast Agents: Biophysical Mechanism of Action

Contrast agents can also be classified in terms of their contrast generating mechanism of action. We have grouped contrast agents into four major classes (1) paramagnetic, (2) superparamagnetic, (3) chemical exchange saturation transfer (CEST), and (4) direct detection.

3.2.1. Paramagnetic Contrast Agents. Paramagnetic contrast agents are by far the most prominent MRI contrast agents. They are also called positive contrast agents because they increase the MR signal in regions where they distribute.

Paramagnetic contrast agents comprise a metal ion that has unpaired electrons. Gd(III) with its half-filled f^7 shell and high spin Mn(II)- and Fe(III)-complexes with their half-filled d^5 shells all exhibit a large magnetic susceptibility compared to other metal ions. The symmetric S electronic ground state also endows these compounds with a relatively slow electronic relaxation rate which is necessary to promote strong nuclear relaxation. Of all the potential metal complexes that could be imagined, discrete Gd(III) chelates have been the most successful paramagnetic contrast agents so far and clearly dominate the contrast agents used in the clinic. We will start with a description of approved contrast agents as this will inform discussions of newer agents.

Clinically used Gd(III)-based contrast agents (GBCAs) all utilize an octadentate polyaminopolycarboxylato-based ligand and have a ninth coordination site available for water ligation. The coordinated water ligand can be rapidly exchanged with bulk water molecules. GBCAs that have been approved for clinical use are illustrated in Figure 3. As outlined above, some of these are no longer available for commercial use.

To date, only two manganese-based contrast agents have ever been approved: Mn-DPDP (Figure 3) and an orally administered contrast agent that consists of liposomal encapsulated manganese chloride (LumenHance).[58]

Contrast agents containing Gd(III) shorten the observed longitudinal (T_1) and the transverse (T_2) relaxation time of water protons in their vicinity. The rate constants corresponding to the T_1 or T_2 relaxation times are defined as $1/T_1$ and $1/T_2$, respectively, which are generally referred to as relaxation rates. In this review, we will use the general term relaxation rate when referring to the rate constant of spin relaxation. On T_1-weighted scans, tissue with short T_1 appears bright and thus T_1-shortening contrast agents generally make the signal bright. On the contrary, T_2-weighted scans show tissue with long T_2 as being bright, so T_2-shortening agents reduce the signal. The extent to which a contrast agent can change the T_1 or T_2 of solvent water is termed relaxivity r_1 or r_2, respectively; this is

sometimes referred to as longitudinal (r_1) and transverse (r_2) relaxivity. Relaxivity is defined by eq 1, where ($1/T_i^0$) is the inherent relaxation rate of the tissue, ($1/T_i$) is the relaxation rate in the presence of contrast agent (r_i), and [CA] is the concentration of the contrast agent.

$$\frac{1}{T_i} = \frac{1}{T_i^0} + r_i[CA]; \quad i = 1,2 \tag{1}$$

Low molecular weight Gd(III) complexes have similar r_1 and r_2 values in water that have very little variation with field at magnetic fields generally used for MRI (Figure 5).

The relaxation times of water hydrogen nuclei in pure water are very long. But in different tissues the relaxation times can be much shorter due to the interaction of water with macromolecules and also because of the presence of endogenous paramagnetic species such as ferritin.[60] In the body, water T_2 is generally 5−20 times shorter than T_1. As a result, the effect of a Gd(III) contrast agent will be much more pronounced on T_1. This is illustrated in Figure 6 where the
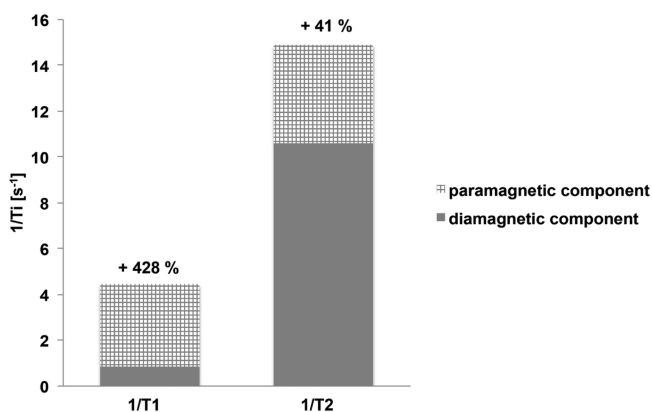

Figure 6. Paramagnetic contribution of 1 mM of T_1 contrast agent Gd-DOTA on $1/T_1$ and $1/T_2$ in cortical gray matter at 1.5 T.

endogenous relaxation rates of gray matter at 1.5 T are plotted (solid). Addition of 1 mM Gd-DOTA (r_1 = 3.6 mM^{-1} s^{-1}, r_2 = 4.3 mM^{-1} s^{-1}) will increase the $1/T_1$ and $1/T_2$ by 3.6 and 4.3 s^{-1}, respectively. Because of the low baseline T_1 relaxation rate, the effect of the contrast agent on $1/T_1$ is much larger (+ 428%) than on $1/T_2$ (+ 41%). Because of this effect, Gd(III) based agents are often referred to as T_1-contrast agents because on a percentage basis they have a much larger effect on T_1.

Figure 7 is an exemplary T_1 weighted image of the brain of a patient with glioblastoma and shows the effect of the T_1 contrast agent gadoteridol at 3 T. Twenty minutes after injection of gadoteridol, the tumor becomes strongly and positively enhanced (image on right) in comparison to the T_1 weighted image acquired before injection (left).[61]

3.2.2. Superparamagnetic Contrast Agents. Superparamagnetic contrast agents are colloidal materials made up of particles (∼5−200 nm in diameter) in suspension. These particles are composed of small crystallites (1−10 nm) that contain thousands of magnetic ions, usually iron, that are randomly oriented. In the presence of an external magnetic field, the crystallites align with the field, leading to a superspin which renders the material magnetic. The total spin of the particle is much larger than the sum of the individual metal ion spins which can result in a very high relaxivity. In the absence of the applied field, the material is no longer magnetic. The
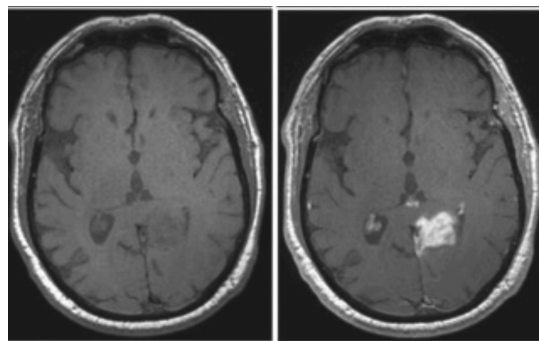
Figure 7. Axial T_1-weighted MR images obtained at 3 T before (left) and 20 min after intravenous gadoteridol administration (right) of patient with glioblastoma. Reproduced with permission of ref 61. Copyright 2013 Radiological Society of North America (RSNA).

crystallites are made of a core of nonstoichiometric metal (usually iron) oxides covered by a coating, such as dextran, citrate, oleate, or other nonimmunogenic polymers in order to avoid aggregation and reduce their toxicity.[62−66] The first superparamagnetic contrast agents had very high r_2/r_1 ratios and predominantly affected T_2. As a result, they were referred to as T_2-agents or negative contrast agents because they provide darkened MR images. However, there are many examples of superparamagnetic iron oxide particles that also have a large r_1 and can serve as effective T_1 or T_2 contrast agents.

Superparamagnetic iron oxides can be classified in three groups according to the size of the particulate: (1) ultrasmall superparamagnetic iron oxide (USPIO) particles with a diameter of d < 50 nm; (2) small superparamagnetic iron oxide (SPIO) particles with a diameter of 1 μm > d > 50 nm; and (3) micron-sized particles of iron oxide (MPIO) with a diameter in excess of a micron.[67] Iron oxides that have been approved for clinical use or that have undergone human clinical trials are listed in Table 2 and Table 3 above. These agents are also referred to generically as superparamagnetic iron oxide nanoparticles (SPION).

Figure 8 shows the effect of a T_2 agent on tissue relaxation times. Although the contrast agent shortens T_1, the effect on T_2 is very large. The large magnetic moment of superparamagnetic relaxation agents also generates a local magnetic

Figure 8. Paramagnetic contribution of 1 mM of T_2 contrast agent ferucarbotran on $1/T_1$ and $1/T_2$ in cortical gray matter at 1.5 T.

inhomogeneity and shortens the T_2* of tissue which creates signal loss on gradient echo T_2* weighted images.

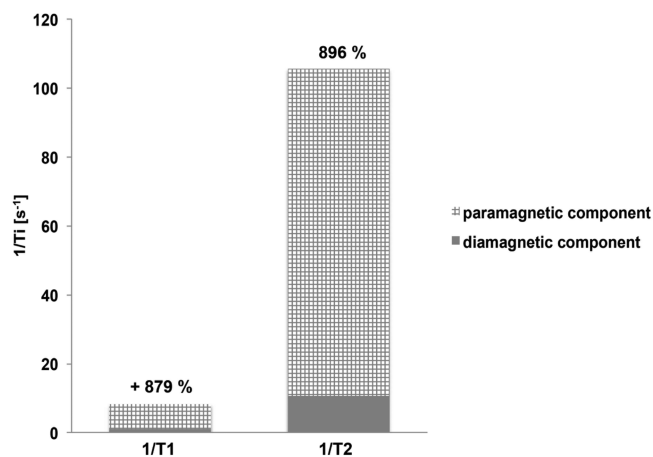Exemplary images from a patient with primary central nervous system (CNS) lymphoma are shown in Figure 9
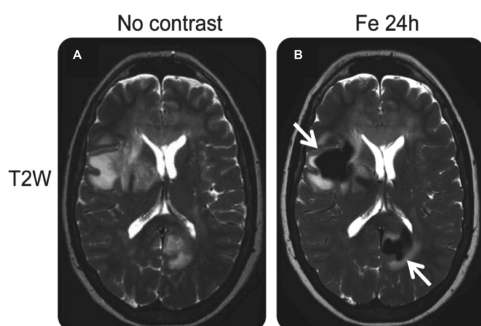

Figure 9. T_2-weighted images obtained before and 24 h after intravenous ferumoxytol administration show deep white matter lesions, demonstrated through several areas of confluent, focal, strong signal loss due to ferumoxytol uptake (arrows). Reproduced with permission from ref 68. Copyright 2013 Wolters Kluwer Health, Inc.

before and 24 h after intravenous injection of ferumoxytol.[68] T_2-weighted images obtained before ferumoxytol show regions of hyperintensity due to tumor-associated edema. After 24 h, ferumoxytol has accumulated in the tumors and several areas of deep white matter lesions are enhanced through strong signal loss due to ferumoxytol uptake in these regions.

3.2.3. Chemical Exchange Saturation Transfer (CEST) Agents.

CEST agents are molecules that possess exchangeable protons, such as NH, OH, or exchangeable water molecules, that resonate at a chemical shift that is different from the bulk water signal. In a CEST experiment, the exchangeable protons of the CEST agent are irradiated with an off-resonance saturation pulse. Their magnetization (i.e., spin polarization) is transferred to the protons of the bulk water pool by exchange between both pools (saturated proton pool and bulk water proton pool), which leads to a reduced intensity of the water signal. This in turn generate a MRI contrast.

For a CEST agent to be effective, there needs to be good frequency separation between the exchangeable protons and the bulk water resonances, especially since the bulk water resonance is broadened in vivo because of local magnetic field inhomogeneities.[69] To overcome this problem, the chemical shift difference needs to be maximized. This can be achieved by either increasing the magnetic field strength (higher field strengths for the MR experiment) or by using paramagnetic CEST (ParaCEST) agents. Typically, ParaCEST agents contain paramagnetic ions to shift the signal of the labile proton tens to hundreds of ppm away from the bulk water resonance.

Some CEST contrast agents are known molecules that are already approved for intravenous administration. Examples include glucose (exchangeable OH) and the X-ray contrast agent iopamidol (exchangeable NH) (Figure 10) that are currently being used in human clinical trials.[70−72]

3.2.4. Direct Detection Agents.

MRI is an insensitive technique. To overcome this low sensitivity, clinical MRI detects hydrogen, the most sensitive NMR nucleus, and primarily detects water because of its very high (10s of molar) concentration in tissue. Other proton-containing molecules or heteronuclei can be detected, such as ^{13}C, ^{23}Na, ^{31}P, and ^{19}F,
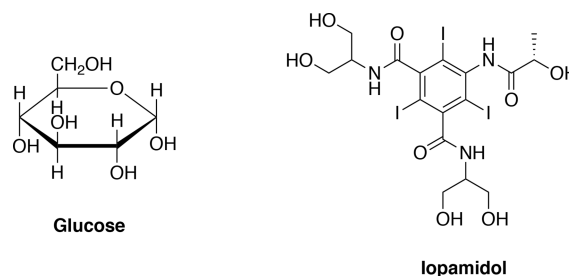
Figure 10. CEST agents that are approved for use in clinical trials: glucose and iopamidol.[70−72]

but very high concentrations are usually required. Nonetheless, there are numerous examples of direct detection agents. The T_1-, T_2-, and CEST agents described above are contrast agents that change the local MR water signal and create image contrast. These agents are not directly detected but are seen via their effect on the bulk water signal. Direct detection agents do not generate contrast and in general have little to no background signal but do suffer from poor sensitivity.

To overcome the sensitivity problem, nanoparticle containing perfluorocarbon (PFCs) emulsions, providing huge payloads of ^{19}F atoms, have been used for direct detection in ^{19}F MRI.[73,74] These perfluorocarbons are the most biologically inert organic xenobiotics, and usually, even at high doses, their toxicity is very low.[75] Selected examples of PCFs are illustrated in Figure 11.
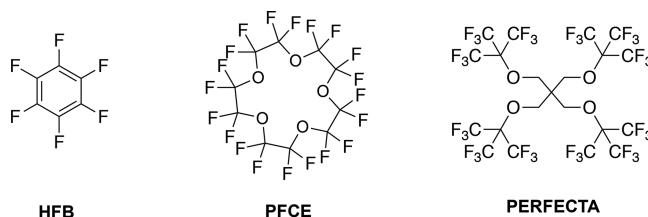
Figure 11. Chemical structures of some PFCs: left, hexafluorobenzene (HFB); center, perfluoro-15-crown-5-ether (PFCE); and right, tetra(perfluorotertbutyl)pentaerythritol (PERFECTA).

To overcome the low water solubility of traditional PFCs, a new generation of hydrophilic fluorinated molecules has emerged. Annapragada and co-workers developed stable liposomal formulations of hydrophilic fluorinated molecules that allow simultaneous imaging of multiple targets (Figure 12).[76]

The natural abundance of ^{19}F (100%), its spin (1/2), its high gyromagnetic ratio (40.08 MHz/T, ^1H: 42.58 MHz/T), and sensitivity (83% of ^1H) makes ^{19}F a promising candidate for direct detection imaging. In addition, the chemical shifts of ^{19}F containing compounds vary over a broad range (>350 ppm), and the in vivo background signal is very low due to the low natural abundance of the element in the human body. In addition, the concentration of agent can be measured directly from the intensity of the signal. While not widely available, it is possible to modify MRI hardware to directly detect both ^1H and ^{19}F, and in this way, the visualization of the ^{19}F agent can be localized to the anatomic ^1H (water) image.

It is also possible to directly detect the ^1H resonance of a direct detect agent, but because of the narrow chemical shift range of ^1H, there is usually a significant background signal from metabolites. A further limitation of direct detection
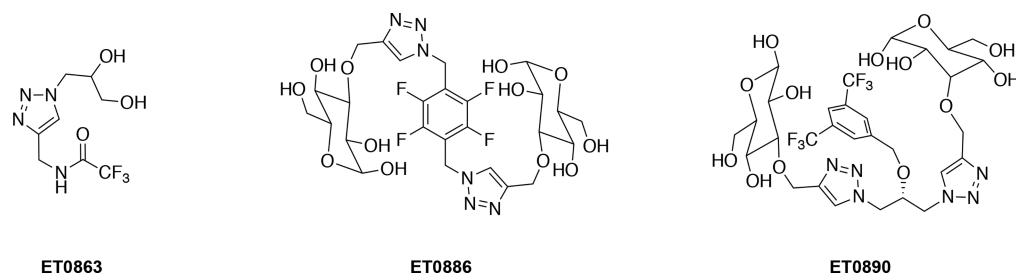
Figure 12. Examples of hydrophilic fluorinated molecules studied by Annapragada and co-workers.[76]

Ln = Tm, Er, Dy, Ho or Tb
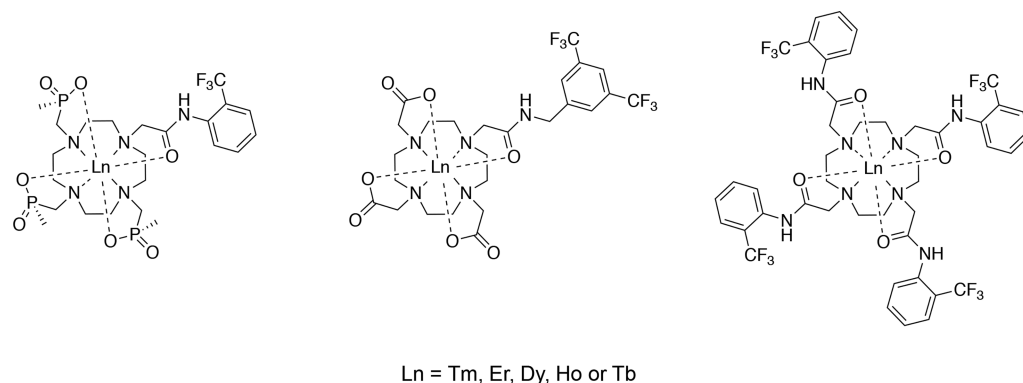
Figure 13. Examples of fluorinated compounds studied by Parker and co-workers in order to boost the ^{19}F MRI signal.[83,84]

agents is the long T_1 of the nucleus being detected. After excitation one has to wait until the T_1 magnetization is sufficiently recovered before applying a second excitation pulse. The acquisition time window in vivo is limited because the agent may be washing out of tissue with time, and there is a practical limit of keeping the subject in the scanner. If the T_1 was very short then excitation pulses could be acquired continuously allowing for signal averaging. Aime et al. showed over 20 years ago that a paramagnetic complex exhibiting a large chemical shift could overcome these problems to some extent.[77] Yb-DOTMA has 4 equiv CH_3 groups (12 H per molecule) that are well-shifted outside the diamagnetic window. Moreover, the Yb(III) ion causes efficient T_1 relaxation of the CH_3 protons but does not result in severe linebroadening. The chemical shift of the CH_3 group is very sensitive to temperature, and several lanthanide complexes of DOTMA have been used in MR thermometry applications.[78,79] Yang et al. took a different approach and encapsulated sodium 3-(trimethylsilyl)-1-propanesulfonate (DSS) at a high concentration inside liposomes.[80] DSS has a zero ppm chemical shift, outside the range of metabolites. A small amount of Gd-HPDO3A was included to shorten the T_1 of the DSS protons. They showed that liposomes could be directly detected at concentrations as low as 50 pM.

Parker and co-workers used a rational, systematic approach to design what they termed ParaSHIFT agents (Figure 13). They first designed compounds with a large number of equivalent fluorine atoms and incorporated a lanthanide ion at an optimal distance to the fluorine to optimize T_1 shortening. In this way, they showed that the sensitivity could be increased by a factor of 25 compared to the diamagnetic compound. More recently, they have extended this approach to lanthanide complexes with a shifted proton signal (e.g., from a t-butyl group with 9 equiv protons).[81,82]

The insensitivity of NMR arises from the low energy difference between the ground and excited state which results

in a large population of spins in the excited state at thermal equilibrium. If the nuclear spins could be polarized far beyond thermal equilibrium conditions then the sensitivity could be increased by several orders of magnitude. The polarization of spins is enhanced by a nonequilibrium distribution of nuclear spins called the hyperpolarized state.[85] This technique requires nuclei with long T_1 values such that relaxation does not occur in the time the molecule is hyperpolarized to when the image is acquired and includes nuclei such as ^3He, ^{129}Xe, ^{13}C, ^{15}N, and ^6Li.[86]

Initially hyperpolarization was applied to gases like ^3He and ^{129}Xe which have very long T_1 values. These gases are used clinically at a number of sites to image the lung architecture after inhalation of the gas.[87−90] In the past decade, ^{13}C hyperpolarization has been widely employed and there is now a commercial apparatus available to hyperpolarize ^{13}C for human applications. For example, hyperpolarized [1-^{13}C] pyruvate was used by Nelson et al. in patients with prostate cancer.[9] Pyruvate is metabolized to lactate, alanine, and bicarbonate in a matter of seconds, and each of these can be visualized and quantified because of the chemical shift differences between these metabolites. The ratio of pyruvate metabolites can be used to grade tumor aggressiveness and monitor treatment response.

The most widely used method for hyperpolarization is dynamic nuclear polarization (DNP).[91] In this method, a stable organic radical, usually trityl, is frozen along with the compound to be hyperpolarized. This sample is placed inside a DNP polarizer, comprising a superconducting magnet ($B_0 = 3$ to 5 T) and a liquid helium cooled sample space (maintained cold at 1 to 5 K). Under these conditions, the radical's unpaired electrons are aligned with the external magnetic field, which leads to a hyperpolarized state, and this electron hyperpolarization is transferred to the ^{13}C nucleus using microwave radiation close to the MR frequency of the electron
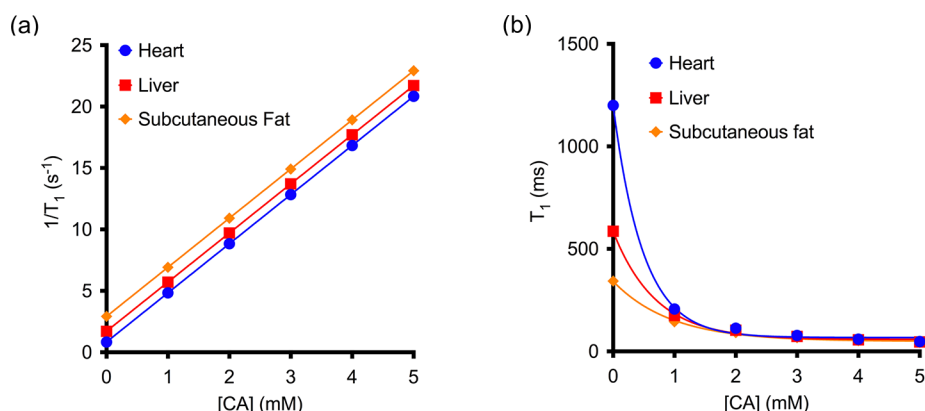
(a)

(b)

Figure 14. Change in the (a) longitudinal relaxation rate and in the (b) relaxation time as a function of the concentration of contrast agent in three different tissues: heart (T_1^0 = 1200 ms), liver (T_1^0 = 590 ms), and subcutaneous fat (T_1^0 = 340 ms), supposing in every case, r_1 = 4 mM^{-1} s^{-1}.

spin. Before the hyperpolarized sample can be used in vivo, it needs to be rapidly dissolved in an appropriate solvent, heated to physiological temperature, and separated from the radical. Generally a superheated solvent at 180 °C and 10 bar is used.[92]

Another frequently used method for polarization is the parahydrogen-induced polarization (PHIP)[93] that induces hyperpolarization through the reaction of parahydrogen (its two proton spins are aligned antiparallel) with an unsaturated substrate containing double or triple bonds.[91] Typically, parahydrogen is introduced through catalytic hydrogenation to the unsaturated compound. Subsequently, the nuclear polarization of a vicinal ^{13}C nucleus is achieved by converting the nonequilibrium spin polarization of parahydrogen by diabatic-adiabatic magnetic field cycling or by radiofrequency pulses.[94]

A third and related approach is signal amplification by reversible exchange (SABRE). SABRE involves the transient coordination of a substrate molecule (usually containing a coordinating atom like a pyridyl N) to an organometallic catalyst. Parahydrogen (H$_2$) also coordinates the catalyst and then transfers its polarization to the substrate in a catalytic manner. Unlike in PHIP, the substrate molecule is unchanged.[95,96]

3.3. Biophysics of Magnetic Resonance Imaging

There are many ways to achieve contrast in a MR image without giving an exogenous contrast agent.[3,97−99] Chemical shift difference can provide contrast between mobile lipids and water. The density of water protons in tissue also provides contrast (low in lung and bone, higher in soft tissue and fluids). There are a number of contrast mechanisms that exploit differences in the properties of water in different tissues. For instance, the relaxation times T_1, T_2, $T_{1\rho}$ (T_1 in the rotating frame) can be very different in adjacent tissues and images can be acquired using pulse sequences that are weighted to provide more (or less) signal intensity for a short relaxation time. Contrast can also be generated from physicochemical properties of water such as diffusion and flow. Magnetization transfer from the solid-like macromolecules to bulk water is another mechanism, as is saturation transfer (discussed in CEST contrast). Exogenous contrast agents can further exploit these mechanisms by amplifying the effect. The majority of contrast agents serve to shorten the relaxation times of water, while CEST agents exploit a saturation transfer mechanism. In this section, we describe the mechanisms by which contrast agents affect relaxation times or saturation transfer.

3.3.1. Relaxation Agents. Relaxation agents are primarily described by their "relaxivity" (r_1 or r_2), that is defined as the extent to which the contrast agent can modify the relaxation rate of tissue water ($1/T_1$ or $1/T_2$). The conventional units for relaxivity are mM^{-1} s^{-1} (per millimolar per second, and sometimes L mol^{-1} s^{-1}). Sometimes, the relaxation rate enhancement of the contrast agent is referred to as $1/T_{ip}$ (i = 1,2) as the paramagnetic contribution to the relaxation rate.

Figure 14 shows the effect of a typical ECF agent on (a) the relaxation rate and on (b) the relaxation time of three different tissues: heart (T_1^0 = 1200 ms), liver (T_1^0 = 590 ms), and subcutaneous fat (T_1^0 = 340 ms).[100] Panel (a) shows that increasing the contrast agent concentration increases the tissue relaxation rate in the same linear fashion for all three tissues, although the intercept differs among the tissue types. The slope of the lines in panel (a) is the relaxivity, r_1. Panel (b) shows the same data expressed as relaxation times. At lower concentrations (left part of the graph), the amount of contrast agent has a higher effect on tissue with longer T_1, whereas at higher concentrations of contrast agent (right part of the graph), all tissues approach a similar relaxation time. Thus, the detection sensitivity of the contrast agent will be greater in tissues with long relaxation times.

The relaxation rate of the tissue ($1/T_1^0$) varies with tissue type, usually in the range of 0.5−2 s^{-1} for most tissues and tumors, and decreases with magnetic field strength.[60,101] In designing experiments and new contrast agents, it is important to consider both the relaxivity of the agent and the inherent relaxation rate of the tissue, since both are involved in determining the signal change observed. Figure 15 illustrates this point using relaxivity data for Gd-DOTA[59] and MS-325[15] measured in human plasma and compared to brain gray matter (GM) and white matter (WM) T_1 values measured at 1.5 and 4.7 T.[60] The relaxation times of GM and WM increase by about 50% with increasing field, while Gd-DOTA relaxivity only decreases by about 10%. As a result, the percent change in brain tissue relaxation rate that one would observe for a given Gd-DOTA concentration is actually higher at 4.7 T, despite its lower relaxivity at this field strength. Even for MS-325 where the relaxivity at 1.5 T is more than double that at 4.7 T, the change in brain tissue relaxation rate for a 0.3 mM MS-325 concentration is only about 40% higher at 1.5 T.

In the case of transverse relaxation, the T_2 of tissues is generally very short and usually decreases with increasing field strength. Thus, much higher concentrations of contrast agent
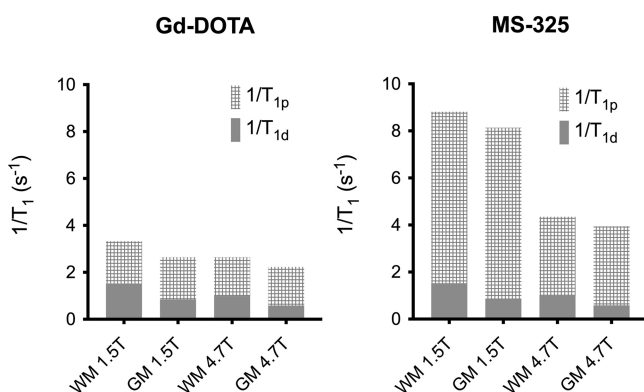
Figure 15. Effect of field strength on relaxivity and contrast in the case of Gd-DOTA (left) and MS-325 (right) in white matter (WM) and gray matter (GM). The paramagnetic ($1/T_{1p}$) and diamagnetic ($1/T_{1d}$) contributions to the relaxation rate are indicated by hatched and solid shading, respectively.

and/or much higher relaxivities are required to measurably affect T_2.[102]

T_1-Contrast Agents. Brownian motion of a paramagnetic complex or particle generates a fluctuating magnetic field that induces relaxation in nearby water molecules. In order to transmit the relaxation effect to the bulk, the exchange between the water interacting with the metal ion and the bulk needs to be fast ($>10^6$ s^{-1}). Paramagnetic induced T_1 relaxation directly depends on the spin quantum number [as a function of S(S +1)] and inversely on the distance (r_{MH}) between the metal ion and the proton of the water as a function of $1/r_{MH}$.[6] Gadolinium(III) with S = 7/2 and high spin manganese(II) or iron(III) with S = 5/2 have been the most widely used as contrast agents. The shortest r_{MH} distance can be achieved through a direct bond between the metal ion and the water molecule, thus occupying a coordination position in the inner-coordination sphere of the metal ion. The exchange rate of this water molecule must be fast ($>10^6$ s^{-1}) in order to maximize the transfer of the relaxation effect to the bulk water. The absence of ligand field stabilization energy of Gd(III) and Mn(II) makes their complexes quite labile, thus favoring the fast chemical exchange of the bound water molecule. These ions also have a symmetric S electronic ground state which results in electronic relaxation typically in the nanosecond time scale, and this allows an efficient nuclear T_1 relaxation.

From a chemical standpoint, three contributions to relaxivity can be considered:[103] (1) Inner-sphere relaxation where a water ligand directly bound to the metal is relaxed and transmits the relaxation effect to the bulk water through exchange with another water molecule. (2) Second-sphere relaxation where hydrogen bonded water molecules in the second coordination sphere, or exchangeable hydrogen atoms (such as O−H, N−H) undergo relaxation and exchange. (3) Outer-sphere relaxation, where water molecules that diffuse close to the paramagnetic compound can also be relaxed.

Because of the difficulty to experimentally distinguish water molecules in the second-sphere from outer-sphere water, these two groups are often referred to as outer-sphere water molecules. Relaxivity can be factored into these two components of inner-sphere r_1^{IS} and outer-sphere (r_1^{OS}) relaxivity (eq 2):

$$r_1 = r_1^{IS} + r_1^{OS} \qquad (2)$$

It should be noted that r_1^{OS} can represent a major component of the observed relaxivity and is about 40% of the relaxivity of approved ECF agents.

Inner-Sphere Relaxivity. For water ligands in the inner-sphere, relaxivity depends on the extrinsic parameters applied magnetic field strength and temperature, and on intrinsic molecular factors, including the number of water molecules in the inner-coordination sphere, q; the kinetics of water exchange $k_{ex} = 1/\tau_m$, where τ_m is the mean residency time of the water ligand; the rotational dynamics of the molecule, described by a rotational correlation time τ_R; the electron spin S of the complex; and the electronic relaxation times T_{1e} and T_{2e}, which are sometimes referred to as τ_S. Figure 16
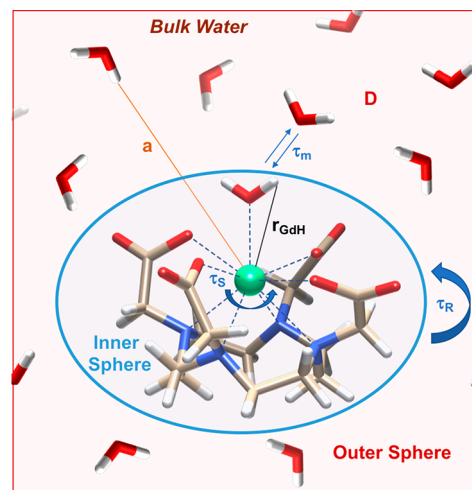
Figure 16. Pictorial description of the parameters that influence the relaxivity of a MRI contrast agent.

summarizes these molecular factors along with outer-sphere relaxation that is described by the translational diffusion correlation time τ_D and a distance of closest approach a (Figure 16).

Combining the definition of relaxivity with the Bloch equations for a system in fast two site exchange, where one pool (bulk water) is present at much higher concentration than the other pool (metal bound water), one arrives at eqs 3 and 4 which describe inner-sphere relaxivity. Here T_{im} is the T_i ($i = 1$ or 2) of the coordinated water molecule and is described by the Solomon-Bloembergen-Morgan equations of paramagnetic relaxation theory,[104−108] eqs 5 and 6. Here r_{MH} is the metal ion to water hydrogen distance, γ_H is the proton magnetogyric ratio, g is the electronic g factor, μ_B is the Bohr magneton, μ_0 is the vacuum permeability, and ω_S and ω_H are the Larmor frequencies of the electron and proton, respectively. There is also a correlation time for the magnetic fluctuation (τ_c) that is the shorter of the rotational correlation time (τ_R), the electronic relaxation time (T_{1e} or T_{2e}), or the water residency time (τ_m) defined by eq 7. The T_1 effect is dipolar, and $1/T_{1m}$ depends on the electronic spin state of the complex, indicating that larger S values give greater relaxation. It depends on both the nuclear and electron magnetogyric ratios, indicating that relaxation is greater for H than for other nuclei with lower γ values.[109] The T_2 effect is contributed by both dipolar (through space) and scalar (contact, through bonds) interactions. The scalar contribution depends on the hyperfine coupling constant between the metal ion and the water proton

and a correlation time τ_{sc} for that interaction, eq 8. The scalar contribution to proton relaxation is small for Gd(III) complexes but can be appreciable for Mn(II) and Fe(III).

$$r_1^{IS} = \frac{q/[H_2O]}{T_{1m} + \tau_m} \tag{3}$$

$$r_2^{IS} = \frac{q}{[H_2O]} \frac{1}{\tau_m} \left(\frac{T_{2m}^{-1}(\tau_m^{-1} + T_{2m}^{-1}) + \Delta\omega_m^2}{(T_{2m}^{-1} + \tau_m^{-1})^2 + \Delta\omega_m^2} \right) \tag{4}$$

$$\frac{1}{T_{1m}} = \frac{2}{15}\left(\frac{\mu_0}{4\pi}\right) \frac{\gamma_H^2 g_e^2 \mu_B^2 S(S+1)}{r_{MH}^6} \left[\frac{7\tau_{c2}}{1+\omega_S^2\tau_{c2}^2} + \frac{3\tau_{c1}}{1+\omega_H^2\tau_{c1}^2} \right] \tag{5}$$

$$\frac{1}{T_{2m}} = \frac{1}{15}\left(\frac{\mu_0}{4\pi}\right) \frac{\gamma_H^2 g_e^2 \mu_B^2 S(S+1)}{r_{MH}^6} \left[4\tau_{c1} + \frac{13\tau_{c2}}{1+\omega_S^2\tau_{c2}^2} + \frac{3\tau_{c1}}{1+\omega_H^2\tau_{c1}^2} \right]$$
$$+ \frac{S(S+1)}{3}\left(\frac{A}{\hbar}\right)^2 \tau_{sc} \tag{6}$$

$$\frac{1}{\tau_{ci}} = \frac{1}{\tau_R} + \frac{1}{\tau_m} + \frac{1}{T_{ie}}; \quad i = 1,2 \tag{7}$$

$$\frac{1}{\tau_{sc}} = \frac{1}{\tau_m} + \frac{1}{T_{1e}} \tag{8}$$

$$\frac{1}{T_{1m}} = \frac{C}{r_{GdH}^6} \times \left[\frac{3\tau_C}{1+\omega_H^2\tau_C^2} \right] \tag{9}$$

$$r_1^{IS} = C \times q \times \tau_r \tag{10}$$

Because the electron Larmor frequency is much higher than the proton frequency, the term $\omega_s\tau_{c2}$ becomes very large by about 0.1 T, and thus the "7" term in eq 5 becomes negligible at applied fields above 0.1 T and reduces to eq 9 where C represents the physical constants in eq 5. For simple metal complexes, T_{1m} is always large (several microseconds) compared with the mean residency time of the metal-bound water molecule (submicrosecond at 37 °C for most Gd(III) and Mn(II) complexes, so $T_{1m} \gg \tau_m$). For such complexes, the dominant correlation time at most imaging fields ($B_0 > 0.2$T) will be the rotational correlation time. In these cases, inner-sphere relaxivity can be approximated to eq 10 and depends on only q and the rotational correlation time.

In these complexes, the relaxivity is almost always limited by the fast rotation of the complex (short τ_R, ~ 50−200 ps at 37 °C).[110,111] The relaxivity could be increased by slowing down its rotation (longer τ_R) by enhancing the molecular weight of the paramagnetic compound. For instance, this can be accomplished by immobilizing the complex, covalently or noncovalently, on a macromolecule.

The fluctuating field can also be caused by the water molecules that are in contact with the metal complex, but this is only observed when the rotational correlation time is very long and water exchange is extremely fast.[112]

Electronic Relaxation. At very low fields (<0.1 T), electronic relaxation is the dominant correlation time for Gd(III) and Mn(II) complexes. The influence of the electronic relaxation on the relaxivity of paramagnetic complexes depends mainly on the decay of the electron spin magnetization in the direction parallel to the external magnetic field (T_{1e}). This decay is often too fast in order to be directly measured, but the transverse electronic relaxation (T_{2e}) can be estimated by EPR. For high spin ions like Gd(III) and Mn(II), the main

relaxation mechanism is a transient zero-field splitting (ZFS). ZFS describes interelectronic interactions in paramagnetic compounds with two or more unpaired electrons. The modulation of the zero-field splitting depends on the perturbation of the ligand field through rotation, vibration, and other motions. This splitting is the result of interelectronic repulsion, spin−orbit coupling, and the action of the ligand field on the unpaired electrons of the paramagnetic metal center. The spin Hamiltonian formalism can be written as follows (eq 11):[113]

$$\hat{H}_{ZFS} = \hat{S}\cdot\hat{D}\cdot\hat{S} = D\left(\hat{S}_z^2 - \frac{1}{3}\hat{S}^2\right) + E(\hat{S}_+^2 + \hat{S}_-^2) \tag{11}$$

where D and E describe the magnitude of the operator $\hat{D}$ parallel and perpendicular to the z axis. This perturbation lifts the $2S + 1$ degeneracy at zero field, giving $S + 1/2$ (for half-integer S) doubly degenerated zero-field spin states or $S + 1$ (for integer S) zero-field spin states where one of them is nondegenerated (since $m_S = 0$), that can be written as linear combinations of the Zeeman m_S states. If an external magnetic field (B_0) is applied, the doubly degenerated levels will be lifted. In the case of high spin ions in a symmetrical environment, such as the aqua ions of Cr(III), Fe(III), Mn(II), Gd(III), or Eu(II), the zero-field splitting is averaged out. An extension of this reasoning can be applied for Gd(III) and Eu(II) complexes with polyaminocarboxylates, where f electrons are mostly shielded from the ligand field and result in a small but nonzero ZFS.

Although Gd(III) and Mn(II) complexes have nonzero ZFS, the effect of this static ZFS can usually be ignored at most field strengths where the Zeeman energy is much larger than the ZFS energy. However, NMRD relaxometers can operate at very low proton Larmor frequencies (e.g., 10 kHz), and there the Zeeman energy may be lower than the ZFS. In such instances, the widely used SBM relaxation theory does not apply.[114−117] As alternatives to Gd(III) are increasingly proposed, it is important to consider the magnitude of the ZFS of those complexes. If the ZFS is much larger than the Zeeman energy, then SBM theory may no longer apply.

In addition to this static ZFS, solvent collisions can induce distortions in the molecule resulting in a transient ZFS, and this transient ZFS can serve as an efficient relaxation mechanism. The transient ZFS broadens the line in EPR spectra.[118] The electronic relaxation rates are given by eqs 12 and 13,[119] where τ_v is a correlation time that describes the modulation of the transient ZFS, and Δ^2 is the square of the trace of the ZFS tensor.

$$\left(\frac{1}{T_{1e}}\right) = \frac{12}{5}\Delta^2\tau_v\left(\frac{1}{1+\omega_S^2\tau_v^2} + \frac{4}{1+4\omega_S^2\tau_v^2}\right) \tag{12}$$

$$\left(\frac{1}{T_{2e}}\right) = \frac{12}{10}\Delta^2\tau_v\left(3 + \frac{5}{1+\omega_S^2\tau_v^2} + \frac{2}{1+4\omega_S^2\tau_v^2}\right) \tag{13}$$

Thus, $1/T_{1e}$ decreases with the square of increasing applied field. As the field is increased, eventually $1/T_{1e} < 1/\tau_R$ and rotation dominates the overall correlation time. For instance, at 0.02 MHz, the relaxivity of Gd-DOTA is $r_1^{0.02\ MHz} = 11.3$ mM^{-1} s^{-1} compared to 7.7 mM^{-1} s^{-1} for Gd-DTPA at 25 °C, owing to the much longer T_{1e} of Gd-DOTA. But, at 20 MHz, the relaxivity of these two complexes is almost identical: $r_1^{20\ MHz} = 4.7$ mM^{-1} s^{-1} for Gd-DOTA and 4.8 mM^{-1} s^{-1} for
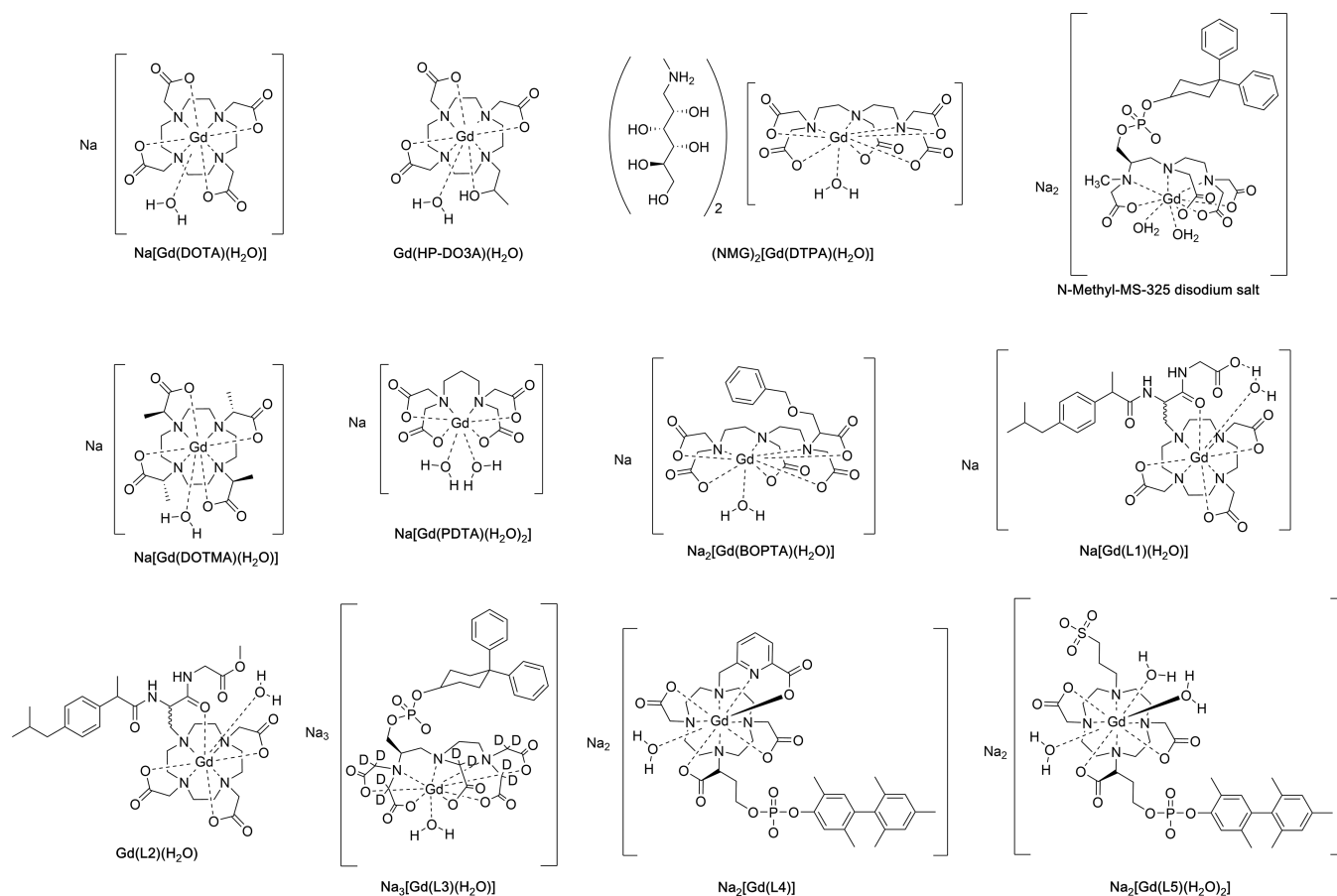
Figure 17. Gadolinium(III) complexes studied by ^{1}H ENDOR where the Gd–H(water) distance was determined.

Gd-DTPA.[120] Complexes with higher symmetry will have smaller ZFS energies and, thus, longer electronic relaxation times. For example, the axial ZFS parameter D is 24 mT for Gd-DOTA but 56 mT for Gd-DTPA.[107] Intramolecular electronic relaxation between several Gd(III) ions can shorten T_{1e} if the metals are very close ($\ll 10$ Å).[121,122] However, this effect is only manifest on relaxivity at low fields. In the design of novel optimized MRI contrast agents, electronic relaxation is usually not taken into account, since its contribution to relaxivity is negligible at the magnetic field strengths that are typically used in clinic (≥ 1.5 T).

Metal–Water Hydrogen Distance (r_{MH}). Because this distance enters as the inverse sixth power to the relaxation rate, small changes in r_{MH} could have a profound effect on relaxivity, especially if this distance could be tuned. Caravan, Raitsimring, and co-workers showed that the Gd–H(water) distance could be determined on frozen solutions using high field proton electron nuclear double resonance (^{1}H ENDOR) spectroscopy.[121,123−128] They investigated a range of $q = 1$ and $q = 2$ complexes with different water exchange kinetics and found that r_{GdH} was consistently 3.05 Å distributed within a range of ±0.07 Å. That is, there is a normal distribution of Gd–H distances ranging from 2.98–3.12 Å with the average distance being 3.05 Å (note that the initial paper gave a distance of 3.1 Å obtained at a lower field; this was refined by measurements at very high field).[121,127] They compared the DTPA derivatives Gd-DTPA, Gd-BOPTA, and MS-325 and found that the ENDOR spectra were superimposable, indicating a common r_{GdH}, although earlier reports using indirect measures of r_{GdH} had proposed differences in r_{GdH}

among these complexes.[129,130] They measured Gd-DOTA, Gd-DOTMA, Gd-HPDO3A, and two Gd-DOTAla derivatives and again found $r_{GdH} = 3.05$ Å and no difference in the ENDOR spectra. They also measured 3 different $q = 2$ complexes and there too observed the same r_{GdH} value, see Figure 17.

Number of Water Molecules (q). Inner-sphere relaxivity is directly proportional to the number of water ligands (see eqs 3 and 4). Increasing the hydration number (q) should increase the inner-sphere relaxivity, but an increase in q is often accomplished at the cost of decreased thermodynamic stability and/or kinetic inertness.[131] A second consideration is that two cis coordinated water ligands can often be displaced by a coordinating anion in vivo. Thus, it is important to know the hydration state of the complex in solution. Unlike certain other metal ions, the coordination number of Gd(III) and high spin Mn(II) varies and may not be easily predicted. Gd(III) complexes in aqueous solution are often CN9 but many CN8, and even CN7 and CN10 examples exist.[132,133] Mn(II) complexes in aqueous solution tend to be CN6 and CN7.

There are several physical methods that allow estimation of the number of water ligands coordinated to Gd(III). There are surrogate approaches where Gd(III) is replaced by another Ln(III) similar in ionic radius. For instance, the induced paramagnetic shift of $H_2^{17}O$ is proportional to q under fast exchange conditions. Geraldes and Peters and co-workers showed that the $H_2^{17}O$ shift induced by the Dy(III) complex could be measured and compared to $[Dy(H_2O)_8]^{3+}$ to estimate q for the new complex.[134] However, this method requires large amounts of sample (>10 mM).
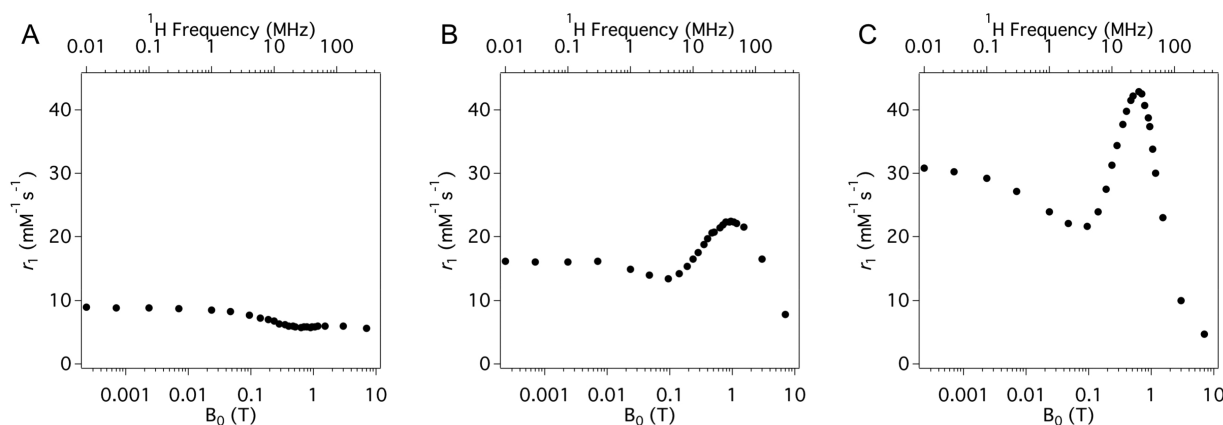
Figure 18. Experimental ^{1}H NMRD profiles showing relaxivity [per Gd(III)] versus field strength for Gd-DTPA derivatives with short (A, MS-325), intermediate (B, EP-1084), and long (C, MS-325 in HSA solution) rotational correlation times.

Another method is based on luminescence lifetime measurements of the corresponding Eu(III) or Tb(III) analogs measured in both H_2O and D_2O. Coordinated H_2O quenches the emission of Eu(III) or Tb(III) more efficiently than D_2O. The reason for this lies in the different energy levels of the vibrational overtones of the O−H and O−D oscillators. The vibrational overtones of O−D are lower in energy in comparison to an O−H oscillator, which makes the energy transfer from Eu(III) or Tb(III) excited states into the O−D oscillators higher harmonics less likely. Horrocks and Sudnick showed that a simple empirical equation could be used to relate these decay rate constants to q,[135] and some refinements on this approach have been reported.[136,137] A benefit of this approach is that low micromolar concentrations can be used, and the method is also generally useful for estimating q in complex matrices such as biological samples.

Another more direct method is electron−nuclear double resonance (ENDOR) spectroscopy of the Gd(III) complex.[126] Raitsimring et al. used high field pulsed [17]O ENDOR and showed that the presence of coordinated water ligands was associated with two narrow lines with a splitting of about 1.33 MHz originating from the $-1/2 \Leftrightarrow +1/2$ transitions of the [17]O nuclei.[125] By comparison of the amplitude of these transitions to the Gd(III) aqua ion ($q = 8$), the number of coordinated waters in the unknown complex could be determined.

As noted above, the Gd−H(water) distance determined by ^{1}H ENDOR was invariable and about 3.05 Å. As a result the position of the ENDOR transition associated with this coordinated water was constant. Raitsimring et al. exploited this effect to estimate q by ^{1}H ENDOR. The difference in the intensity of the ^{1}H ENDOR spectra measured in H_2O and in D_2O is proportional to the number of exchangeable protons. This technique allows the direct utilization of the gadolinium-(III) compound, and also protein bound Gd(III)-complexes can be directly measured.[124,126]

Theoretical calculations can also provide an idea of the hydration number of the Gd(III); however, one should be cautioned that the energy difference between CN9 and CN8 Gd(III) complexes is small and can also be strongly influenced by the presence of solvent water. X-ray crystallography provides evidence of the hydration number in the solid state, but again, this may not reflect the hydration number in solution.[109] Furthermore, weakly coordinating ions such as nitrate or acetate may crystallize coordinated to a Gd(III)

complex, but these will typically be displaced by water ligands in aqueous solution.

Gale et al. developed a simple NMR method to measure the hydration number of Mn(II) complexes.[138] They demonstrated that the maximum in a plot of transverse O-17 relaxivity (r_2^O) versus temperature was directly proportional to the number of coordinated water ligands. This technique could be performed with micromolar concentrations of chelate, allowing for its use in interrogating the hydration number of protein-bound chelates. From the same data set, one can also determine the water exchange kinetics.

Tumbling of the Molecule (τ_R). As discussed above, at the most common field strengths used for imaging, the dominant correlation time is almost always rotational diffusion. For instance, for small monomeric gadolinium(III) complexes, τ_R is about 0.1 ns, and at low magnetic field strength and 37 °C, slowing down the rotation will result in an increase of the relaxivity. Reducing the rate of molecular tumbling (that is, making τ_R longer) will enhance the relaxivity of a T_1 contrast agent at low field strength. However, at higher fields, relaxivity will increase with increasing τ_R up to a point, after which relaxivity will decrease with further increases in τ_R. This is because of the $3\tau_c/(1+\omega_H^2\tau_c^2)$ term in eq 5; as τ_c increases, relaxivity will increase until the product $\omega_H^2\tau_c^2 > 1$, which will occur at high fields and/or high values of τ_c. This is illustrated in Figure 18 where field-dependent relaxivity profiles, so-called nuclear magnetic relaxation dispersion (NMRD), are shown for Gd(III) complexes with increasing rotational correlation times. Figure 18A shows the NMRD profile for MS-325 in phosphate-buffered saline where τ_R is on the order of 0.1 ns. In the presence of human serum albumin (Figure 18C), much of the MS-325 is protein bound with an effective τ_R of about 10 ns.[17,18,139−141] Slow rotation results in a multifold increase in relaxivity at low fields, but at 7 T, the relaxivity has dispersed to the point that the unbound form of MS-325 has slightly higher relaxivity. Figure 18B shows the per Gd(III) NMRD profile of EP-1084 which is a contrast agent comprising 4 Gd-DTPA chelates and two fibrin binding peptides.[142] This compound has a relatively high molecular weight, resulting in an intermediate τ_R. While the relaxivity of EP-1084 is lower than MS-325/HSA at low fields by 1.5 T, the relaxivity is almost the same, and at 3 T and 7 T, the relaxivity of EP-1084 is higher than MS-325/HSA. All three examples involved a Gd-DTPA derivative where the differences in relaxivity arose solely because of differences in rotational correlation time. Strategies
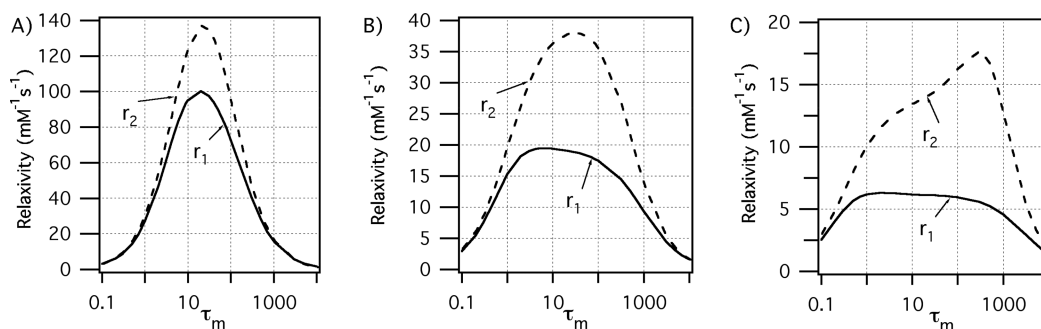
Figure 19. Effect of water residency time (τ_m, ns) for an inner-sphere water on r_1 (—) and r_2 (---) under optimal rotational conditions (τ_R, ns) at 0.47 T (A, 20 ns), 3 T (B, 0.5 ns), and 9.4 T (C, 0.5 ns). The optimal τ_m range increases as field increases. Reproduced with permission from ref 144. Copyright 2009 John Wiley and Sons.

to optimize the rotational correlation time are further discussed in section Optimizing the Rotational Correlation Time (τR) of Gd(III)-Based Contrast Agents.

Rotational diffusion can be estimated through several physical methods, such as NMR relaxation, fluorescence lifetime measurements, or can be calculated from the Stokes−Einstein equation.[2]

Exchange Rate of the Water Molecule. The water exchange rate k_{ex} ($1/\tau_m$ where τ_m is the residency time of the coordinated water) is another key and tunable molecular parameter. Relaxivity has a $1/(T_{1m} + \tau_m)$ dependence. For small Gd(III) and Mn(II) complexes, $T_{1m} \gg \tau_m$, and so these complexes tend not to be limited by slow water exchange. However, if rotation is slowed and T_{1m} is decreased then water exchange may limit relaxivity. For other metal ions, water exchange may be slow relative to T_{1m}.[143]

Figure 19 shows a simulation of the effect of the water exchange on gadolinium(III) complexes at three different magnetic fields: 0.47, 3.0, and 9.4 T. At each of these field strengths, the rotational correlation time (τ_R) is near the optimum value for that specific field strength, that is 20, 1.5, and 0.5 ns, respectively.[144] Note that the y axis range differs because the theoretical maximum relaxivity decreases with increasing field strength. At 0.47 T, very high relaxivities can be attained but only for a narrow range of water exchange rates. At the higher fields, a broader range of water exchange rates can yield near optimal relaxivity.

Relaxivity is limited by both very slow (long τ_m) and very fast exchange (Figure 19). In the latter case, if exchange is too fast then water is not present long enough for there to be a high probability of relaxation. Modifications of τ_m are usually related to the stabilization or destabilization of intermediates that participate in the water exchange mechanism and/or with changes in the population of the isomers present in solution. For instance, for DOTA-type ligands, it was found that water exchange is around 50 times faster in the twisted-square antiprismatic (TSAP) isomer compared to the square antiprismatic (SAP) isomer. The main explanation for this is the steric crowding at the water binding site, which favors the release of the metal-bound water in a dissociative mechanism.[145] Figure 20 shows a simplified vision of the SAP and TSAP conformations in a DOTA-type complex. From a geometric point of view, these two isomers can be distinguished by the twist angle between the plane defined by the chelating oxygen atoms and the chelating nitrogen atoms: ∼ 25° for the TSAP isomer and ∼40° in the case of the SAP form.
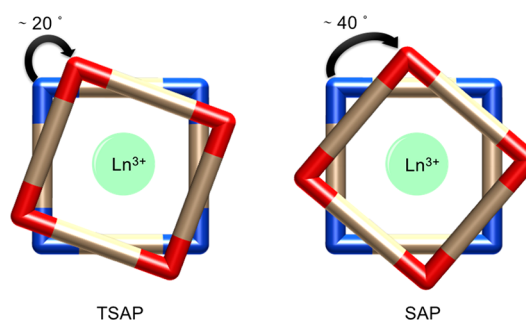
Figure 20. TSAP and SAP isomers of DOTA-type ligands of macrocyclic lanthanide chelates.

For DOTA-like structures, two sources of chirality should be considered: the orientation of the chelates ($\delta\delta\delta\delta$ or $\lambda\lambda\lambda\lambda$) and the helicity of the pendant arms [Δ (clockwise arrangement) or Λ (counter clockwise arrangement)] (Figure 21).[146−148]

The TSAP isomer has the same stereochemistry at both positions [$\Delta(\delta\delta\delta\delta)$ or $\Lambda(\lambda\lambda\lambda\lambda)$], whereas the SAP isomer has the opposite stereochemistry at the two positions [$\Delta(\lambda\lambda\lambda\lambda)$ or $\Lambda(\delta\delta\delta\delta)$]. Interconversion between the two isomers is possible by ring inversion ($\delta\delta\delta\delta \leftrightarrow \lambda\lambda\lambda\lambda$) or by arm rotation ($\Delta \leftrightarrow \Lambda$). Both arm rotation and ring inversion performed in a successive manner or concerted way lead to an enantiomerization process. Because of steric repulsion between the nitrogen and oxygen donors, the distance between the N4 and O4 plane is increased in the TSAP isomer,[149] thereby making the metal center less accessible for the coordination of a water molecule.[145] On the other hand, within this isomer more bulky pendant arms can be accommodated. Substitution on the α position of the pendant arms slows or completely eliminates the arm rotation process,[150−153] while substitution on the cyclen backbone restricts the ring inversion motion.[154−157] Substitution at both positions effectively locks the macrocycle into a single conformation.[158−161]

The water-exchange rate can be measured from the temperature dependence of the ^{17}O NMR transverse relaxation rate of solvent water in the presence and absence of the metal complex at high fields.[143]

Outer-Sphere Relaxivity. In addition to the inner-sphere contribution to relaxivity, the second-sphere and, in general, the outer-sphere contribution also needs to be taken into account. The relaxivity derived from the water molecules diffusing close to the gadolinium(III) complex can be predicted from the hard-sphere model of Hwang and Freed,[162] where the relaxation depends primarily on the
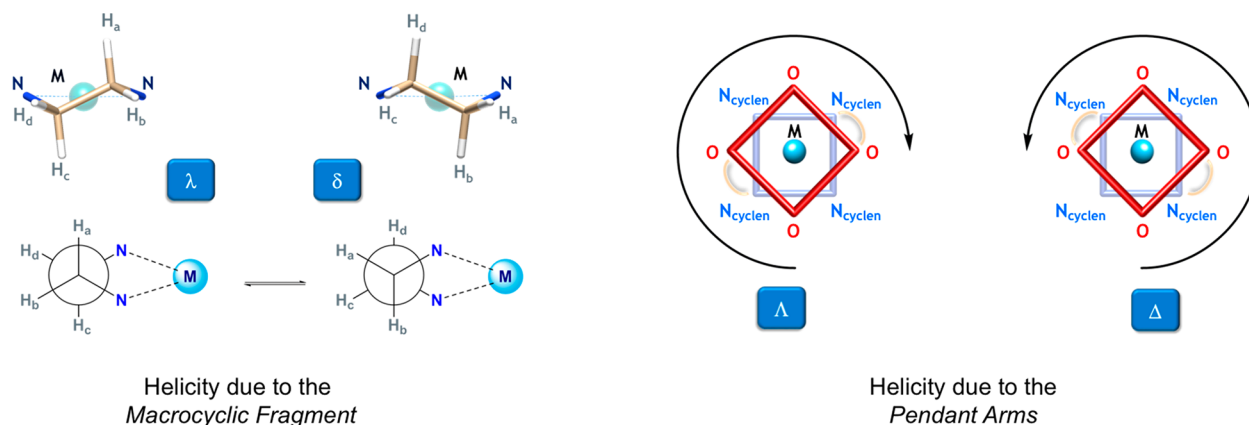
Figure 21. Chirality sources within DOTA-like macrocyclic structures.
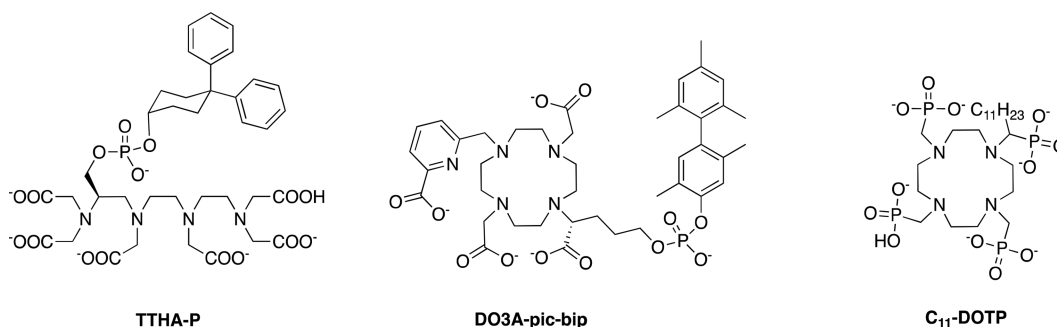
Figure 22. Ligands forming HSA-binding Gd(III) complexes without any water molecules in the inner-sphere ($q = 0$).[17]

diffusion coefficient of water and the distance of closest approach to the metallic center.

Second-sphere relaxivity is an operational definition that refers to complexes that have water molecules or exchangeable protons in the second coordination sphere that have a residency time longer than the diffusion lifetime. Second-sphere relaxivity is described by the same equations as inner-sphere relaxivity, but here, the dominant correlation time is the residency time of the second-sphere protons. In general, this effect is seen when independently determined molecular parameters cannot account for the observed relaxivity.[109] Figure 22 shows some selected examples of $q = 0$ complexes with an important second sphere effect.

For instance, the relaxivities of $[Gd(TTHA-P)]^{3-}$ in buffer and in the presence of HSA are 2.1 and 8.0 mM^{-1} s^{-1}, respectively, and the relaxivities of $[Gd(DO3A-pic-bip)]^{2-}$ in buffer and in the presence of HSA are 3.1 and 7.0 mM^{-1} s^{-1}, respectively. Although these values are lower than that of $q = 1$ compounds, their relaxivity is non-negligible. When bound to human serum albumin, the relaxivity is increased by 3 to 4-fold due to the long-lived proton(s) near the Gd(III)-center.[17] $[Gd(C_{11}-DOTP)]^{5-}$ is also a $q = 0$ complex, but its relaxivity is much higher than that of $[Gd(TTHA-P)]^{3-}$, that is a molecule of similar size. The reason for this is the negatively charged surface due to the phosphonate moieties, which also furnish a favorable arrangement of the water molecules in the second coordination sphere.

T_2-Contrast Agents. In the case of T_2-contrast agents, as T_2 is shortened, the water line width increases, so the signal decreases, leading to a negative image contrast. At the molecular level, the rotation of the complex in solution creates a fluctuating magnetic field that gives rise to T_2 and can be described according to the Solomon-Bloembergen-Morgan (SBM) theory, eq 6.[2] Pure T_2 relaxation requires access of the water molecule to the contrast agent. For discrete complexes, SBM theory can also describe T_2 relaxation. However, for $1/T_{2m}$, there is a field independent term for both dipolar and scalar relaxation such that r_2 does not decrease at high fields the way that r_1 does. In addition there is an additional relaxation mechanism called Curie spin relaxation that results in increased r_2 at high fields, especially for ions with large magnetic moments.[163]

T_2^* takes into account the inhomogeneity of the local magnetic field (B_0) and is related to T_2 by eq 14:

$$1/T_2^* = 1/T_2 + \gamma \Delta B_0 \tag{14}$$

The magnetic susceptibility of the paramagnetic agent causes local changes in B_0 and induces this T_2^* effect. This magnetic susceptibility depends on the concentration of the contrast agent and its molar susceptibility. Since Tb(III) and Dy(III) have larger moments than Gd(III), their complexes could be used as contrast agents with increased susceptibility.[164] These effects can be pronounced in vivo where compartmentalization of the contrast agent naturally occurs. For instance as the contrast agent passes through the blood vessels in the brain, there is a large susceptibility gradient between the blood, where the contrast agent resides, and the brain tissue where the contrast agent is absent. This creates a large T_2^* relaxation effect and is used clinically to measure brain perfusion.[165]

Iron oxide nanoparticles have much larger magnetic susceptibilities than discrete coordination complexes. SPIONs are all T_2-contrast agents that dephase the spins of the nearby protons of the water molecules, leading to a decrease in the signal. In the case of superparamagnetic particles, outer-sphere
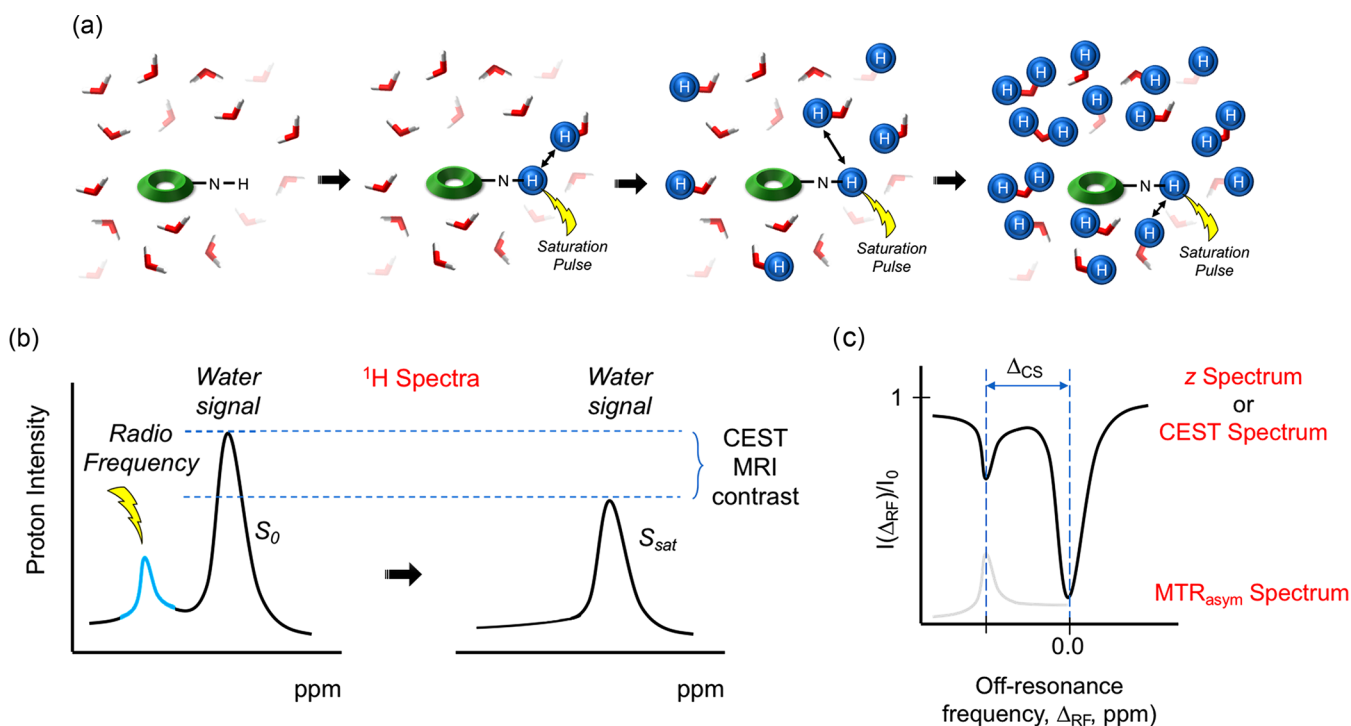
Figure 23. (a) Illustration of a CEST process: exchangable amine protons of a CEST agent are selectively saturated using radio frequency (RF) irradiation, leading to a reduction of the amine ^{1}H signal intensity. Because of chemical exchange, the saturated protons (shown as blue spheres) are transferred to the bulk water pool. Continuous chemical exchange during the saturation experiment leads to the amplification of the water signal reduction. (b) Continuous application of RF pulses leads to the saturation of more bulk water protons, thereby decreasing the ^{1}H NMR signal. (c) Z-spectrum (top) normalized water intensity (I/I_0) vs off-resonance frequency (Δ_{RF}), taking as 0.0 ppm the water resonance and the magnetization transfer ratio asymmetry (MTR$_{asym}$) (Δ_{CS} = separation in chemical shift between the two proton pools) spectrum and (bottom) which shows the Z-spectrum asymmetry vs off-resonance frequency (Δ_{RF}).[180,181]

theory for T_2 relaxivity predicts that their effectiveness is highly dependent on both the saturation magnetization (M_S) value and the effective radius (r) (eq 15):

$$\frac{1}{T_2} = (256\pi^2\gamma^2/405)\kappa M_S^2 r^2/D(1 + l/r) \qquad (15)$$

where D is the diffusivity of water molecules, l is the thickness of an impermeable surface coating, and $\kappa = V^*/C$ where V^* is the volume fraction and C is the total iron concentration.

Recently, many novel platforms, such as carbon nanotubes (iron oxide-doped),[166] zeolites (Dy(III)-doped),[65] and metal–organic frameworks (MOFS) (Dy(III) and Gd(III)-doped),[167] have been studied as potential T_2-based contrast agents.

Another type of T_2 contrast is derived from chemical exchange and is denoted T_{2ex}.[168,169] The effect arises from chemical exchange of protons that have a different frequency than bulk water. Here the ideal chemical exchange rate ($10^4 - 10^7$ Hz) of protons is slower than what is required for good T_1 relaxation agents.[170] Large pseudocontact shift of the protons that are close to a paramagnetic MRI contrast agent can produce a very large MR frequency for the proton that depends on the external magnetic field applied and that can generate a large T_{2ex} relaxation effect.[92] However, this mechanism produces relaxivities that are much lower than dipolar relaxation from Gd(III) or Mn(II) complexes.

3.3.2. Chemical Exchange Saturation Transfer. Comparison of pre- and postinjection images allows the detection of enhanced regions using an exogenous relaxation agent. Ideally these pre- and postinjection images should be acquired during the same scanning session, otherwise there may be problems of coregistering the pre- and postinjection data sets because the subject moved. However, for targeted imaging and imaging with nanoparticles, it often takes hours for the agent to accumulate at its target and/or for the background signal to clear. Another potential limitation of relaxation agents is that it can be difficult to quantify the agent in vivo, especially if the relaxivity changes.[171,172] Theoretically, all of these short-comings can be solved by using chemical exchange saturation transfer (CEST) agents.[45]

CEST agents contain a pool of labile protons that can be exchanged with the protons of the bulk water in an intermediate to slow rate on the NMR time scale ($k_{ex} \leq \Delta\omega$, where $\Delta\omega$ is the chemical shift frequency difference between the exchangeable pool frequency and the bulk water frequency.[170,173] A slow water exchange rate is optimal for the production of a CEST signal at a low radiofrequency pulse for in vivo studies.[174] The application of a presaturation pulse at the frequency of the exchangeable protons leads to the transfer of some saturated spins into the water pool, which attenuates the signal of the bulk water.[175−177] One of the major advantages of this technique is that despite the small concentration of the solute molecules (micromolar to millimolar range), the signal can be amplified several orders of magnitude[171] through the transmission of the magnetization to the bulk water.[178]

When a radiofrequency (RF) pulse is applied at the resonance frequency of the labile protons of the CEST agent then saturation will occur. Because of chemical exchange, the magnetic saturation will spontaneously be transferred to the bulk water over time (Figure 23A). This saturation transfer will
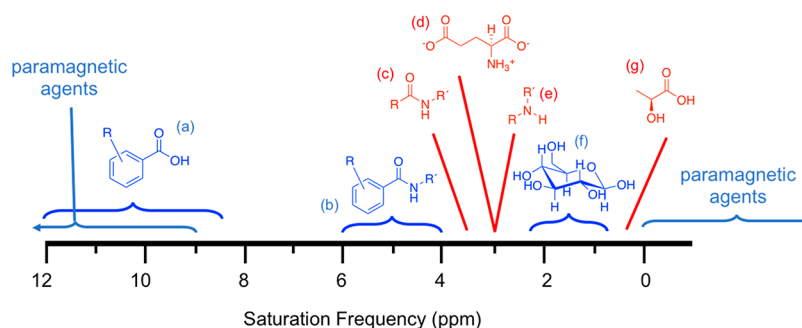
Figure 24. Exogenous agents (blue) and endogenous biomolecules (red) that can be detected when applying a saturation pulse at the magnetic resonance frequencies listed in the chart. (A) Aryl acid agents, (B) aryl amide agents, (C) amides, (D) glutamate, (E) amines, (F) glucose, and (G) lactic acid.[189] Paramagnetic compounds have much wider chemical shift ranges.
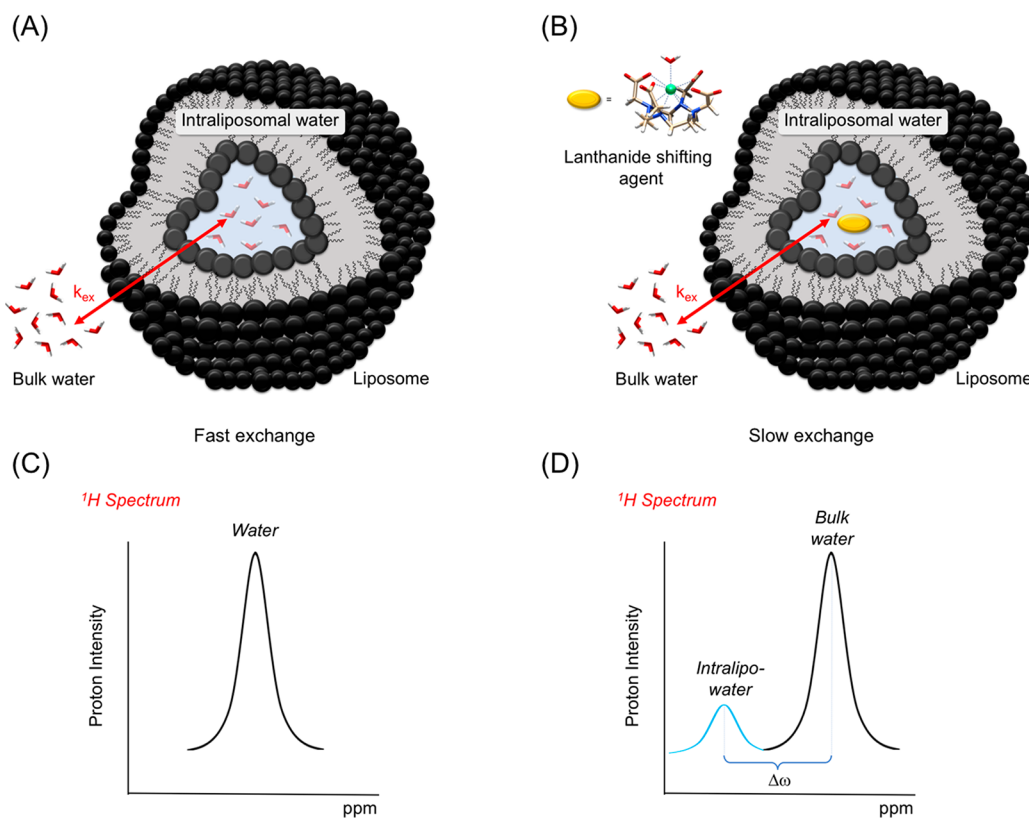
Figure 25. Simplified scheme of a (A) liposome and a (B) lipoCEST agent. ¹H NMR spectra focused on the region of the water signal, in a (C) regular liposome and in a (D) lipoCEST agent.

lead to a decrease in the water signal, through the continuous transfer of excited protons to the pool water (Figure 23, panels B and C).[179]

The CEST effect is sensitive to environmental parameters, such as temperature, pH, membrane fluidity and cation concentration, as well as the concentration of the CEST agent.[171] The saturation will continue until a steady state is reached or until the RF pulse is turned off. Using an exchange model consisting of two distinguishable pools (a small solute pool and large bulk water pool, with no back exchange of saturated protons), the proton transfer ratio (PTR) in the steady state can be estimated under the assumption that the radiofrequency irradiation of the solute pool does not affect the bulk water pool (eqs 16 and 17):[176]

$$PTR = x_S \times \alpha \times k_{sw} \times T_{1w}(1 - e^{-t_{sat}/T_{1w}}) \tag{16}$$

where

$$x_s = \frac{[\text{exchangeable solute protons}]}{[\text{water protons}]} = \frac{k_{ws}}{k_{sw}} \tag{17}$$

According to these equations, the CEST effect increases with the fractional concentration x_s, saturation efficiency α, the exchange rate k_{sw}, and the longitudinal relaxation time of bulk water T_{1w}.[182] The CEST effect depends on the applied field. High fields allow a better frequency separation in the slow-exchange condition and reduces interference of direct water saturation. With the assumption that transverse relaxation is negligible, the saturation efficiency at a given power (B_1) can be estimated as follows (eq 18):

$$\alpha \approx \frac{(\gamma B_1)^2}{(\gamma B_1)^2 + (k_{sw})^2} \tag{18}$$

For analyzing the CEST effect, the most common metric used is the "zero-order-spillover correction", called magnetization transfer ratio asymmetry (MTR_{asym}) (eq 19):

$$MTR_{asym}(\Delta_{CS}) = \frac{I(-\Delta_{CS}) - I(\Delta_{CS})}{I_0} \quad (19)$$

where $I(\Delta_{CS})$ and $I(-\Delta_{CS})$ are signal intensities acquired with RF irradiation applied on-resonance with the exchanging pool ($I(\Delta_{CS})$) and at the frequency symmetric around water ($I(-\Delta_{CS})$), and I_0 is the reference signal intensity acquired without RF presaturation. In the z spectrum, the normalized water signal intensity is monitored versus the frequency of the off-resonance saturation.[175,183] The CEST signal is commonly represented as a percent decrease in total bulk water intensity. With the assumption that the saturation of the bound water signal is complete, the net magnetization of water protons at steady-state (M_z/M_0) can be estimated as follows (eq 20):

$$M_z/M_0(\%) = 100(1 + cqT_1/55.5\tau_M)^{-1} \quad (20)$$

where c is the concentration of the CEST agent, q is the number of exchanging protons, 55.5 represents the molar concentration of bulk water, T_1 is the relaxation time of bulk water, and τ_M is the exchange lifetime of the exchanging proton ($1/\tau_M = k_{ex}$).[184]

Common CEST agents include amino acids, sugars, nucleotides, or heterocyclic rings in their structure.[185] The paramagnetic metal ion present in ParaCEST agents can be a lanthanide [such as Eu(III), Tm(III), and Yb(III)] or a transition metal ion [Fe(II), Co(II) or Ni(II)], with a short electronic relaxation time. In this case, the election of the macrocyclic backbone as well as the pendant arms are key to control the oxidation state and the spin state of the metal, and hence, the stability of the complex.[174,186]

There are four categories of exogenous CEST contrast agents: diamagnetic (DiaCEST), paramagnetic (ParaCEST), liposomal (lipoCEST), and hyperpolarized gas (hyperCEST, see in section on hyperpolarized molecules).[176,187,188] Even if all rely on exchanging protons, the nature of the exchanging protons is different. For example, in the case of diamagnetic agents (DiaCEST agents), the exchangeable protons usually belong to −NH and −OH groups, and the chemical shift difference ($\Delta\omega$) with the bulk water protons is less than 6 ppm (Figure 24). This relatively small chemical shift difference requires slow exchange rates in order to be detected, and this slow exchange usually limits the magnitude of the CEST effect. In the case of paramagnetic (ParaCEST) agents (chelates that contain paramagnetic ions), the chemical shift difference ($\Delta\omega$) of the labile protons with the bulk water protons can be much larger, up to a few hundred ppm, depending on the metal structure. This larger shift difference means that there can be much faster proton exchange, but that still obeys the slow exchange condition.[171]

LipoCEST agents are composed of liposomes that encapsulate a chemical shift agent in the inner cavity, thus shifting the resonating frequency of intraliposomal water protons by 1 to 5 ppm from that of extraliposomal water protons (Figure 25).[190] The separation in chemical shift ($\Delta\omega$) between the two proton pools in slow exchange ($\Delta\omega > k_{ex}$, k_{ex} = exchange rate) is described in eq 21:

$$2\pi \times |\nu^{bulk\ water} - \nu^{Intraliposomal\ water}| = \Delta\omega \quad (21)$$

Liposomes present large amounts of equivalent water molecules with exchangeable protons ($10^6 - 10^8$) in their inner cavities, that are in exchange with the bulk water protons.[190] By introducing a shift agent inside the liposome, the resonance of the intraliposomal water is shifted relative to the water outside the liposome. The shift agent in LipoCEST agents is usually a lanthanide complex in which the ninth coordination site of the metal ion is occupied by a water molecule in fast exchange with the intraliposomal water molecules. The CEST effect is generated by applying a radiofrequency pulse at the resonance frequency of the intraliposomal water.

HyperCEST is a technique that combines CEST with hyperpolarized MRI and has been typically performed with ^{129}Xe. ^{129}Xe is very soluble in organic solvents and aqueous solutions (including blood plasma) and possesses a highly polarizable electron cloud (being highly sensitive to the molecular environment and thus allowing the display of well-resolved chemical shifts of solvents, small molecules or proteins it associates with) and can be easily hyperpolarized, usually using spin-exchange optical pumping (SEOP) where the polarization is transferred from electronically polarized rubidium atoms in the vapor state to ^{129}Xe nuclei.[191] Because the natural abundance of xenon in the air is at the trace level, no background signal is observed. ^{129}Xe can be encapsulated in molecular cages that have been functionalized to bind to a desired target; however, direct detection of the hyperpolarized encapsulated Xe is limited because the Xe can diffuse out of the cage, with only about 1% of the cage being occupied at a given time.[192] Schröder et al. showed that the caged ^{129}Xe resonance could be saturated and the saturation transferred to the larger unbound ^{129}Xe resonance in a manner that increased the detection sensitivity over 3300 fold relative to direct detection of the bound species.[193] This had led to various targeted, caged ^{129}Xe compounds.[187,193−197] A further potential benefit of ^{129}Xe is that it can be inhaled and transferred to the bloodstream in the lungs. Thus, the hyperpolarized signal can be replenished over time by having the subject breathe ^{129}Xe enriched air.

CEST benefits from imaging at high field (7 T and above), since high magnetic fields increase the chemical shift in Hz, and can improve the specificity of the technique when several CEST agents are present. Also, at higher fields the T_1 relaxation time of water is increased, making possible a longer accumulation of the saturation of the bulk water, thus increasing the detectable CEST effect.[179]

While CEST has several advantages compared to relaxation agents, it also has some inherent limitations. A primary limitation is the sensitivity which is about 2 orders of magnitude lower than relaxation agents.[170] In addition, in the body there is an endogenous magnetization transfer effect that can interfere with the CEST signal. Finally, there are limitations to the saturation power that can be applied, otherwise dangerous heating of the subject will occur. Thus, while ParaCEST agents with very fast exchanging protons may exhibit theoretically large CEST effects compared to DiaCEST agents, this gain may not necessarily be realized in vivo because of the inability to apply enough radiofrequency power to achieve full saturation.

In order to overcome these shortcomings, Sherry and co-workers prepared europium complexes with highly shifted exchange sites (large $\Delta\omega$) and very slow water molecule exchange rates, which allows its activation through relatively

low-power RF pulses.[170,198−201] In general, there is a correlation between the polarity of the ligand pendant arms and the Eu(III)-bound water lifetime ($\tau_M = 1/k_{ex}$): phosphonates ≥ carboxylates ≫ alkyl groups ≥ simple amides.[202] For ParaCEST agents, the optimal residence time of the bound water molecule (τ_m) is from 10^{-4} to 10^{-2} s, depending on the magnetic field applied during the presaturation period.[54]

3.4. Thermodynamic Stability/Kinetic Inertness of Gd(III)-Based MRI Contrast Agents

High stability is essential for all metal-based MRI contrast agents used in medicine due to the well-known toxicities of the dissociated metal ions. For example, Gd(III) ions can irreversibly bind to skeletal tissue and are also known to block Ca(II) binding sites.[2,203]

The prediction of in vivo stability of newly developed Gd(III)-based contrast agents is based on fundamental physical properties, like solution thermodynamics, selectivity, and dissociation kinetics. The thermodynamic stability constant K_{GdL} (eq 22) provides the affinity of Gd(III) for a given ligand and gives the amount of dissociated Gd(III) that is released in the environment if the system reaches equilibrium.

$$Gd + L = GdL \qquad K_{GdL} = \frac{[GdL]}{[Gd][L]} \qquad (22)$$

The thermodynamic stability constants for the commercially approved GBCAs (Figure 3) are all large (Table 5) so that the

Table 5. Thermodynamic and Conditional (pH 7.4) Stability Constants for Commercially Approved Gd(III)-Based MRI Contrast Agents[206]

	charge	log K_{GdL}	log K_{cond}
$[Gd(DTPA)(H_2O)]^{2-}$	−2	22.46[207]	18.4
$[Gd(DTPA\text{-}BMA)(H_2O)]$	0	16.85[203]	14.8
$[Gd(DTPA\text{-}BMEA)(H_2O)]$	0	16.6[208]	15.0
$[Gd(BOPTA)(H_2O)]^{2-}$	−2	22.6[208]	18.4
$[Gd(EOB\text{-}DTPA)(H_2O)]^{2-}$	−2	23.46[209]	18.7
MS-325	−3	22.1[210]	18.9
$[Gd(DOTA)(H_2O)]^{-}$	−1	24.7[211]	17.2
$[Gd(HP\text{-}DO3A)(H_2O)]$	0	23.8[208]	17.1
$[Gd(DO3A\text{-}butrol)(H_2O)]$	0	21.8[212]	14.7

equilibrium lies heavily on the side of the intact complex GdL. Table 5 shows as well that more basic ligands form thermodynamically more stable complexes with Gd(III), which is expected given that the Gd(III) ion is a hard acid and therefore prefers hard donor atoms. The linear correlation between the sum of the ligand protonation constants (Σ log K_{1-n}) and thermodynamic stability (log K_{GdL}) was pointed out many years ago.[204] For instance, the DOTA ligand is much more basic than the DTPA-BMA ligand (sum of ligand protonation constants: Σ log K_{1-4} = 30.94 vs Σ log K_{1-4} = 19.3, respectively)[205] and forms a thermodynamically much more stable complex with Gd(III) (log K_{GdL} = 24.7 vs log K_{GdL} = 16.85, respectively). The stability constant does not factor in competition with other ions or with the acid. Very basic ligands will also show strong competition with the proton. The conditional stability constant, K_{cond}, is a useful number that gives the equilibrium constant at a given pH (e.g., pH 7.4) and is defined by eq 23,

$$K_{cond} = \frac{K_{GdL}}{(1 + K_1[H^+] + K_1 K_2[H^+]^2 + ... K_1 K_2 K_n[H^+]^n)} \qquad (23)$$

where $K_1, K_2, K_3, ..., K_n$ are the stepwise protonation constants of the ligand.

Note that $[Gd(DOTA)(H_2O)]^{-}$ with the highest basicity among these compounds exhibits the highest thermodynamic stability constant (24.7[211]). In contrast, $[Gd(DOTA)(H_2O)]^{-}$ exhibits one of the lowest conditional stability constants (17.2), which stems from its high basicity and therefore high competition for protons. Note, that the thermodynamic stability constant and the conditional stability constant for a complex with a less basic ligand like $[Gd(DTPA\text{-}BMA)(H_2O)]$ are much closer together (16.9[203] vs 14.8) since there is much less competition for protons at pH 7.4.[206] An alternate value sometimes reported is pM (-log[M]) which refers to the unchelated metal ion under a given set of conditions ($[M]_{total}$, $[L]_{total}$, pH), where the higher the pM value, the more stable the complex. In the body, there is of course competition from other metal ions and from coordinating anions. There are software programs that can model these systems of equilibria provided the individual stability constants are all known. In a highly cited paper, Cacheris et al. introduced a selectivity factor (K_{sel}) that also considers the stability constants for the corresponding Zn(II), Cu(II), and Ca(II)-complexes as well as pH (eq 24).[79]

$$K_{sel} = K_{GdL}/(1 + K_1[H^+] + K_1 K_2[H^+]^2 + ... K_1 K_2 K_n[H^+]^n$$
$$+ K_{ZnL}[Zn^{2+}] + K_{CuL}[Cu^{2+}] + K_{CaL}[Ca^{2+}]) \qquad (24)$$

The authors found selectivity factors for $[Gd(DTPA\text{-}BMA)(H_2O)]$ and $[Gd(DTPA)(H_2O)]^{2-}$ of log K_{sel} = 9.04 and log K_{sel} = 7.04, respectively, which reversed the stability trend usually seen for these two compounds ($[Gd(DTPA\text{-}BMA)(H_2O)]$: log K_{GdL} = 16.85 and log K_{cond} = 14.90 (pH 7.4) vs ($[Gd(DTPA)(H_2O)]^{2-}$: log K_{GdL} = 22.46 and log K_{cond} = 17.70 (pH 7.4)). The authors argued that this higher selectivity value for $[Gd(DTPA\text{-}BMA)(H_2O)]$ explained acute toxicity results chelates: LD$_{50}$ = 14.8 versus 5.6 mmol kg^{-1} for $[Gd(DTPA\text{-}BMA)(H_2O)]$ versus $[Gd(DTPA)(H_2O)]^{2-}$; LD$_{50}$ is the dose at which half of the animals die. The authors claimed that the lower acute toxicity of $[Gd(DTPA\text{-}BMA)(H_2O)]$ was caused by an decreased amount of Gd(III) release in comparison to $[Gd(DTPA)(H_2O)]^{2-}$.[80] However, in several studies, it was found that actually more Gd(III) is released from administration of $[Gd(DTPA\text{-}BMA)(H_2O)]$ than from $[Gd(DTPA)(H_2O)]^{2-}$.[213−216] This demonstrates that care has to be taken when predicting the in vivo stability or toxicity of Gd(III)-based contrast agents using only thermodynamic stability data.

In addition to thermodynamics, the rate at which Gd(III) can dissociate from the complex or be exchanged with an endogenous cation is an equally important factor. In this regard, the approved macrocyclic contrast agents are much more kinetically inert than the approved acyclic agents.

Unlike the thermodynamic stability constant, there is no uniform measure of inertness. This is because different complexes will undergo decomplexation or transmetalation by different mechanistic pathways. For example, for transmetalation of approved agents with Zn(II), the rate is first-order in [Zn] for acyclic chelates but is zeroth-order for the macrocyclic chelates. Note, that exchange rate constants are

Table 6. Kinetic Measures for Dissociation of Gd(III) from Commercially Approved MRI Contrast Agents under Different Conditions

	acid-catalyzed dissociation rate constants[219]	1 eq Zn, phosphate buffer pH 7.0, 37 °C[110,217]	10 mM phosphate, human plasma, 37 °C[206,220]
	k_1 (M^{-1} s^{-1})	$t_{0.8}$ (min)[a]	$t_{2\%}$ (h)[b]
[Gd(DTPA)(H$_2$O)]$^{2-}$	0.58	260−280	8.73
[Gd(DTPA-BMA)(H$_2$O)]	12.7	50−60	0.51
[Gd(DTPA-BMEA)(H$_2$O)]	8.6		0.89
[Gd(BOPTA)(H$_2$O)]$^{2-}$	0.41	600	9.08
[Gd(EOB-DTPA)(H$_2$O)]$^{2-}$	0.16	1500	51.3
MS-325	2.9×10^{-2}	3800	34.4
[Gd(DOTA)(H$_2$O)]$^{-}$	(8.4×10^{-6})[221]	>5000	>1000
	(1.8×10^{-6})[222]		
[Gd(HP-DO3A)(H$_2$O)]	(6.4×10^{-4})[204]	>5000	>1000
	(2.6×10^{-4})[223]		
[Gd(DO3A-butrol)(H$_2$O)]	2.8×10^{-5}	>5000	>1000

[a]Competition against Zn(II): 2.5 mM Gd(III)-based contrast agent, 2.5 mM ZnCl$_2$, pH = 7.0, 50 mM phosphate buffer ($t_{0.8}$ = time for R$_1$ to reach 80% of its initial value). [b]$t_{2\%}$ = time when 2% of the Gd(III) ions are released from the complex.

only comparable if the exchange mechanism per metal complex is the same. Kinetic inertness is reported in various ways. A common approach is to measure the dissociation rate constant at a low pH. Another is to measure the rate of Gd(III) release in the presence of another metal ion or by a competing ligand. Laurent et al. used a semiquantitative method where they incubated the chelate with a mixture of Zn(II) and phosphate.[110,217] Frenzel et al. studied the rate of Gd(III) release from approved agents when incubated in human plasma.[218] Table 6 shows different kinetic measures for Gd(III) dissociation from commercially approved contrast agents under acidic conditions, in the presence of Zn(II) and after incubation in human plasma.

Under all applied conditions, the macrocyclic Gd(III) complexes are the most kinetically inert, which is in line with what has been observed in in vivo studies where Gd(III) release was examined in animal models.[224] The rigidity of the macrocyclic Gd(III) complexes leads to considerably slower dissociation rates in comparison to the linear Gd(III) chelates. In general, it is believed that kinetic inertness is the most critical factor with respect to Gd(III) release. Among the acyclic chelates, kinetic inertness also appears to predict Gd(III) release in vivo.[213,214,216,224−226]

It is obvious that novel gadolinium(III)-based MR contrast agents have to meet or exceed the stability/inertness properties of the approved contrast agents. This is especially important for targeted and/or macromolecular MRI contrast agents that are expected to have longer in vivo retention times than simple hydrophilic complexes. Kinetic inertness combined with thermodynamic stability is the best predictor of in vivo toxicity so far, but the ultimate standard is how the compounds behave in vivo.

There is also a strong selection bias in our understanding of contrast agent safety that comes from the data available for the approved contrast agents. Toxicity may arise from different causes. While much can be learned from the approved agents, it should be obvious that for new complexes, increased stability/inertness may not necessarily correlate with safety/toxicity. Ultimately these compounds would need to be tested in vivo.

4. CONTRAST AGENTS OF IMPROVED SAFETY

4.1. Safety Concerns

4.1.1. Nephrogenic Systemic Fibrosis. There is a low incidence of adverse drug reactions associated with the approved contrast agents, and for years these products were considered very safe. Prince et al. reviewed data for 160000 GBCA enhanced MRI studies and found that acute adverse events occurred at a rate of 5.9 per 10000 exams, and that severe adverse events occurred about 1 in 40000 injections.[4] They also mined the FDA adverse events reporting that the system database found reports on 40 GBCA associated deaths between 2004 and 2009 that were unrelated to nephrogenic systemic fibrosis (NSF) which gave with an incidence per million doses of 0.15, 0.19, 0.97, 2.7, and 0.7 for gadodiamide, gadoversetimide, gadopentetate dimeglumine, gadobenate dimeglumine, and gadoteridol, respectively. In general the use of GBCAs is considered to be very safe.

Throughout the 1990s and early 2000s, it was commonplace to administer repeat doses of GBCA within a short time frame and to administer double and triple dose injections for angiography or perfusion weighted scans.[165,227] However, in 2006, a strong link between Gd(III)-based contrast agents and a devastating disease termed nephrogenic systemic fibrosis (NSF) was identified in renally impaired patients.[5,6] The precise mechanism of NSF onset remains undetermined, but it appears to be strongly connected to exposure to gadolinium.

The risk of NSF increases with diminishing renal function. GBCAs are eliminated almost exclusively via renal filtration and thus the agent dwells for longer in renally impaired subject, prolonging the time window for Gd(III) exposure.[228−230] Renal function is often assessed by creatinine glomerular filtration rate (GFR), and the GBCA elimination time increases with decreasing GFR. For example, GBCAs typically exhibit blood half-lives on the order of 90 min in patients with normal renal function (GFR > 90 mL/min/1.73).[230−236] In subjects experiencing moderate renal insufficiency GFR = 30−60 mL/min/1.73), the half-life is increased to 4−8 h. In cases of severe renal impairment (GFR < 30 mL/min/1.73 m^2), half-lives ranging from 18 to 34 h have been reported. Gd(III) recovery in the urine of patients with normal renal fucntion is typically >90% within 12 h of GBCA injection, but recovery decreases with decreasing renal function. For example, Gd(III) recovery as low as 76% after 5

days was reported for patients with GFR under 10 mL/min/1.73 m^2.[230] NSF incidence among the 8 FDA approved contrast agents appears to reflect the relative kinetic inertness of the Gd(III) complex as determined by in vitro assays.[237,238]

Following the linkage between NSF and gadolinium exposure, regulatory agencies like FDA placed restrictions on the use of GBCAs. In 2010, the FDA contraindicated the use of Gd-DTPA, Gd-DTPA-BMA, and Gd-DTPA-BMEA in patients with GFR < 30 mL/min/1.73 m^2 and recommended that GFR be tested for and that the use of all GBCAs should be avoided in patients with impaired renal function.[239] The American College of Radiology (ACR) 2015 manual recommends GFR screening of any patients with known or suspected renal impairment.[240] The ACR also recommends extreme caution in administering any Gd(III) contrast agent to patients of GFR < 40 mL/min/1.73 m^2, suffering acute injury or in need of dialysis. These guidelines are necessary and have essentially eliminated new incidences of NSF.

4.1.2. Brain and Body Retention of Gd(III). Mounting evidence since 2013 indicates that Gd(III) from contrast agents is irreversibly retained in the central nervous system (CNS). Concerns were first raised after reports of prolonged and nondiminishing signal enhancement in the dentate nucleus and globus pallidus of patients receiving Gd(III) contrast agents.[241] The relative degree of CNS enhancement correlated to the number of contrast enhanced examinations received.[242] A 2015 analysis of autopsy specimens confirmed that the CNS enhancement was indeed due to Gd(III) deposition.[7] As with NSF risk, the risks of CNS Gd(III) accumulation associated with each agent appear to reflect kinetic inertness, a greater degree of CNS accumulation is observed following exposure to the less kinetically inert linear agents.[243,244] However, a significantly elevated signal in the dentate nucleus has also been observed in Multiple Sclerosis patients exclusively receiving multiple doses of the macrocyclic agents Gd-DO3A-butrol or Gd-DOTA.[245,246] Here too, dentate nucleus signal enhancement reflects cumulative dose. A conflicting study did not detect any significantly elevated signal in the dentate nucleus or globus pallidus of brain tumor patients receiving multiple doses of Gd-DO3A-butrol exclusively.[247] The long-term effects of Gd(III) deposition in the CNS remain unknown, and no toxic effect has yet been identified. However, these new findings have triggered a high degree of anxiety about the safety of Gd(III)-based agents and stimulated a new wave of regulatory activity and debate.

Gadolinium deposition has also been identified in the body of patients with normal renal function after receiving GBCAs. Gd(III) retention has been identified in femoral heads extracted from patients receiving hip replacement surgery who had previously received Gd-DTPA-BMA or Gd-HPDO3A.[248] Bone retention was 2.5 greater in the patients who received Gd-DTPA-BMA. A 2016 autopsy study demonstrated elevated bone levels of gadolinium by mass spectrometry in adult patients after receiving linear or macrocyclic GBCAs.[249] A 2018 study quantified gadolinium retention in tibeas of healthy normal volunteers 5 years after a single dose of Gd-DO3A-butrol using X-ray fluorescence.[250] The study identified long-term bone accumulation that increased with cumulative dose. An average accumulation of 2.5 nmol Gd(III) per g bone mineral for every mmol/kg GBCA administered was observed. Another study identified a positive correlation between liver gadolinium and iron

concentrations in pediatric patients with iron overload after receiving Gd-DOTA.[251]

A few studies have attempted to discern the speciation of accumulated Gd(III). Phosphate-bound Gd(III) was identified by extended X-ray absorbance fine structure (EXAFS) analysis in the skin of NSF patients, which is consistent with dechelated Gd(III).[252] In another study, water-soluble Gd(III) was extracted from the biopsied skin of NSF patients and analyzed by HPLC-ICP-MS.[253] The water-soluble Gd(III)-containing species was identified as Gd-HPDO3A. After extraction of the water-soluble Gd(III)-containing species, the skin sample was analyzed by laser ablation ICP-MS which showed that the distribution of insoluble Gd(III) was strongly correlated with phosphorus distribution.[253] A study of the speciation of accumulated gadolinium in the brains of rats after repeat exposure to high doses of commercially available GBCAs revealed that Gd(III) accumulated after treatment with linear agents existing in 3 forms: intact chelate, soluble macromolecule associated Gd(III), and insoluble Gd(III) deposits, whereas Gd(III) accumulated after treatment with macrocylic agents existing solely as intact chelate.[254] Another study comparing speciation of Gd(III) retained in the rat brain after repeat administration of Gd-DOTA and Gd-DTPA-BMA demonstrated that Gd(III) from Gd-DOTA exists as the intact chelator where Gd(III) from Gd-DTPA-BMA is predominately recovered as insoluble Gd(III).[255]

Chelation therapy has been considered as a method to remediate Gd(III) accumulation. Levels of Gd(III) accumulated in pediatric patients suffering iron overload after Gd-DOTA treatment was shown to decrease after iron chelation therapy.[251] An oral chelator formulation is currently under development as a Gd(III) remediation treatment.[256]

There have also been reports of NSF-like and neurologic symptoms in patients with normal renal function who have received GBCAs.[257−259] However, these cases have primarily been identified through patient self-reporting and the linkage to gadolinium remains controversial.

4.1.3. Current Regulatory Status. In 2010, the FDA forbade the use of the 3 least kinetically inert agents (Gd-DTPA, Gd-DTPA-BMA, Gd-DTPA-BMEA) in patients with GFR ≤ 30 mL/min/1.73 m^2.[238,239] The FDA also labeled all contrast agents with a boxed warning that advises against exceeding the recommended dose and against repeat dosing.[238,239] Following the reports of brain deposition, the European Medicines Agency announced in 2017 that it would suspend the marketing authorization for 3 of the 8 available intravenous formulations (Gd-DTPA, Gd-DTPA-BMA, Gd-DTPA-BMEA), while limiting the use of Gd-DTPA-EOB and Gd-BOPTA to liver imaging applications.[260] FDA did not recommend any product withdrawals but did add new warning labels advising caution and prudence when ordering an MRI scan.[261,262] Japan's Pharmaceuticals and Medical Devices similarly updated their GBCA package inserts.

Limiting the use of GBCAs in patients with impaired renal function eliminates NSF risk but creates challenges in patient management. For instance an estimated 16% of U.S. adults suffer chronic kidney disease stage 3 (GFR ≤ 60 mL/min/1.73 m^2) or greater.[263] Besides their kidney disease, these patients often have other comorbidities like diabetes or cardiovascular disease.[264,265] Physicians managing these patients must now carefully weigh the risk versus benefit of contrast-enhanced examinations that would otherwise be routine for patients with normal renal function. There are often no good clinical
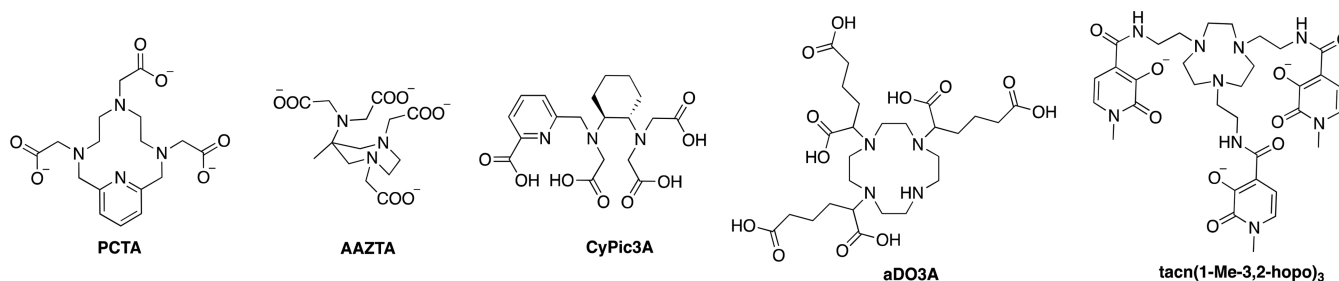
Figure 26. Ligand systems: PCTA, AAZTA, CyPic3A, aDO3A, and tacn(1-Me-3,2-hopo)$_3$ that form thermodynamically stable Gd(III)-complexes with extended hydration sphere.

alternatives available to replace GBCA-enhanced scans. Intravenous X-ray contrast agents, which can be used for blood vessel imaging also poses a potentially severe nephrotoxicity risk to renally impaired patients.[266]

The current concerns over the safety of MRI contrast agents is driving chemistry innovations toward the design of imaging products of enhanced safety. Four main approaches have been taken. One approach is to focus on developing higher relaxivity gadolinium(III) based contrast agents which can be administered at a lower dose than current GBCAs. A second approach is to identify Gd(III) complexes that are even more inert to Gd(III) dissociation/transmetalation. A third approach is to use molecular targeting to improve specificity and lower the dose. Another approach is to develop a next generation of MRI contrast agents that moves away from Gd(III) altogether. We will review progress toward these goals below.

It should be kept in mind though that GBCAs have a very good safety profile over all, and so far, it is better than the more limited experience with iron oxide based nanoparticles. For instance with the iron oxide ferumoxytol, the FDA found 79 anaphylactic reactions in its Adverse Event Reporting System between June 2009 and June 30, 2014, involving patients aged 19 to 96 years.[267] Half of the reactions occurred with the first dose of ferumoxytol and three-quarters began during infusion or within 5 min of completion. Eighteen of those seventy nine patients died despite immediate medical intervention. The incidence rates of anaphylaxis or serious hypersensitivity reaction varied between 0.2% and 0.9%, depending on the patient population in clinical trials of ferumoxytol.[268] This is in the range of 2−10 serious events per 1000 injections. On the other hand, GBCAs have a more favorable safety profile, with a rate of 0.04 serious events per 1000 injections (40 per million). Over a 5 year reporting period the total number of deaths associated with GBCAs was 41 deaths out of 51 million GBCA administrations (0.9 deaths per million administrations). New compounds will have to meet a high safety standard.

4.2. High Relaxivity Gd(III)-Based Contrast Agents

There are currently 7 Gd(III)-based ECF agents that are FDA approved, and these have r_1 values in blood plasma in the range from 3.6 to 6.3 mM^{-1} s^{-1} at 1.5 and 3T. For clinical use, the approved dose range from 0.1 to 0.3 mmol kg^{-1}. For those agents, it is estimated that the local concentrations of Gd(III) must be around 125 μM to robustly observe contrast differences in tissue (this corresponds to a relaxation rate change of about 0.5 s^{-1}). With regard to absolute sensitivity, the detection limit for the MRI contrast agent Gd-HPDO3A (Figure 3) in mouse skeletal muscle was reported to be 30 μM.[269] Hence, for targeted MR contrast agents with similar T_1

relaxivity values as the commercial contrast agents, the biological target should be present in excess of 100 μM.

Research has focused on improving sensitivity and expanding the scope of clinical MR contrast agents for higher efficiency, without sacrificing safety. Relaxivity is a measure of the sensitivity of the contrast agent. The typical T_1 relaxivity values of commercially available gadolinium(III) based contrast agents are relatively small compared to what is theoretically possible.[270] Contrast agents with higher relaxivity could provide greater tissue enhancement for better detection of smaller lesions or could produce equivalent contrast at a lower dose compared to existing approved compounds, which may lower the risk of Gd(III)-induced toxicity. For targeted or activatable contrast agents, using high relaxivity compounds would also allow the detection of lower concentration targets.

Several molecular parameters that govern the T_1 relaxivity of MR contrast agents need to be tuned to achieve higher relaxivity.[271] Such parameters are the hydration number (q), the rotational correlation time (τ_R), and the water residency time (τ_m). An optimum relaxivity can be reached if the hydration number q is increased ($q = 1$ in approved contrast agents), if the rotational correlation time (τ_R) relative to commercial CAs is increased,[270] and if the coordinated water residency time τ_m is decreased to 1−30 ns ($\tau_m = 150−1000$ ns for approved contrast agents).

4.2.1. Increasing the Hydration Number *q* of Gd(III)-Based Contrast Agents. Inner-sphere relaxivity is directly proportional to hydration number. There has been considerable effort to generate coordination cages capable of forming highly stable and kinetically inert Gd(III) complexes (inert with respect to Gd(III) dissociation) with an extended inner-sphere hydration number. The hydration number can be increased by lowering the denticity of the multidentate coligand (e.g., using heptadentate instead of octadentate chelators). However, this often reduces the thermodynamic stability and/or kinetic inertness of the resulting Gd(III) complex and increases the risk of Gd(III) release into the body. Increasing the hydration sphere also raises the risk of anion binding and displacement of coordinated water ligands. For instance, the stable $q = 2$ complex Gd-DO3A can form ternary complexes with endogenous coordinating anions such as phosphate or bicarbonate.[272] Anion coordination results in the displacement of the coordinating water ligands, and as a result, the T_1 relaxivity is reduced.

Figure 26 shows 5 ligand systems that form stable gadolinium(III) complexes with increased hydration number: the heptadentate chelators PCTA, AAZTA, CyPic3A, and aDO3A and the hexadentate chelator tacn(1-Me-3,2-hopo)$_3$. Gd-PCTA is thermodynamically less stable than Gd-DOTA (log K_{cond} = 16.2 vs log K_{cond} = 17.2),[206] but it is kinetically
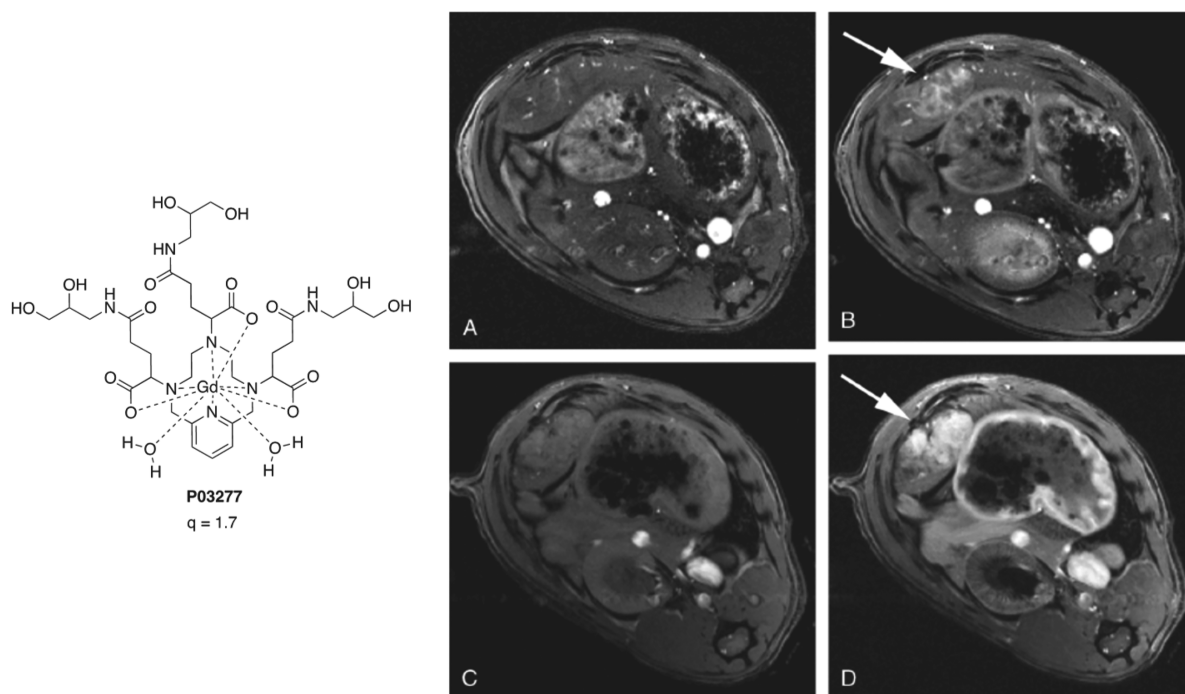
Figure 27. (Left) Structure of P03277; (right) axial T_1-weighted images of the hepatic metastasis (A) before and (B) after intravenous injection of 0.1 mmol kg^{-1} gadobutrol and (C) before and (D) after intravenous injection of 0.1 mmol kg^{-1} P03277. Arrow shows tumor. Reproduced with permission from ref 288. Copyright 2015 Wolters Kluwer Health, Inc.

quite inert. In acid-assisted gadolinium decomplexation experiments, Gd-PCTA reacts only an order of magnitude faster than Gd-DOTA, which makes it superior to the approved macrocyclic contrast agents Gd-HPDO3A and all commercially approved acyclic contrast agents. Due to its two metal-bound water molecules, the T_1 relaxivity of Gd-PCTA ($r_1 = 6.9$ mM^{-1} s^{-1} at 20 MHz, 25 °C) is higher than that of the approved ECF agents.[273−276]

Gd-AAZTA (log $K_{cond} = 16.4$)[206] is also thermodynamically less stable than Gd-DOTA, but its kinetic inertness may be sufficient for in vivo applications. Although it was shown that Gd-AAZTA reacts faster in acid-catalyzed decomplexation experiments than Gd-DTPA, it undergoes transmetalation reactions with Cu(II) or Eu(III) more slowly than Gd-DTPA.[277] Its hydration sphere features two water molecules leading to a high T_1 relaxivity of 7.1 mM^{-1} s^{-1} (20 MHz, 25 °C).[278−280]

Gd-CyPic3A affords two metal-coordinated water molecules ($q = 2$) and an r_1 value of 5.70 mM^{-1} s^{-1} (60 MHz, 37 °C), which is 1.7 fold higher than that of Gd-DTPA measured under the same conditions ($r_1 = 3.26$ mM^{-1} s^{-1}). Its thermodynamic stability is comparable to that of the approved contrast agent Gd-HPDO3A, and its kinetic inertness is in the range of acyclic clinically used Gd(III) complexes. It was also shown that the complex is resistant to anion coordination.[281]

Parker and co-workers synthesized Gd-aDO3A, a bishydrated Gd-DO3A derivative with remarkably high relaxivity values ($r_1 = 12.3$ mM^{-1} s^{-1} at 20 MHz, 25 °C). Unlike Gd-DO3A, Gd-aDO3A is not prone to inner-sphere water displacement by endogenous anions, presumably because of repulsion by the negatively charged pendant carboxylate groups. The kinetic inertness of this complex was reported to be 10 times higher than that of Gd-DTPA.[282]

Raymond and co-workers developed a series of thermodynamic stable Gd(III) complexes that utilized three hydroxypyridinone (HOPO) bidentate chelators. These complexes exhibited hydration numbers of up to $q = 3$, and hence, they were able to obtain exceptionally high T_1 relaxivity values [e.g., 13.1 mM^{-1} s^{-1} at 20 MHz, 25 °C for Gd-tacn(1-Me-3,2-hopo)$_3$]. Moreover, those complexes are resistant to anion coordination.[283−287]

Recently, Fries and co-workers reported a comparative study of the experimental high relaxivity agent P03277 (Figure 27, left) with the approved contrast agent gadobutrol (Figure 3).[288] P03277 is a Gd-PCTA derivative with a low molecular weight (0.97 kDa) and a measured value of $q = 1.7$. Its T_1 relaxivity in human blood plasma at 37 °C is approximately 2.5 times higher than that of gadobutrol at clinical field strength [12.8 vs 5.2 mM^{-1} s^{-1} (1.5 T) and 11.6 vs 5.0 mM^{-1} s^{-1} (3.0 T), respectively]. Increases in relaxivity due to increased hydration should be maintained at high fields, and P03277 has 2-fold higher relaxivity than gadobutrol (9.3 vs 4.8 mM^{-1} s^{-1} at 7.0 T, 8.6 vs 4.7 mM^{-1} s^{-1} at 9.4 T, respectively, in human plasma, 37 °C). An in vivo comparison of both agents in a rat model of hepatic colorectal cancer metastases at 9.4 T revealed that P03277 has similar pharmacokinetics as gadobutrol but demonstrates significantly better tumor enhancement properties as depicted in Figure 27, right. P03277 is currently undergoing human clinical trials (NCT02633501, www.clinicaltrials.gov).

4.2.2. Optimizing the Rotational Correlation Time (τ_R) of Gd(III)-Based Contrast Agents. As discussed above, r_1 for simple chelates is limited by fast rotation at all accessible field strengths above 0.1 T. Slowing down the rotational motion of the complex is an effective way to increase relaxivity. This can be achieved by increasing the molecular weight of the contrast agent. This in turn can be achieved by making the complex larger or by the covalent or noncovalent binding of the contrast agent to a macromolecule (e.g., a protein, a polypeptide, a nanosphere, or micellar nanoparticles). The
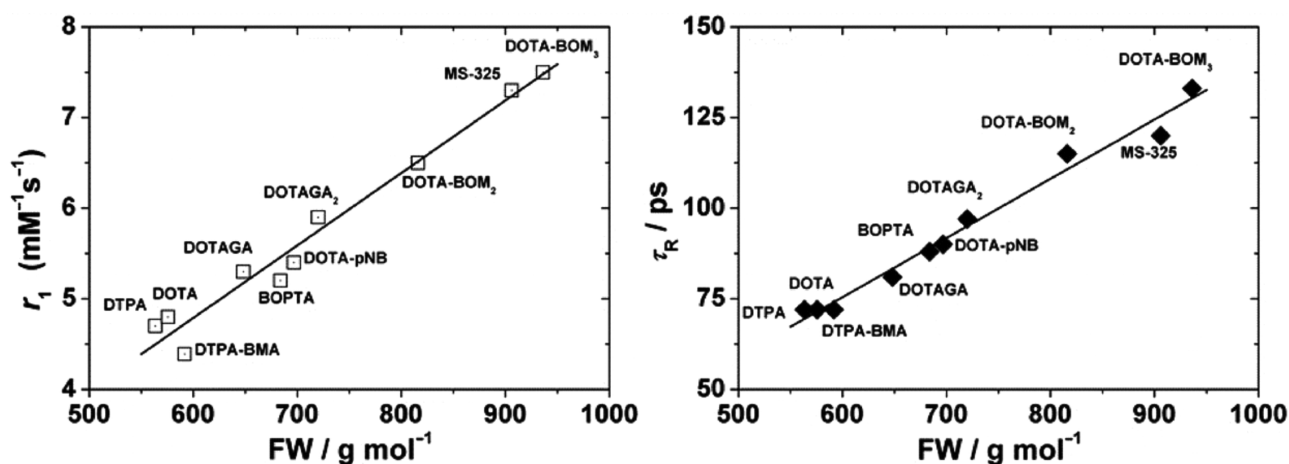
Figure 28. (Left) Plot of r_1 (0.5 T and 25 °C) for monohydrated DOTA-based Gd(III) complexes vs molecular weight ($R = 0.984$). (Right) Plot of τ_R evaluated from the NMRD profiles vs molecular weight ($R = 0.991$). Reproduced with permission from ref 289. Copyright 2018 Royal Society of Chemistry.
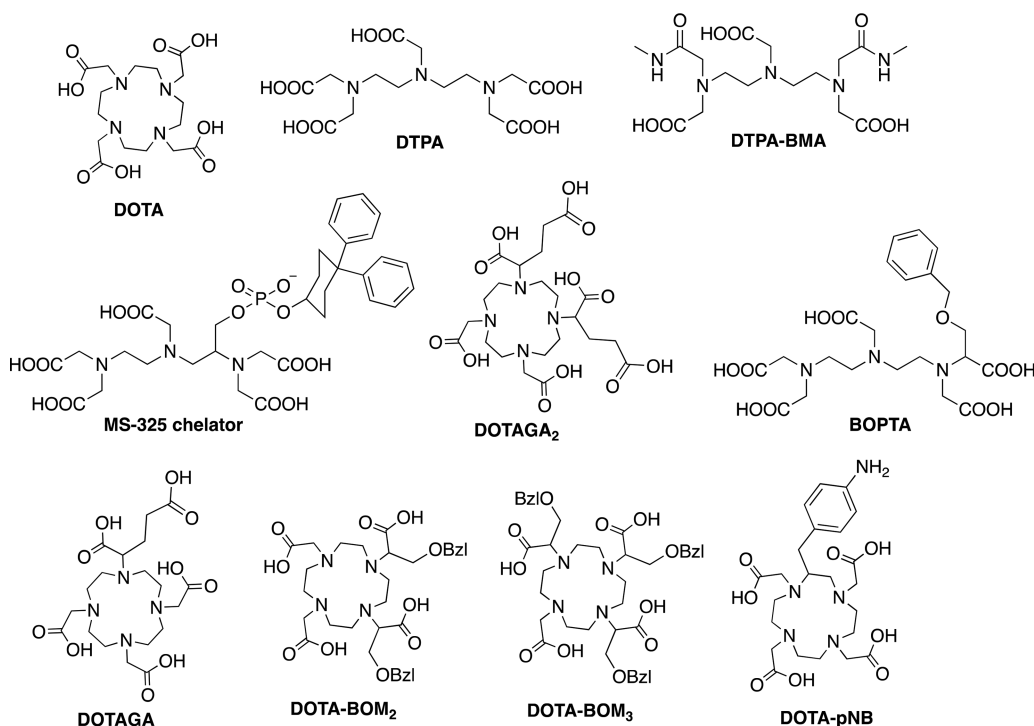
Figure 29. Chemical structures of the chelators mentioned in Figure 28.[289]

linear dependence of the molecular weight of monohydrated Gd-DOTA derivatives and their T_1 relaxivities (0.5 T, 25 °C) is illustrated in Figure 28, left (see Figure 29 for structures of chelators).[289] Similarly, the rotational correlation time exhibits the same linear correlation with the molecular weight of those Gd(III) complexes Figure 28, right.

In order to attach paramagnetic agents to macromolecules, bifunctional chelates have been developed.[290] Typically, they are based on the chelators DOTA or DTPA and are bearing an electrophilic group, such as an isothiocyanate, *N*-hydroxysuccinimide ester, maleimide etc., that is available for conjugation to nucleophilic groups on macromolecules. Excellent reviews are available, in which those agents are covered.[291−293]

In an early example, Gd-DTPA chelates were covalently attached to HSA yielding the macromolecular contrast agent albumin-(Gd-DTPA)$_{19}$ with a molecular weight of 92 kDa.

The T_1 relaxivity per Gd(III) ion was found to be 3 times higher than that of the monomeric chelate (20 MHz, 37 °C), which is attributed to the larger molecular weight of the contrast agent and, hence, its higher rotational correlation time.[294−296] Gd-DTPA has been also conjugated to poly-L-lysine.[297] The resulting macromolecular compound (average molecular weight: 49 kDa) possesses a r_1 value that is also 3 times higher than that of the monomeric chelate.[298]

Aside from tethering a Gd(III) complex to a macromolecular structure through a linker, peptides or proteins were designed with embedded Gd(III) binding sides. Franklin and co-workers prepared the peptide chimera GdP3W, a 4 kDa metallopeptide with an EF-hand Gd(III) binding site and DNA binding domain.[299] The rigid structure and extended hydration sphere ($q = 2$) of GdP3W furnishes a r_1 value that is 6 times higher than that of Gd-DTPA (60 MHz, 37 °C).

Moreover, a 100% increase in its T_1 relaxivity was observed upon binding to DNA.

Another example are the protein-based Gd(III) MRI contrast agents (ProCAs).[300] Yang et al. showed that engineered proteins chelated with Gd(III) (average molecular weight: 12 kDa) have relaxivities that are 20-times higher than that of Gd-DTPA and are inert to Gd(III) release.[301] Protein engineering with tumor targeting modalities allowed imaging of, for example, prostate or liver cancer in mouse models.[302,303]

Another strategy to increase the molecular weight of the MR contrast agent is to link multiple Gd(III) complexes together, which in turn also enhances the number of Gd(III) ions per molecule and therefore the overall contrast. In this approach, the coupling of multiple Gd(III) compounds to spherically shaped carriers (e.g., dendrimers) is more effective than linking Gd(III) complexes in a linear fashion. Although there is internal motion in both instances (see below), dendrimers rotate in a more isotropic fashion, whereas linear oligomers rotate anisotropically. Linear oligomers will rotate more rapidly about their long axis, and this faster rotation will limit relaxivity. A Gd-DO3A derivative assembled to a spherical dendrimer[59] has 40% higher relaxivity per gadolinium ion than the same Gd-DO3A derivative assembled to a linear dextran polymer,[304] although the molecular weight of the linear polymer (52 kDa) is higher than that of the dendrimer (17 kDa). The different types of motion are depicted in Figure 30.[109]
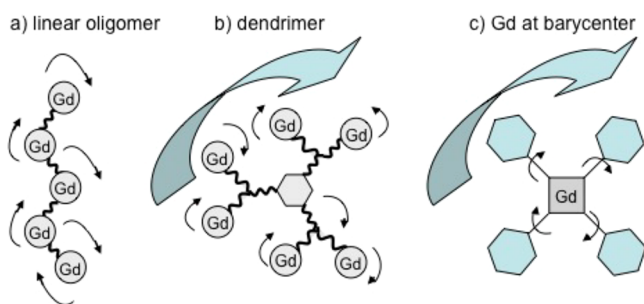

Figure 30. Different strategies to increase relaxivity by modulating rotational motion: (A) linear polymer of Gd(III)-complexes that rotates anisotropic (low relaxivity); (B) Gd(III) chelates assembled to a dendrimer that rotates isotropically, but internal motion is still possible (higher relaxivity); and (C) Gd(III)-complex at the barycenter of the molecule, so that it can only rotate at the rate of the entire molecule (highest relaxivity).[109]

Internal Motion. The nuclear relaxation induced by the chelate is dependent on the rotation about the M−H(water) vector. To this point, we have considered that the rotational motion of this vector is isotropic and mirrors that of the complex. This is a good approximation in many cases. But there are often internal rotations that are occurring faster than the overall reorientation of the entire molecule. The simplest of these is rotation about the M−O bond. Over 40 years ago, Dwek pointed out that for water coordinated to a metal ion, fast rotation about the metal−oxygen bond will decrease the efficiency of the paramagnetic relaxation effect.[305] For MRI contrast agents, this fast intramolecular motion will reduce the relaxivity of the complex.

Direct experimental assessment of water rotation is challenging. Using the Ln-DOTAM system where the water exchange rate is very slow, Dunand et al. were able to measure

the ^{17}O and ^1H relaxation times of the coordinated water for the Eu(III) complex and determine the effect of this fast rotation.[306,307] However, water exchange in most lanthanide complexes is too fast for direct observation of the coordinated water ligand. Nonetheless, this fast intramolecular rotation is assumed to occur in many Gd(III) complexes, including those used as commercial MRI contrast agents.[144,293] The effect of this fast rotation is to reduce inner-sphere relaxivity by about 30%.

Recently Boros et al. showed that this fast water rotation could be reduced by the formation of an intramolecular hydrogen bond between the coordinated water hydrogen and a suitable H-bond acceptor (Figure 31) and that the resultant

Figure 31. Restricting the water ligand mobility (specifically rotation about the Gd−O bond) in Gd(III) complexes through interaction with an intramolecular H-bond acceptor. Reproduced with permission from ref 123. Copyright 2017 John Wiley and Sons.

complex would have a higher relaxivity than similar compounds lacking the H-bond acceptor.[123] In that study, the authors used Gd-DOTAla derivatives with pendant H-bond acceptors as well as control compounds that were structurally very similar but lacking this H-bond acceptor. There are several reports of gadolinium(III) complexes having anomalously high relaxivity compared to related complexes of similar size, shape, and charge. For instance, work of Lowe et al. describes Gd(III) complexes with a pH-dependent, intramolecular ligation of a β-arylsulfonamide nitrogen which results in changes in the hydration state at the lanthanide center.[308] The relaxivity observed for the $q = 2$ complexes was found to be anomalously high and possibly indicative of interaction with the bound water by pendant, noncoordinating carboxylates. Similarly, Dumas et al. described Gd(III) complexes with unexpectedly enhanced relaxivity that possess pendant noncoordinating carboxylate donor arms.[309,310] Previously, these cases of high relaxivity have usually been ascribed to a second-sphere effect, wherein water molecules in the second hydration sphere have extended residency times because of interactions with H-bond acceptor(s) on the chelating ligand. However, in many of those complexes it is likely that the H-bond acceptor could also be interacting with the inner-sphere coordinated water and hindering the water rotation.

For more complicated molecules such as multimeric agents or chelates (non)covalently attached to a macromolecule, there can be additional internal motions that reduce relaxivity. For example, if the chelate is covalently attached to a macromolecule by a linker group then the chelate can rotate about this linker so that the rotation of the chelate is decoupled from the macromolecule and the relaxivity is not as high as predicted based on the overall motion of the macromolecule.[311−314] For these complex systems where there are a number of internal motions, the data are usually analyzed by a model-free approach described originally by Lipari and Szabo.[315] They showed that the usual spectral density function for isotropic motion could be replaced by two terms, one that reflected the

overall rotation [or global motion (τ_g)] of the molecule and another that reflected internal (or local) motions (τ_l) (eq 25),

$$\frac{1}{T_{1m}} = \frac{C}{r_{GdH}^6} \times \left(\frac{3F\tau_{cg}}{1 + \omega_H^2 \tau_{cg}^2} + \frac{3(1 - F)\tau_{cl}}{1 + \omega_H^2 \tau_{cl}^2} \right) \quad (25)$$

$$\frac{1}{\tau_{cg}} = \frac{1}{\tau_g} + \frac{1}{T_{1e}} + \frac{1}{\tau_m} \quad (26)$$

$$\frac{1}{\tau_{cl}} = \frac{1}{\tau_{cg}} + \frac{1}{\tau_l} \quad (27)$$

with C as a constant (as in eq 9) and F as a measure for the degree of isotropic motion.

The relative contributions to the global and local motions is given by an order parameter S^2 (sometimes denoted F to avoid confusion with the spin quantum number). At one extreme, the rotational motion of the chelate is completely decoupled from the macromolecule $(F = 0)$. On the other extreme $(F = 1)$, the chelate is immobilized on the macromolecule such that internal motion is prevented, and the spectral density function is the same as for isotropic rotation. In Figure 32, the effect of
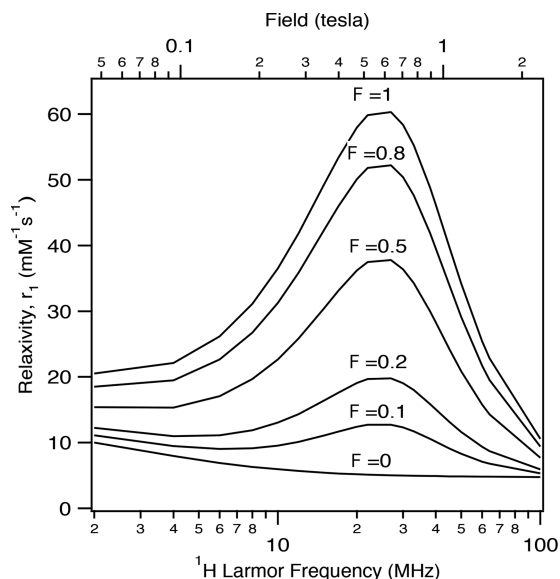

Figure 32. Simulation illustrating the effect of internal motion on the field-dependent T_1 relaxivity (hypothetical Gd(III)-compound with a global correlation time of 10 ns and a local correlation time with 0.1 ns. F gives the degree of internal motion.[109]

internal motion on relaxivity is simulated for a system with a very long rotational correlation time (10 ns) associated with a macromolecule and a local rotational correlation time of 0.1 ns at proton Larmor frequencies ranging from 1 to 100 MHz. Figure 32 shows that internal motion can dramatically reduce relaxivity. However, the effect of internal motion on relaxivity is more pronounced at lower fields (<1 T).[109]

Strategies to Minimize Internal Motion. One effective strategy to minimize internal motion is to force the metal-water proton vector to rotate isotropically with the entire molecule. Parker and co-workers showed that this can be done by placing metal at the molecular barycenter (Figure 30) to create contrast agents with low molecular weight (3−7 kDa) but still remarkably high relaxivity in the region of 20−40 mM^{-1} s^{-1}.[31,316,317] In these studies, they used 4 large

hydrophilic pendant arms to increase the molecular size of Gd-DOTA derivatives. The blood pool agent P792 utilized the same strategy.[32]

Another approach is to limit internal motion by connecting the chelate to the macromolecular structure by two points of attachment. Early examples were the self-assembled metallostar compounds, where the rigid and multimeric structure of the MR contrast agent is formed in the presence of Fe(II) ions.[318−320]

In another example, Zhang et al. combined a multimeric approach with protein binding to boost relaxivity.[321] They synthesized a tetrameric Gd-DTPA oligomer with two HSA binding groups (Figure 33). In the absence of protein, the relaxivity is relatively low because of the flexible multimeric structure. But upon binding to HSA, the contrast agent is rigidified and rotational motion slowed, dramatically increasing relaxivity. This is shown schematically in Figure 33. For small molecules like MS-325, relaxivity is low (Figure 33a) but is increased several fold upon protein binding (Figure 33b). However, for multimeric agents, the gain in relaxivity upon protein binding is often offset by the internal motion (Figure 33c). But using a dual anchor strategy overcomes this relaxivity loss (Figure 33d). Indeed, the authors obtained an enhanced r_1 of 39.1 mM^{-1} s^{-1} (20 MHz, 37 °C, pH 7.4) for their dual binding Gd(III) tetramer in the presence of HSA (Figure 33e)). This was 50% higher than the relaxivity obtained for the same tetramer with only one HSA binding unit (schematic illustration in Figure 33c)) where r_1 = 26.2 mM^{-1} s^{-1} measured under the same conditions. On a molecular basis, the relaxivity is 4 times higher.

Another example of a dual anchor strategy applied to liposome-based contrast agents was reported by Botta, Tei, and co-workers.[322,323] Amphiphilic Gd(III)-chelates can be incorporated into liposomal bilayers resulting in increased relaxivity. However, if the chelate has one alkyl chain for incorporation, significant internal motion can occur. The authors used Gd-DOTA(GA)$_2$ derivatives that had near optimal water exchange kinetics and two points of attachment to the lipid bilayer. As a result relaxivity was doubled compared to the analogous compound with only a single point of attachment.

Contrast agents with very long rotational correlation times (on the order of 10 ns) can have near optimal relaxivity at low fields (0.5−1 T), but for these types of compounds the relaxivity falls off dramatically at higher field strength. For higher field strengths, one requires an intermediate rotational correlation time (on the order of 1 ns) which will result in very good relaxivity at 1.5 T and close to optimal relaxivity at 3 and 7 T.

As an example, Figure 34 shows the influence of the magnetic field strength on the T_1 relaxivity of three compounds with different rotational correlation times: Gd-HPDO3A (short τ_R, see Figure 3), Gd$_3$L$_3$ (intermediate τ_R, see Figure 35), and MS-325 bound to HSA (long τ_R, see Figure 3).[324] Gd$_3$L$_3$ employs the Gd-DOTAla chelate which allows it to be incorporated into a peptide structure via two points of attachment, thereby limiting internal motion. Figure 34A presents r_1 per molecule and Figure 34B presents r_1 per Gd(III). At 0.47 T, the compounds with intermediate or long τ_R exhibit similar molecular T_1 relaxivities, but with increasing field strength (here, to 11.7 T), the difference between those agents becomes larger. Gd$_3$L$_3$ with its intermediate correlation time is superior to HSA-bound MS-325, 50% higher at 1.5 T,
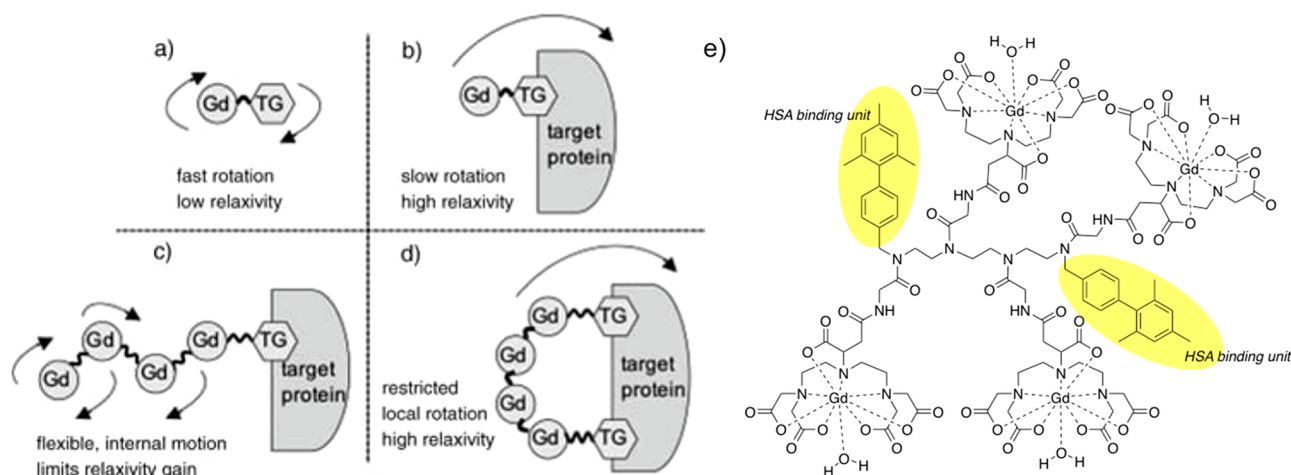
Figure 33. Strategies for increasing relaxivity: (a) Gd(III)-complex with targeting moiety that tumbles fast (low relaxivity); (b) binding of the Gd(III)-complex to the targeting protein slows tumbling and the relaxivity increases; (c) Gd(III)-based multimer bound to the target protein, relaxivity might be limited through internal motion; (d) Gd(III)-based multimer bound to the target protein via two points of attachment, limited internal motion increases relaxivity; and (e) structure of the Gd-DTPA-based multimer. Reproduced with permission from ref 321. Copyright 2005 John Wiley and Sons.
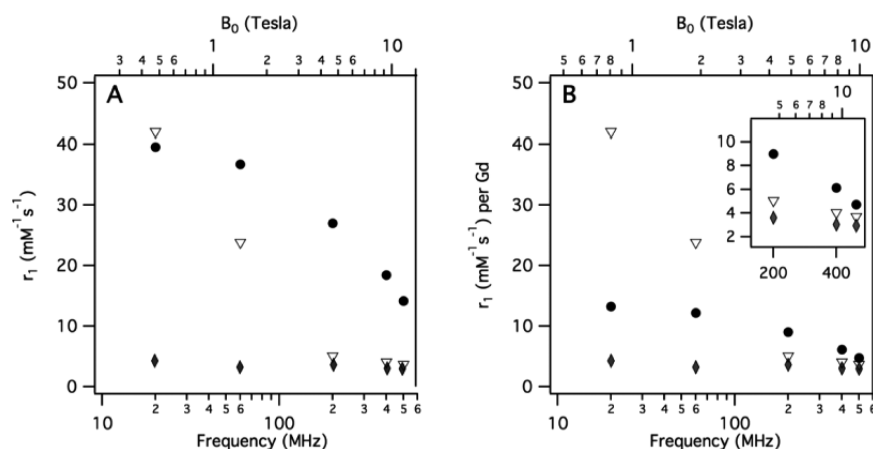
Figure 34. T_1 relaxivities of Gd_3L_3 (○), MS-325 with excess HSA (▽), and Gd-HPDO3A (♦) as a function of magnetic field strength at 37 °C. (A) T_1 relaxivity plotted per molecule, at 60 MHz and higher frequency: molecules with intermediate correlation time (Gd_3L_3) are much more potent relaxation agents than slow (MS-325 with excess HSA) or fast Gd-HPDO3A tumbling compounds and (B) T_1 relaxivity plotted per Gd(III)-ion. Reproduced from ref 324. Copyright 2012 American Chemical Society.
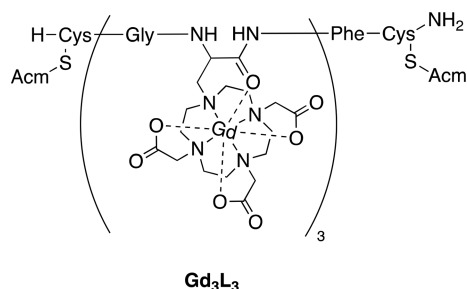
Figure 35. Chemical structure of Gd_3L_3.

and 350−450% higher at 4.7−11.7 T. On a per Gd(III) basis, Gd_3L_3 has 50−220% higher r_1 than HSA-bound MS-325 at high fields. Note that the T_1 relaxivity of Gd-HPDO3A (short τ_R) stays roughly the same at all field strengths.

Since clinical imaging is increasingly moving to higher field strengths, it is important to develop contrast agents that are applicable at high field. For 3−7 T, a rotational correlation time in the range of 0.5−2 ns is desirable. Still, it should rotate

isotropically with limited internal motion. Recently, several examples for high field Gd(III)-based MR contrast agents were reported.[320,324−330]

It should be noted that the same strategies apply to Mn(II), Fe(III), and Mn(III) chelates. Slowing down rotation by protein binding results in large increases in relaxivity at lower field strengths.[331−333] Similarly, rigid multimers with multiple chelates can provide intermediate rotational correlation times that provide enhanced high field relaxivity.[334]

4.2.3. Tuning the Water Residency Time (τ_m) of Gd(III)-Based CAs. Another parameter that can be tuned to increase r_1 is the water residency time (τ_m). The coordinated water must be in rapid exchange with bulk solvent in order to transmit the relaxation effect to the solvent. Relaxivity can be limited if τ_m is too slow or too fast. It is important to note that for fast tumbling complexes, $T_{1m} \gg \tau_m$, and so changing τ_m has little to no effect on relaxivity. However, once the rotational correlation time begins to be optimized then τ_m can play a major role.
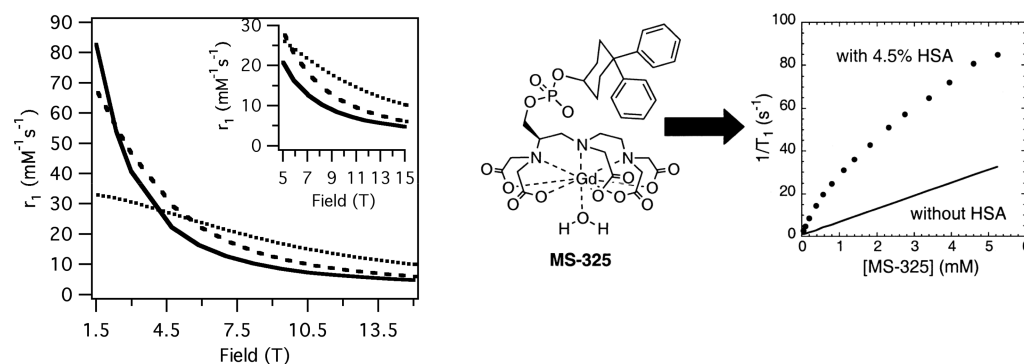
Figure 36. (Left) Effect of rotational correlation time on T_1 relaxivity as a function of field for a Gd(III) complex with a water residency time 100 ns. $\tau_R = 0.1$ ns (···), 1.0 ns (---), 10 ns (—). Reproduced with permission from ref 144. Copyright 2009 John Wiley and Sons. (Right) Effect of HSA binding on T_1 relaxation rate for MS-325. Reproduced from ref 17. Copyright 2002 American Chemical Society.

As an example, optimal values for contrast agents with a water residency time similar to Gd-DTPA or Gd-DOTA ($\tau_m \sim$ 100 ns at 37 °C) are around 10 ns (Figure 36, left). However, incorporation of the gadolinium(III) compound into a macromolecule might affect the other parameters that influence the relaxivity. MS-325 is a Gd-DTPA derivative that can noncovalently bind to the plasma protein human serum albumin (HSA) (Figure 36, right). MS-325 (unbound) has a τ_R of 115 ps. Once bound to HSA, MS-325 (bound) has a τ_R of 10.1 ns, which causes a dramatic increase in T_1 relaxivity. However, the observed T_1 relaxivity is not as high as it theoretically should be because another parameter that governs relaxivity, the water residency time (τ_R), is influenced by this modification. Indeed, MS-325 (unbound) has a τ_R of 69 (± 20) ns and MS-325 (bound) has a τ_R of 170 (± 40) ns. The water residency time becomes crucial when the rotational motion is slowed, which limits the observed T_1 relaxivity.[17] This shows that the lability of the water molecule at the metal side can be influenced when a supramolecular adduct is formed.[335]

The effect of water exchange of slow tumbling systems is also seen when comparing MS-325 and its bis(N-methyl)-amide derivative: MS-325-BMA (Figure 37). Gd(III) complexes with amide oxygen donor atoms are known to have

slower water exchange rates compared to the analogous carboxylate derivatives.[111] The water exchange rate of MS-325-BMA is 10 times slower than the water exchange rate of MS-325. Since both MS-325 and MS-325-BMA have a similar size, their rotational correlation times and T_{1m} values should be similar in phosphate buffered saline (PBS) or when bound to HSA. In PBS, the relaxivity of these complexes is alike, indicating that $T_{1m} \gg \tau_m$. However, once bound to HSA, the relaxivity of MS-325 is 3 times higher than that of MS-325-BMA. When bound to HSA, T_{1m} is shortened to the point that the long τ_m of MS-325-BMA limits its relaxivity.[109]

The water exchange rate can be accelerated by increasing the steric compression around the water binding site. This was originally demonstrated by Merbach and co-workers in octadentate chelates, such as Gd-DTPA (Figure 3) and Gd-EPTPA (Figure 39).[111,143,336−338] However, for these Gd-DTPA derivatives, the rate enhancement is achieved at the cost of lower thermodynamic stability.

The steric crowding in Gd-DOTA derivatives can also be enhanced by introducing bulky groups. Dumas et al. found that exchanging one acetate arm by a different donor group led to an increase in τ_m in the following order: phosphonates $\sim$ phenolates < alpha-substituted acetates < acetate < hydroxamates $\sim$ sulphonamides < acetamide $\sim$ pyridyl $\sim$ imidazole, which is also in line with the general trend that neutral donors slow down water-exchange kinetics in comparison to negatively charged donor groups.[112] In these complexes, the coordinated water is released through a dissociative exchange process that is favored by steric crowding.[270]

In total, Dumas et al. reported 38 Gd-DOTA derivatives with HSA binding groups, and the water residency time varied over 3 orders of magnitude. In the absence of HSA, r_1 was similar for all compounds with a given q value and correlated with molecular weight. As expected, the relaxivity did not correlate with τ_m. The influence of τ_m on relaxivity becomes apparent when the relaxivity was measured in the presence of HSA. Slow tumbling shortens T_{1m}, and now τ_m can limit relaxivity. Figure 38 shows the relaxivity for this series of chelates bound to HSA as a function of their water residency time at two different field strengths (0.47 and 1.4 T). As predicted by theory there is an optimal water residency time at low field for slow tumbling compounds, which peaks between 10 and 30 ns (0.47 T). When increasing the field strength to 1.4 T, the range of τ_m for optimal relaxivity becomes broader.

With phosphonate groups in particular, the steric crowding combined with the favorable arrangement of the water
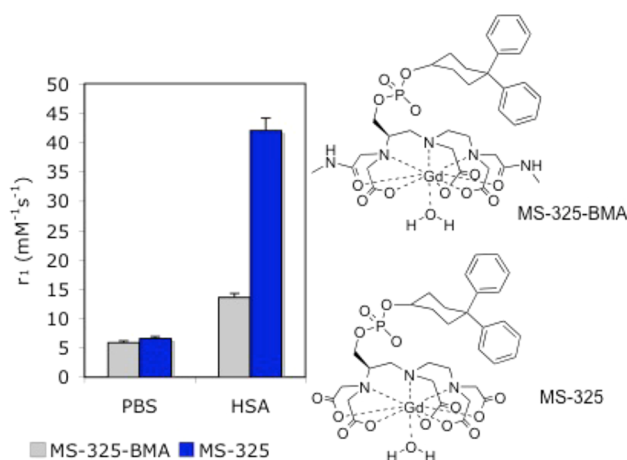

Figure 37. Relaxivity of 0.1 mM MS-325 and MS-325-BMA in pH 7.4 phosphate buffered saline or 0.67 mM HSA solution at 37 °C and 0.47 T. MS-325 is 88% bound to HSA under these conditions and MS-325-BMA is 83% bound.[109]
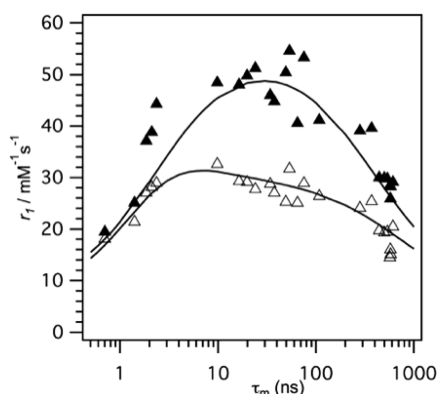
Figure 38. Relaxivity of slow tumbling HSA-bound Gd-DOTA derivatives plotted vs measured water residency time at 37 °C at 20 MHz (▲) or 60 MHz (△), respectively. τ_m limits relaxivity at a given field strength if it is either too short or too long. The range of τ_m for optimal relaxivity becomes broader at higher field.[339] Reproduced with permission from ref 112. Copyright 2010 Wolters Kluwer Health, Inc.

molecules in the second coordination sphere leads to a faster water exchange rate.[340] For instance, Gd-DO3A-pyNox (Figure 39), a Gd-DO3A derivative bearing a sterically demanding group has a water residency time of 39.0 ns (25 °C) while Gd-DOTA has a water residency time of 244 ns (25 °C).[341] The water residency time in a monophosphinic acid derivative Gd-DO3AP^{ABn} (Figure 39) was found to be even shorter with τ_m = 16.2 ns (25 °C).[340] Boros et al. recently showed that for slow tumbling systems with exceptionally fast water exchange that the water residency time becomes the correlation time influencing relaxivity and results in a useful strategy to achieve high field, high relaxivity.[342]

4.2.4. High Relaxivity Gd(III)-Nanomaterials. Gd(III)-nanomaterials have been the subject of intensive research for the past two decades since they have unique potential to overcome the sensitivity disadvantage of contrast agents. Their ability to carry high Gd(III) payloads combined with their long rotational correlation times makes them excellent candidates in the design of high relaxivity MRI contrast agents. Additionally, these materials offer great flexibility in terms of surface modifications, for example, multifunction or bioconjugation for therapeutic or diagnostic applications, respectively.

Nanoparticles engineered as MRI contrast agents have been based on carbon nanotubes and fullerenes, polymers and dendrimers, gold, silicon, viral nanoparticles, and liposomes and micelles. A comprehensive overview of the recent progress on Gd(III)-nanomaterials as MRI contrast agents is beyond

the scope of this review. Excellent reviews are available that cover those agents.[343−347]

An impressive example for a Gd(III)-nanosystem with exceptional high relaxivity was reported by Wilson and co-workers. They developed gadonanotubes (Gd$^{3+}_n$@US tubes) that consist of aquated Gd(III)-ion clusters confined within single-walled carbon nanotube capsules.[348] At clinical field strength, the r_1 values were found to be 40 times higher than that of the Gd(III)-based ECF contrast agents (r_1 = ∼170 mM^{-1} s^{-1} per Gd(III)-ion, 60 MHz, 40 °C).

Meade and co-workers took a different approach and conjugated Gd-DO3A derivatives to the surface of nano-diamonds.[349] The resulting Gd(III)-nanodiamond conjugate affords a T_1 relaxivity that is 10 times higher than that of the monomeric Gd(III)-complex (r_1 = 58.8 mM^{-1} s^{-1} per Gd(III) ion, 60 MHz, 37 °C).

In a recent example, it was shown that water permeable silica nanoparticles with confined monohydrated Gd-ebpatcn chelates (Figure 39) feature a nanosized contrast agent with an extraordinary high r_1 value of 84 mM^{-1} s^{-1} at 35 MHz (25 °C).[350]

In another example, Chuburu and co-workers incorporated Gd-DOTA chelates into a polysaccharide-based hydrogel (Gd-DOTA-NPs).[351] As illustrated in Figure 40, the T_1 relaxivity of
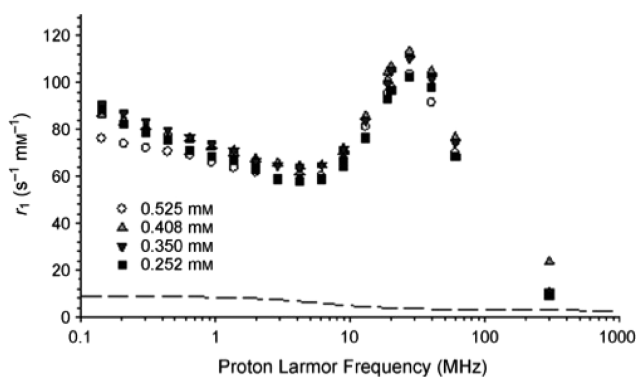
Figure 40. NMRD relaxivity profiles of Gd-DOTA-NPs at different concentrations (T = 37 °C) showing the characteristic shape of a compound with slow rotational correlation times. These results indicate that the rotational motion of Gd-DOTA inside the hydrogel is restricted. Dotted line: NMRD relaxivity profile of Gd-DOTA (T = 37 °C). Reproduced with permission from ref 351. Copyright 2012 John Wiley and Sons.

the Gd(III)-loaded nanoparticle was found to be 24 times higher than that of the monomeric Gd-DOTA complex (r_1 = 72.3 mM^{-1} s^{-1} per Gd(III)-ion, 60 MHz, 37 °C).
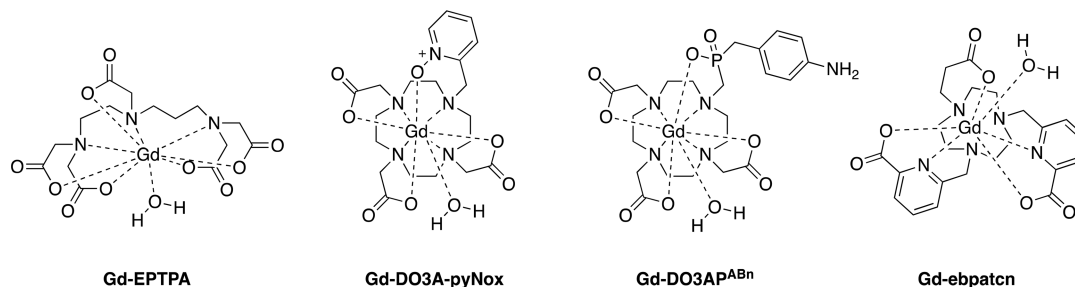
Figure 39. Chemical structures of Gd-EPTPA, Gd-DO3A-pyNox, Gd-DO3AP^{ABn}, and Gd-ebpatcn.

4.3. Increasing Resistance to Gd(III) Release

Trivalent gadolinium is an oxyphilic hard cation that favors coordination numbers of 8 and 9 with negatively charged oxygen atom donors preferred to neutral oxygen donor atoms. This becomes apparent by comparing the stability constants of $[Gd(DOTA)(H_2O)]^-$ and $[Gd(HP-DO3A)(H_2O)]$, in which a negatively charged acetato donor was replaced by an uncharged hydroxyl donor (Figure 3; log K_{GdL} = 24.7 vs log K_{GdL} = 23.8, respectively).

The formation of 5-membered chelate rings is generally preferred, whereas the chelate ring size is one of the dominating factors that govern stability. It is well-known that changes in chelate ring size greatly influence stability. As an example introducing one or two additional methylene units in the macrocyclic backbone of Gd-DOTA gives Gd-TRITA and Gd-TETA (Figure 41), respectively, and causes a drop in

Gd-TRITA

log K_{GdL} = 19.2

Gd-TETA

log K_{GdL} = 13.8
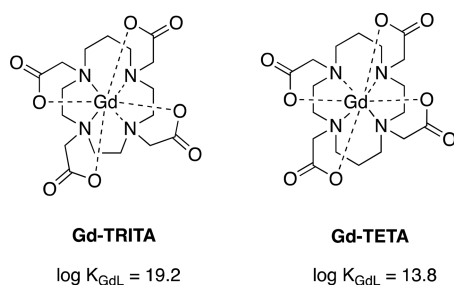
Figure 41. Thermodynamic stability of Gd-TRITA and Gd-TETA.[353]

thermodynamic stability of 5 orders of magnitude each.[206] Such a drop in stability can also be observed by changing the pendant acetato moiety against a pendant propionato moiety, which also increases the chelate ring size from a 5-membered to a 6-membered ring.[352]

Expanding the macrocyclic backbone by additional methylene units does not only decrease the thermodynamic stability but also increases the kinetic lability. This can be explained by a higher degree of flexibility that is introduced within the macrocyclic backbone with every additional methylene unit. This in turn accelerates the dissociation rates. Hence, Gd-DOTA is kinetically 3 orders of magnitude more inert than Gd-TRITA and 6 orders of magnitude more inert than Gd-TETA.[354] Moreover, this example nicely illustrates that macrocyclic chelators do not automatically guarantee superior kinetic inertness. Other macrocyclic systems that show rather fast dissociation kinetics were reported recently.[131,355] Increasing the chelate ring size of the pendent carboxylate by replacing an acetato group through a propionato group also lowers the kinetic inertness of the system.[352]

Another factor that has been identified to increase the kinetic inertness of the Gd(III)-based agent is to reduce the basicity of the ligand. In those systems, protonation of the chelator is less favored. As a result proton-catalyzed dissociation is further hampered, which decelerates the dissociation rate. Indeed, Gd-DOTA-tetraamide based complexes (Figure 42) that are less basic than the parent DOTA compound were found to be considerably more inert, but at the same time they are 10−11 orders of magnitude thermodynamically less stable than Gd-DOTA.[221]

Recently, a highly rigid open-chain derivative Gd-cddadpa was reported with dissociation rates that become comparable to inert macrocyclic complexes and sufficient thermodynamic stability (log K_{GdL} = 20.68, Figure 42).[356] Its kinetic inertness was characterized by studying the rate of the metal exchange reaction occurring with Cu(II) (c = 1 μM, 25 °C) at physiological pH. Under those conditions, the dissociation half-life of Gd-cddadpa is 3 orders of magnitude higher than that of Gd-DTPA ($t_{1/2}$ = 1.49 × 10^5 h vs $t_{1/2}$ = 202 h, respectively) and in the range of that of Gd-DO3A ($t_{1/2}$ = 2.10 × 10^5 h).

Ln(III) complexes of a cross-bridged cyclam derivative containing two picolinate pendant arms show exceptional kinetic inertness, which even overcome that of Ln-DOTA complexes by far (Figure 42).[357] Under very harsh conditions, such as 2 M HCl, no sign of dissociation has been observed for those complexes for at least 5 months. In contrast, Ln-DOTA has a half-live of <12 h when subjected to the same conditions. Unfortunately, the corresponding Eu(III) cross-bridged cyclam derivative only exhibits a hydration state of q = 0.25−0.35, limiting the relaxivity of this class of contrast agents. However, the correlation between the rigidity of a molecular framework and the kinetic properties of the resulting complex is once more highlighted with this example.

Recently, Law and co-workers reported a series of chiral, backbone-substituted Gd-DOTA derivatives, that are kinetically more inert than the parent Gd-DOTA complex.[358] For instance, Gd-L2A (SAP isomer) (Figure 42) showed almost no sign of Gd(III) release in 1 M HCl after 8 days while $t_{1/2}$ for Gd-DOTA is <25 h when subjected to the same conditions. Notably, these compounds afford modestly higher r_1 values than Gd-DOTA (e.g., GdL2A: r_1 = 4.7 mM^{-1} s^{-1}, 60 MHz, human blood plasma, 37 °C) and possess very fast water exchange rates that are in an optimal range for high field imaging (e.g., Gd-L2A: τ_m = 6.6 ns at 37 °C).

A special kind of MR contrast agent are gadofullerenes that are based on carbon nanomaterials. Fullerenes are closed up, hollow, and spheroidal structures that are composed of carbon atoms. Gd(III) can be entrapped within those carbon cages to yield paramagnetic particles, such as Gd@C$_{60}$, Gd@C$_{82}$, or Gd$_3$N@C$_{80}$. The high chemical stability of fullerenes can resist

schematic DOTA-tetraamide schaffold

cddadpa-ligand

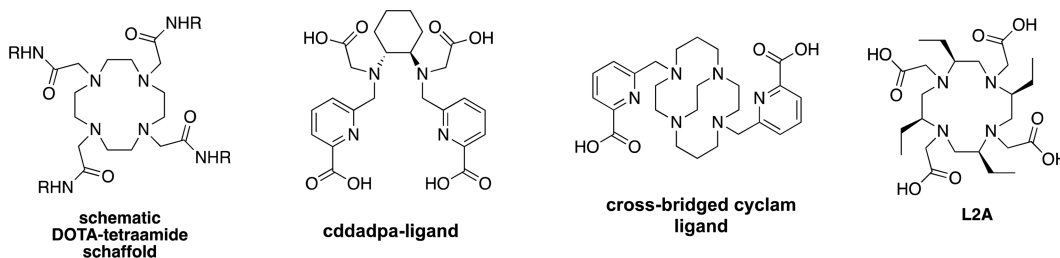**cross-bridged cyclam ligand**

L2A

Figure 42. Chemical structure of selected ligand systems.

any potential metabolic cage-opening process and, hence, completely prevents the release of Gd(III) ions.[359−361]

4.4. Gadolinium(III)-Free Alternatives

4.4.1. Gd(III)-Free Small Molecule Relaxation Agents.
The Gd(III) ion is a potent relaxation agent due to its 7 unpaired electrons and isotropic electronic ground state, but there are a few other metal ions, namely, high spin Mn(II), high spin Mn(III), high spin Fe(III), and Eu(II) that can serve as effective relaxation agents.[102]

The d^5 Mn(II) ion is a very effective relaxation agent due to its preference for a high-spin (S = 5/2) electronic configuration and characteristically long T_{1e}.[102] Aqueous Mn(II) complexes typically have coordination numbers (CN) of 6 or 7.[362] Whereas Gd(III) complexes can typically accommodate both an octadentate chelator and a water coligand, Mn(II) chelators cannot exceed hexadenticity and simultaneously accommodate an exchangeable water ligand. In general the stability constants of Mn complexes are lower compared to Gd(III) complexes utilizing comparable donor groups, and the Mn complexes tend to be more labile (Table 7). For example, log K_{ML} for $[Gd(DTPA)(H_2O)]^{2-}$ and $[Mn(EDTA)(H_2O)]^-$ are 22.5 and 13.9, respectively.[2,362] The dissociation half-lives of $[Gd(DTPA)(H_2O)]^{2-}$ and $[Mn(EDTA)(H_2O)]^-$ in the presence of 10 μM challenging Zn(II) at pH 7.4 are 330 and 0.07 h, respectively.[362,363] The lower stability/inertness of Mn(II) complexes is due to its lower charge-to-radius ratio and its absence of ligand field stabilization energy. The poor stability and kinetic inertness of Mn(II) complexes have been the main barriers toward the development of Mn-based contrast agents that are capable of replacing Gd(III) complexes.

A number of Mn complexes supported by various linear and macrocyclic ligands have been evaluated as potential MRI contrast agents. (Figure 43 and Table 8).[362] Linear ligands like EDTA form 7-coordinate ternary Mn complexes with a water coligand that are also among the most thermodynamically stable Mn complexes. A number of high-relaxivity Mn-EDTA derivatives have been evaluated as MRI contrast agents. The benzyloxymethyl (BOM) functionalized complexes Mn-EDTA-BOM and Mn-EDTA-BOM₂ were among the first reported Mn complexes of very high relaxivity. The peripheral BOM functional group promotes high affinity interactions with HSA, and Mn-EDTA-BOM and Mn-EDTA-BOM₂ exhibit r_1 values of 55.3 mM^{-1} s^{-1} and 48.0 mM^{-1} s^{-1}, respectively, upon HSA binding at 20 MHz and 25 °C. Mn-L1 is a high-relaxivity, serum albumin-binding Mn-EDTA derivative analogous to MS-325. Mn-L1 was used to conspicuously detect narrowing of the carotid artery and jugular vein in a rabbit model of arterial and venous stenosis. A hexameric Mn-EDTA-derived agent was also designed for high-relaxivity at higher (>3.0 T) field strengths. At 4.7 T and 37 °C, a relaxivity of 6.6 mM^{-1} s^{-1} per Mn was measured for the hexamer, whereas the monomeric EDTA-derived chelator had a relaxivity of 3.0 mM^{-1} s^{-1}.

EDTA-type ligands form Mn complexes that are very rapidly dissociated, but replacement of the ethylendiamine backbone with a trans-1,2-cyclohexylenediamine (trans-1,2,-cyclohexylenediaminetetraacetic acid, CyDTA) linker increased kinetic inertness by nearly 3 orders of magnitude (Table 9).[363] CyDTA also supports Mn complexes of q = 1. Recent work evaluating the kinetic inertness of phenylenediaminetetraacetic

Table 7. Comparison of Formation Constants of Previously Reported Mn Chelates[a]

	log K_{ML}	log K_{ML} pH 7.4	pMn[b]
acyclic chelates, q < 1			
AAZTA[368]	14.19[c]	11.31[c]	8.15[c]
DTPA[363]	14.54[c]	10.93[c]	7.77[c]
EGTA[363]	11.60[c]	8.82[c]	6.91[c]
AAZ3A[368]	11.00[c]	8.15[c]	6.58[c]
AAZ3MA[368]	10.67[c]	7.77[c]	6.39[c]
BIMP[363]	9.74[c]	7.57[c]	6.30[c]
MeAAZ3A[368]	11.43[c]	7.03[c]	6.47[c]
PMDPA[369]	11.37[g]	6.82[g]	5.94[g]
TMDTA[363]	9.70[c]	6.54[c]	5.81[c]
DPDP[370]	15.10[e]	6.33[e]	5.72[e]
HBED[370]	14.78[e]	6.33[e]	5.72[e]
PLED[370]	12.56[e]	6.09[e]	5.61[e]
acyclic chelates, q ≥ 1			
CyDTA[363,371]	14.32[c], 14.69[e]	12.34[c], 12.64[e]	8.67[c], 8.82[e]
PyC3A[363]	13.86[c]	11.34[c], 11.40[d]	8.06[c]
EDTA-BOM₂[332]	13.90[f]	11.02[f]	8.12[f]
EDTA-BOM[332]	13.50[f]	10.62[f]	7.82[f]
EDTA[332,363,371]	12.46[c], 12.61[e], 13.88[f]	10.49[c], 10.67[e], 11.02[f]	7.82[c], 7.83[e], 8.01[f]
CyHBET-NO₂[371]	13.66[e]	10.10[e]	7.55[e]
HBET-NO₂[371]	11.29[e]	8.73[e]	7.01[e]
HBET[371]	13.07[e]	7.97[e]	6.62[e]
HBET-OMe[371]	13.32[e]	7.91[e]	6.48[e]
CyHBET[371]	14.16[e]	7.76[e]	6.68[e]
CyHBET-OMe[371]	14.61[e]	6.95[e]	6.24[e]
macrocyclic chelates, q < 1			
DOTA[372]	19.89[h]	13.27[h]	8.94[h]
DO3A[372]	19.49[h]	12.25[h]	8.62[h]
HPDO3A[372]	17.89[h]	12.18[h]	8.59[h]
NOTA[373,374]	14.90[h], 16.3[h]	10.88[h], 10.52[h]	7.94[h], 7.76[h]
1,4-DO2A[j372]	16.13[h]	10.10[h]	7.55[h]
1,7-DO2A[372]	14.54[h]	8.21[h]	6.61[h]
macrocyclic chelators, q ≥ 1			
15-pyN₅[367]	10.89[h]	7.72[h]	6.37[h]
12-pyN₄P[366]	14.06[h]	7.35[h]	6.19[h]
12-pyN₄A[366]	11.54[h]	7.14[h]	6.09[h]
NO2A[365]	11.56[I]	7.11[I]	5.96[I]
NODAHA[375]	10.15[g]	6.43[g]	5.76[g]
NODAHep[375]	10.98[g]	6.37[g]	5.73[g]
NODABA[375]	9.90[g]	6.10[g]	5.61[g]
15-pyN₃O₂[367]	7.18[h]	5.20[h]	5.27[h]
9-aneN₂O-2P[365]	10.61[h]	5.07[h]	5.23[h]
9-aneN₂O-2A[365]	7.43[h]	4.36[h]	5.06[h]
9-aneN₂O-2PH[365]	4.30[h]	3.34[h]	5.01[h]
9-aneN₂O-2PPh[365]	4.82[h]	2.98[h]	5.00[h]

[a]In each group, chelates are ordered by conditional log K_{ML} at pH 7.4. [b]pMn at 10 μM MnL, pH 7.4. [c]I = 0.15 M NaCl, 25 °C. [d]Determined from K_{comp} with CDTA challenge, pH 7.4, Tris 50 mM, RT. [e]I = 0.10 M NaCl, 25 °C. [f]I = 1.0 M KCl, 25 °C. [g]I = 0.1 M KCl, 25 °C. [h]I = 0.1 M Me₄NCl, 25 °C. [I]I = 0.1 M NaNO₃, 25 °C. [j]Mn-DO2A is 0 < q < 1.

acid (PhDTA) shows that this ligand too provides a very kinetically inert Mn complex.[356]

Although macrocyclic ligands often form complexes that are more inert than linear ligands, Mn complexes with hexadentate macrocyclic ligands like NOTA form 6-coordinate Mn complexes that are q = 0 and thus low-relaxivity.[362] The macrocyclic chelator 1,4-DO2A has been shown to support a q
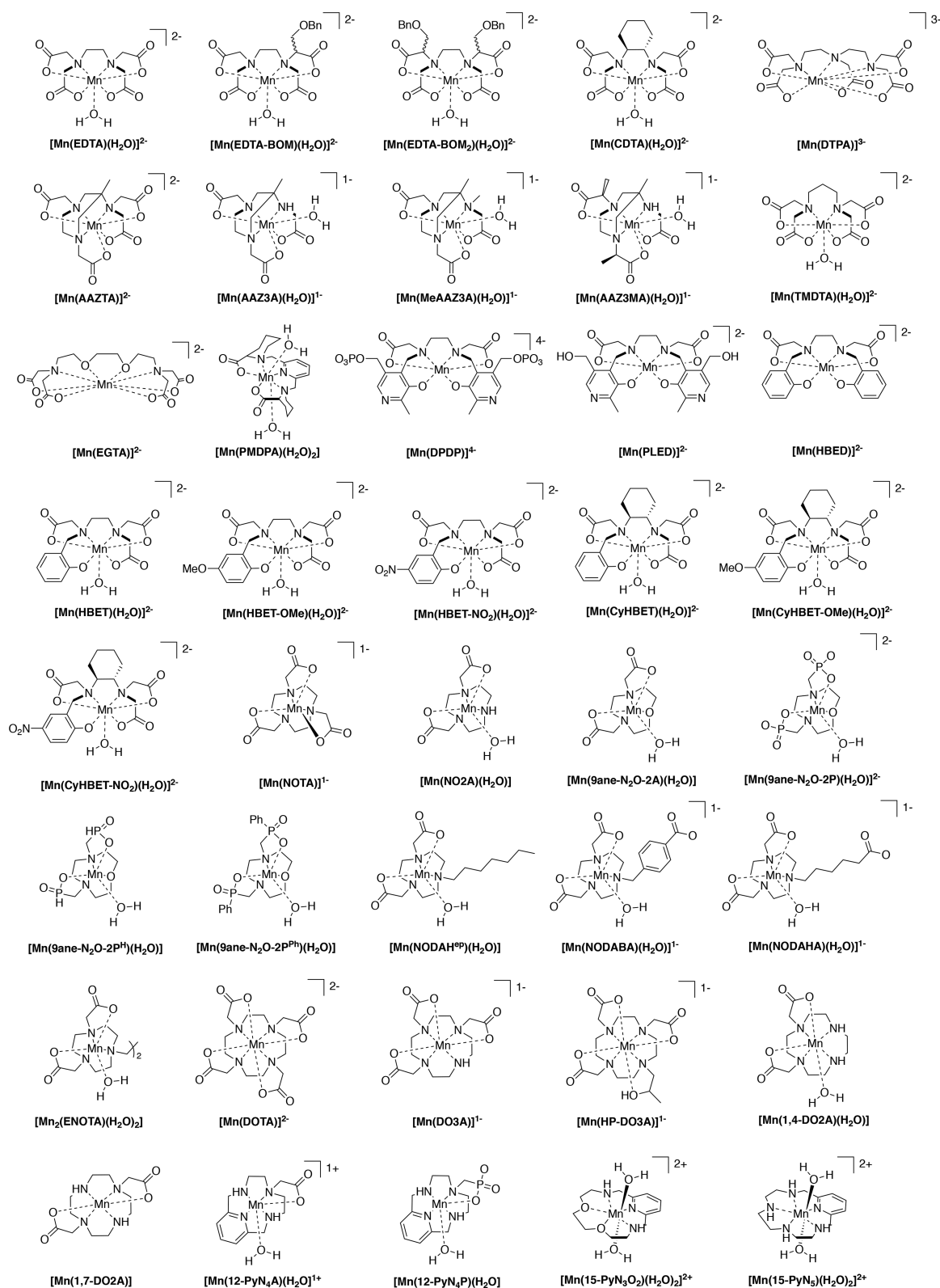
Figure 43. Mn(II) complexes previously considered in the context of MRI contrast.

= 1 Mn(II) complex, but we are unaware of any studies to evaluate the kinetic inertness of this complex.[364] However, a number of pentadentate ligands have been reported that form q = 1 or 2 Mn(II) complexes that are less thermodynamically stable than the complexes formed by linear and macrocyclic

hexadentate chelators but may be sufficiently inert to merit evaluation as MRI contrast agents.[365−367]

The chelate Mn-PyC3A was rationally designed as a potential alternative to Gd(III)-based extracellular agents.[377] The rigidifying *trans*-1,2-cyclohexylenediamine backbone provides high thermodynamic stability and a high degree of

Table 8. Comparison of r_1, r_2, Hydration State (q), Water Exchange Rate (k_{ex}), Enthalpy of Activation of Water Exchange ($\Delta H^{\neq}$), and Mn−H(Water) Hyperfine Coupling Constant for Mn(II) Complexes That Have Been Considered as MRI Contrast Agents

	r_1^{298} (mM^{-1} s^{-1})	r_1^{310} (mM^{-1} s^{-1})	r_2^{310} (mM^{-1} s^{-1})	q	k_{ex}^{310} (× 10^7 s^{-1})	$\Delta H^{\neq}$	$A_o/\hbar$ (× 10^7 rad/s)
PyC3A	2.8[a], 3.3[b]	2.1[a], 2.5[b]	4.9[a]	1	11	37.2	2.87
EDTA[332]	3.0[c]	2.2[a]	3.7[a]	1	59	36.7	3.79
EDTA-BOM[332]	3.6[b]	–	–	1	19	43.1	3.79
EDTA-BOM$_2$[332]	4.3[b]	–	–	1	25	38.4	3.79
EDTA-Tyr iso[334]	–	3.2[a], 3.6[b]	–	1	30	35.6	2.92
Mn-453[138,331]	5.8[b]	–	–	0.8	30	21.1	3.33
CDTA[138]	–	2.1[a]	3.5[a]	1	27	35.8	3.14
AAZTA[368]	1.6[b368]	–	–	0	–	–	–
AAZ3A[368]	2.5[b]	–	–	0 < q < 1	7.0	22.8	–
MeAAZ3A[368]	2.0[b]	–	–	0< q < 1	20	26.5	–
AAZ3MA[368]	1.9[b]	–	–	0 < q < 1	18	16.7	–
HBET[371]	–	2.8[a]	9.4[a]	1	370	33.8	3.54
HBET-OMe[371]	–	3.1[a]	11.1[a]	1	360	40.7	4.15
HBET-NO$_2$[371]	–	2.3[a]	4.8[a]	0.5	48	41.2	3.48
CyHBET[371]	–	3.3[a]	6.0[a]	1	770	41.2	3.36
CyHBET-OMe[371]	–	3.3[a]	5.8[a]	1	300	20.7	4.02
CyHBET-NO$_2$[371]	–	2.3[a]	3.7[a]	1	190	31.3	3.97
ENOTA[376]	3.4[b]	2.7[b]	–	1	7.9	20.5	3.27
9-aneN$_2$O-2A[365]	2.8[b]	2.3[b]	–	1	2.3	38.8	3.33
9-aneN$_2$O-2P[365]	5.1[b]	4.3[b]	–	1	140	11.7	3.33
1,4-DO2A[364]	2.1[b]	–	–	0 < q < 1	110	29.4	4.10
1,7-DO2A[364]	1.5[b]	–	–	0	–	–	–
DO1A[364]	2.4[b]	–	–	1	500	17.6	3.94
12-pyN$_4$A[366]	2.4[b]	1.9[b]	–	1	330	13.0	3.66
12-pyN$_4$P[366]	2.8[b]	2.3[b]	–	1	250	14.0	3.99
15-pyN$_5$[367]	4.5[b]	3.6[b]	–	2	13	37.7	3.86
15-pyN$_3$O$_2$[367]	3.6[b]	3.1[b]	–	2	0.69	35.3	3.86
15-pyN$_5$[367]	4.5[b]	3.6[b]	–	2	13	37.7	3.86

[a] 1.4 T. [b] 0.47 T. [c] 0.56 T.

Table 9. Dissociation Half-Lives of Mn(II) Complexes in the Presence of Competing Divalent Metal Ions[a]

ligand	$t_{1/2}$ (h)
EDTA[b]	0.08
CyDTA[b]	12
PhDTA	19.1
NOTA[c]	74
PyN5[c]	11.4
12-pyN$_4$A[c]	2.4
nompa[c]	0.02
dompa[c]	0.16
pcma[c]	2.4
NJC-L1[b]	0.02
NJC-L2[b]	2.8
NJC-L3[b]	55

[a] Conditions: 10 μM Mn(II) complex, 10 μM Cu(II) or Zn(II), pH 7.4. [b] Cu(II). [c] Zn(II).

kinetic inertness but leaves a vacant coordination site for a rapidly exchanging water coligand. Upon challenge with 25 mol equiv Zn(II) at pH 6.0, Mn-PyC3A was 20 times more inert than Gd-DTPA. Mn-PyC3A has a very modest affinity for blood plasma proteins and this provides a r_1 of 3.8 mM^{-1} s^{-1} in blood plasma at 1.4T, 37 °C, comparable to the r_1 of Gd-DTPA and Gd-DOTA measured under similar conditions (4.1 and 3.6 mM^{-1}·s^{-1}, respectively).[59] Mn-PyC3A also provides comparable contrast to Gd(III) contrast agents in vivo. Side-

by-side comparison of Mn-PyC3A versus Gd-DTPA in MR angiography performed in a nonhuman primate model revealed no statistically significant difference in vessel versus adjacent muscle contrast-to-noise ratios (Figure 44).[378] The cyclohexylene backbone and N-pyridyl donor also provides a degree of lipophilicity which promotes mixed renal and hepatobiliary clearance.[377] Partial hepatobiliary clearance is a favorable attribute in the context of renal impairment, as reduced kidney function should less profoundly influence elimination of an agent with an alternate route of elimination. Mn-PyC3A was also demonstrated to be rapidly eliminated and highly robust against metabolic transformation or degradation.[378]

High spin Mn(III) complexes such as Mn-porphyrin and Mn complexes of 1,2-phenylenediamine derived bis-amidate ligands (Mn-PDA) have also been demonstrated as effective MRI contrast agents (Figure 45).[379,380] Both porphyrins and PDA type ligands form quaternary Mn(III) complexes with two water coligands. The complexes are octahedral with the tetradentate porphyrin and PDA ligands comprising the equatorial plane and the water coligands occupying the apical positions. The water exchange rates of Mn-TPPS and Mn-TPMPyP were shown to be 1.4 × 10^7 s^{-1} and 1.0 × 10^7 s^{-1} at 298 K.[381]

The relaxivity of Mn(III)-porphyrins has been described as "anomalously" high considering the S = 2 spin state.[379] The mechanisms that dictate the relaxivity of Mn(III) complexes are largely underexplored relative to those of Gd(III) and
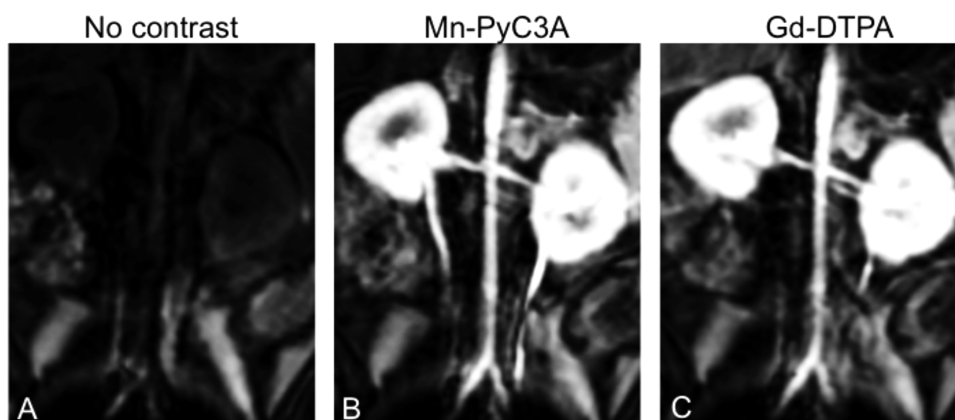
Figure 44. Multiplanar reformatted coronal images from three-dimensional T1-weighted gradient echo (volume-interpolated breathhold examination) sequence acquired at 3.0 T show abdominal aorta and renal arteries, (A) prior to injection of contrast agent, (B) 9 s after injection of 0.1 mmol/kg Mn-PyC3A, and (C) 9 s after injection of 0.1 mmol/kg Gd-DTPA. Reproduced with permission from ref 378. Copyright 2018 Radiological Society of North America (RSNA).
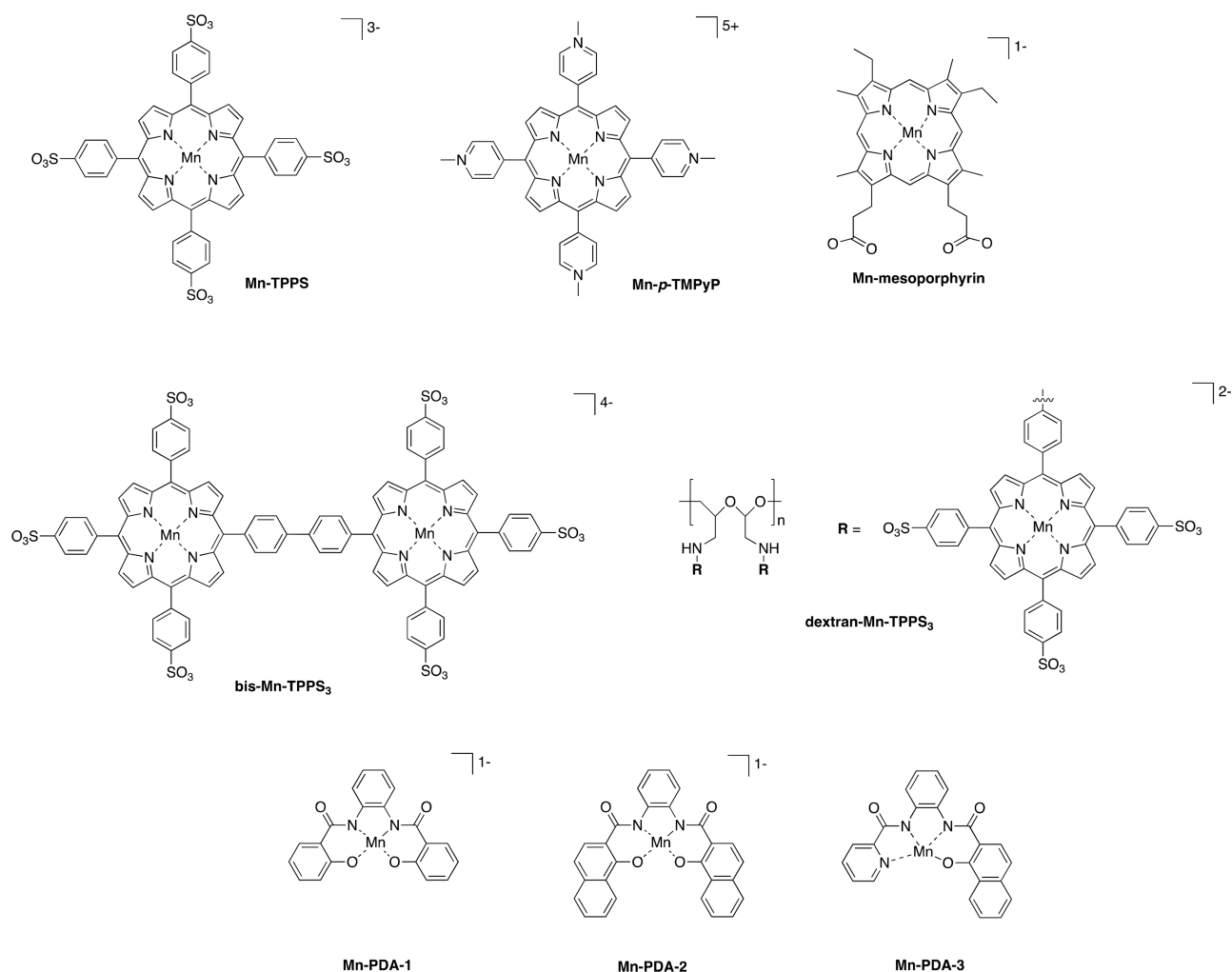
Figure 45. Mn(III) complexes explored as high-relaxivity MRI contrast agents.

Mn(II), but it is believed that the high relaxivity of Mn(III) porphyrin is at least partially due to elongation of the singly occupied d_z^2 orbital which lies across the Mn(III)-OH$_2$ bond axis. This favorable asymmetry effectively reduces the distance between the Mn(III) spin density and the water ^{1}H nuclei, and it has been proposed that the r^6 term in eq 5 may not

adequtely describe the efficiency with which the Mn(III) ion induces ^{1}H relaxation.[379] NMRD data recorded on Mn(III) porphyrin complexes indicate that T_{1e} is rapid compared to Gd(III) and Mn(II) complexes and provides significant contributions to the correlation time up to 100 MHz.[102,379,382] Fast electronic relaxation will limit the

relaxivity gains from slow rotation. For example, cyclodextrin encapsulation of the Mn(III) complex Mn(III)-tpps results in only a 2-fold increase in r_1 at 0.47 T, while the corresponding Mn(II) sister complex, Mn(II)-tpps, showed a 6-fold increase.[382]

Anionic Mn(III)-porphyrin complexes have been considered as Gd(III)-free contrast agents. For example, the tetracarboxylate functionalized complex Mn(III)-TCP was shown to exhibit comparable T_1 enhancement and biodistribution to Gd-DTPA in a mouse model.[383] Dimerization of a trisulfonated Mn(III)-porphyrin resulted in a complex that exhibited a per Mn relaxivity that is 3-fold greater than Gd-DTPA at 3 T and 25 °C.[384] This porphyrin dimer was shown to be an effective blood pool imaging agent in a rat model.[385] Mn(III)-mesoporphyrin has been considered for use as a hepatobiliary contrast agent and was shown to be effective for delineation of liver tumors and liver abcesses.[386,387] A trisulfonated Mn(III)-porphyrin conjugated to a 30000 kDa dextran-derived polymer was used to visualize lesions in a mouse model of hepatoma.[388] The Mn-PDA complexes were shown to be cell permeable and have been further elaborated for detection of intracellular enzymes.[380]

High spin Fe(III) is also an effective relaxation agent. Fe(III) complexes are typically much more stable even than Gd(III) complexes. For example, log K_{ML} for Fe-DTPA is 27.3, whereas log K_{ML} for Gd-DTPA is 22.5. The complexes Fe-DTPA ($q = 0$) and Fe-CDTA ($q = 1$) have been evaluated as extracellular contrast agents in a breast cancer xenograft mouse model.[389] The relaxivity of Fe-DTPA and Fe-CyDTA are 0.9 mm^{-1}s^{-1} and 2.2 mM^{-1} s^{-1}, respectively, in blood serum at 9.4 T, room temperature, compared to a value of 4.1 mM^{-1} s^{-1} for Gd-DTPA under the same conditions. Up to 5-fold larger doses of the Fe(III) complexes were required to visualize the tumors with comparable conspicuity to that observed with Gd-DTPA. Coordinatively saturated ($q = 0$) complexes such as Fe-HBED and Fe-EHPG have been evaluated as potential hepatobiliary MRI contrast agents (Figure 46).[390−392]

High spin Fe(II) has also been considered as a contrast agent (Figure 46). The $q = 1$ Fe(II) complexes Fe-DPTACN

(DPTACN = 1,4-dipicolyl-1,4,7-triazacyclononane) and Fe-DTTACN (DTTACN = 1,4-ditetrazoylmethyl-1,4,7-triazacyclononane) have been explored as MRI contrast agents.[393,394] A relaxivity of 0.6 mM^{-1} s^{-1} was recorded for both Fe(II) complexes at 7 T. Fe-DTTACN was shown to provide prolonged contrast enhancement after direct intramuscular injection into a mouse.[393]

The Eu(II) ion is isoelectronic with Gd(III) and complexes of Eu(II) have been demonstrated to be potent relaxation agents. The Eu(II)$_{(aq)}$ ion has one of the fastest water-exchange rates measured.[395,396] However, the Eu(II) oxidation state is disfavored relative to the diamagnetic Eu(III) ion in the polyaminocarboxylato ligands typically utilized for Gd(III)-based contrast agents.[397,398] Eu(II)-based MRI contrast agents can be stabilized by 2.2.2 cryptands comprised of neutral donor groups, Figure 47.[399,400] The 2.2.2 cryptand cavity is ideally suited to Ln(II) binding, and the soft nature of the neutral donors accommodate the Eu(II) oxidation state. Eu(II)-2.2.2 cryptands form ten coordinate quaternary complexes with two rapidly exchanging water coligands and thus afford high relaxivity contrast agents. The relaxivity values and associated molecular parameters for previously reported Eu(II) cryptand complexes are summarized in Table 10. Like Gd(III), the symmetric S electronic ground state of Eu(II) is characterized by a T_{1e} on the order of nanoseconds, and high relaxivity Eu(II) complexes can be achieved by increasing τ_R. For example, the relaxivity of the biphenyl-appended complex Eu(II)-2.2.2-BiPh increased from 4.2 to 8.7 mM^{-1} s^{-1} and 12.5 mM^{-1} s^{-1} upon forming inclusion complexes with β-cyclodextrin and poly-β-cyclodextrin, respectively, and to 16.6 mM^{-1} s^{-1} upon binding to HSA. Intriguingly, the relaxivity values of Eu(II) complexes at 7 T are typically ∼30−35% greater than the values recorded at 3 T, and in this regard, Eu(II) agents have received consideration for imaging applications at field strength >3 T.[401−403]

Thermodynamic stability and kinetic inertness have been evaluated for a few Eu(II)-based agents. Potentiometric titration of the Eu(II) complexes of ODDM, ODDA, and DTPA yielded log K values ranging from 9.9 to 13.1.[398] Similarly, log $K_{ML} = 13$ for Eu-2.2.2 was determined indirectly through electrochemical measurements.[399] These Eu(II) complexes are roughly 10 orders of magnitude less stable than the Gd(III)-based contrast agents, but they are remarkably inert. Kinetic inertness of complexes Eu-2.2.2 and Eu-2.2.2-Ph was evaluated under a standard set of conditions that has been applied to all of the clinical agents (2.5 mM contrast agent, 2.5 mM ZnCl$_2$ as challenging ion, pH 7.0 phosphate)[217,404] and indicates that the Eu(II) complexes are comparably inert to the macrocyclic agents such as Gd-DOTA and Gd-HPDO3A.[401]

Although capable of supporting the Eu(II) oxidation state, the 2.2.2 cryptand complexes reported to date still undergo oxidization to the corresponding Eu(III) complex under aerobic conditions.[405−407] Eu-2.2.2 is rapidly oxidized in the bloodstream, providing no positive contrast enhancement 3 min after intravenous injection in mice.[408] However, prolonged contrast enhancement on the order of minutes occurred following intratumoral injection of Eu-2.2.2 and for hours following intratumoral injection of Eu-2.2.2-F.[406,408] The oxidation kinetics of EuCl$_2$, Eu-2.2.2-F, and Eu-DOTAM-Gly$_4$ have been evaluated in the presence of the bromate anion and the biologically relevant oxidant glutathione disulfide.[409] The data suggests that the kinetics of Eu(III) formation reflect

A

Fe-HBED   **Fe-EHPG**
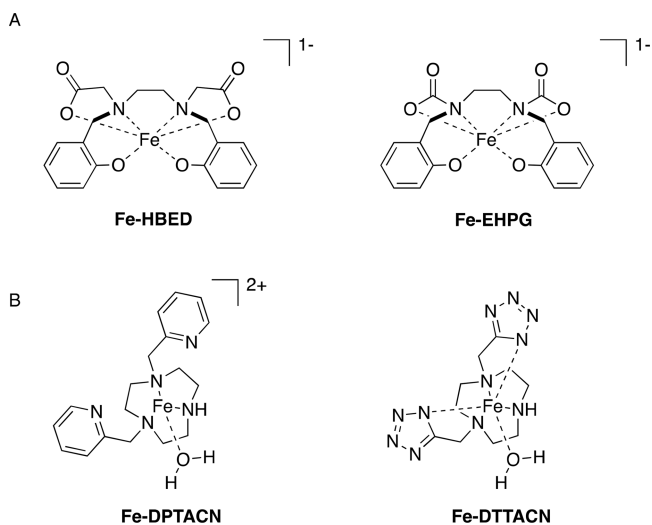
B

Fe-DPTACN   **Fe-DTTACN**

Figure 46. (A) The Fe(III) complexes Fe-HBED and Fe-EHPG and (B) have been considered as hepatobiliary specific contrast agents. (B) The Fe(II) complexes Fe-DPTACN and Fe-DTTACN have been considered as contrast agents.
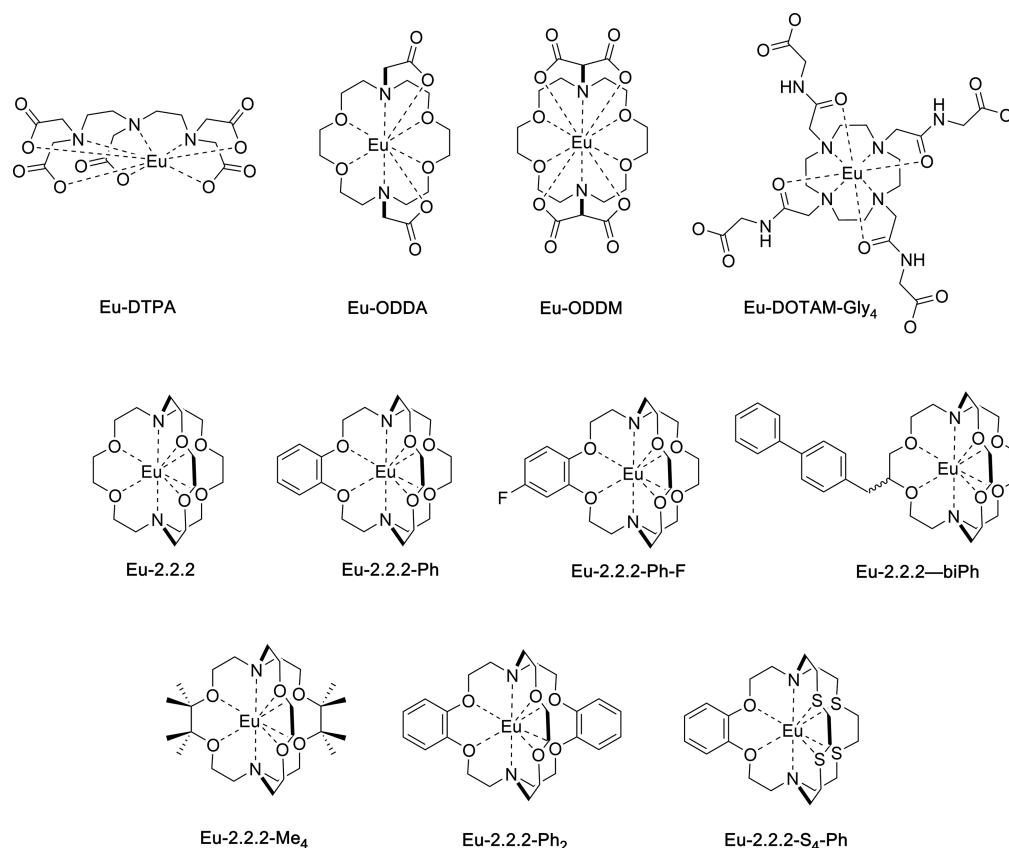
Figure 47. Eu(II) complexes considered as potential MRI contrast agents (coordinated water molecules not shown).

Table 10. Summary of Relaxivity, Water Exchange Kinetics, Electronic Relaxation, Thermodynamic Stability (in 0.15M NMe₄Cl Electrolyte Solution), and Oxidation Potentials of Selected Eu(II) Complexes

	r_1 (mM^{-1} s^{-1})	q	τ_m^{310} (ns)	$\Delta H^{\ddagger}$	$T_{1e}310$ (ns)	log K_{ML}	$E^{1/2}$ (V)
Eu-2.2.2[410]	2.1,^{a} 2.7^b	2	2	33.4, 30.6	1.1,^{c} 3.0^d	13.0^f	-0.21^g, -0.336^h
Eu-2.2.2-Ph[410]	3.7,^{a} 3.3^b	2	10	39.9	1.2,^{c} 3.8^d	–	-0.208^h
Eu-2.2.2-BiPh[410]	4.2,^{a} 4.8^b	2	12	31.1	1.3,^{c} 4.2^d	–	–
Eu-2.2.2-BiPh/b-CD[410]	8.7^a	2	12	–	39,^{c} 155^d	–	–
Eu-2.2.2-BiPh/poly bCD[410]	16.6^a	2	12	–	56,^{c} 215^d	–	–
Eu-2.2.2-BiPh/HSA[410]	12.5^a	2	12	–	191,^{c} 763^d	–	–
Eu-2.2.2-Ph-F	–	–	–	–	–	–	-0.079^h
Eu-2.2.2-Me₄	–	–	–	–	–	–	-0.169^h
Eu-2.2.2-Ph₂	–	–	–	–	–	–	-0.211^h
Eu-2.2.2-S₄-Ph	–	–	–	–	–	–	-0.035^h
Eu-ODDM	–	–	–	–	–	13.1^e	-0.92^g
Eu-ODDA	–	1	–	22.5	4.0,^{c} 15^d	9.9^e	-0.82^g
Eu-DTPA	–	1	–	26.3	2.3,^{c} 8.7^d	10.1^e	-1.35^g
Eu-DOTAM-Gly₄	–	1	–	–	–	–	-0.701^g

^{a}1.4 T, 37 °C. ^{b}7 T. ^{c}1.5 T. ^{d}3.0 T. ^{e}In 0.1 M (CH₃)₄NCl at 25 °C.^{f}Determined indirectly via cyclic voltammetry methods; vs. ^{g}Ag/AgCl, vs. ^{h}Fc/Fc⁺.

the overpotential between Eu(II) and chemical oxidant. It is thus feasible that stable intravenous Eu(II) formulations could be developed by ligand modifications to shift the oxidation potential to more positive values.

Nitroxide radicals, Figure 48, have also been considered as MRI contrast agents but are much less effective relaxation agents than metal ion based systems.[411−415] Nitroxide r_1 values typically range between 0.1 and 0.5 mM^{-1} s^{-1}. The low relaxivity compared to paramagnetic metal ions is due to the low spin quantum number (S = 1/2) as well as the fact that the nitroxide radicals do not benefit from inner sphere interactions

Figure 48. Nitroxide radicals 3-CP and chex have been evaluated as MRI contrast agents.

Figure 49. Iodinated X-ray contrast agents have been evaluated as DiaCEST contrast agents.

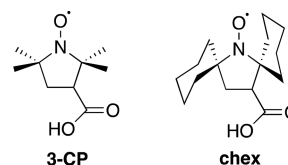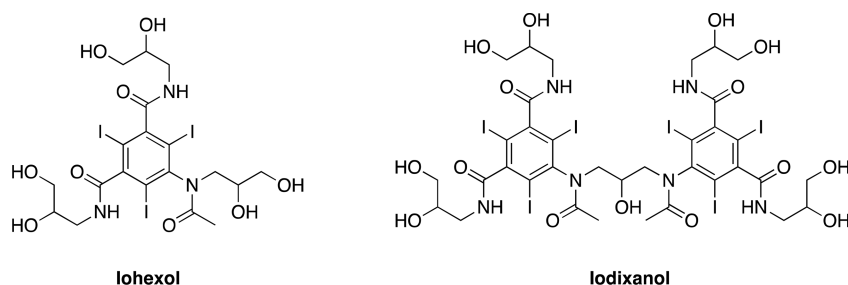to place the ^{1}H into close proximity with the paramagnet. Indeed, nitroxide radicals require stabilization from adjacent sterically encumbering and hydrophobic functional groups.

Nitroxide radicals are rapidly reduced to diamagnetic hydroxylamines and typically exhibit in vivo half-lives on the order of minutes.[416−420] Nitroxide reduction kinetics can be influenced by their local chemical environment. For example, it was shown that replacing the nitroxide adjacent geminal dimethyl groups of 3-carboxy-2,2,5,5-tetramethyl-1-pyrrolidinyloxy (3-CP) with spirocylohexyl (chex) groups results in a 2-fold decrease in the rate of reduction by excess ascorbate.[421] Upon incorporation of chex into polyethylene glycol decorated polypropylenimine dendrimers, a fraction of dendrimeric nitroxides become 20-fold more resistant to ascorbate reduction than the corresponding monomer.[422] These nitroxide functionalized dendrimers provide strong and persistent intravascular contrast enhancement that persists out to at least 1 h in a mouse model. A recently developed nitroxide and PEG-functionalized bottlebrush arm star polymer was used to visualize subcutaneous tumors in a mouse model 20 h following intravenous injection.[423]

4.4.2. Iron-Oxide Nanoparticles. SPIONs are generally too large to extravasate into extracellular spaces and are not excreted. The ultimate fate of SPIONs is macrophage capture and subsequent metabolism to labile iron.[424] Particle distribution is largely a function of size.[425] SPIONs of >80 nm diameter are very rapidly captured by macrophages. However, smaller particles can evade macrophage capture and exhibit circulatory lifetimes that span hours to days.[426] Particles >80 nm diameter are well-suited for imaging of the reticuloendothelial system (RES). For example, the SPION formulations ferumoxide and ferucarbotran, which are comprised of 120−180 nm dextran coated SPIONs and 45−60 nm carboxymethyldextran coated SPIONs, respectively, were developed for the detection of liver lesions.[49,424,427] Liver tissue is populated with phagocytic Kupffer cells, but malignant hepatocellular lesions are typically devoid of Kupffer cells. The strong SPION T_2^* effect thus renders liver parenchyma hypointense relative to lesions containing comparatively low populations of phagocytic cells. Similarly, the SPION T_2^* effect has been used to differentiate normal from malignant, macrophage-deficient lymph nodes.[50,428] SPION opsonization also offers an effective mechanism to detect and visualize the dynamics of inflammation.[429−431] SPION-enhanced MRI has been used to visualize atherosclerotic plaque,[432−434] the macrophage infiltration following stoke and myocardial infarction,[435−437] as well the detection and monitoring of numerous other disease states characterized by an acute inflammatory response.

The smaller SPIONs are more slowly captured by the RES and are eliminated from the bloodstream with half-lives on the order of hours to days. These smaller particles typically have good T_1 relaxivity as well and are thus ideal for contrast-enhanced MR angiography. Ferumoxytol is a SPION formulation with an FDA indication for iron replacement therapy that occasionally receives off label use as an angiographic contrast agent.[438] For example, ferumoxytol has been used for aortic imaging,[439] renal artery imaging,[440] detection of arteriovenous fistula,[441] detection of deep vein thrombosis,[442] and to characterize the vasculature of brain tumors.[443]

Recently, a new class of iron-oxide nanoparticles small enough to clear via glomerular filtration were introduced.[444] These particles, termed exceedingly small SPIONs (ES-SPIONs), are derived from a maghemite core which does not affect T_2 relaxation as strongly as magnetite. The maghemite core and <5.5 nm particle diameter provide an r_2/r_1 of 2.1, which is lower than that of any other SPION. The favorable signal generating and excretion profile of ES-SPIONs implicate these particles as potential candidates for Gd(III) free angiography agents.

Oral SPION formulations comprised have also been developed for contrast enhanced imaging of gastrointestinal structures. Ferumoxsil is a formulation comprised of poly-N-(2-aminoethyl)-3-aminopropyl siloxane magnetite particles ∼300 nm in diameter.[54] An oral formulation named Ferristene comprised of particles ∼3500 nm in diameter has also been developed for contrast-enhanced MRI of the bowels.[47]

SPIONs typically have a higher incidence of serious adverse drug reactions than Gd(III)-based agents.[445,446] SPION immunogenicity is influenced by the nature of the surface coating, and it may be possible to develop formulations of improved safety via careful tuning of chemistry at the particle surface.[447] Because SPIONs are metabolized to labile iron rather than excreted, there are also toxicity concerns related to iron overload.[448] On the other hand, some SPIONs are highly resistant to metabolism and can persist for prolonged periods in the liver. This can also pose a toxicity concern. For example, development of the SPION formulation feruglose, which was designed for MR angiography, was discontinued due to concerns over long-term liver retention.[47]

A very large number of SPION contrast agents have been proposed, and several were approved for imaging indications in the U.S. and Europe. However, none are currently marketed.

4.4.3. CEST Agents. Although a very large number of CEST agents have been reported over the past decade, very few have been pursued with the goal of potentially replacing relaxation agents. CEST agents are detected with poor sensitivity relative to relaxation agents, and thus larger doses are required to generate conspicuous MRI contrast. For this reason, the vast majority of CEST agent development has focused on utilizing the versatility of the CEST effect for

specialized molecular imaging applications and are discussed in the sections below.

Iodinated X-ray contrast agents have been evaluated as alternatives to Gd(III)-based relaxation agents, Figure 49.[449] The X-ray agents contain multiple CEST active exchangeable amide and alcohol protons, exhibit comparable pharmacokinetics to commercial Gd(III) agents, and are well-tolerated at the high doses required for CEST detection. Side-by-side comparisons of contrast enhancement generated using 10 mmol/kg of iopamidol, iohexol, and iodixanol compared to the clinically indicated 0.1 mmol/kg dose of Gd-HPDO3A were performed in a murine tumor model.[450] CEST enhancement of the tumor (expressed as % saturation transfer) generated using the iodinated agents correlated with Gd-HPDO3A contrast enhancement (expressed as % signal intensity increase). There was also a strong correlation between the extravasation fractions calculated using the iodinated contrast agents and the Gd-HPDO3A enhanced data.

A number of paramagnetic metal–ligand complexes have also been evaluated as CEST agents. Paramagnetic ions can shift labile proton resonances by up to 500 ppm from the bulk water resonance and thus permit utilization of a number of proton exchanging functional groups that would otherwise violate the $\Delta\omega > k_{ex}$ constraint in an analogous diamagnetic system. For example, saturation of the exchangeable Eu(III) coordinated water of Eu-DOTA tetramide complexes has been demonstrated to provide a strong CEST effect at 7 T despite the fact that water exchange occurs on the order of 10^4-10^5 s^{-1}, which far exceeds the slow k_{ex} required to observe the CEST effect with a diamagnetic agent, typically $<10^3$ s^{-1}, at the same field strength.[451] CEST observation is enabled by the Eu induced >14000 Hz shift. For a paramagnetic CEST agent, the benefits of a large paramagnetically shifted exchangeable proton resonance must be carefully balanced against the effects of paramagnetic relaxation. For example, the amide protons of Dy-DOTAM (Figure 50) provide a greater per
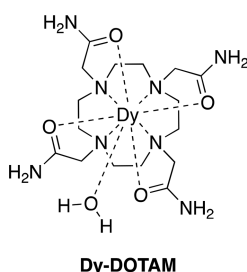

Dy-DOTAM

Figure 50. Exchangeable amide protons of Dy-DOTAM provide a greater CEST effect than the protons of the exchangeable water coligand because the amide protons are further from the Dy(III) ion and thus experience a weaker paramagnetic relaxation effect.

exchangeable CEST effect compared to the Dy(III) bound water because the amide protons are less effectively relaxed by the Dy(III) paramagnet.[452] Thus, the majority of newly developed paramagnetic CEST agents utilize second sphere exchangeable protons as the spectroscopically saturable handle. Amides, alcohols, amines, N-hydroxylamines, diazoles, and benzimidazoles have all been considered as second sphere proton exchangers. There are elegant examples of paramagnetic CEST agents prepared with lanthanide ions, including Nd(III), Eu(III), Tb(III), Tm(III), Dy(III), and

Yb(III) and transition metal ions such as Fe(II), Co(II), Cu(II), and Ni(II).[199,453−461]

5. TARGETED CONTRAST AGENTS

Biochemically targeted agents are designed to adhere with high specificity to a molecular target and provide prolonged local contrast enhancement after clearance of the unbound agent. There are myriad biochemical targets that if visible by MRI could profoundly impact the detection, staging, prognosis, and treatment monitoring of disease, as well as elucidating complex biology. However, developing biochemically targeted MR contrast agents is extremely challenging. A number of considerations must be accounted for in developing a suitable biochemically targeted agent: appropriate affinity for the target, high-specificity for the target, rapid clearance of the unbound agent relative to washout of the target bound agent, and high relaxivity in the target bound form.

5.1. Case Study: EP-2104R, a Fibrin-Targeted Contrast Agent

We introduce this section with a detailed case study of a fibrin-targeted contrast agent to highlight the challenges and strategies available to develop a biochemically targeted agent. To the best of our knowledge, the fibrin-targeted agent EP-2104R is the only biochemically targeted MRI contrast agent that has been used to directly detect a pathologic biomarker in humans.[462,463] Fibrin is the most highly abundant protein constituent of thrombus (clotted blood) at up to 100s of micromolar, but it is not present in circulating blood or any healthy tissue. Fibrin is formed by the actions of the enzymes thrombin and Factor XIII on fibrinogen. Fibrinogen circulates in blood at about 7 μM and is polymerized and cross-linked into the insoluble protein fibrin during the clotting cascade. An immediate challenge is to identify a targeting vector that recognizes fibrin specifically over circulating fibrinogen to which it shares great homology. Kolodziej et al. reported three families of short, cyclic peptides that were identified by phage display to selectively bind fibrin.[464] The specificity was engineered by first screening the phage libraries against fibrinogen, removing fibrinogen binders, and then screening the depleted library against fibrin.

EP-2104R is comprised of 4 Gd-DOTA chelators appended to a 6 amino acid, disulfide bridged cyclic peptide, Figure 51A. The peptide contains some unnatural amino acids found to improve fibrin affinity.[142,464−466] The 4 Gd-DOTA chelators are included to increase the relaxivity of the compound. It was found that conjugation of the chelates at both the C- and N-termini resulted in compounds that were more resistant to in vivo metabolism but at the same time did not substantially decrease fibrin affinity.[467] The per Gd(III) relaxivity of EP-2104R was 11.1 mM^{-1} s^{-1} in buffer and increased to 24.9 mM^{-1} s^{-1} when bound to fibrin (0.47 T, 37 °C). EP-2014R binds with little to no affinity to fibrinogen, albumin, or other blood proteins, and this is evidenced by the observation that relaxivity in blood plasma is virtually unchanged from that recorded in the buffer. The high fibrin-binding affinity (K_d = 1.6 μM for human fibrin) is reflected in the >2-fold relaxivity increase in the presence of fibrin.[466]

In humans, EP-2104R exhibits comparable distribution to an extracellular contrast agent and is rapidly eliminated via renal filtration with the blood signal returning to near baseline values within 6 h after injection.[462] EP-2104R showed efficacy in
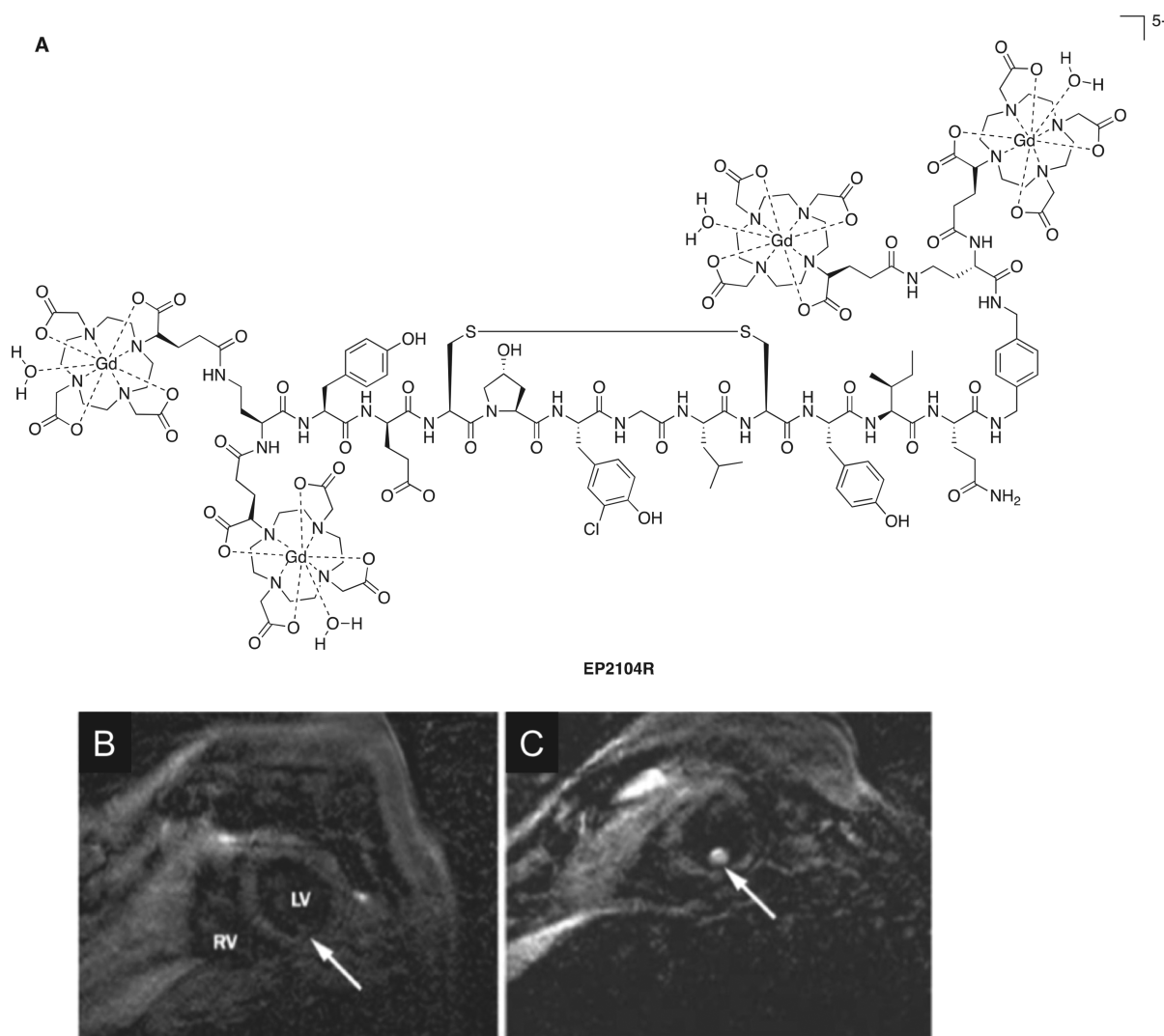
EP2104R

Figure 51. (A) Fibrin-targeting contrast agent EP-2104R is the first biochemically targeted agent to be used to detect a pathologic biomarker in humans. (B) Short axis view of the heart before EP-2104R injection. The arrow indicates the location of a left ventricular thrombus that is difficult to discern in the baseline scan. (C) The thrombus is highly conspicuous for several hours after EP-2104R injection. Reproduced with permission from ref 463. Copyright 2008 Springer Nature.

detecting thrombus in the heart, aorta, carotid arteries, deep veins, and pulmonary emoboli.[462]

5.2. Challenges and New Frontiers

MR imaging of fibrin provides but one illustrative example of the potential impact of a biochemically specific MRI contrast agent. Successful translation of EP-2104R was the culmination of years of dedicated research and development effort and provides several valuable lessons for the design of a biochemically targeted contrast agent. In this section, we will review prior accounts describing the design and application of MRI contrast agents targeting various biomarkers in order to illustrate the challenges and innovative solutions toward this new frontier in contrast-enhanced MRI. To extend this work to other targets, a number of technical challenges must be addressed. Identifying targeting vectors to bind to a specific molecular target with high affinity and high specificity is itself very difficult. Appending a contrast generating moiety to the targeting vector in a manner that does not compromise target affinity adds another layer of complication.

A third challenge is that micromolar concentrations of metal ion are required to generate detectable contrast with T_1- or T_2- weighted imaging sequences. Few biochemical targets are present at high enough concentration to be imaged with a targeted agent containing only a single metal ion. However, very innovative strategies have been explored to amplify contrast upon encountering its biochemical target. These strategies can be broadly divided into 4 general approaches, each with their own strengths and weaknesses: (1) increase the contrasting payload by conjugating multiple relaxation agents to the targeting vector. This strategy was successfully pursued in the EP-2104R example with 4 chelates per peptide. Such agents are chemically well-defined molecules that can be reproducibly synthesized. They are relatively small molecules which allow them to rapidly distribute in the body, bind to the target, and see the unbound agent be quickly eliminated from the body. The small size also typically results in ultimately complete elimination from the body. Drawbacks include the increasing complexity of the molecule and its synthesis, as well as the dearth of relevant molecular targets at high enough concentration. (2) Take advantage of an endogenous
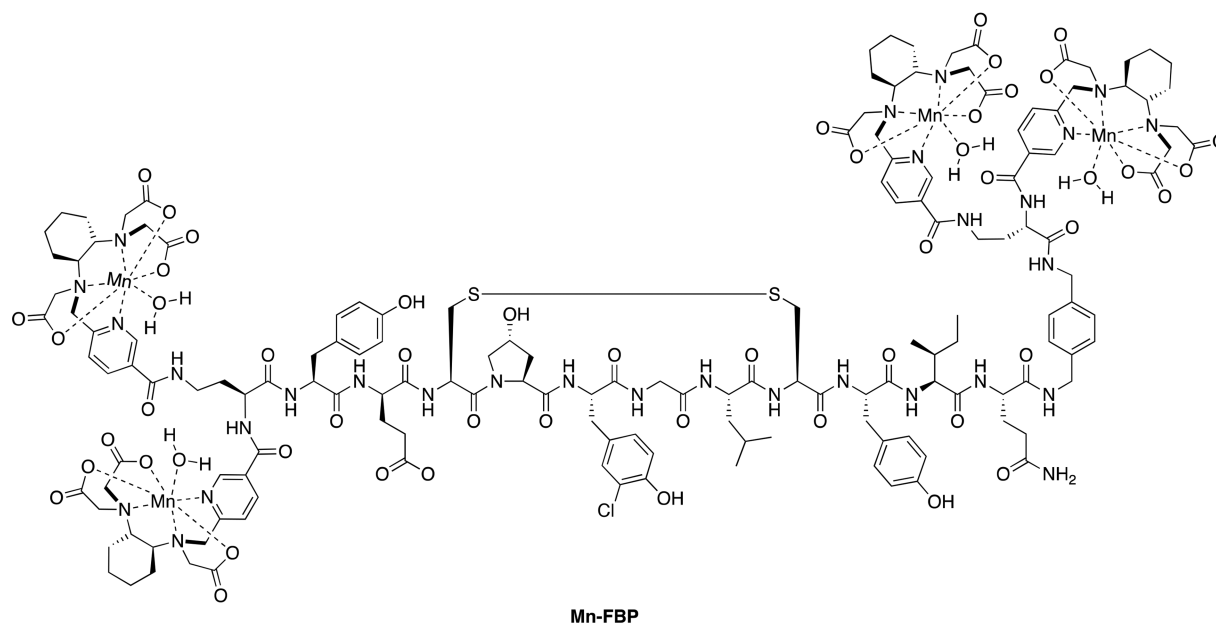
Mn-FBP

Figure 52. Mn-based fibrin-seeking contrast agent Mn-FBP is comprised of 4 Mn-PyC3A chelators conjugated to a fibrin-binding peptide.

mechanism such as receptor-mediated internalization to accumulate the targeted agent at MR visible concentrations. This is in principle a very attractive technique; however, the internalization process must be very efficient to accumulate the micromolar concentrations required for detection. (3) Utilize nanoparticles that bring hundreds or thousands of metal ions to increase the detection sensitivity into the low nanomolar range. (4) Use nanoparticle approaches to deliver a very high payload of nonendogenous (i.e., background free) magnetically resonant nuclei such a F-19. Both nanoparticle approaches are attractive solutions to overcoming sensitivity but bring challenges in terms of reproducibility, pharmacokinetics, and elimination. For clinical translation, the agent must be well-defined and there are obvious challenges in controlling the distribution of nanoparticles both with respect to their size and their surface derivatization, although these can be overcome. Nanoparticles typically distribute in the blood and are captured by macrophages in the liver, spleen, and lymph nodes. Tumor accumulation can occur either via capture in tumor associated macrophages or via the enhanced permeability of many tumors, but these process take several hours. In general, nanoparticles are not completely eliminated from the body and this can also create concerns for clinical translation.

5.3. Fibrin

As discussed above, fibrin is the main protein constituent of clotted blood and also present in the tumor microenvironment, making it a useful protein target in the molecular imaging of thrombosis,[462,468] cancer,[469] and other disease states that possess a coagulative component. In addition to the EP-2104R enhanced human imaging described above, a few additional fibrin targeting contrast agents merit note. A Mn-based fibrin seeking contrast agent, Mn-FBP, was also reported, Figure 52.[377] This agent uses the same peptide as EP-2104R, but the 4 Gd-DOTA chelators are replaced with 4 Mn-PyC3A moieties. Mn-FBP demonstrated equivalent fibrin affinity to EP-2104R in vitro and provided equivalent contrast enhancement of arterial thrombi in rats. The high-payload strategy was extended even further in liposomal fibrin-targeted agents,

where fibrin antibody was conjugated to liposome comprised of self-assembled amphiphilic Gd(III) complexes.[470−472] The direct nuclear detection strategy has been pursued by conjugating ^{19}F perfluorocarbon nanoemulsions to antiplasmin peptide fragments which become chemically cross-linked to fibrin.[473]

5.4. Serum Albumin

Albumin is a serum protein that is present at ∼660 μM and thus represents an abundant target for intravascular contrast agents. Small molecule agents with high affinity for albumin will confine largely to the blood pool (the 66 kDa protein does not extravasate) and provide prolonged and strong intravascular contrast. For example, MS-325 is an FDA-approved albumin targeting agent that noncovalently binds to the albumin drug binding site II with K_d = 85 μM.[17,139,474,475] MS-325 binding is promoted by a 4,4-diphenylcyclohexyl moiety connected to the Gd-DPTA chelate via a phosphodiester linkage.[16,476] The micromolar binding of MS-325 affinity ensures that a small fraction (10−20%) of MS-325 remains unbound at all times, and this unbound fraction can be cleared via glomerular filtration. Le Chatelier's principle ensures that this unbound fraction is constantly reestablished. Albumin is also present in the lymphatic system, and MS-325 has been used to detect metastatic invasion of lymph nodes.[477] In certain pathologies, albumin can leak out of the blood vessels into the interstitial space. Montesi et al. showed that patients with idiopathic pulmonary fibrosis had extensive vascular leak in their lungs, readily detected by MS-325-enhanced MRI.[478] A Mn-EDTA analogue of MS-325 has also been reported.[331]

A number of additional albumin targeting functionalities also have been appended to relaxation agents for intravascular imaging. For example, the Gd-DTPA based agents B22956/1, which have been extensively evaluated as an angiographic contrast agent, utilizes 3-deoxycholic acid as an albumin targeting group.[23−26,479−482] A biological function of serum albumin is to transport lipophilic anions. The high concentration of serum albumin and its ability to promiscuously bind many classes of compounds makes it possible to generate a
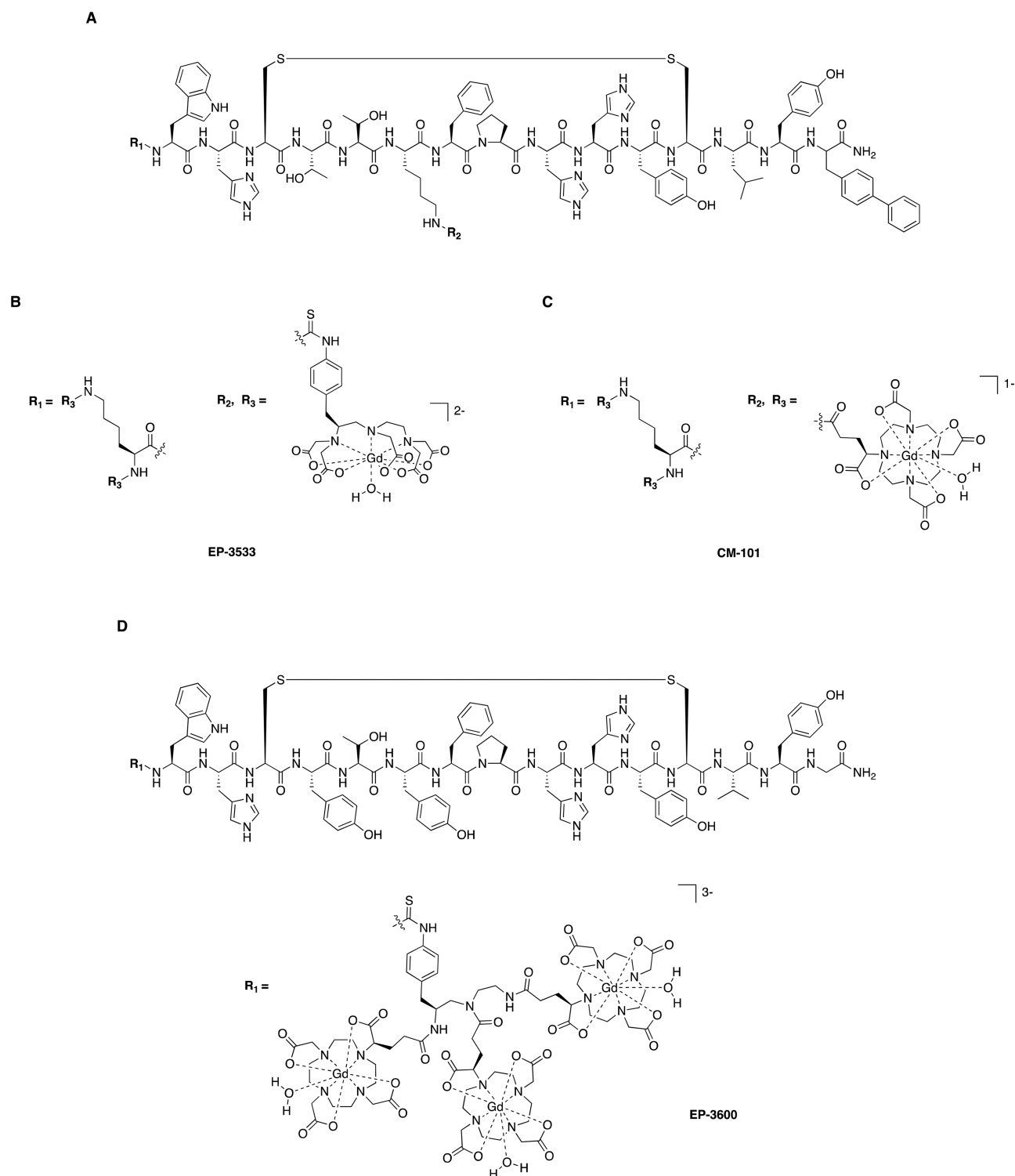
Figure 53. (A) Collagen-targeting MRI contrast agents are derived from a collagen-binding peptide identified via high-throughput screen to possess high specificity and affinity for typeI collagen. (B and C) The collagen-targeted agents EP-3533 and CM-101 are comprised of the collagen-binding peptide and 3 Gd-DTPA or Gd-DOTA chelators connected to the peptide N-terminus and lysine ε-side chains via thiourea or amide linkages, respectively. (C) EP-3600 is comprised of the collagen-binding peptide and a trimeric Gd-DOTA containing scaffold linked via the peptide N-terminus.

large number of albumin-targeted agents.[483−485] Additional examples of albumin binding MRI contrast agents have been reported,[333,476,486−489] but there are too many to acknowledge even for this extensive review.

5.5. Type I Collagen

Type I collagen is the most abundant protein constituent of connective tissue. In fibrosis, or organ scarring, collagen is overexpressed and is present at 10s of micromolar concentration. Fibrosis occurs in a number of major diseases such as
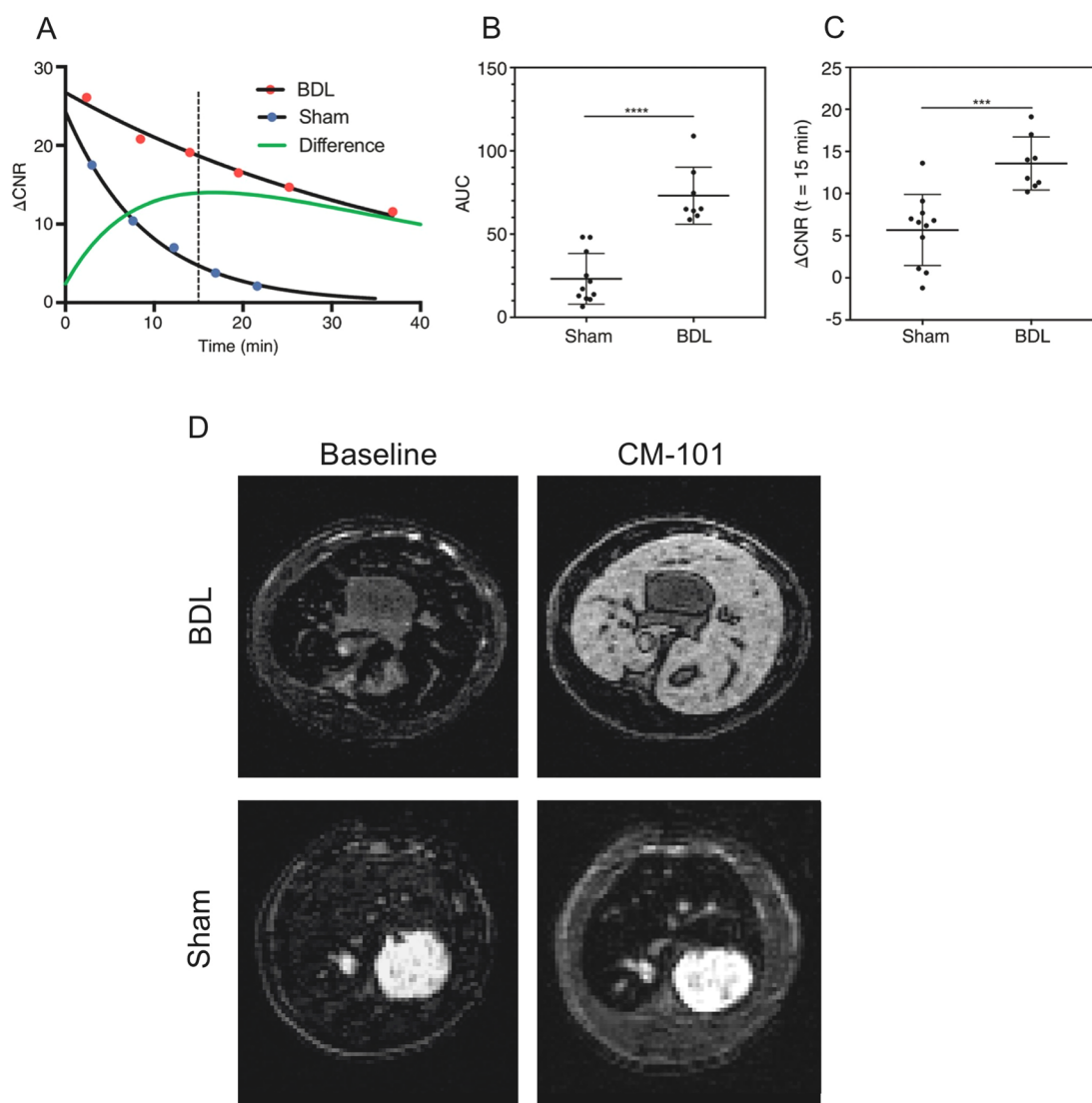
Figure 54. Change in contrast-to-noise ratio (CNR) following CM-101 injection in bile duct ligated (BDL, liver fibrosis) and sham-operated (healthy nonfibrotic liver) rats. (A) Representative dynamic time courses of the change in CNR between liver and muscle tissue for BDL (red ●) and sham (blue ●) treated rats following injection of CM-101. The maximal difference in ΔCNR (green line) between sham operated and BDL rats was observed at approximately 15−20 min following CM-101 injection. (B) A statistically significant difference in the area under the ΔCNR curve (AUC) between sham operated and BDL rats was observed. (C) A statistically significant difference in ΔCNR between sham operated and BDL rats was also observed at 15 min post CM-101 injection. (D) Representative T1-weighted images acquired pre CM-101 (baseline) and 15 min post CM-101 injection. Notice that the fibrotic liver is markedly enhanced with CM-101 but healthy liver is not. Reproduced with permission from ref 492. Copyright 2018 Radiological Society of North America (RSNA).

myocardial infarction, heart failure, atrial fibrillation, hepatitis and cirrhosis, diabetic nephropathy, pulmonary fibrosis, inflammatory bowel disease, and a number of cancers. The type I collagen-targeting contrast agents EP-3533,[490] EP-3600,[491] and CM-101[492] were developed by conjugating Gd-DTPA or Gd-DOTA chelators to peptides that were identified by high-throughput screening methods to bind to type I collagen with high specificity, Figure 53. These collagen-targeting agents all capitalize on the increased payload strategy, with 3 Gd(III) chelates per peptide in each compound. EP-3533 has been used to stage liver fibrosis in mice and rats and also to monitor response to drug therapy.[493,494] It was also shown to be effective to detect and quantify the extent of myocardial infarction,[495] to stage tumor-associated fibrosis,[496] and to stage pulmonary fibrosis in mouse models.[497] EP-3600 was used to image perfusion defects in a porcine model,[491] and

CM-101 was reported for imaging liver fibrosis in rat and mouse models.[492]

Figure 54 compares liver imaging data acquired in healthy rats and rats experiencing liver fibrosis resulting from bile duct ligation (BDL). Figure 54A compares the time course of liver-to-muscle contrast to noise ratio (CNR) observed in control (sham surgery) and BDL rats following injection of equal doses CM-101. CM-101 is rapidly distributed and eliminated, and liver contrast in control rats is accordingly diminished to near baseline levels within 15 min of injection. In the fibrotic liver, however, CM-101 adheres to collagen and provides high liver CNR at delayed time points after washout of the unbound agent. Figure 54 (panels B and C) further illustrates this concept by comparing liver CNR integrated over 0−30 min for the sham surgery and BDL rats and liver CNR between sham surgery and BDL rats 10 min after CM-101 injection. Figure
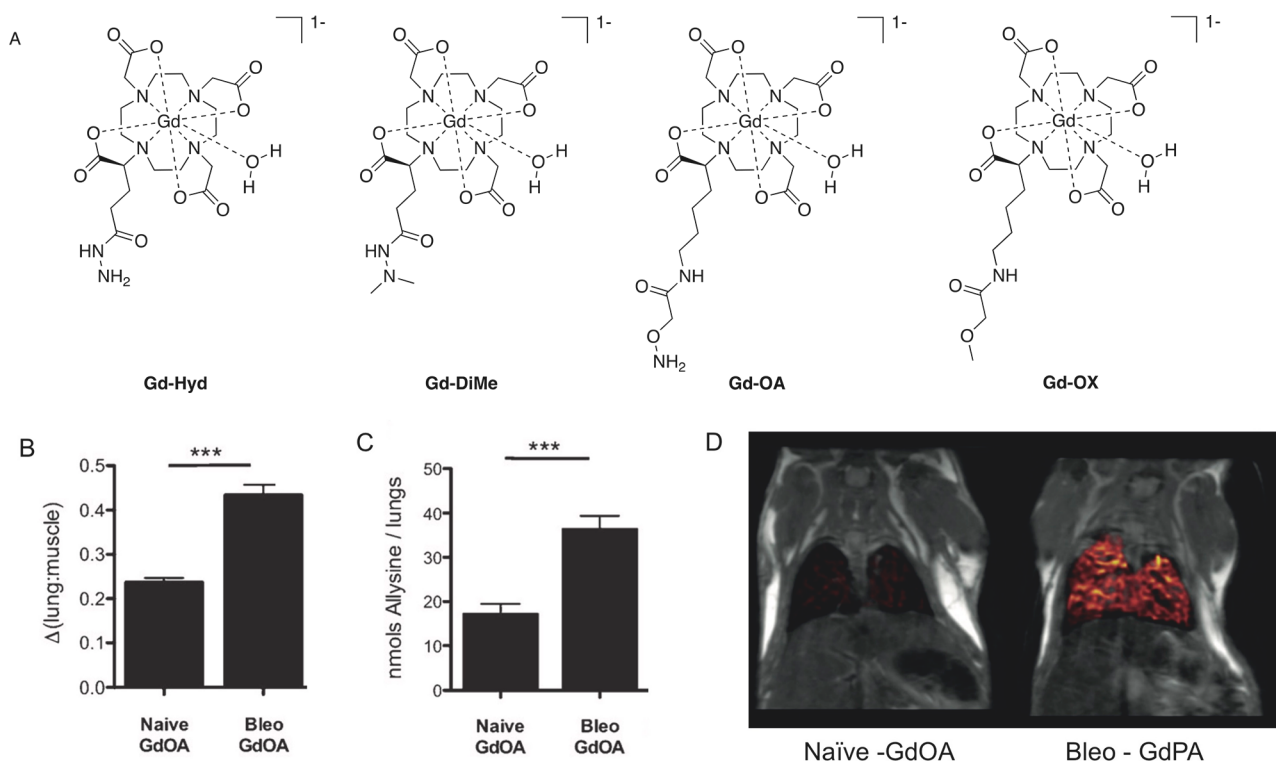
Figure 55. (A) Allysine-targeted agents Gd-Hyd and Gd-OA, and their corresponding nontargeted control agents Gd-DiMe and Gd-OX. (B–D) Imaging and ex vivo tissue analyses for Gd-OA (allysine-targeting) in naive (no fibrogenesis) and bleomycin (Bleo)-injured (active fibrogenesis) mice. (B) Quantification of the change in lung-to-muscle signal intensity ratio following injection of Gd-OA to naive and Bleo injured mice. (C) Quantification of allysine in naive and Bleo injured mice. (D) Coronal MR images of naive and bleomycin injured mice where the false color overlay is the difference image of the post Gd-OA image and the baseline image. Reproduced with permission from ref 500. Copyright 2017 John Wiley and Sons.

54D compares T1-weighted MR images of the sham and BDL (fibrotic) rats prior to and 15 min after CM-101 injection.

5.6. Fibrogenesis

Fibrogenesis, or the active deposition of scar tissue, is characterized by high levels of reactive aldehydes which are generated as part of a lysyl oxidase (LOX)-mediated collagen cross-linking process. LOX catalyzes oxidative deamination of lysine side chains to form allysine, which goes on to participate in condensation reactions with nearby lysine and allysine residues, resulting in cross-linking between collagen strands. Although allysine is reactive, the transiently generated aldehyde is present in sufficiently abundant concentrations for MR detection using an aldehyde-targeting imaging probe.[498] Allysine has been targeted using Gd(III)-based agents functionalized with hydrazide and oxyamine targeting moieties, which attach to allysine via reversible formation of hydrazone and oxime bonds. The hydrazide containing, aldehyde targeting agent Gd-Hyd, Figure 55A, was used to measure the natural history of bleomycin-induced fibrogenesis in the lungs of mice, as well as the response to treatment with a LOX inhibitor.[499] Gd-Hyd was also capable of monitoring liver fibrogenesis in a CCl_4 mouse model.

Similarly, Gd-OA, Figure 55A, with a pendant oxyamine moiety was used to detect bleomycin-induced pulmonary fibrogenesis in mice.[500] Figure 55 (panels B–D) compares lung imaging data and lung allysine content in normal, naive mice versus mice experiencing pulmonary fibrogenesis as a result of bleomycin injury. Figure 55B compares the change in lung-to-adjacent muscle signal intensity ratio following contrast agent injection and demonstrates strong lung enhancement in the bleomycin-treated mice. The MRI measurement reflects ex vivo quantification of tissue allysine content, Figure 55C, which is present at high micromolar concentrations in the injured lung. Contrast enhancement is clearly evident in the lungs of the bleomycin-injured mice as compared to naive mice, Figure 55D.

The aldehyde-targeting mechanism of both agents was confirmed using the control agents Gd-DiMe and Gd-OX, Figure 55A, which exhibit comparable pharmacokinetics and relaxivity but are incapable of forming hydrazone and oxime bonds, respectively. These control agents provide no contrast enhancement in tissues experiencing active fibrosis.

5.7. Fibronectin

Aggressively metastatic tumors are typically characterized by interstitial coagulation, and thus proteins such as fibrin and fibronectin represent promising prognostic molecular imaging targets. In addition to the fibrin-binding peptides discussed above, other high-throughput screens have yielded low-molecular weight peptides that bind to an epitope formed by the fibrin-fibronectin complex with good affinity.[501] Two small fibrin-fibronectin targeting peptides CGLIIQKNEC (CLT1) and CREKA have been utilized for molecular imaging of cancer, Figure 56A. CLT1 conjugated to Gd-DTPA via an amide linkage at the peptide N-terminus was shown to provide strong delayed enhancement of human colon carcinoma xenografts in mice long after probe washout.[502,503] High payload fibronectin-targeting contrast agents have also been developed by appending a tetrameric Gd(III)-complex to the
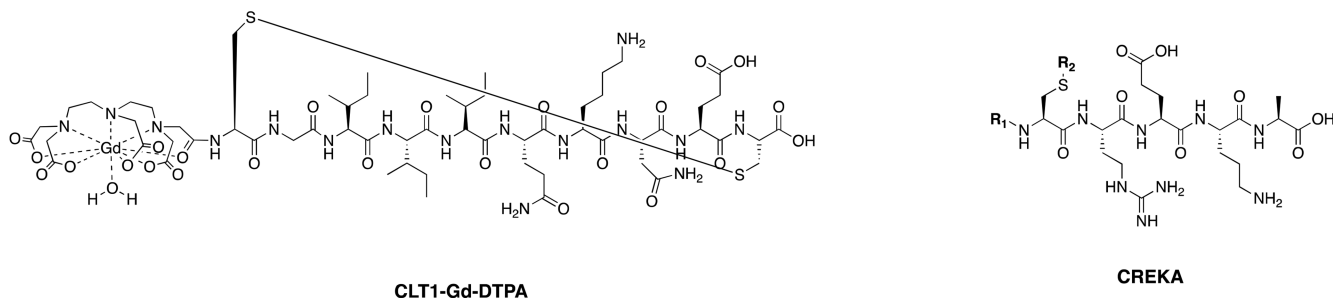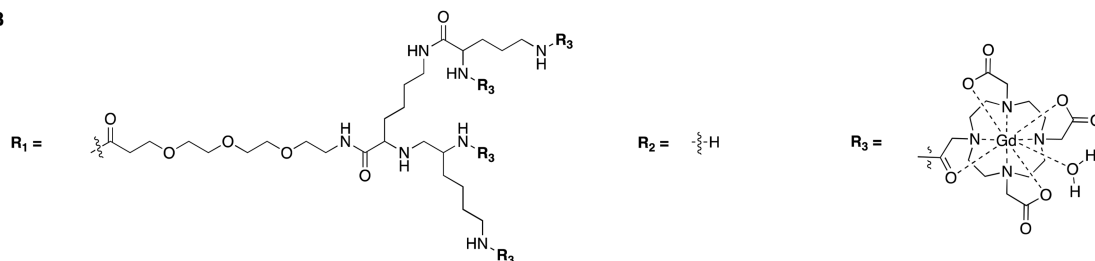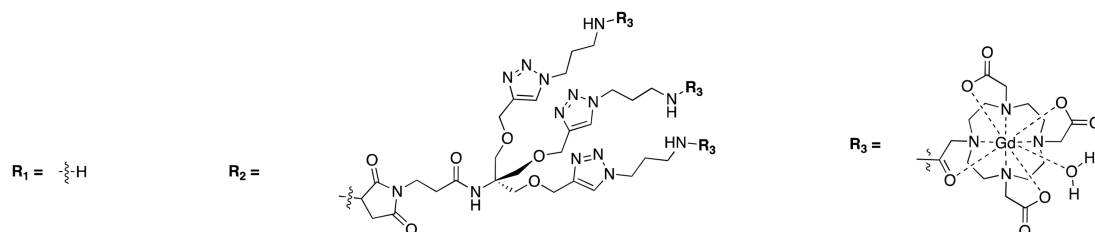
Figure 56. CLT1 and CREKA peptides identified via high-throughput screen to bind to the fibrin-fibronectic complex with high affinity. (A) A fibronectin-targeting agents comprised of Gd-DTPA conjugated to CLT1 via the peptide N-terminus and high payload fibronectin-targeting agents comprising multimeric Gd(III)-complexes (R1 and R2) conjugated to the CREKA peptide. (B) One high-payload fibronectin-targeting agent was assembled by conjugating a tetrameric Gd-DOTA scaffold to the CREKA N-terminus, and (C) another was assembled via conjugation of a trimeric Gd-DOTA scaffold to the cysteine side chain S.

N-terminus, Figure 56B, or a trimeric Gd(III)-complex to the cysteine-S, Figure 56C, of the CREKA peptide. These higher relaxivity agents have been used to effectively detect orthotopic prostate and breast tumors in mouse models as well as micrometastases <0.5 mm in diameter, which are difficult to detect using conventional extracellular contrast agents.[504−506] The fibronectin selectivity of the CREKA-based agent was further evidenced by comparing localization of a fluorescent peptide with a fibronectin specific immunohistochemical stain using fluorescence microscopy ex vivo. Imaging performed with an otherwise identical agent built from the scrambled CERAK peptide (nonbinding control) does not provide delayed tumor enhancement.

Fibronectin-targeted "platelet-mimetic" SPIONs have been developed that promote further particle accumulation around particles bound to the vessel wall.[503] These fibronectin-targeting SPIONs accumulate in the vessel walls of proliferating tumors and were used for fluorescence-based imaging of human breast cancer xenografts in mice. The fibronectin-targeting SPIONs did not localize to the same tumor phenotype in fibrinogen knockout mice which are incapable of expressing the fibrin-fibronectin complex, further confirming the mechanism of tumor localization. These particles have not yet been applied to MR imaging studies,

however, but one could expect the "platelet-mimetic" mechanism of SPION accumulation to provide very strong contrast enhancement in similar models.

5.8. Elastin

Elastin is an abundant protein component of load-bearing tissues, and levels of this protein are largely increased as part of the compensatory response following injury. Molecular imaging of elastin was performed with the elastin-seeking contrast agent, Gd-ESMA, Figure 57A, which comprises an elastin-binding small molecule conjugated to Gd-DTPA via an amide linkage involving one of the DTPA carboxylates. Gd-ESMA was used to monitor changes in elastin composition in the vessel wall of arterial aneurysm,[507] vascular remodeling following atherosclerotic plaque disruption,[508] and changes in the extracellular matrix of cardiac tissue following myocardial infarction.[509,510]

The images in Figure 57 (panels B−G) show the abdominal aortas of a mouse bearing a pharmacologically induced abdominal aortic aneurysm (B−D) and a placebo treated mouse (E−G). The red lines in the angiograms shown in Figure 57 (panels B and E) marks the axial cross sections of the vessels depicted in the images in Figure 57 (panels C and D and F and G, respectively). The cross-sectional images were
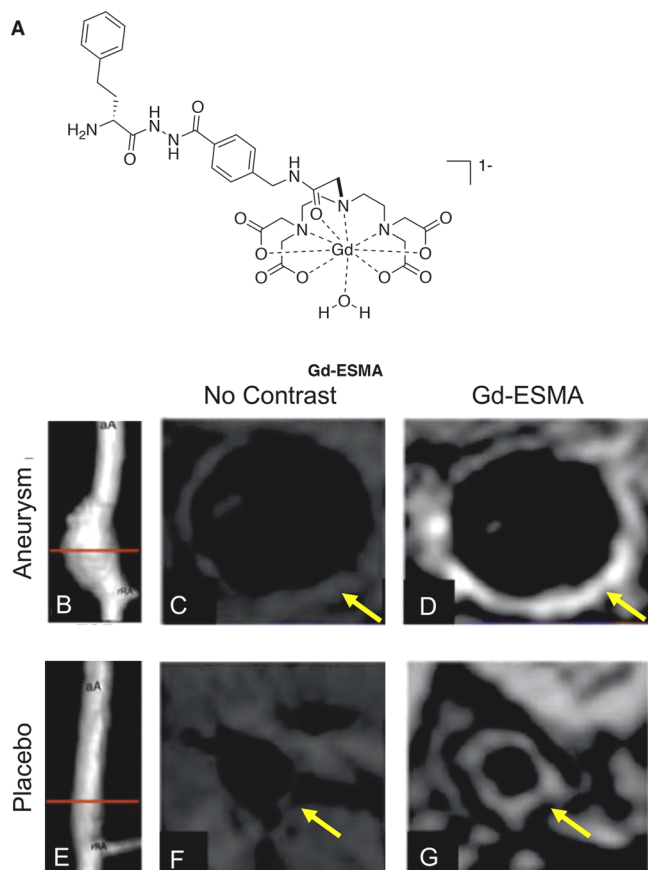
A

Gd-ESMA

No Contrast   Gd-ESMA

Aneurysm

B   C   D

Placebo

E   F   G

Figure 57. (A) Elastin-targeting MRI contrast agent Gd-ESMA. (B−G) show MR imaging of the suprarenal abdominal aorta in (B−D) placebo treated mice and (E−G) mice bearing a pharmacologically induced abdominal aortic aneurysm. Time of flight MR angiograms are shown in (B) and (E), the red lines mark the axial cross sections of the vessels depicted in images (B−D) and (F−G). Images (C−D) and (F−G) were acquired using the same T1-weighted protocol. (C) and (F) were acquired without contrast enhancement, whereas (D) and (G) were contrast-enhanced using Gd-ESMA. The aneurysm bearing vessel is strongly enhanced compared to the vessel in the negative control animal because an increase in elastin content accompanies the compensatory remodeling of vessel wall at the site of the dilation. Reproduced with permission from ref 507. Copyright 2014 Wolters Kluwer Health, Inc.

collected with no contrast enhancement and several minutes after Gd-ESMA injection. Elastin is present in all aortas, and the vessel wall in the placebo treated mouse is slightly enhanced but the compensatory remodeling of the vessel wall at the site of the aneurysm results in increased elastin content in the vessel wall, which is very strongly contrast enhanced.

5.9. Myelin

A number of neurodegenerative disorders are characterized by disruption to the myelin sheath surrounding the axons of white matter nerve cells. A myelin-seeking contrast agent was developed by appending a Gd(III) complex to a 3-(4-aminophenyl)-2H-chromen-2-one, termed Case Myelin Compound, or CMC, Figure 58.[511,512] CMC was identified from a screen of myelin-adhering coumarins as the molecule with the greatest affinity to myelin. Myelin localization of CMC was confirmed by MR imaging of contrast agent incubated slices of excised mouse brain in vitro and comparing the patterns of coumarin fluorescence to myelin specific immunohistochem-
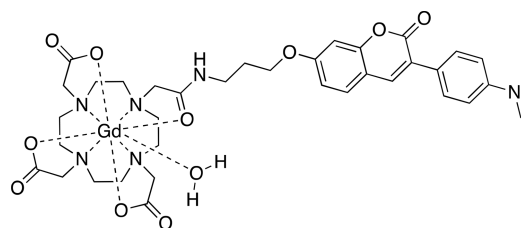

Figure 58. Myelin targeting MRI contrast agent, Case Myelin Compound.

ical staining.[512] CMC was also shown to bind myelin sheaths in vivo following intravenous injection.[513] Intracranially administered CMC enabled MR visualization of pharmacologically induced demyelination in a rat model in vivo.[511]

5.10. Amyloid-β Peptides

Insoluble amyloid-β (Aβ) peptides are an important biomarker for detection of Alzheimer's Disease. Aβ is a particularly challenging target because most contrast agents are incapable of penetrating the intact blood-brain barrier. However, innovative chemistry has yielded a handful of contrast agents that can cross the blood-brain barrier and provide enhancement at the site of Aβ deposits. For example, an Aβ fragment containing amino acids 1−40 (Aβ1−40) conjugated to Gd-DTPA and putrescine at the N- and C-termini, respectively, was shown to penetrate the blood brain barrier and adhere to Aβ depositions.[514] Incorporation of the polyamine putrescine confers blood brain barrier permeability. This effect had been previously demonstrated with putrescine-conjugated proteins.[515] The Aβ1−40 aggregates with the insoluble Aβ. In vivo imaging was not performed with this agent, but ex vivo brain slices from an Alzheimer's Disease mouse model, excised after injection of the agent, were imaged with MRI. The T1 enhancement patterns of the brain slices localized well with Thioflavin S staining for insoluble Aβ. A similar strategy has been taken to access Aβ-deposits with USPIONs. The USPIONs were decorated with a Aβ1−42 as the targeting vector and polyethylene glycol in order to increase membrane permeability.[516] The Aβ-seeking nanoparticles provided strongly enhanced T2* contrast 4 h after injection in the brains of Alzheimer's bearing mice compared to wild-type mice. In another study, an Aβ-targeted agent comprising Gd-DTPA coupled to N-terminus of a K6Aβ1−30 peptide was coinjected with mannitol in order to relax the blood-brain barrier in a mouse model.[517] A series of Gd-DOTA complexes conjugated to Pittsburgh Compound B, a well-established PET tracer for imaging Aβ deposits, were shown to bind to Aβ1−40 in vitro.[518,519]

Alzheimer's disease can also be accompanied by neuro-inflammation that can significantly compromise endothelial integrity. Aβ-targeted agents comprising SPIONs coupled to Aβ protein precursor antibodies (anti-AβPP) have been shown to access Aβ depositions via this endogenous mechanism of blood-brain barrier breakdown. Imaging was performed ex vivo on brain slices and correlated to Aβ histologic staining after administration of the anti-AβPP nanoparticles to Alzheimer's bearing mice.[520]

5.11. Organic Anion Transporting Peptides

Organic anion transporting peptides (OATPs) are highly expressed on the surface of hepatocytes. OATP-mediated internalization has been utilized to develop liver targeting agents such as the commercially available Gd-BOPTA and Gd-
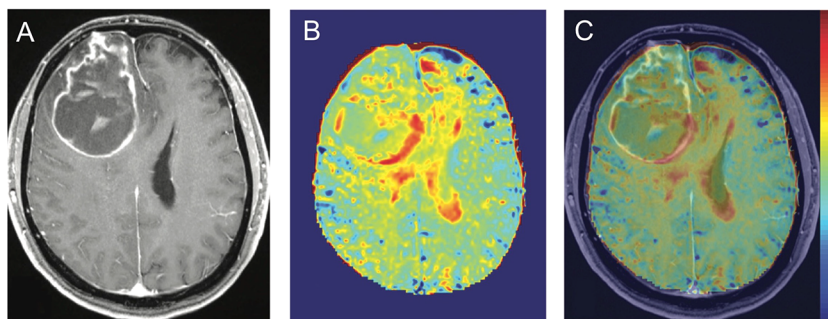
Figure 59. Comparison of (A) Gd-DOTA-enhanced and (B) glucose-enhanced imaging in a 45 year old woman with glioblastoma, the Gd-DOTA and glucose-enhanced images are fused in (C), glucose accumulates in proliferating cells and provides strong contrast enhancement in T1ρ-weighted images. The glucose-enhanced images provide strong signal intensity in the dorsomedial regions of the tumor that overlap with T_1-enhancement but also strong enhancement beyond the blood-brain barrier disruption. Reproduced with permission from ref 531. Copyright 2017 Radiological Society of North America (RSNA).

EOB-DTPA.[521−523] Although these clinical agents are not typically thought of as biochemically targeted contrast agents, the strong liver contrast observed following injection is the result of receptor-mediated pooling of the agent in hepatocytes. OATPs are highly abundant on the surface of normal hepatocytes but are under-expressed on the surface of malignant cells, and thus OATP-targeted agents are used to render malignant hepatocellular lesions conspicuously hypo-intense relative to healthy liver parenchyma. Hepatocellular phase images are typically acquired 20−40 min after injection in humans. OATP agents are also used in the differential diagnosis of hepatocellular lesions from benign, dense clusters of normal hepatocytes termed focal nodular hyperplasia (FNH). FNH typically exhibits avid arterial phase enhance-ment similar to many malignant lesions, but unlike malignant lesions, FNH is strongly enhanced by OATP-targeting agents during the delayed hepatocellular phase.[524] Recently, a Mn-based hepatocyte seeking agent was developed by conjugating Mn-EDTA to a benzothiazole aniline (BTA) moiety.[525] Hepatocyte uptake presumably occurs via OATP-mediated transport, but the mechanism has not yet been formally interrogated. A 0.05 mmol/kg dose of Mn-EDTA-BTA was used to visualize liver tumors in a mouse model with high contrast. The liver tumors were hypointense relative to the strongly enhanced liver parenchyma, consistent with previously developed OATP targeting agents.

Patrick et al. utilized the tremendous accumulating power of OATP as a gene reporter. They expressed the OATP receptor into cancer cells and implanted them into mice. Using Gd-EOB-DTPA for detection, they showed that cells expressing the reporter showed readily reversible, intense, and positive contrast (up to 7.8-fold signal enhancement) in T1-weighted magnetic resonance images acquired in vivo.[526]

5.12. Proliferating Cells

Increased glucose metabolism is a hallmark feature of proliferating tumors. Malignant cells have high glycolytic activity compared to noncancerous cells and typically over-express insulin-independent glucose transporters. Indeed, this is the physiologic basis of clinical [^{18}F]fluorodeoxyglucose (FDG) PET scans to detect malignancies. Innovative studies have demonstrated that analogous imaging can be performed using glucose and glucose derivatives as DiaCEST MRI contrast agents, making use of the chemical exchange of the hydroxyl protons. This targeted imaging is another example of receptor-mediated concentration of contrast agent. The

efficacy of this approach has been demonstrated in both animal models and human patients.[527−530] It was recently shown that glucose can be used to generate strong contrast enhancement in newly diagnosed, untreated glioblastomas using chemical exchange spin locking scans, which are analogous to CEST scans but more clinically robust and sensitive to hydroxyl proton exchange.[531] Figure 59B shows glucose-enhanced visualization of the proliferative micro-environment in a human glioblastoma patient.

The hallmark leaky vasculature of solid tumors enables targeting cancer cells and extracellular proteins with macro-molecular agents, although the pharmacokinetics of these agents are markedly slower and imaging must be performed hours later than would typically be done using biochemically targeted small molecule agents. The high metabolic demands of proliferating cells lead to increased consumption of nutrients such as iron, and this increased nutrient demand has been exploited for targeted molecular imaging (i.e., receptor mediated accumulation). For example, transferrin-SPION conjugates have been used to image mammary carcinoma in a rat model.[532]

The protein nucleolin is highly overexpressed on the surface of continuously proliferating cells and plays a critical role in promoting antiapoptotic activity. A proliferation-seeking contrast agent was developed by derivatizing SPIONs with AS1411 aptamers, which bind surface-expressed nucleolin with high affinity. This agent was shown to selectively adhere to cells with surface-expressed nucleolin and was successfully used to delineate proliferating tumors via T2-weighted scans in a mouse model.[533]

Angiogenesis is another hallmark feature of the proliferative microenvironment as the formation of new blood vessels enables continued nourishment of the proliferating cells and an avenue for metastasis. In this regard, contrast agents have been developed to target the $\alpha_\nu\beta_3$ integrin receptors highly expressed on endothelial cells participating in angiogenesis. An $\alpha_\nu\beta_3$-seeking contrast agent was developed by linking a biotinylated $\alpha_\nu\beta_3$-specific monoclonal antibody, DM101, to a biotin-coated Gd(III)-labeled perfluorocarbon nanoparticle. Avidin, which binds biotin with sub-picomolar affinity was used to link the biotinylated particle and antibody.[534] The antibody-based contrast agent provided 25% signal enhance-ment at the locus of corneal angiogenesis in a rabbit model 4 h following intravenous injection, whereas no contrast enhance-ment was observed at the same time point using the paramagnetic nanoparticle alone, the corresponding non-
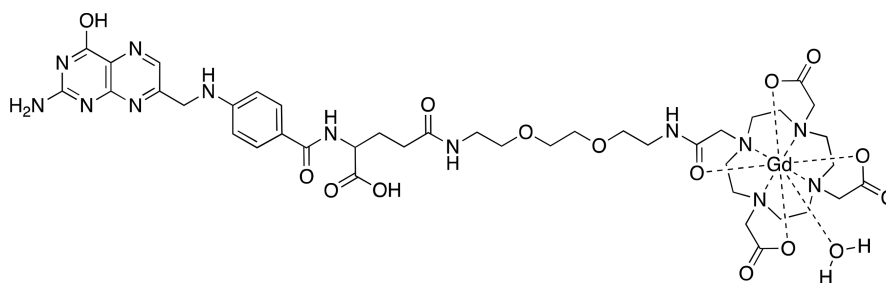
Figure 60. High-affinity folate receptor-targeting MRI contrast agent comprised of folate conjugated to Gd-DOTA via a bis(aminoethyl)glyocol linker.

binding isotype control, or administration of the $\alpha_{\upsilon}\beta_3$-seeking agent following preinjection receptor blocking using a competing substrate. Numerous $\alpha_{\upsilon}\beta_3$-seeking agents have been developed using the cyclic tripeptide RGD as the integrin-binding moiety. For example, RGD-functionalized SPIONs have been used to detect $\alpha_{\upsilon}\beta$ positive vasculature.[535,536] One study demonstrated that relative SPION-induced change in intratumoral T_2 was shown to correlate with immunohistochemically determined $\alpha_{\upsilon}\beta_3$ per unit area coverage.[536] Polymeric and liposomal Gd(III)-based agents and CEST reporters have also been developed as high-payload integrin-targeting agents.[537,538]

High-affinity folate receptors (HFR) are overexpressed on several tumor phenotypes originating from endothelial cells. A HFR targeting contrast agent was developed by conjugating DOTA to folate via bis(aminoethyl)glycol linker which formed amide bonds with both DOTA and folate carboxylates, Figure 60. This small molecule agent was successfully used to provide delayed enhancement of a HFR-positive human ovarian cancer xenograft in a mouse model for hours after injection of Gd-DOTA-folate, whereas no delayed enhancement was observed in control mice bearing HFR-negative xenografts.[539] A high relaxivity, folate-targeting Gd(III)-based agent of undisclosed structure has also been developed. This agent, termed P866, was used to provide strong contrast enhancement of HFR positive tumors in mice for hours after injection.[540,541] Contrast enhancement due to HFR binding was confirmed via imaging with a non-HFR binding control agent and by imaging using P866 under conditions where HFR was blocked by injection of free folate. Folate-functionalized SPIONs have also been used for visualization of HRF-positive tumors.[541] HFR has also been targeted with high-payload agent comprising a fourth generation PAMAM dendrimer functionalized with both folate and Gd-DTPA. A typical dendrimer was functionalized with 3−5 folate molecules but dozens of Gd-DTPA complexes. These folate targeting agents were shown to provide strong contrast enhancement of HFR-positive ovarian cancer xenografts in mice 24 h after injection.[542] Although no imaging was performed using a nontargeted control dendrimer, enhancement due to a folate-targeting mechanism was retrospectively confirmed by comparing Gd(III) retention in tumors using targeted and nontargeted dendrimers labeled with ^{153}Gd(III) by gamma counting methods.[543] A number of groups have also developed HFR-targeted agents using polymers and liposomes to deliver a high-payload of Gd(III)-based contrast agent.[544−547]

5.13. Inflammation

Inflammation has been imaged using agents that target the cell adhesion molecules that play a critical role in the early stages of inflammation by recruiting circulating leukocytes to the site of injury. A "leukocyte-mimetic" SPION agent was developed by coating 1 μm diameter SPIONs with antibodies against the cell adhesion molecules P-selectin and vascular cell adhesion molecule-1 (VCAM-1).[548] These particles were used to image endothelial activation during the onset of atherosclerosis in the aorta of mice. MR contrast correlated with lesion macrophage content. Flow cytometry experiments confirmed that these "leukocyte-mimetic" agents adhered to activated endothelial cells and were not internalized by phagocytic macrophages. A SPION functionalized with P-selectin antibodies was also used to monitor the dynamics of spinal cord endothelial activation in mouse models of chronic and relapsing multiple sclerosis.[549] The cell adhesion molecule E-selectin has been targeted using a dextran-coated SPION functionalized with a small molecule mimic of the E-selectin targeting polysaccharide sialyl Lewis^x (sLe^x) and was used to image liver endothelial cell activation in a mouse model of hepatitis.[550] This small molecule sLe^x mimic was also conjugated to Gd-DTPA type contrast agents.[551] The resultant agent, Gd-DTPA-B(SLe^x)A Figure 61, was shown to exhibit an
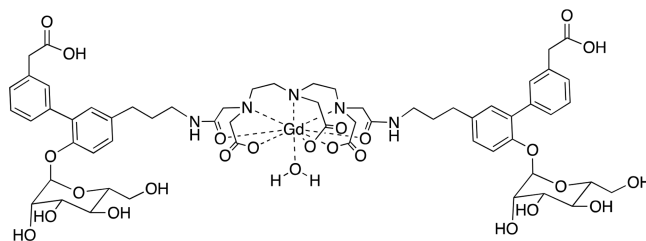
Figure 61. Gd-DTPA-B(SLe^x)A is an E-selectin-targeting agent. This agent has been used to image endothelial cell activation in a mouse model of fulminant hepatitis.

∼67% increase in blood-half-life in a rat model of fulminant hepatitis (30 min vs 49 min in healthy vs hepatitis rats, respectively) which was attributed to interactions with endothelial cell adhesion molecules in the diseased rats.[552] In mice, Gd-DTPA-B(SLe^x)A, was shown to provide strongly enhanced intravascular contrast out to 1 h after injection, whereas blood signal returned to near baseline within minutes after injection of Gd-DTPA.[552]

The inflammatory microenvironment is rich with phagocytic macrophages. Phagocytosis has been pursued by a number of groups as an endogenous mechanism to concentrate macromolecular contrast agents such as SPIONs,[430,553] Gd(III)-loaded liposomes,[554] and ^{19}F perfluorocarbon nanoemulsions[555−557] for targeted imaging of inflammation.

5.14. Apoptosis

Apoptosis is programmed cell death in response to cell stress or cell signals, but dysregulated apoptosis is often encountered in the proliferative microenvironment of solid tumors. Apoptotic cells are characterized by highly negatively charged phosphatidylserine rich cell membrane, and this unique cell surface has been used as a targeting mechanism. A high payload, protein-based apoptosis-targeting agent was developed by conjugated Gd-DTPA to the surface-exposed lysines of glutathione-S-transferase-C2A fusion protein, which binds to the phosphatidylserine rich surface of apoptotic cells with high affinity.[558] This protein-based agent was shown to bind selectively to apoptotic and necrotic cells in vitro and was used to image apoptotic cells in a mouse model of lymphoma. Another way to target apoptosis with high payload is to use Gd(III)-chelate loaded liposomes conjugated to Anexin 5, which also has high affinity for apoptotic cells.[559] These liposomal agents have been used for targeted imaging of apoptosis in atherosclerotic plaque in mice.[560] Anexin 5 functionalized SPIONs have also been used to image cardiomyocyte apoptosis in a mouse model of myocardial ischemia.[561]

5.15. Necrosis

There are high concentrations of extracellular DNA in acutely necrotic tissue, as macromolecular detritus requires hours to days to clear from the newly necrotic region. In this regard, an extracellular DNA-binding agent was developed for molecular imaging of necrosis.[562] The DNA-binding agent, termed Gd-TO, Figure 62, is comprised of Gd-DOTA coupled to the
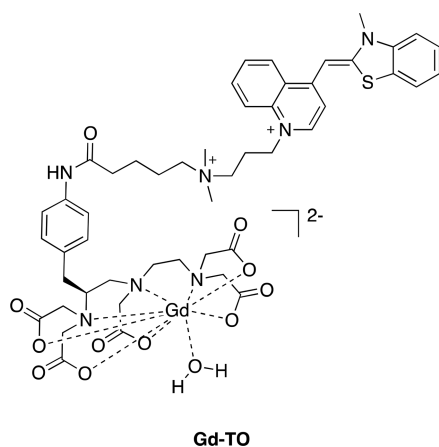
Gd-TO

Figure 62. Gd-TO binds to extracellular DNA via DNA intercalation of the appended thiazole orange dye. This agent has been used to image necrosis in a mouse model of myocardial infarction and to monitor the dynamics of extracellular DNA clearance after an acute necrotic event.

DNA intercalator thiazole orange. Gd-TO was used for molecular imaging of acute necrosis following myocardial infarction in a mouse model. The dynamics of extracellular DNA clearance were monitored by Gd-TO-enhanced imaging at various time points between 0 to 72 h after myocardial infarction.[562]

6. ACTIVATABLE CONTRAST AGENTS

Besides direct targeting, molecular MRI can also exploit changes in relaxivity or chemical exchange to detect specific biological processes or pathologies. Ion flux, pH, enzymatic activity, chemical potential (redox), and temperature are all features of the microenvironment that can be altered in disease processes. Activatable contrast agents, sometimes called responsive or "smart" contrast agents, exhibit altered relaxivity or altered CEST effect in response to a stimulus. Unlike targeted agents which accumulate at a specific site because of protein binding or cellular internalization, activatable agents produce signal change because they themselves are chemically altered. Activatable contrast agents that are capable of revealing biochemical or physiologic abnormalities may offer unique insights into the human body and enable the earlier and more precise diagnosis of specific diseases, as well as monitoring the treatment of these disorders.

This section provides an overview of the chemistry, properties, and applications of activatable para- and diamagnetic contrast agents. The probes discussed here can be viewed as MR sensors of physiological events whose relaxivity or CEST effect depends on the absence/presence of the biological stimulus of interest.

As outlined in section 3.3, the T_1 relaxivity of a paramagnetic metal complex is primarily determined by three factors: q, the number of water molecules in the inner coordination sphere, τ_m, the residence lifetime of these inner-sphere water molecules, and τ_R, the rotational correlation time of the molecule. Thus, for the development of a biochemically responsive contrast agent, one or more of these molecular factors must be changed by a biochemical stimulus. In the ideal case, the agent features an "off" state associated with low relaxivity in the absence of the biochemical trigger and an "on" state associated with high relaxivity in the presence of the trigger. Similarly, superparamagnetic nanoparticles can exhibit activatable T_2^* change based on aggregation of the particles. CEST agents can be made responsive by altering the chemical exchange rate or the chemical shift of the exchangeable hydrogen in response to a stimulus, which causes the CEST effect to appear, disappear, or change in magnitude.

6.1. Case Study: A Gd(III)-Based β-Galactosidase Sensor

Pioneering work in the development of activatable Gd(III)-based contrast agents was led by Meade and co-workers with their studies on agents responsive to the enzyme β-galactosidase.[563] β-Galactosidase catalyzes the hydrolysis of β-galactosides and is commonly used in molecular biology as a reporter marker to monitor gene expression.[564,565] The Meade group sought to make a MR probe that could report on β-galactosidase function and gene expression. The initial sensor (Figure 63A) consisted of a Gd-DO3A chelate coupled to a galactopyranose moiety that acts as a lid for the access of water to the inner sphere coordination cage. Enzymatic cleavage of the glucosidic linkage irreversibly frees a coordination site to yield a Gd-HPDO3A-like complex with an increased number of inner-sphere water molecules resulting in higher relaxivity. Using lifetime luminescence measurements on the Tb analog, the authors estimated that the hydration state of the complex changes from 0.7 to 1.2 upon cleavage of the sugar group. The relaxivity change was modest but could be improved by modifying the complex to introduce an additional α-methyl group within the molecular scaffold as depicted in Figure 63 (panels B and C).[566] This modification appears to reduce the relaxivity of the uncleaved complex with the galactopyranose moiety intact, presumably by limiting water access to the gadolinium(III) center. Using this second generation probe, β-galactosidase activity could be detected in living *Xenopus laevis*
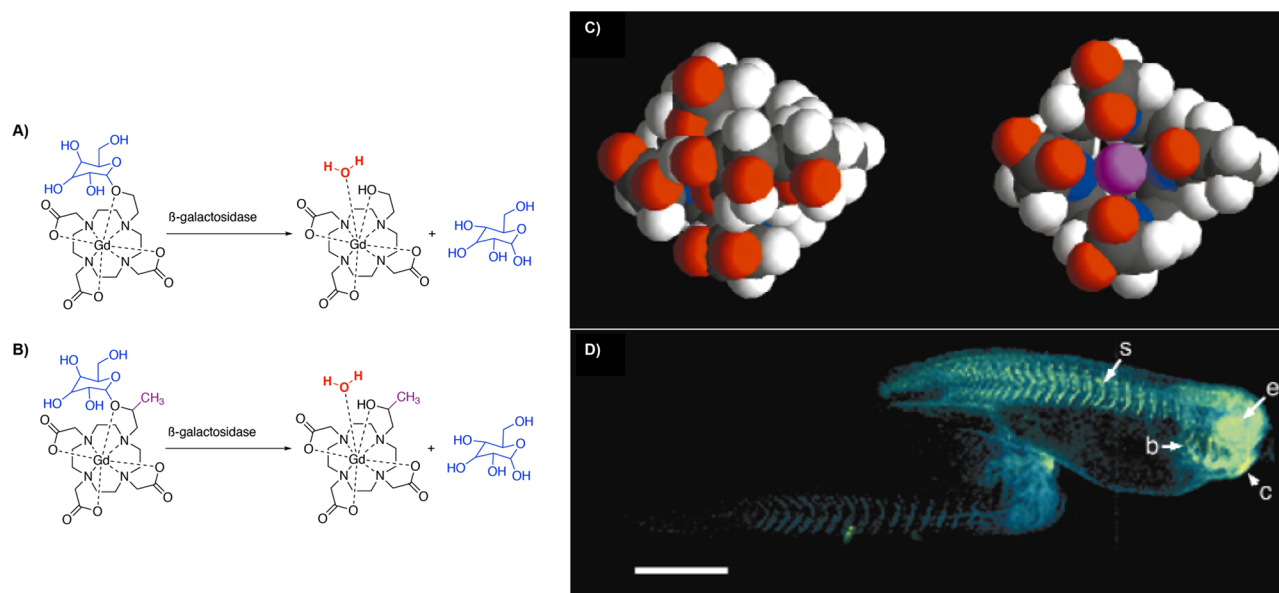
Figure 63. Detecting enzyme activity with a Gd(III)-based MR contrast agent through changes in T_1 relaxation caused by modulation of inner-sphere hydration state. Chemical structures of the (A) first and (B) second generation β-galactosidase sensors. (C) Enzymatic cleavage of β-galactose frees one coordination side that becomes accessible by water molecules. (D) Two living *Xenopus laevis* embryos were injected with the second generation of the β-galactosidase sensor. The embryo shown on the right was also injected with β-galactosidase mRNA. The pseudocolor rendering of MR images shows that the signal strength is 45−65% greater in the embryo treated with ß-galactosidase mRNA, demonstrating the detection of β-galactosidase activity. Labeled anatomy: (e) eye, (c) cement gland, (s) somite, and (b) brachial arches. Reproduced with permission from ref 566. Copyright 2000 Springer Nature.

embryos (Figure 63D). Two embryos were injected with the activatable contrast agent, while one embryo was additionally injected with β-galactosidase mRNA. The MR signal intensity was 45−65% greater within the embryo that was treated with β-galactosidase mRNA, thereby demonstrating the detection of β-galactosidase activity.

This study demonstrates the power of activatable agents to detect biochemical events, notably enzymatic activity. In this case, 55 M water signal was imaged and this signal was augmented by 0.5 mM contrast agent which in turn was augmented by a 4 μM enzyme concentration. Thus, activatable agents offer an avenue to detect low concentration molecular events, despite the sensitivity limitations of MRI. The study also points to some requisites for activatable agents. The difference in relaxivity (or CEST effect) between the "off" and "on" state should be large to detect meaningful change. Additionally, the reaction to activate the agent must be very fast; for enzyme sensing, the kinetics must be fast enough to turnover micromolar concentrations of agents in a short period of time.

6.2. Challenges and New Frontiers

Activatable agents have the same primary challenge as all the other MR contrast agents described in this review: detection sensitivity. For relaxation agents, micromolar concentrations of metal ion are required, and millimolar concentrations are needed for CEST. Direct detection typically requires even higher concentrations. Regardless of the mechanism of activation and the magnitude of change in signal generating property (relaxivity, chemical exchange rate), the activatable agent can only be effective if it is present at concentrations above its detection threshold.[567]

Another consideration is whether the activation is reversible or irreversible. Reversible responsive MRI contrast agents return to their original state when they no longer interact with

their specific biomarker. This makes them especially suitable for monitoring rapidly changing physiological conditions (e.g., ion flux). But in this case, the MR detection sensitivity is target-limited, which means that the biomarker of interest has to be present in relatively high concentrations to be detectable with a reversible activatable probe. Irreversible responsive agents do not return to their original state in the absence of their specific biomarker. With irreversible responsive agents, signal change is one way and oscillations in biomarker concentration cannot be detected. On the other hand, the complete conversion to the activated state can greatly amplify detection sensitivity.

There are two main approaches to enhance dynamic range of both reversible and irreversible responsive agents. One strategy is to maximize the signal change between the inactivate and the activated agent. This can be done by optimizing the relaxivity (or CEST effect) of the activated agent or by suppressing the relaxivity of the inactive form, or a combination of both. Again, one must keep in mind that the overall detection threshold must be reached, so for relaxation agents the relaxivity of the activated agent must be high enough to render the agent detectable at physiologically achievable concentrations. In another strategy, the responsive agent is not only "turned-on" in the presence of a particular biological stimulus but also additionally retained and thereby accumulated at the target. This approach can be seen as a combination of targeted and activatable probes and will be further discussed in section 7.

Another question to address is whether one wants to simply detect the presence of a biomarker (e.g., the presence of a specific enzyme) or whether one wants to quantify a biomarker (e.g., measure pH). Quantification presents a particular challenge because the MR signal depends not only on the response to the biochemical stimulus (relaxivity change) but also on the concentration of the imaging probe. Even for
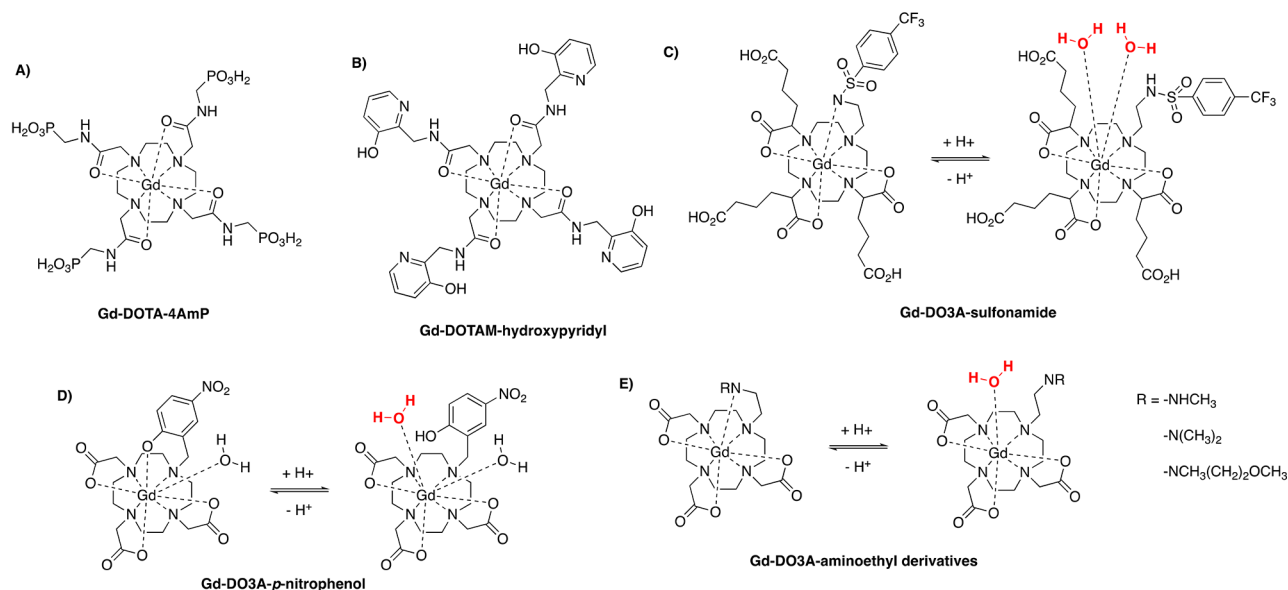
pH-responsive T$_1$ relaxivity agents

Figure 64. Selected pH-responsive T_1 relaxivity agents.[574,308,577,580−582]

qualitative detection, it is necessary to ensure that the signal change observed is a result of activation and not just pooling of the inactive agent. Three general methods have been employed to address this problem: (1) the utilization of ratiometric methods where the measured effect is independent of concentration, (2) successive injections of responsive and nonresponsive agents with similar structure and pharmacokinetics where the signal change of the nonresponsive agent is used to estimate the concentration, or (3) utilization of a bimodal agent and simultaneous bimodal imaging, where one image modality (PET or SPECT) is used to quantify the agent and this is used to deconvolute the MR signal and quantify the degree of activation. These strategies will be discussed on the basis of exemplary examples.

As seen below, a large number of activatable agents have been reported. However, unlike with targeted agents, there have been relatively few successful examples of activatable agents being deployed in vivo. On the other hand, the ability to image and quantify enzymatic activity, ion flux, redox status, pH, etc deep within tissue with submillimeter resolution would have a tremendous impact on our understanding of biology and pathobiology. The development of truly functional activatable agents remains a worthy goal.

Excellent reviews of activatable MR contrast agents have been published in recent years.[185,567−572] In this section, our primary goal is to provide an overview of the different strategies and creative ideas that have been employed in the design of activatable MR contrast agents. Due to the large number of examples in the literature, this section is not meant to be comprehensive. We regret the omission of interesting studies for the sake of conciseness.

6.3. pH-Responsive Molecular Imaging Agents

Decreased extracellular pH values are associated with cancer and various ischemic diseases. pH quantification could be a useful biomarker for early identification of disease or to monitor treatment efficacy.[573] Hence, the development of smart MR contrast agents, which show pH-dependent relaxivity profiles or CEST effects, has been the subject of intensive research for the past two decades.

6.3.1. pH-Responsive Gd(III)-Based Contrast Agents.
An early and effective example of a pH-responsive agent was Gd-DOTA-4AmP (Figure 64A) reported by Sherry and co-workers.[574,575] This complex is a DOTA derivative where the carboxylate groups have been derivatized as amides with pendant phosphonate groups. Inner-sphere water exchange is extremely slow for this complex, but exchange of protons of the bound water molecule with bulk water is fast and is catalyzed by pendant phosphonates. Protonation of the phosphonate groups, which have pK_a values in the physiological range, alters this prototropic exchange rate and also alters second-sphere relaxivity. The relaxivity is 51% higher at pH 6.0 compared to pH of 9.5. The magnitude of the pH-dependent relaxivity effect can be increased by slowing the overall tumbling rate of the molecule. Coupling of this agent to the macromolecule G5-PAMAM dendrimer yielded a product that contained on average 96 molecules of Gd-DOTA-4AmP and exhibits an average hydrodynamic volume consistent with a molecular weight of ~140 kDa. The T_1 relaxivity of this macromolecular sensor increases by 122% (r_1 = 10.8 to 24.0 mM^{-1} s^{-1}) over the pH range from 9.5 to 6.0.[576]

The Sherry group reported another example of modulating prototropic exchange and water distribution in the second coordination sphere. The Gd-DOTA tetraamide with pendant hydroxypyridyl moieties was used to image changes in pH values (Figure 64B).[577] Deprotonation of the amides in those moieties result in intramolecular acid–base pair interaction with the phenolic protons, leading to a highly organized second hydration sphere. As a result, the relaxivity of this agent is enhanced at higher pH (pH 8.5) and decreases by 84% at lower pH (pH 6.0).

The pH-dependent relaxivity changes of most gadolinium-(III)-based pH sensors are realized through modulation of the inner-sphere hydration state, q. An impressive example was reported by Parker and co-workers who designed a Gd-DO3A derivative with a pendant sulfonamide (Figure 64C).[308] The hydration state changes from q = 0 to q = 2, associated with the on/off ligation of the sulfonamide nitrogen donor which occurs in a region of great interest for extracellular pH change.
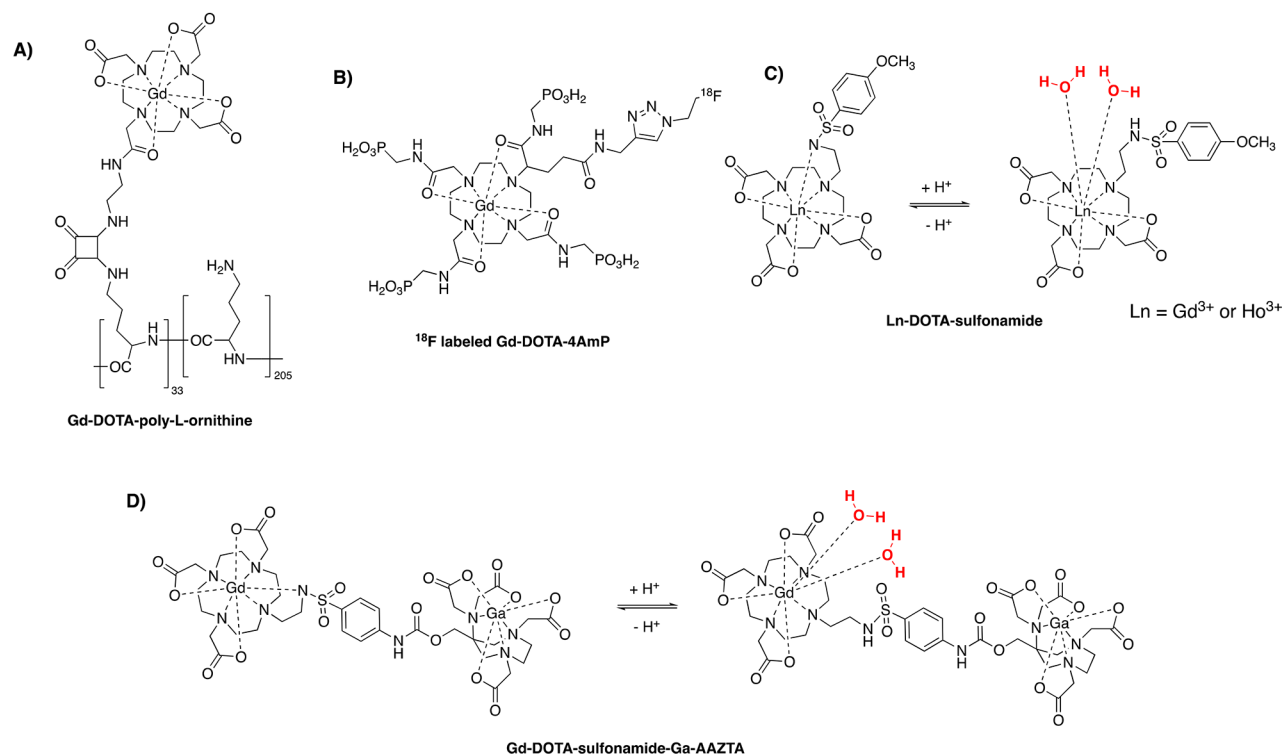
pH-responsive T₁ relaxivity agents

Figure 65. Selected pH-responsive T_1 relaxivity agents.[586−589]

Decreasing the pH from 7.4 to 6.8 resulted in a r_1 enhancement of 35% when measured in a simulated extracellular anion background and 48% when measured in human serum. Bis-hydrated Gd-DO3A is known to coordinate endogenous anions like bicarbonate and phosphate.[308,578,579] The Parker group employed pendant anionic carboxylate groups (Figure 64C) which served to block anion coordination and inner-sphere water displacement. The pendant carboxylate groups also resulted in unexpectedly higher relaxivity than expected based on molecular weight, which is presumably due to a second sphere effect. In addition, this complex had modest affinity to HSA while maintaining its pH-dependent T_1 relaxivity profile.[487] Increasing the molecular weight and thereby the rotational correlation time of the Gd(III) compound through binding to HSA should dramatically increase the initial r_1 enhancement [Gd(III)-complex without HSA: $r_1 = 2.4$ to 9.0 mM^{-1} s^{-1} from pH 5.0 to 8.5, 37 °C, 0.47 T]. In fact, binding of the Gd(III)-complex to HSA resulted in an unexpectedly low r_1 enhancement of 42% (pH 5.0) and 260% (pH 8.5), respectively, which was attributed to displacement of inner-sphere water ligands when the complex is bound to HSA. This finding was confirmed using a derivative with increased HSA affinity.[487]

Another donor group that can be protonated around neutral pH is phenolate. Sherry and co-workers showed that a Gd-DO3A derivative with a pendant *p*-nitrophenolate arm underwent a switch in hydration state from $q = 1$ to $q = 2$ (Figure 64D) as pH was lowered.[580] The protonation and dissociation of the phenolate oxygen donor atom resulted in a 71% enhancement in r_1 from pH 9 to 5. Moreover, at low and at high pH, the compound is resistant to water ligand displacement by anion coordination.

In a recent study, Giovenzana and co-workers exploited the suitability of Gd-aminoethyl-DO3A derivatives as a pH-sensitive platform (Figure 64E).[581,582] On average, their compounds showed a percentage enhancement around 100% in the pH region of 9 to 5, also provoked by a switch in hydration state.

A major obstacle in applying these systems to image tissue pH is the unknown concentration of the contrast agents in tissue. In order to measure pH, one must know the relaxivity, and relaxivity depends on both concentration and T_1 change. MRI can measure T_1 change, but the challenge of measuring concentration must be addressed.

Gillies, Sherry, and co-workers applied a dual injection strategy to determine concentration. They administered the pH-independent agent Gd-DOTP and measured the time-dependent signal change. They then administered pH-responsive Gd-DOTA-4AmP (Figure 64A) and measured the signal change with time.[583,584] With the assumption that both agents had similar tissue biodistribution and pharmacokinetics, the differences in the signal-versus-time curves for Gd-DOTA-4AmP and Gd-DOTP were attributed to differences in relaxivity. As a result, the extracellular tissue pH could be successfully mapped in the kidneys in a renal acidosis model and in a tumor in a brain tumor model.[583,584]

The same group used a different strategy to map pH in a rat brain glioma model.[585] Instead of a sequential injection of two agents, this time they mixed Gd-DOTA-4AmP with Dy-DOTP. Dy-DOTP has extremely low r_1 but does exhibit a large R₂* effect. By coinjecting an appropriate mixture, Gd-DOTA-4AmP dominates the ΔR_1 effect, while Dy-DOTP dominates the ΔR_2* effect. The concentration of Dy-DOTP was estimated from ΔR_2*, and since the ratio of Gd:Dy was known, the Gd-DOTA-4AmP concentration could be
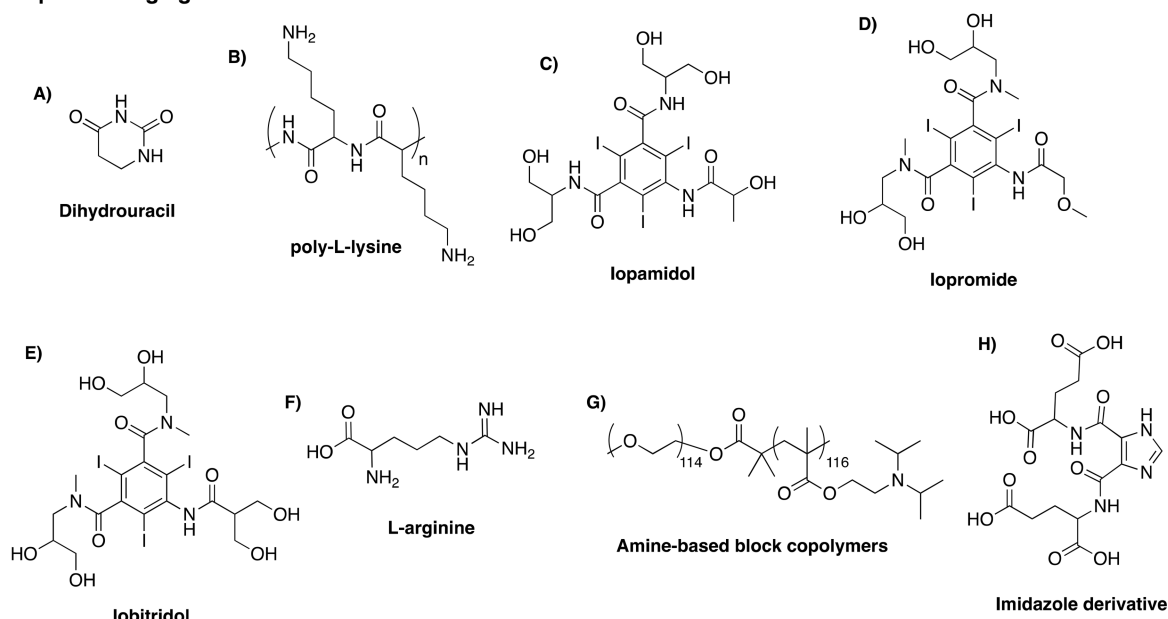
DiaCest pH sensing agents:

Figure 66. Selected pH-responsive DiaCEST agents.[8,449,590−595]

estimated and pH determined from the ΔR_1 measurement. This again assumed that both contrast agents had the same distribution and pharmacokinetics. Simply replacing Gd(III) with Dy(III) would likely give identical pharmacokinetics.

Rather than injecting two different agents, Aime and co-workers proposed a $\Delta R_2/\Delta R_1$ ratiometric method.[586] As described above (sections 3.3 and 4.2.2), slow tumbling agents show increased r_1 at low fields but this decreases rapidly with increasing field strengths. On the other hand, r_2 is high at low fields and remains constant or increases with increasing field strength. Thus, the r_2/r_1 ratio increases with increasing field strength but also increases at a given field strength when τ_R is increasing. This ratio is independent of concentration. This group designed a Gd-DOTA functionalized polypeptide (poly-L-ornithine, Figure 65A) that exhibits a pH-dependent conformation. At low pH, it assembles randomly and exhibits a shorter τ_R, while at higher pH an ordered α-helix is formed resulting in an increase in τ_R. This resulted in a r_2/r_1 ratio that increased with pH. By measuring $\Delta R_2/\Delta R_1$ (the difference in relaxation rate in the presence and absence of the agent), the authors could detect pH changes that were independent of contrast agent concentration. A limitation of this type of approach is that the r_2 relaxivity must be very high to measurably change T_2 in tissue where T_2 values are generally very short. That is, although $\Delta R_2/\Delta R_1$ is independent of concentration, if the measured ΔR_2 and ΔR_1 values are small then the error associated with the measurement will be very large.

A third strategy to determine concentration independently was reported by Frullano et al. They incorporated the radionuclide ^{18}F into the framework of the already established pH-responsive contrast agent Gd-DOTA-4AmP (Figure 65B). By mixing the ^{18}F compound with the stable ^{19}F analog, they achieved ^{18}F and Gd(III) concentrations suitable for detection by both PET and MRI. Using a simultaneous MR-PET scanner, they could achieve absolute quantification with PET while contemporaneously measuring T_1 with MRI.[587] Combin-

ing the PET (concentration) and MRI (ΔR_1) measurements, they could compute relaxivity and hence obtain pH maps.

Other bimodal activatable pH agents have since been reported. Aime and co-workers proposed a dual MR-SPECT agent by adding a small amount of the gamma-emitting [166]Ho(III) analog to a previously described pH-responsive Gd-DO3A derivative with a pendant sulfonamide[308] (Figure 65C).[588] This system is actually two separate compounds, but it is assumed that the Ho(III) complex would have the same biodistribution and pharmacokinetics as the Gd(III) analog, which is a reasonable assumption. A limitation of this approach is that there are no simultaneous MR-SPECT scanners, while MR-PET scanners are commercially available. For in vivo measurements, the MRI and PET (or SPECT) measurement must be simultaneous, otherwise the concentration measured would not be reflective of the concentration present when T_1 was measured. Another elegant bimodal MR-PET pH sensor was invented by Tei and co-workers.[589] They prepared a heteroditopic complex that contains Gd(III) as a MRI reporter and [68]Ga(III) as the PET reporter (Figure 65D). The dimeric ligand consists of two different chelating cages: a DO3A-sulfonamide derivative for the encapsulation of Gd(III) (Figure 65C) and one chelator based on AAZTA for the complexation of [68]Ga(III). A sulfonamide moiety acts as a linker between the two chelating cages and provides pH-sensitivity at the same time since the on/off ligation of the sulfonamide nitrogen donor to the Gd(III) center is pH-dependent. Hence, a switch in hydration state (low pH: $q = 2$/high pH: $q = 0$) leads to a percentage enhancement in r_1 of 150% over the pH range from 8.5 to 5.0.

6.3.2. pH-Responsive CEST Contrast Agents. CEST agents can also be used as pH-responsive agents since their mechanism of action is based on the selective saturation of exchangeable protons, followed by the transfer of the saturated protons to the bulk water leading to an alteration in water signal intensity. Typically, for a chemical species with labile protons, the exchange rate k_{ex} of those protons with bulk water is pH-modulated due to base catalysis of proton exchange.
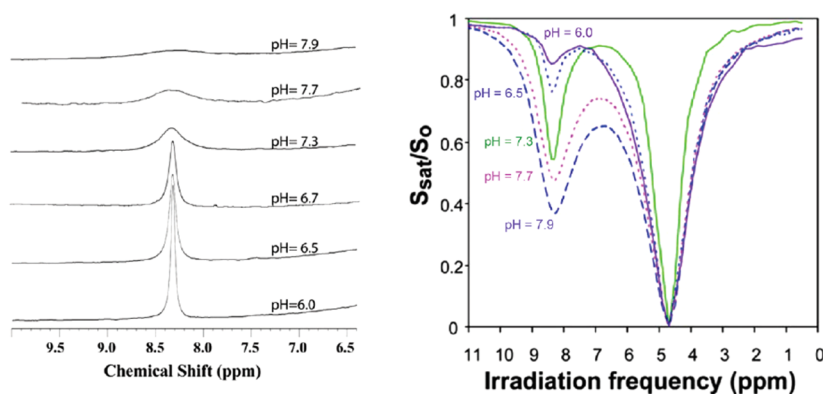
Figure 67. pH dependency of proton exchange and its relationship to CEST. (Left) ^{1}H NMR spectra of poly-L-lysine at different pH. (Right) CEST spectra of poly-L-lysine at different pH. The proton exchange accelerates with increasing pH, which broadens the corresponding ^{1}H NMR signal but amplifies the CEST signal. Reproduced with permission from ref 591. Copyright 2006 John Wiley and Sons.

pH-Responsive DiaCEST Agents. In their seminal 2000 paper describing CEST imaging, Ward and Balaban also demonstrated that proton chemical exchange agents could be used to image pH.[8] They showed that dihydrouracil (Figure 66A) with its two labile amide protons can be employed as a pH-sensitive imaging agent. They further showed how a ratiometric method could be used to measure pH in a way that was not dependent on the concentration of the agent. In general, the magnitude of the CEST effect for one type of exchangeable proton is different and has a different pH dependence than another exchangeable proton. For example in dihydrouracil selective irradiation of each of the amide N—H protons results in a different CEST effect. The ratio of these two CEST effects is pH-dependent and independent of concentration. Similar methods could be applied using two different CEST contrast agents where the signal of one is ratioed against the other. However, in this case, the two agents should have similar pharmacokinetic properties. Longo, Sun, et al. showed that one does not need two separate exchangeable proton pools for quantitative pH CEST imaging. They recognized that the efficiency of the saturation power in creating saturation transfer also has a pH dependence. They showed that by ratioing the CEST effect at different saturation powers they could quantify pH using the compound iobitridol.[590]

A limitation of diamagnetic CEST agents is their poor sensitivity requiring the administration of high concentrations to obtain measurable MR contrast. Two strategies can be adopted to improve their sensitivity with a concentration threshold in the micromolar range: (1) the chemical shift between the exchangeable proton resonance and the bulk water resonance is increased by using strong deshielding groups like, for example, aromatic rings, halogen substituents, or paramagnetic shift reagents, or (2) the number of mobile protons per molecule is increased by using macromolecular systems like dendrimers and peptides.

Applying the latter strategy, van Zijl and co-workers used a poly-L-lysine scaffold to measure the pH-dependence of its amide proton exchange rates in the physiologic range (Figure 66B).[591] The pH-dependent NH proton exchange and its relationship to CEST imaging is illustrated in Figure 65. As shown in the high-resolution ^{1}H NMR spectrum of poly-L-lysine (Figure 67, left), at lower pH (pH = 6), the NH proton exchange is rather slow, resulting in a sharp NH proton resonance. In contrast, at the same pH, the corresponding CEST spectrum (Figure 67, right) shows only a rather small CEST effect. Increasing the pH to 7.9 accelerates the NH proton exchange, which dramatically broadens the corresponding NH proton signal in the ^{1}H NMR spectrum and in turn amplifies the CEST signal.

X-ray contrast agents are given at very high doses, literally 10s of grams of these highly soluble iodinated aromatic compounds. Aime and co-workers recognized that X-ray agents like iopamidol also contain two different amide proton pools with downfield chemical shifts (Figure 66C) and thus could be used as a pH sensor in MR imaging applications.[449] Iopamidol was successfully employed to acquire pH maps of kidney cortex, medulla, and renal pelvis in healthy mice and to image the pH evolution of an acute kidney injury mouse model.[72,596] Additionally, in a breast cancer mouse model, tumor pH mapping was performed using iopamidol in a combined PET and MR-CEST imaging study.[597] Other approved CT contrast agents with similar structure: iopromide[592] (Figure 66D) and iobitridol[590] (Figure 66E) were also utilized in vivo for accessing changes in tumor acidosis.

In another approach, liposomes were filled with L-arginine, a molecule with multiple exchangeable NH protons (Figure 66F) and subsequently assembled to microcapsules (LipoCEST). With those pH-nanosensors, transplanted cell viability could be monitored in vivo.[593]

Gao and co-workers reported ionizable, tertiary amine-based block copolymers (Figure 66G) as pH sensors for MR-CEST imaging. Near physiological pH, the polymers form micelles turning the CEST signal "off", whereas in an acidic environment the CEST signal is turned "on" through dissociation of those micelles.[594]

Recently, McMahon and co-workers showed that imidazoles (Figure 66H) can also be used as DiaCEST MRI pH sensors as demonstrated by in vivo mapping of kidney pH in mice.[595]

pH-Responsive ParaCEST Agents. One limitation of DiaCEST agents is their small chemical shift difference from bulk water which can have interference from endogenous biomolecules that generate CEST in a similar range. A second limitation is sensitivity. For CEST, the chemical shift difference (in Hz) must be greater than the proton exchange rate. Faster exchange would produce a larger CEST effect, but if exchange is faster than the chemical shift difference then the chemical shifts merge and CEST is impossible. One can increase the shift difference by moving to higher fields or by turning to ParaCEST agents. These exhibit a much larger chemical shift
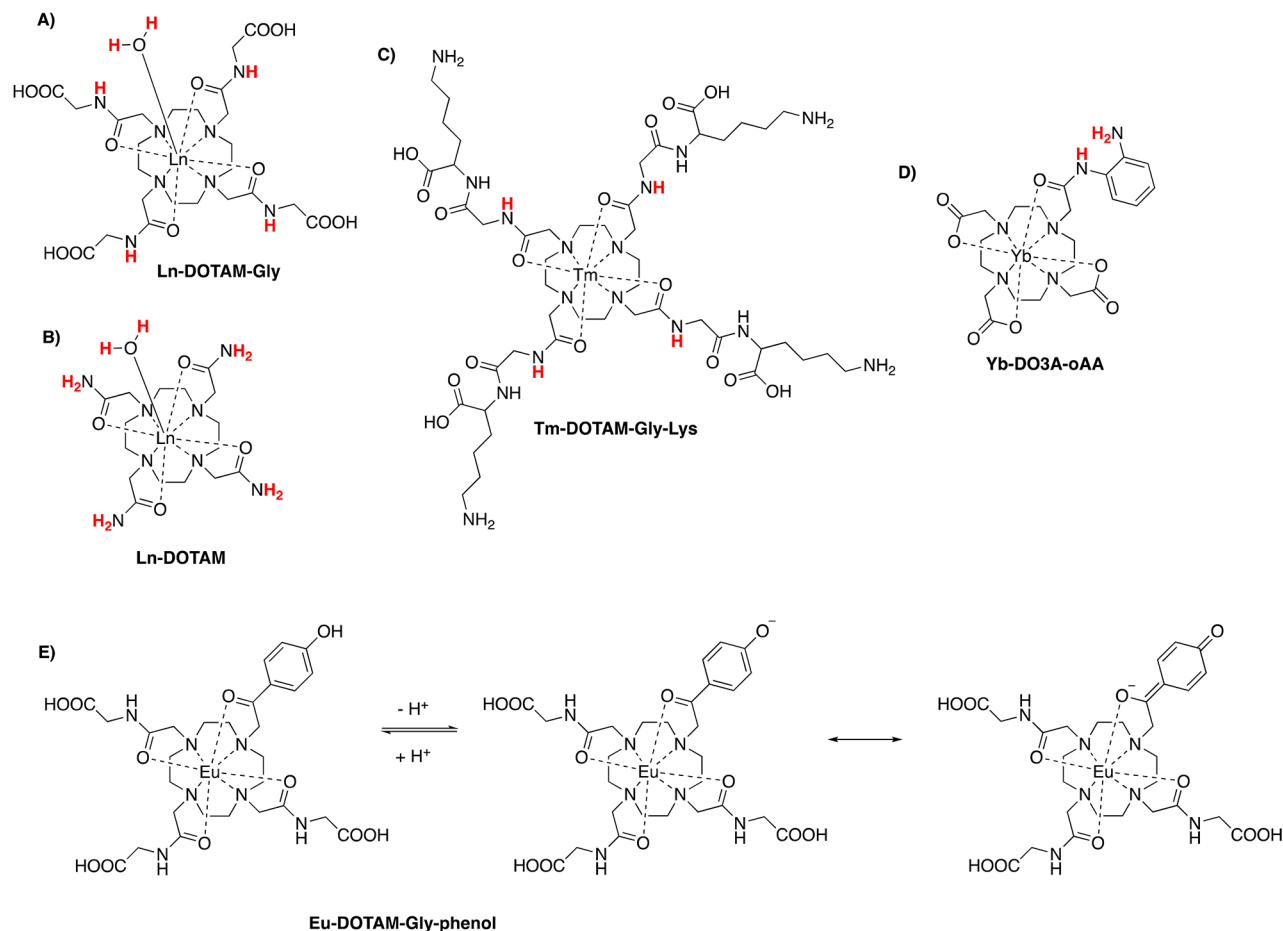
ParaCEST pH sensing agents:

Figure 68. Selected pH-responsive ParaCEST agents (protons employed for CEST imaging are shown in red).[600−606]

difference between the exchangeable proton resonance and the bulk water resonance, allowing faster exchange rates to be sampled with concomitant increased sensitivity.

As outlined in section 3.3, the water exchange rate between the inner sphere of a paramagnetic center and bulk water is an important parameter that governs CEST sensitivity. The water exchange rate strongly depends on geometric or steric factors that are created by macrocyclic ligands encapsulating the paramagnetic ion. Recently, Udugamasooriya and co-workers reported design principles for Eu(III)-DOTAM-based ParaC-EST MR contrast agents to optimize the water exchange rate and thereby enhance the CEST sensitivity.[598,599]

Aime and co-workers investigated the ability of Yb-DOTAM-Gly as a pH-responsive ParaCEST agent (Figure 68A).[600] The compound contains four chemically equivalent amide protons in close proximity to a paramagnetic ytterbium center. Applying an irradiating radiofrequency pulse at the amide N−H resonances at different pH values gave a change in the net saturation transfer effect from 70% to 10% in the pH region of 6.0 to 8.8. Moreover, the authors discovered that the concentration of the ParaCEST agent and the saturation transfer effect are not linearly related. They applied a ratiometric approach by using two agents differing only in the coordinated lanthanide center: Yb-DOTAM-Gly and Eu-DOTAM-Gly. In the latter agent, the amide protons are only slightly shifted in a region where they cannot longer be distinguished from bulk water signals. The CEST spectrum

obtained for a mixture containing both complexes gave three peaks, one for the bulk water, one for the amide protons associated with Yb-DOTAM-Gly, and for the metal coordinated water protons associated with Eu-DOTAM-Gly. Under the assumption that the saturation transfer effect of the two different sets of protons (amide protons vs metal coordinated water protons) have a different pH-dependency, the observed CEST effect depends only on the relative concentration ratio of both lanthanide complexes. An improvement of this ratiometric concept was demonstrated by irradiating two kinds of mobile protons (amide protons and metal-coordinated water protons) that are part of the same paramagnetic DOTAM-Gly complex. The single-molecule CEST procedure was realized through employment of lighter Ln(III) ions, like, for example, Pr(III), Nd(III), and Eu(III), where Pr-DOTAM-Gly (Figure 68A) showed the highest accuracy and sensitivity in its pH-dependent behavior in the pH region of 6.0−8.0.[601,602] However, detecting the CEST effect from the metal-bound water molecule can require high saturation power that can hamper the safe in vivo application of those agents because of local heating effects.[603]

Pikkemmat and co-workers functionalized different generations of poly(propyleneimine) dendrimers with Yb-DOTAM (Figure 68B) to obtain macromolecular ParaCEST agents, thereby combining the two strategies (increasing the chemical shift and the number of exchangeable protons) to improve the sensitivity of the MR contrast agent (vide supra).[604] In this
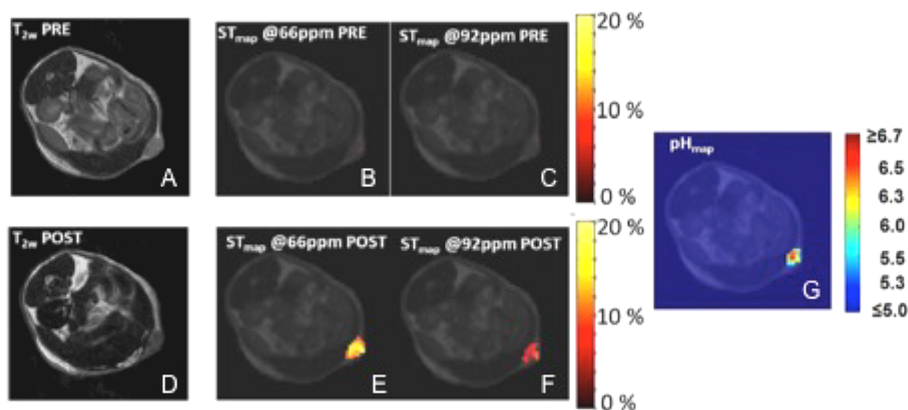
Figure 69. T_{2W} images (7 T) acquired (A) pre and (D) 2 min post i.v. injection of Yb-HPDO3A (dose: 1.2 mmol kg^{-1}); STmaps calculated at 66 ppm (B) pre and (E) 2 min post i.v. injection of Yb-HPDO3A; STmaps calculated at 92 ppm (C) pre and (F) 2 min post i.v. injection of Yb-HPDO3A; (G) pH map of a region of a tumor isolated in one slice plane calculated from the corresponding ST maps. Reproduced with permission from ref 611. Copyright 2014 John Wiley and Sons.

way, they could reduce the detection sensitivity by a factor of 15 and observe a 5% CEST effect at 20 μM dendrimer solution.

Another paramagnetic DOTAM-Gly derivative: Tm-DOTAM-Gly-Lys (Figure 68C) was used as pH responsive ParaCEST agent.[605] Interestingly, in this study the pH was determined from the line width of the asymmetric magnetization transfer ratio curve, which has an exponential relation to pH. As a result, pH mapping was successfully realized independent from agent concentration and temperature for a given saturation pulse. This method was also successfully demonstrated in vivo in healthy mice.

Yb-DO3A-oAA (Figure 68D) has two different exchangeable proton pools which also enables pH imaging via an intramolecular ratiometric approach. This compound was used to assess pH in a mouse model of MDA-MB-231 mammary carcinoma.[603,607,608]

A direct readout of pH by MR imaging is provided by a Eu-DOTAM-Gly derivative (Figure 68E).[606] In this elegant example, one of the amide side chains of the DOTAM-Gly ligand is replaced by a ketone oxygen donor, which in turn is directly conjugated to an ionizable phenolic moiety. Deprotonation of the phenolic proton leads to conjugation of the resulting quinone-like structure with the acetyl oxygen donor coordinated to the europium center. Since the metal-bound water exchange rate is extremely sensitive to alterations in the electronic structure of the ligand pendant arms, the CEST signal can be manipulated through this effect. With a pK_a value of 6.7 for the phenolic entity, the agent has ideal properties for sensing pH in biological systems and shows a large change in exchange frequency over the pH range from 6.0 to 7.6. Using ratiometric CEST imaging, the pH could be determined independent of Eu-DOTAM-Gly derivative concentration. Utilization of this frequency-dependent ParaCEST agent allowed imaging of the pH gradient in kidneys of healthy mice.[609]

Aime and co-workers used the Yb(III) analog of the approved contrast agent Gd-HPDO3A as a pH responsive ParaCEST agent (Figure 3).[610] The labile hydroxylic proton shows a pH-dependent CEST effect in the pH region from 5.0 to 7.0 (37 °C). Moreover, the chemical shift of the hydroxylic proton is temperature-dependent, making Yb-HPDO3A a multiresponsive ParaCEST agent that can report on pH and temperature simultaneously. Yb-HPDO3A exists as two major

isomeric forms in solution with different chemical shifts for the hydroxylic protons, and this enables a ratiometric approach in a single-molecule CEST procedure. This agent was successfully employed for in vivo pH mapping of the tumor region in a melanoma murine model, as depicted in Figure 69.[611]

Recently, a pH-responsive transition-metal-based ParaCEST probe was reported.[612] The high-spin Fe(II) complex of a 2-amino-6-picolyl-appended cyclen ligand shows a pH-dependent frequency shift at pH 7.7 to 4.8 (37 °C). This shift in the CEST peak correlates with the protonation of the unbound pendant 2-amino-6-picolyl units as illustrated in Figure 70.
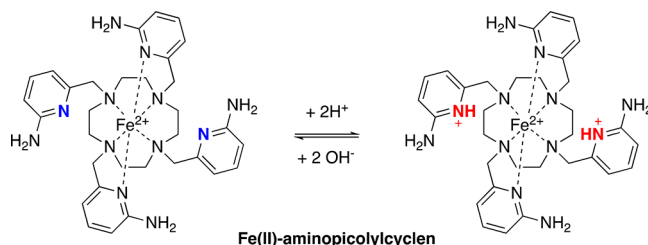
Figure 70. First frequency-responsive transition-metal based ParaCEST agent that reports on pH.[612]

Noteworthy, in this example, the CEST peak changes in frequency with changing pH and not in intensity. In contrast to intensity-responsive contrast agents, frequency-responsive probes do not require a correction for tissue concentration of the probe.

6.3.3. pH-Responsive ParaSHIFT Contrast Agents. Recently, the Parker group developed a ParaSHIFT agent for accurate pH and temperature mapping using MR chemical shift imaging (Figure 71).[613] Unlike indirect detection methods (e.g., CEST methodology), where the interaction between the contrast agent and bulk water is detected, in this approach the MR signal of paramagnetically shifted resonances is enhanced by increased relaxivity from Ln(III) complexes itself. Their Ln-DOTP-like ParaSHIFT agent contains a pendant pyridine moiety, which in turn is labeled with a homotopic ^{t}butyl group, whose protons undergo fast relaxation in the field range from 1 to 7 T. In direct proximity to the ^{t}butyl group, the pyridine ligand also contains a phosphonate group, whose pK_a lies in the physiologically relevant pH region. As a result, the chemical shift of the adjacent ^{t}butyl group
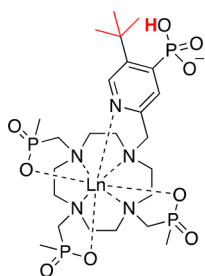
Ln-DOTP derivative

Figure 71. pH-Responsive ParaSHIFT agent.[613]

varies as a function of pH. Using the corresponding Dy(III) and Tm(III) complexes in a ratiometric CEST experiment, the pH and temperature in the liver, kidney, and bladder in healthy mice could be mapped. In comparison to the ParaCEST MR contrast agents discussed in this section, the sensitivity of this agent is substantially enhanced. Consequently, the in vivo experiment could be performed using a dose comparable to clinical MR contrast agents (0.05 mmol kg^{-1} of a 1:1 mixture of the Dy(III)/Tm(III) complexes).

6.3.4. pH-Switchable Contrast Agents. Macromolecular and nanoparticle-based agents have been reported that undergo a pH-dependent transition resulting in signal change and/or accumulation. These agents cannot quantify pH, but they may be able to detect regions of tissue with low pH. For example, Gd(III) containing linear[614] and spherical[615] copolymers have been developed that undergo pH-dependent conformational changes. At low pH, the polymers show a higher degree of cross-linking (i.e., the polymers shrink), which alters the rotational correlation time and hence enhances r_1.

pH-sensitive polymeric micelles encapsulating Gd(III) complexes can be disassembled under acidic conditions.[616] The release of the Gd(III) chelates into solution decreases the T_1 relaxation time constant of the system. Similarly, acidification of a pH-sensitive liposome provokes the release of Gd(III) chelates into the environment.[617]

pH-responsive manganese oxide nanoparticles have also been reported.[618,619] In this approach, the poor stability of MnO under weak acidic conditions is exploited. The more acidic tumor microenvironment dissolves MnO, which in turn

causes a relaxivity enhancement by releasing Mn(II) ions into the environment.

In another impressive example, Mn(II) ions were confined in pH sensitive calcium phosphate nanoparticles comprising a poly(ethylene glycol) shell.[620] Upon activation at lower pH in the solid tumor microenvironment, calcium phosphate disintegrates and Mn(II)-ions are released into the environment. In a C26 tumor-bearing BALB/C nude mice model, it was shown that the released Mn(II)-ions bind to surrounding proteins, which rapidly brighten solid tumors and also detect micrometastases in the liver.

Recently, it was shown that SPIONs can be released from hydrogels[621] or polymeric micelles[622] under acidic condition, which changes their superparamagnetism and therefore their T_2*-relaxivity.

6.4. Enzyme-Responsive Molecular Imaging Agents

The central role of enzymes is to act as biological catalysts, thereby being responsible for most of the functions in cellular and molecular biology. In many disease processes, specific enzymes are upregulated or become expressed on cell surfaces or in the extracellular space. Noninvasive sensing of enzymatic activity is, in principle, a powerful tool to detect disease activity and to monitor the effects of therapeutic interventions. As outlined above, the design of a contrast agent that is responsive to enzymatic activity benefits from the fact that (1) the catalytic rate of an enzyme can be high enough to make it feasible to modulate the contrast generating properties of an activatable agent present at micro- to milliomolar concentrations, and (2) there is a high specificity of enzymatic reactions so that a change in MR signal can be attributed to a specific molecular event.

6.4.1. Enzyme-Responsive T_1/T_2*-Based Contrast Agents. *Modulation of the Hydration State.* An established strategy to modulate MR response to enzymatic activity is to utilize a contrast agent that undergoes a change in hydration state upon activation.

Meade and co-workers used a Gd(III) chelate to detect oncologically significant β-glucuronidase.[623] Their agent consists of a Gd-DO3A moiety bearing a pendant β-glucuronic acid moiety connected by a self-immolative linker to the macrocycle (Figure 72A). The glucuronic acid moiety acts as a mask that can be enzymatically cleaved, which in turn triggers

Enzyme-responsive T$_1$ contrast agents
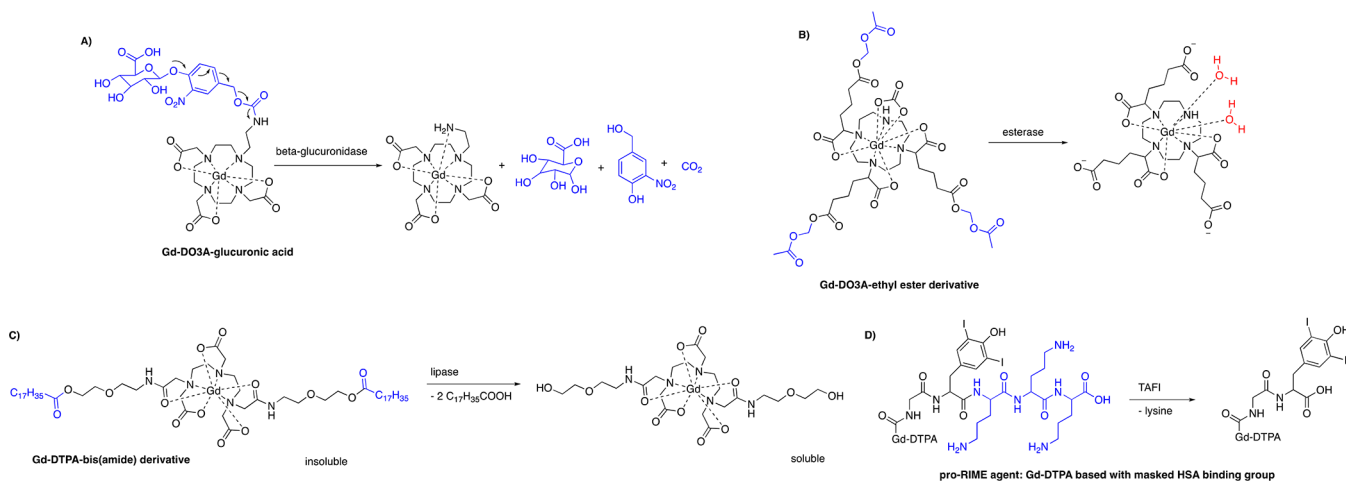
Figure 72. Selected enzyme-responsive T_1 MRI contrast agents (enzyme cleavable entities are shown in blue).[623−625,630]
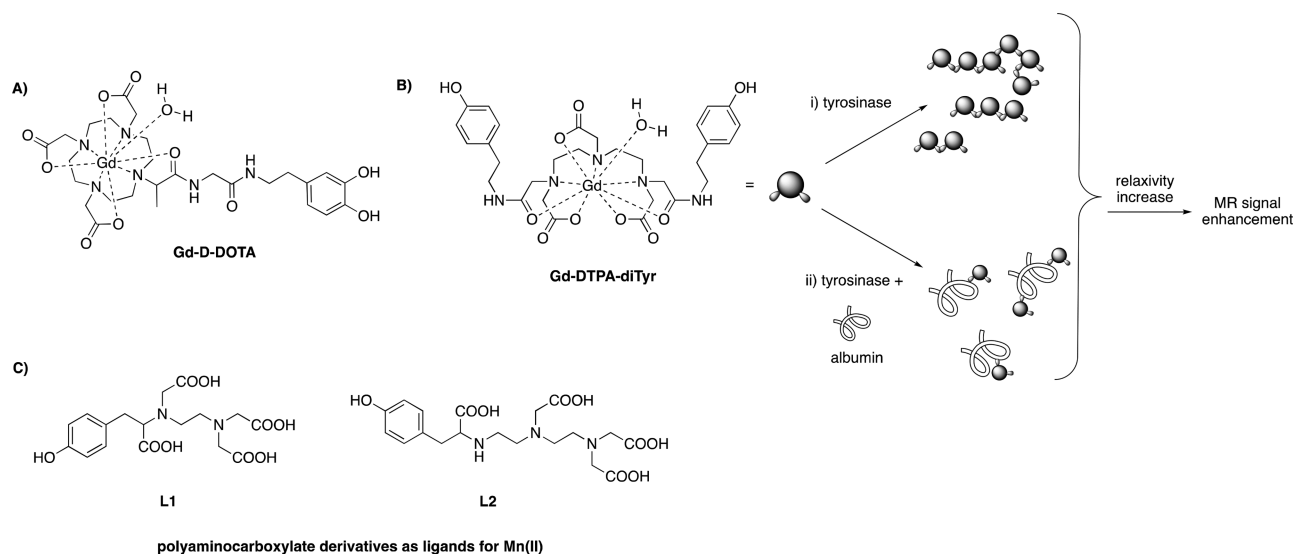
Figure 73. (A) Chemical structure of D-DOTA(Gd); (B) interaction of Gd-DTPA-diTyr with activated tyrosinase can result in (a) oligomers and (b) contrast agent-albumin conjugates. Both products yield an increase in relaxivity. Reproduced with permission from ref 637. Copyright 2007 John Wiley and Sons. (C) Tyrosinase-responsive Mn(II) ligands.[634]

the "self-destruction" of the linkage into two byproducts, as illustrated in Figure 72A, resulting in the release of a Gd-DO3A derivative with an altered hydration state. As a result, the relaxivity in human blood serum decreases by 27% upon enzyme activation. Interestingly, performing the same experiment in a buffer mimicking in vivo anion concentrations leads to an increase in T_1 relaxivity by 17%, which nicely illustrates the influence of buffer compositions upon the efficacy of an MRI contrast agent.

Lowe and co-workers exploited the known tendency of neutral Gd-DO3A complexes to avidly bind bicarbonate anions in vivo and form ternary $q = 0$ complexes.[624] They synthesized a neutral Gd-DO3A derivative with three pendant ethyl ester groups (Figure 72B). This complex forms a stable, $q = 0$ complex with bicarbonate, but in the presence of an esterase the ethyl esters are hydrolyzed to liberate three pendant carboxylates. The resultant anionic complex repels the coordinating anions, which in turn allows water molecules to bind to the paramagnetic center. The change in hydration state from $q = 0$ to $q = 2$ leads to an increase in T_1 relaxivity by 84% (5.7 to 10.5 mM^{-1} s^{-1}).

*Modulation by Change in Solubility.* Insoluble T_1 agents have low relaxivity because of poor access of exchangeable water to the complex. Hoehn and co-workers invented an insoluble Gd-DTPA-bis(amide) based, inactive contrast agent (Figure 72C) that can be internalized into dendritic cells.[625] Lipase triggered cleavage of the stearic acid ester groups renders the contrast agent soluble with access to bulk water. As a result, an increase in MR signal is observed.

In a similar approach, but in the opposite sense, Lepage and co-workers designed a Gd-DOTA based agent linked to a PEG-peptide sequence that exhibits excellent water solubility through the PEG linkage.[626−628] A solubility switch is catalyzed through MMP enzymes, which cleave the PEG peptide, thereby making the chelate insoluble in water. As a consequence, bulk water access to the chelate is reduced resulting in a decrease in MR signal. This strategy was applied in MMP-2-rich tumor-bearing mice and they showed that the contrast agent can additionally be accumulated in tumor cells overexpressing the targeted enzyme.

Figueiredo et al. encapsulated Gd-HPDO3A into anionic liposomes. In the presence of the cationic protein protamine, these Gd(III)-containing liposomes form poorly soluble aggregates with a relaxivity of only 0.2 mM^{-1} s^{-1}. In the presence of the enzyme trypsin, the protamine is degraded, releasing the liposomes and causing a 9-fold relaxivity increase to 1.8 mM^{-1} s^{-1}.[629]

Modulation of the Rotational Correlation Time. Another strategy in the design of enzyme-responsive T_1 contrast agents is to cause the rotational correlation time to change upon activation. The general phenomenon of having contrast agent relaxivity increase upon binding to a receptor was termed RIME (receptor-induced magnetization enhancement) mechanism. Nivorozhkin et al. synthesized a low relaxivity, pro-RIME agent (Figure 72D), which consists of Gd-DTPA and a HSA binding moiety that is masked by a HSA shielding group. Activation by a human carboxypeptidase B, thrombin-activatable fibrinolysis inhibitor (TAFI) releases the shielding group resulting in HSA binding, thereby increasing the relaxivity. Activation in the presence of HSA by micromolar enzyme concentration led to an increase in r_1 of over 150% at 37 °C.[630]

In a similar approach, Wang and co-workers developed the enzymatic contrast agent Gd-DOTA-FPG, which is based on the Gd-DOTA scaffold equipped with a pendant galactopyranose moiety. This agent can be activated with β-galactosidase. In the presence of β-galactosidase and HSA, an increase in T_1 relaxivity by 60% was observed.[631]

Another Gd-DTPA-based RIME agent that shows affinity to HSA after activation with the enzyme ß-galactosidase was invented by Nagano and co-workers. The authors report an r_1 enhancement of 60%.[632]

Recently, Wang and co-workers published a Gd(III)-based chelate with a peptide ligand that is cleaved by legumain, which causes the agent to bind to HSA, boosting the T_1 relaxivity of the agent by 170%.[633]

A different strategy to decelerate τ_R upon activation exploits the enzyme-catalyzed oligomerization of monomeric contrast agents. Bogdanov et al. synthesized Gd-D-DOTA, a Gd-DOTA derivative that contains a pendant hydroxyphenol moiety
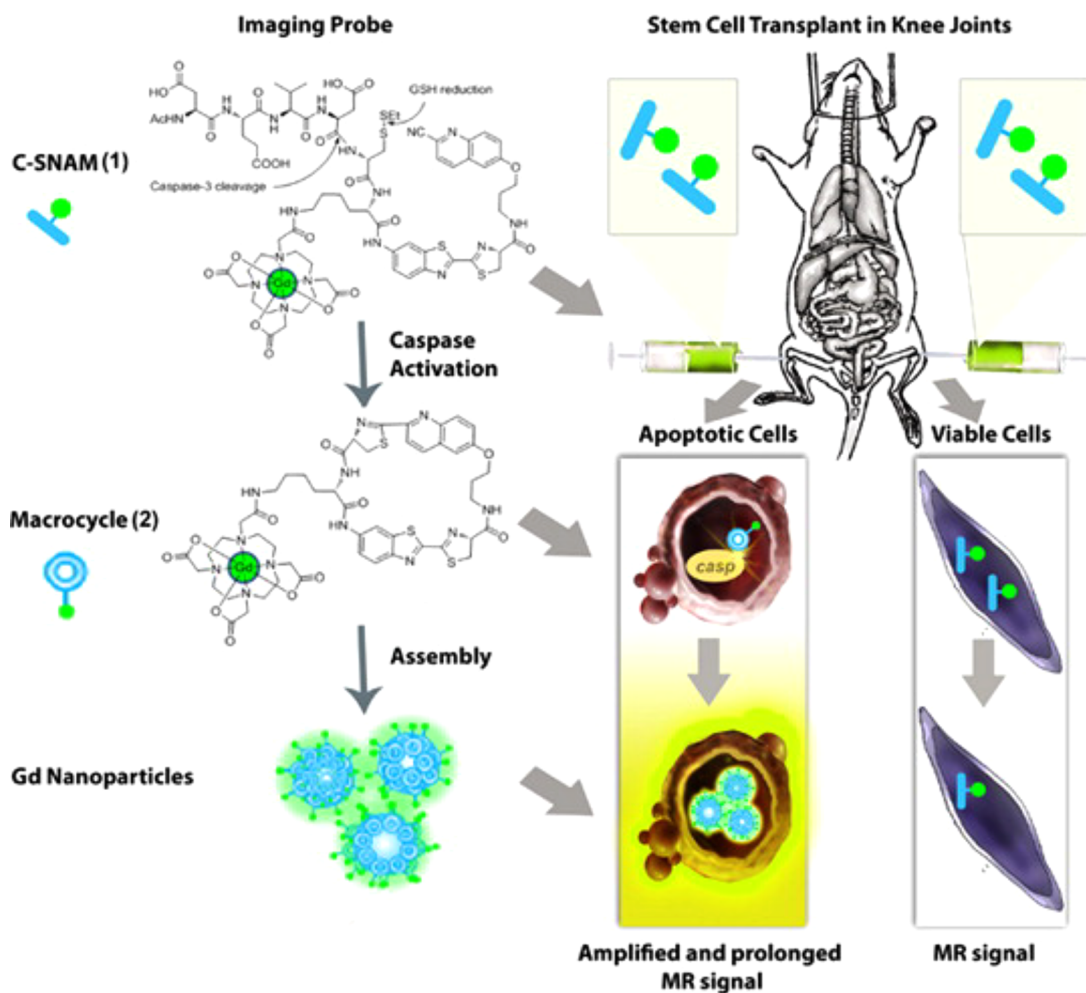
Figure 74. Design and mechanism of action of the caspase-3-sensitive nanoaggregation MRI probe (C-SNAM). (left) Chemical structure of C-SNAM (1). Caspase-3 catalyzed DEVD peptide cleavage and GSH-mediated disulfide reduction triggers a biocompatible intramolecular cyclization reaction that yields the rigid and hydrophobic macrocycle (2). Subsequent self-assembly to Gd(III) containing nanoparticles increases r_1 by 90%. (right) Mechanism of action in vivo: (top) intra-articular injection of C-SNAM into rat knee joints with implants of apoptotic and viable stem cells and (bottom) caspase-3-mediated activation leads to an enhanced MRI signal through increased T_1 relaxivity and retention in apoptotic stem cell transplants. Reproduced from ref 640. Copyright 2015 American Chemical Society.

(Figure 73A).[635] In the presence of peroxidase and hydrogen peroxide, the hydroxyphenol moiety serves as electron donor during enzymatic hydrogen peroxide reduction, which in turn generates hydroxyphenol radicals. The converted Gd(III)-monomers then undergo rapid condensation into paramagnetic dimers or oligomers. As a result, r_1 increases by 200% (3.75 to 11.50 mM^{-1} s^{-1}, 0.47 T).

A second generation of this probe employs Gd-DTPA units bearing either two hydroxytryptamide or hydroxyphenetyla-mide moieties, respectively.[636] The latter compound (Gd-DTPA-diTyr; Figure 73B) was used to sense tyrosinase activity.[637] In the presence of activated tyrosinase, either oligomeric structures were formed [Figure 73B(i)] or in the presence of tyrosinase and HSA, also paramagnetic complex-protein conjugates can be formed [Figure 73B(ii)]. Both products exhibit an increased rotational correlation time upon activation. Hence, both products yield an increase in relaxivity.

Botta and co-workers exploited tyrosine modified Mn(II)-based polyaminocarboxylates as enzyme-responsive MRI contrast agents [Figure 73C (L1 and L2)].[634] In the presence of the enzyme tyrosinase, r_1 increased by 50% for L1 and by 350% for L2, respectively. For Mn-L1, tyrosinase destabilizes

the Mn(II) complex which leads to the release of Mn(II) ions and, consequently, to an increase in MR signal. For Mn-L2, it is believed that the enzyme tyrosinase is catalyzing the formation of oligomeric species, which increases the rotational correlation time of the agent and hence r_1.

The enzyme-catalyzed degradation of a polymer containing MRI contrast agent can be employed to observe changes in MRI contrast. Degradation of the polymer accelerates the rotational tumbling time of the MRI agent leading to a decrease in its T_1 relaxivity upon enzyme activation. For example, hyaluronan-Gd-DTPA-beads were attached to agarose-avidin beads.[638,639] Degradation of the hyaluronan by the enzyme hyaluronidase to lower molecular weight fragments led to altered relaxation rates.

Daldrup-Link and co-workers took a different approach in the design of an enzyme-responsive Gd(III)-based MR contrast agent.[640] They designed a caspase-3-sensitive nano-aggregation MRI probe (C-SNAM) that employs a Gd-DOTA moiety coupled to a DEVD peptide sequence through an amino luciferin-based linkage that contains a terminal disulfide entity (Figure 74 left). Enzymatic cleavage of the DEVD peptide and GSH-mediated reduction of the disulfide entity

Figure 75. Chemical structure of Gd-DOTA-DEVD-Tfb.[651]

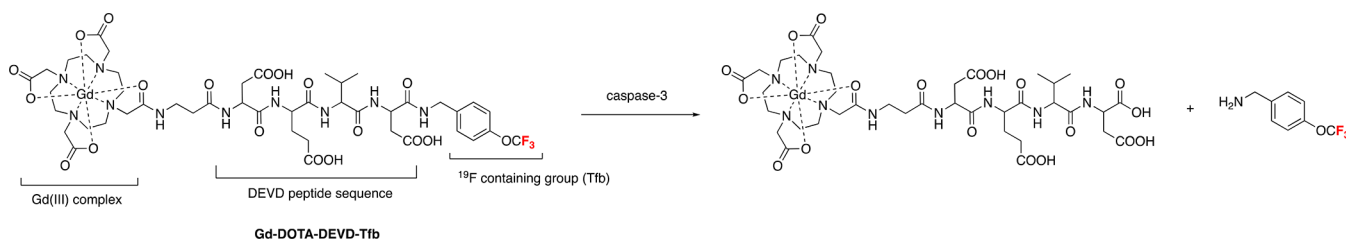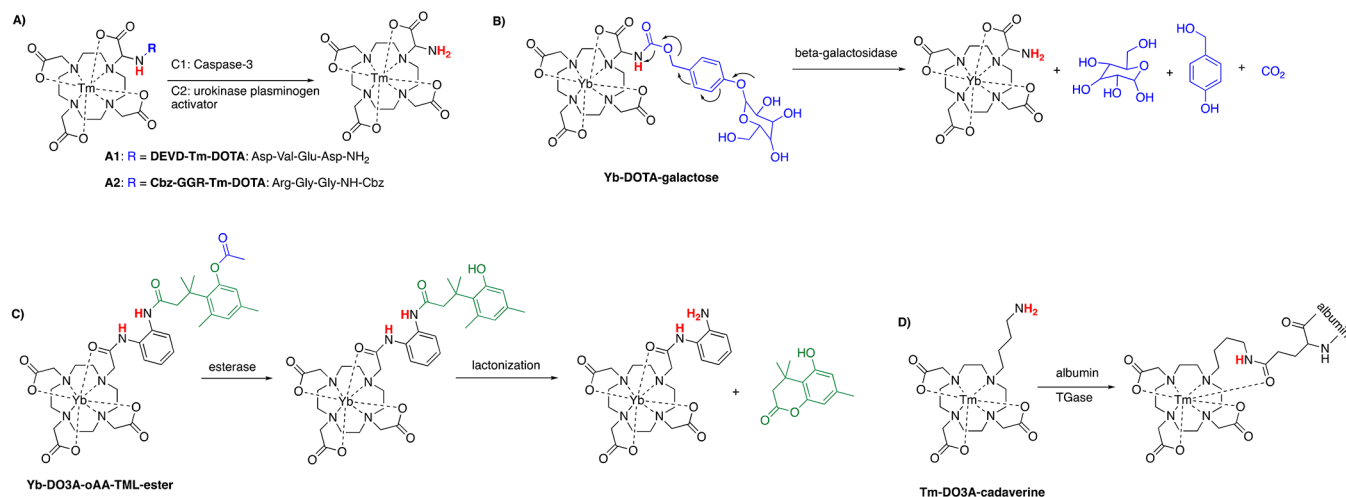**Figure 76.** Selected enzyme-responsive ParaCEST MRI contrast agents (enzyme cleavable entities are shown in blue).[655,657,659,660,662]

triggers an intramolecular cyclization reaction, thereby yielding a rigid and hydrophobic product (Figure 74 left) that will subsequently self-assemble into Gd(III)-containing nanoparticles. The prolonged rotational correlation time of the resulting nanoparticles amplifies the T_1 relaxivity by 90% [r_1 = 10.2 mM^{-1} s^{-1} to 19.0 mM^{-1} s^{-1} (1 T)]. Caspase-3 is a common cell apoptosis biomarker.[641] To investigate if this agent can be applied for in vivo monitoring of transplanted stem cell viability, the authors transplanted viable FLuc-eGFP-transduced rASCs into an osteochondral defect of the left distal femur and MMC-treated apoptotic FLuc-eGFP-transduced rASCs into an osteochondral defect of the right distal femur of athymic female Harlan rats. Intra-articular injection of C-SNAM provoked significant MR signal enhancement in apoptotic matrix associated stem cell implants (MASI) compared to viable MASI. The MR signal enhancement can be attributed to the increased relaxivity of the probe upon activation but also to prolonged tissue retention in apoptotic MASI through its nanoaggregation properties (Figure 74 right).

On the basis of the same approach, the Rao group employed caspase-3-activatable C-SNAMs to image chemotherapy-induced tumor apoptosis in mice[642] and to accurately monitor the response of tumors to either metronomic chemotherapy or radiation therapy.[643]

Enzymes that catalyze the aggregation of SPIONs can increase the superparamagnetism of the nanoparticles and, hence, their T_2^* relaxivity. For instance, the hydrophilic coating of SPIONs can be cleaved by MMP-2 or MMP-9 enzymes, which leads to aggregation of the nanoparticles.[644−646] Aggregation can be also induced by polymerization of phenolic SPIONs through the enzyme peroxidase.[647]

In contrast, also the disaggregation of nanoparticles can be catalyzed by enzymes, which in turn reduces the superparamagnetism of the nanoparticles and therefore decreases their T_2^* relaxivity.[648−650]

6.4.2. Enzyme-Responsive Paramagnetic ^{19}F-Based Contrast Agents. Kikuchi and co-workers proposed a paramagnetic relaxation-based ^{19}F MRI probe to detect enzyme activity. Here a Gd(III) complex is placed in proximity to ^{19}F nuclei such that the T_2 is shortened dramatically resulting in attenuation of the ^{19}F MRI signal. If the Gd(III) complex is released from the vicinity of the ^{19}F nuclei, it will result in an increase in the ^{19}F T_2 and hence enhance the ^{19}F MRI signal. They coupled Gd-DOTA to trifluoromethoxybenzene via a DEVD peptide linker (Gd-DOTA-DEVD-Tfb) (Figure 75).[651] The ^{19}F signal was broadened into the baseline because of the presence of the nearby Gd(III) ion. In the presence of the enzyme caspase-3, the DEVD peptide sequence was cleaved, releasing the ^{19}F reporter from the agent and resulted in a measurable ^{19}F MR signal. This probe was further modified to a dual-function agent capable of detecting caspase-3 activity via fluorescence measurements and ^{19}F MRI.[652]

Tethering a ^{19}F reporter molecule to Gd-DOTA via a different enzyme-cleavable linkage enabled the detection of β-lactamase[653] and β-galactosidase[654] activity, respectively.

6.4.3. Enzyme-Responsive CEST Contrast Agents. *Enzyme-Responsive ParaCEST Agents.* ParaCEST agents can also be utilized for the detection of enzyme activity. The chemical exchange rate of the labile proton is changed by enzyme-catalyzed alteration of the covalent bond structure of the ParaCEST agent. As a result the CEST effect appears, disappears, or changes in magnitude.
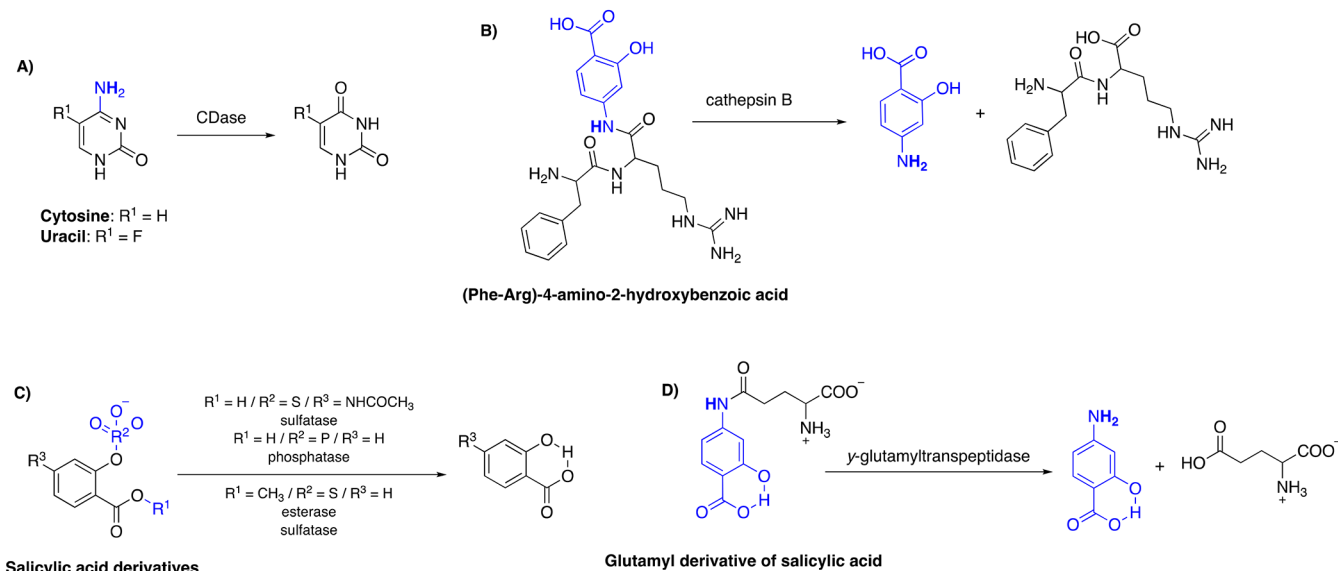
DiaCEST enzyme sensing agents

Figure 77. Selected enzyme-responsive DiaCEST MRI contrast agents (enzyme cleavable entities are shown in blue).[663,665−669]

The first enzyme sensing ParaCEST agent was developed by Pagel and co-workers.[655] A Tm-DOTA derivative was coupled to a DEVD peptide sequence (Figure 76A1), which can be selectively hydrolyzed by caspase-3, thereby converting the DOTA-amide into a DOTA-amine. Under physiological conditions, the disappearance of the CEST effect was observed upon caspase-3 activation. A limitation of a "turn-off" effect is in quantifying the absence of signal. In a second study, the same group successfully exploited the simultaneous application of the enzyme-responsive DEVD-Tm-DOTA agent (Figure 76A1) and an unresponsive ParaCEST agent, Yb-DOTAM-Gly (Figure 68A), to quantify the enzymatic transformation in a ratiometric approach.[656] In this strategy, the unresponsive probe is "always on" and accounts for all factors that could alter the CEST effect except for the enzyme to be measured. This comparative measurement to improve the detection of enzyme activity is referred to as "catalyCEST MRI".

The Pagel group extended this method for the in vivo detection of urokinase plasminogen activator (uPa) in a Capan-2 pancreatic tumor mice model where Cbz-GGR-Tm-DOTA (Figure 76A2) served as a uPa responsive probe and Eu-DOTAM-Gly as control probe.[657] This proof-of-concept study represents the first report of in vivo catalyCEST MRI. Replacement of the peptide sequence of a Tm-DOTA derivative enabled the detection of cathepsin-D activity.[658]

Additionally, modularly designed Yb-DOTA derivatives have been used as enzyme-sensing ParaCEST agents. For instance the Yb-DOTA complex in Figure 76B is coupled to a β-galactose ligand via a self-immolative linker. Selective cleavage of the sugar by β-galactosidase results in elimination of the linker group, and the amide bond is hydrolyzed to an amine thereby generating a CEST effect.[659]

Yb-DO3A-oAA-TML-ester (Figure 76C) is capable of sensing esterases, which cleave the ester of the chelator (shown in blue, Figure 76C).[660] The trimethyl lock moiety can then undergo lactonization (shown in green, Figure 76C) also resulting in the conversion from an amide into an amine in the Yb-DO3A-oAA contrast agent. A similar probe Yb-DO3A-oAA-TML-Q is activated by DT-diaphorase.[661]

It was also shown that for enzyme-activated ParaCEST agents, the CEST effect can be generated through the opposite reaction (i.e., formation of an amide bond from an amine group). Conjugation of Tm-DO3A-cadaverine (Figure 76D) to albumin by transglutaminase produced a "turn-on" CEST effect.[662] Concurrently, a reduced CEST signal from albumin could be observed.

Enzyme-Responsive DiaCEST Agents. DiaCEST agents have also been developed to detect enzyme activity. Gilad and co-workers reported that the enzyme cytosine deaminase (CDase) catalyzed deamination of cytosine to uracil or F5C to 5FU, respectively (Figure 77A).[663] As a result, the previously observed CEST effect is "switched off".

Another example is the DiaCEST peptide (LRRASLG)$_8$ which shows high CEST contrast due to its basic, positively charged lysine and arginine residues. Phosphorylation of this peptide through the enzyme protein kinase A creates a strong negatively charged group within the molecule, which slows down the water exchange between the exchangeable protons and the bulk water protons. Consequently, the authors observed a reduced CEST effect in in vitro experiments.[664]

Recently, (Phe-Arg)-4-amino-2-hydroxybenzoic acid (Figure 77B) was proposed as a catalyCEST MRI agent that contains an enzyme-responsive entity and also a nonresponsive reference. After cleavage of the dipeptidyl ligand through the enzyme cathepsin B (shown in blue, Figure 77B), the aryl-amide proton is converted into an aryl-amine proton (i.e., the CEST signal observed for the aryl amide proton disappears). The salicylic acid moiety is largely unresponsive to cathepsin B activity and acts as nonresponsive reference.[665]

The modular design of salicylic acid derivatives (Figure 77C) facilitated several "turn-on" catalyCEST MRI agents capable of sensing sulfatase,[666] alkaline phosphatase,[667] and the presence of the two enzymes esterase and sulfatase at the same time.[668] Additionally, a glutamyl derivative of salicylic acid (Figure 77D) was successfully employed in mouse models of human ovarian cancers to selectively detect γ-glutamyl transferase.[669]

Redox potential-responsive T_1 contrast agents
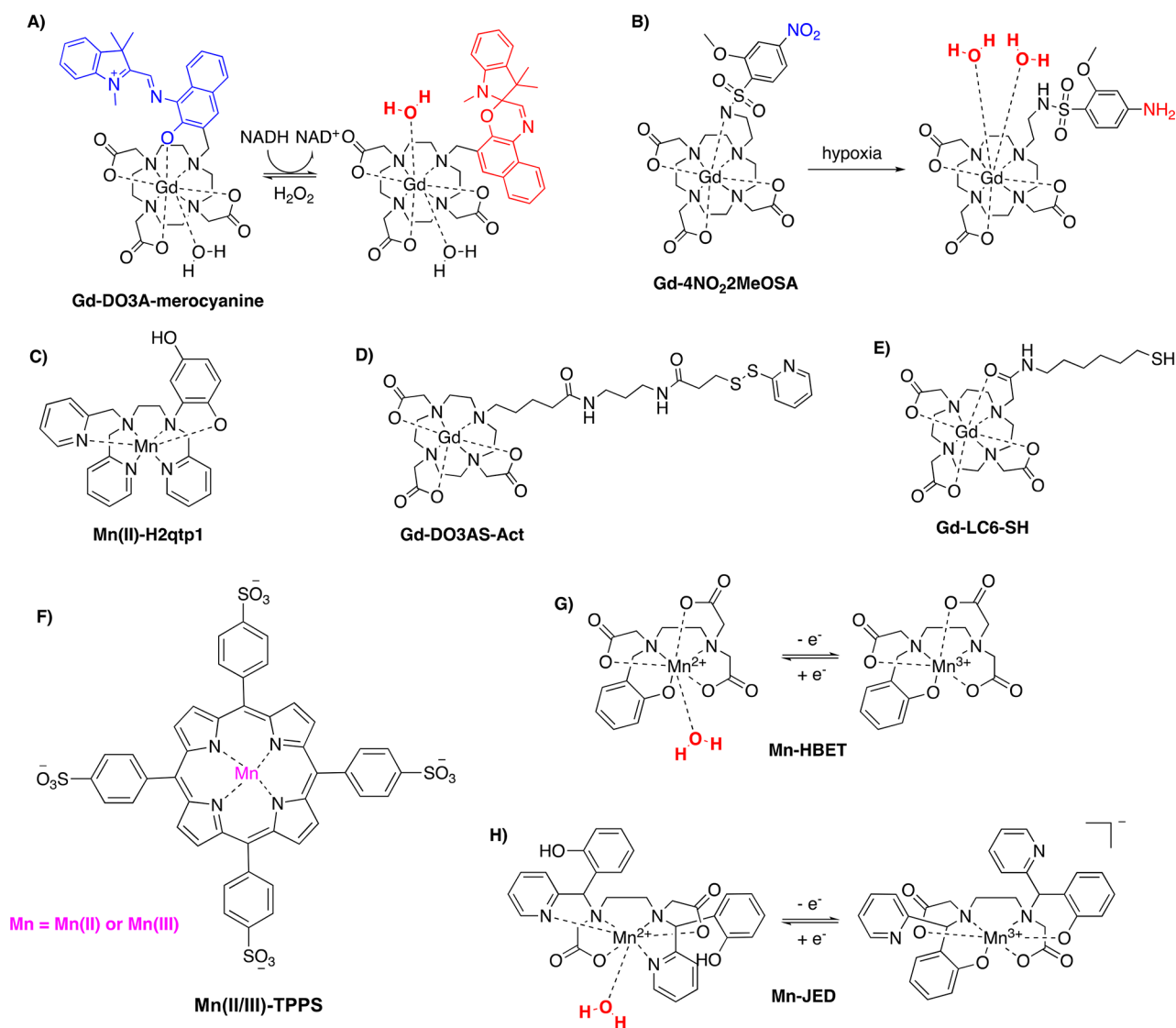
Figure 78. Selected redox potential-responsive T_1 contrast agents.[382,657,670−673,675−679,686,689]

6.5. Redox Potential-Responsive Molecular Imaging Agents

The intra- and extracellular redox environment is tightly regulated in order to maintain normal physiological processes. In disease states the redox environment can become disrupted, so that altered redox is generally associated with wide range of pathophysiological conditions. The redox environment is regulated by metabolites, including NAD/NADH, peroxides, thiol/disulfides (e.g., glutathione), nitric oxide, and oxidase enzymes. Activatable MR contrast agents can be designed to be altered by redox active metabolites. The design of redox sensitive probes can involve a change in oxidation state of the ligand or the metal center to provide the desired change in MR contrast with altered redox environment.

6.5.1. Redox Potential-Responsive T_1 Contrast Agents.
One strategy to sense the redox changes is the modulation of the hydration state of the contrast agent upon activation. Louie and co-workers employed this strategy by introducing a merocyanine moiety into a Gd-DO3A complex in a way that the oxygen donor of merocyanine could

coordinate to the Gd(III) center (Figure 78A).[670,671] After treatment with NADH, the merocyanine group was converted into its spirooxazine isomer, incapable of coordinating the metal center and, hence, leaving space for a water molecule to coordinate to the Gd(III) ion. As a result, the hydration state of the complex changed from $q = 1$ to $q = 2$, thereby increasing r_1 by 55%.

Iwaki et al. showed that Gd-4NO$_2$2MeOSA (Figure 78B) could undergo reduction to the corresponding aminobenzenesulfonamide in the presence of rat liver microsomes under hypoxic conditions but not under normoxic conditions.[672] The agent consists of a Gd-DO3A derivative with a pendant nitrobenzenesulfonamide where the sulfonamide nitrogen is deprotonated and coordinated to the Gd(III) center at neutral pH. Reduction to the aminobenzenesulfonamide raises the pk_a value of the sulfonamide nitrogen resulting in protonation and dissociation from the Gd(III) ion. As a result, the hydration state of the complex switches from $q = 0$ to $q = 2$ and r_1 increases by 70%.

Goldsmith and co-workers developed Mn(II)-H2qtp1 (Figure 78C), a Mn(II) based complex with a redox-active ligand.[673−675] The hexadentate ligand contains a dihydroxybenzyl group that can be oxidized to the weaker-coordinating benzoquinone using hydrogen peroxide. As a consequence, r_1 increases from 4.7 to 5.3 mM^{-1} s^{-1}, presumably because of greater aquation of the Mn(II) ion. By adding a second dihydroxybenzyl group into the ligand scaffold, r_1 could be further increased from 5.5 to 7.2 mM^{-1} s^{-1}.

Another example for a redox potential-responsive agent is Gd-DO3AS-Act (Figure 78D).[676] The Gd-DO3A-based agent bears a 2-pyridyldithio functionality readily available for disulfide exchange reactions. An exchange reaction with glutathione introduces an additional pendant carboxylic acid moiety within the molecular scaffold, which can coordinate the Gd(III) center. This in turn leads to the displacement of the inner-sphere water molecule, and the hydration state of the complex switches from $q = 1$ to $q = 0$, thereby decreasing r_1 by 50%.

Another thiol-bearing Gd-DOTA-monoamide derivative (Gd-LC6-SH) (Figure 78E) was attached to HSA via a disulfide bridge.[677−679] When bound to albumin, the T_1 relaxivity of the gadolinium(III) complex is higher than in the unbound form due to the slower tumbling rate of the Gd(III)-HSA adduct. In a reducing environment, the gadolinium(III) complex is cleaved from HSA by reduction of the disulfide bond, which decreases r_1 by 55%. In a proof-of principle study, Gd-LC6-SH was applied as a MR reporter of tumor redox status in in vivo experiments with mice bearing Mia-PaCa-2 or NCI-N87 tumor xenografts.[680]

Conjugation of thiol-bearing Gd-DO3A derivatives to the surface of liposomes via disulfide linkage led to paramagnetic, supramolecular adducts with slow rotational correlation times. The disulfide linkage makes them sensitive to reducing environments, which was shown in in vitro experiments. Free thiol-mediated cleavage of the Gd(III) complexes from the surface of the liposomes accelerated τ_R and decreased the r_1 from 13.6 to 6.5 mM^{-1} s^{-1}.[681]

Aime and co-workers first proposed the utilization of the Mn(II)/Mn(III) couple as an activation mechanism for the development of redox sensitive T_1 contrast agents.[382] They used the well-known Mn(III)-TPPS (Figure 78F) complex which had been used as a contrast agent for tumor imaging.[682−685] They also prepared the Mn(II) complex by reducing with dithionite. The relaxation mechanism is different for the two complexes at 0.47 T: the dominant correlation time for the Mn(III) complex is the electronic relaxation time, while for Mn(II), it is the rotational correlation time. At 0.47 T, Mn(III)-TPPS has a higher relaxivity than Mn(II)-TPPS. However, when poly-β-cyclodextrin is added, host−guest complexes form, resulting in a longer rotational correlation time. This has a dramatic effect on the relaxivity of Mn(II)-TPPS ($r_1 = 40.8$ mM^{-1} s^{-1}) but much less so with Mn(III)-TPPS (15.2 mM^{-1} s^{-1}). In the presence of 40 Torr pO$_2$ (pO$_2$ of venous blood vessels is approximately 40 Torr), the Mn(II)-TPPS:CD adduct was completely oxidized.

Loving et al. took a different approach to the Mn(II)/Mn(III) couple.[686] They showed that the HBET ligand could stabilize both oxidation states, but the Mn(II)-HBET complex (Figure 78G) is seven coordinate, $q = 1$, while Mn(III)-HBET is six coordinate $q = 0$. In addition to the change in hydration state, the difference in spin state will also result in a lower relaxivity for the Mn(III) form. At pH 7.4, 37 °C, 1.4 T, r_1 was

2.8 mM^{-1} s^{-1} in the divalent state and 1.1 mM^{-1} s^{-1} in the trivalent state. Loving et al. further showed that this system could be reversibly oxidized with hydrogen peroxide and concomitant signal loss or reduced with glutathione and concomitant signal increase. This work was further extended by synthesizing a series of derivatives where the electronic substituent on the aromatic ring was varied from electron-withdrawing to electron-donating.[371] They also examined the effect of changing from an ethylenediamine to a cyclohexamine diamine backbone on relaxivity, thermodynamic stability, pH-dependent complex speciation, hydration state, water exchange kinetics of the Mn(II) complexes, and pseudo-first-order reduction kinetics. They found that they could improve the relaxivity turn-on to a factor of 7.5 ($r_1 = 0.5$ mM^{-1} s^{-1} for Mn(III)-CyHBET compared to 3.3 mM^{-1} s^{-1} for Mn(II)-CyHBET).

Mn-HBET and Mn-CyHBET provided strong proof of concept for Mn complexes as redox-activated MRI contrast agents, but the Mn(II) oxidation state is favored exclusively in blood plasma. Mn(II) and Mn(III) favor disparate and distinct coordination environments, and developing a ligand capable of supporting complexes where both oxidation states can persist in blood plasma is challenging. Mn(II) is best stabilized by polyamino/carboxylate/pyridyl ligands like EDTA or N,N'-bis(pyridyl)-ethylenediaminediacetic acid (BPED), whereas Mn(III) favors Mn more electron-releasing ligands, e.g. phenolate containing ligands like HBED, Figure 43. For example, Mn(III)-EDTA will decompose via disproportionation to Mn(II) and Mn(IV),[687] whereas the Mn(II) complex of HBED will spontaneously oxidize to Mn(III) upon O$_2$ exposure.[688] Mn-HBET was designed as an initial compromise between the Mn(II) and Mn(III) ligand preferences, but the redox potential of Mn-HBET is >500 mV greater than cysteine/cysteine disulfide redox couple. Attempts to depress the Mn(II)/Mn(III) redox potential via incorporating electron-releasing substituents onto the phenolato-O donor resulted in ligand−metal autoredox upon oxidation to Mn(III). One solution was to develop a chelator that was capable of isomerizing between binding modes that favor Mn(III) (BPED) or Mn(II) (HBED) exclusively. The chelator JED (Janus HBED/BPED, Figure 78H) was demonstrated to support stable and high-relaxivity complexes of both Mn(III) and Mn(II) in blood plasma. Switching between the Mn(III) and Mn(II) oxidation states resulted in a 9-fold increase in blood plasma r_1 at 1.4T, 37 °C. Importantly, a large Mn(II) versus Mn(III) r_1 differential was maintained up to 11.7T.[689] Interconversion between the oxidation states can be triggered in the presence of peroxidase enzymes or addition of excess L-cysteine.

A novel procedure for the MR-based assessment of hypoxia was reported by Aime and co-workers.[690] In this innovative example, the combined utilization of Gd-DOTP- and Gd-HPDO3A-labeled red blood cells made it feasible to map tumor hypoxia in a transplanted breast tumor mouse model. Gd-DOTP-labeled red blood cells act as a vascular oxygenation-responsive agent. Gd-DOTP shows 5 times higher affinity for deoxy-hemoglobin in comparison to oxy-hemoglobin. As a result, Gd-DOTP-labeled red blood cells show far higher T_1 relaxivity in hypoxic regions than in normoxic areas. Gd-HPDO3A-labeled red blood cells were used to furnish the local concentration of red blood cells. In the corresponding in vivo study, first Gd-HPDO3A-labeled red blood cells were administered and MRI vascular volume maps were acquired.
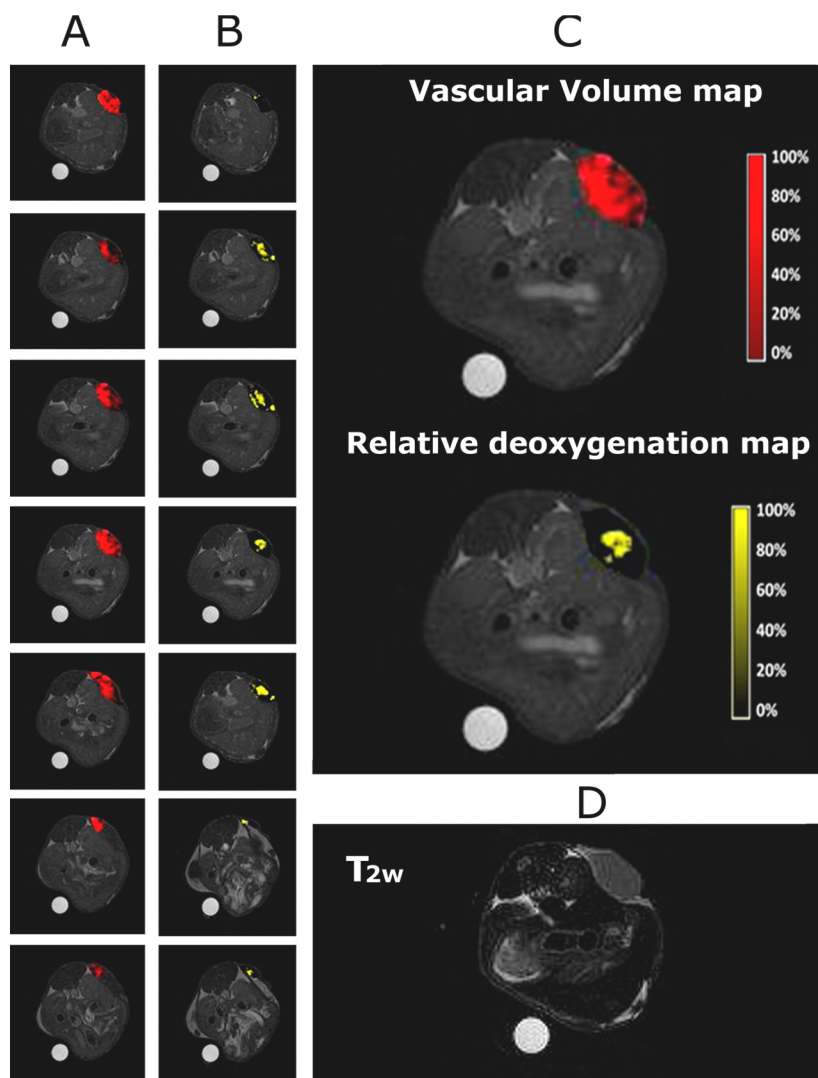
Figure 79. Vascular volume and relative deoxygenation maps of a representative tumor. (A) Vascular volume maps of 7 slices covering the tumor; (B) relative deoxygenation maps of 7 slices covering the tumor; (C) magnification of (top) vascular volume and (bottom) relative deoxygenation maps of the central slice of tumor; and (D) T_{2w} image of the central slice of tumor. Reproduced from ref 690. Copyright 2015 American Chemical Society.

Afterward, Gd-DOTP-labeled red blood cells were injected into the same animal and T_1-weighted images were acquired. The ratio between those two images gave a relative MRI deoxygenation map that reports on O_2 content independently from vascular volume (Figure 79).

6.5.2. Redox Potential-Responsive ParaCEST Contrast Agents. Pagel and co-workers proposed Yb-DO3A-oAA (Figure 80) as a responsive ParaCEST agent capable of detecting NO in the presence of O_2.[691] This compound exhibits two CEST effects, caused by the exchangeable protons from the amine and the amide hydrogens, respectively. In the presence of NO and O_2, the compound undergoes an irreversible covalent conversion to a dinuclear species bridged through a triazene (Figure 80A), thereby losing both CEST effects.

Ln-DOTA-tetraamide derivatives exhibit sufficiently slow water exchange kinetics that the shifted, coordinated water ligand can act as a CEST reporter. Water-exchange kinetics can be tuned by altering the substituents on the amide groups either with respect to charge, lipophilicity, or electronic structure.[451] Sherry and co-workers developed a series of

Eu(III)-based ParaCEST agents where oxidation or reduction altered the water exchange rate and, in turn, the CEST signal. These authors reported an activatable agent with two pendant N-methylquinolinium moieties,[692] designed to mimic the NADH/NAD$^+$ couple. In its oxidized form [Figure 80B (blue)], the agent is nearly CEST MRI silent but was "turned-on" after irreversible reduction with NADH to the corresponding dihydroquinoline derivative [Figure 80B (red)]. The larger CEST signal upon reduction is attributed to the slower water exchange rate of the reduced species.

Another agent utilized a pendant 9-anthryl group [Figure 80C (blue)] that acts as a specific reactive center for singlet oxygen ($^1O_2$), a highly unstable reactive oxygen species (ROS) that is associated with cancer and cardiovascular diseases.[201] Oxidation of the 9-anthryl moiety with $^1O_2$ irreversibly forms the stable endoperoxide derivative [Figure 80C (red)]. Like in the case of Yb-DO3A-oAA (vide supra), the nonequilibrium probe design was chosen to form a sufficient amount of oxidized species to allow CEST detection, considering the short-lived and low concentration of $^1O_2$. Binding of singlet oxygen successfully shifted the position of the metal-bound

Redox potential-responsive ParaCEST agents
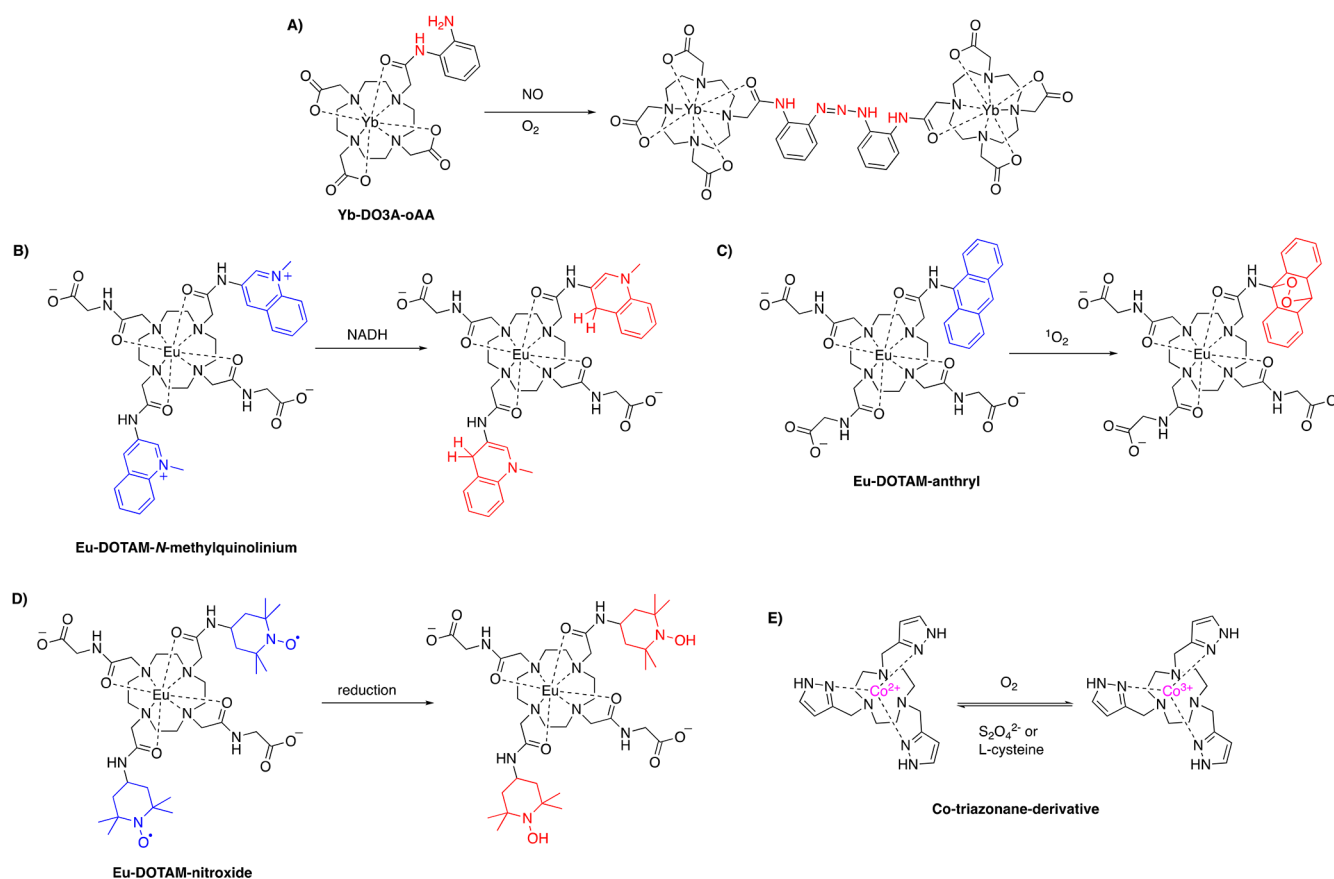
Figure 80. Selected redox potential responsive ParaCEST agents.[184,201,691−693]
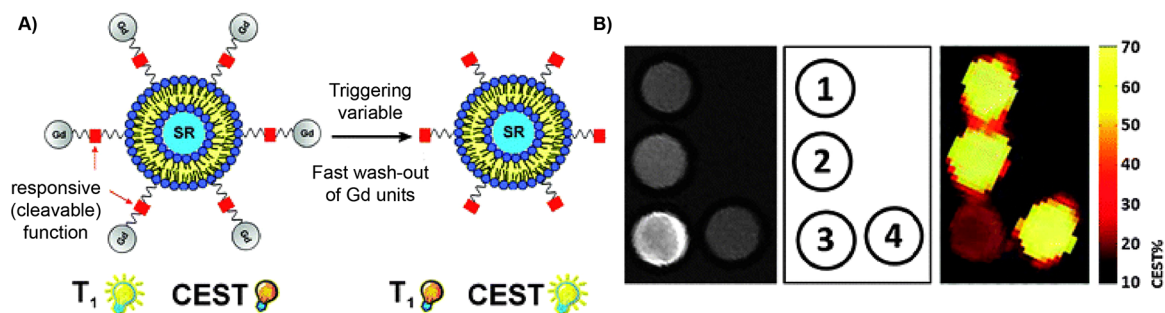
Figure 81. (A) Schematic representation of the dual T_1-CEST liposomal agent. The CEST contrast is activated after cleavage of the Gd(III)-complexes by a biological trigger (e.g., reducing environment). (B) MR images of a phantom at 7 T and 37 °C of (1) LipoCEST agent, (2) LipoCEST agent modified with free thiol groups on the surface, (3) LipoCEST agent modified with Gd-DO3A derivative via disulfide linkage (LipoCEST-SS-DO3A), (4) and treatment of LipoCEST-SS-DO3A with the reducing agent TCEP. (Left) T_1 weighted images and (right) CEST map upon radiation at 3.5 ppm overlaid on a T_2-weighted image of the phantom. Reproduced with permission from ref 695. Copyright 2011 Royal Society of Chemistry.

water CEST peak. Moreover, ratiometric CEST imaging in in vitro systems revealed the potential of this agent to sense $^1O_2$ with high chemical specificity, rapid reaction kinetics, as well as high kinetic and thermodynamic stability.

A different mechanistic approach by the Sherry group was to employ two redox-sensitive nitroxide free radicals, as amide substituents (Figure 80D). The paramagnetic nitroxide radicals serve to shorten the T_1 relaxation time of bulk water protons, and this short T_1 has the effect of nullifying the CEST effect because water relaxes too quickly upon saturation.[184] Nitroxides can be rapidly oxidized or reduced to their diamagnetic

derivatives (e.g., under hypoxic conditions reduction of nitroxide radicals has been demonstrated). Formation of the diamagnetic nitroxide [Figure 80D, (red)] through either a biological or chemical means would lengthen the T_1 of bulk water protons and restore the CEST signal. Injection of the probe in healthy mice showed that the probe was still intact after excretion in the bladder (i.e., the nitroxide radicals were not reduced by biological processes). Subsequent administration of the reducing agent L-ascorbic acid activated the agent as evidenced by the strong CEST signal in the bladder.
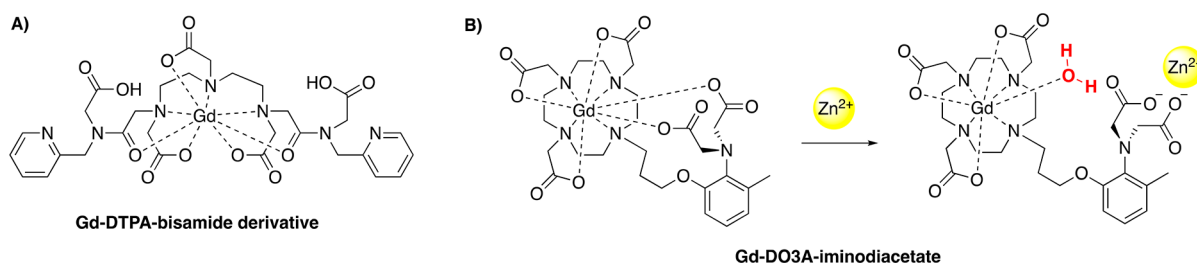
Figure 82. Selected Zn(II) binding MRI contrast agents.[696−699]
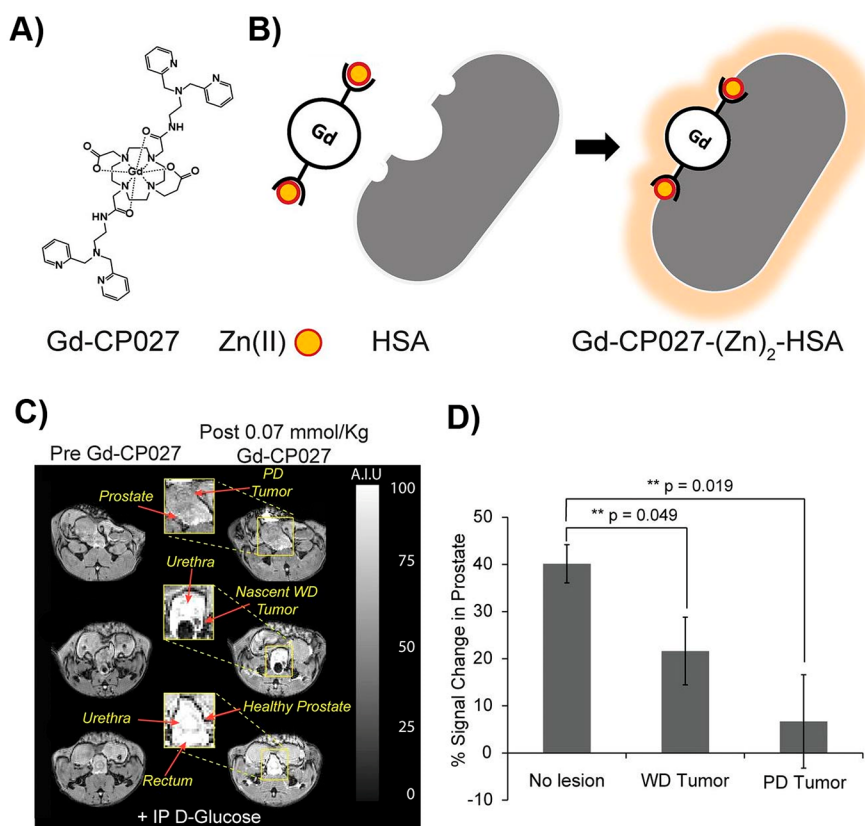
Figure 83. (A) Structure of Gd-CP027; (B) Gd-CP027 binds to Zn(II) and forms a complex with HSA; (C) glucose sensitive contrast enhanced (GSCE) T_1 weighted MR images at 9.4 T of the prostate of mice during various stages of tumor development: (Bottom) image of a normal healthy prostate, (middle) image of malignant prostate with WD tumor shows clear hypointensity due to the presumable lack of intracellular Zn(II), and (top) image of malignant prostate with PD shows no GSCE; and (D) average GSCE measured over the entire prostate of mice (WD tumor = well-differentiated tumors, PD tumor = poorly differentiated tumor). Reproduced from ref 702. Copyright 2016 National Academy of Science.

LipoCEST agents contain a fast-exchanging, paramagnetic Ln(III) shift reagent encapsulated inside a liposome. If the rate of water exchange across the liposomal membrane is slow enough then there will be two water resonances observed in the NMR spectrum: the bulk water outside the liposome and the shifted water inside the liposome. Selective saturation of the intraliposomal resonance generates CEST with high sensitivity due to the large number of water molecules inside the liposome.[293,694] Terreno and co-workers developed a disulfide-based, redox sensitive lipoCEST agent.[695] They attached a Gd-DO3A derivative to the outer surface of the liposome via a disulfide linker (Figure 81). The Gd(III)-modified liposome is CEST silent because of the T_1-shortening effect of the Gd(III), but redox-mediated disulfide reduction results in release of the Gd(III) complexes and restoration of the lipoCEST signal (Figure 81). It is worth noting that the linkage between the Gd(III) complex and the lipoCEST agent

is easily exchangeable, so that these agents could be made sensitive to a variety of other stimuli through sophisticated choice of the biodegradable linker.

Allen and co-workers demonstrated that the Eu(II)/Eu(III) redox switch can be exploited for molecular imaging.[405] The authors encapsulated a Eu(II)-cryptate $(Eu(2.2.2)^{2+})$ in liposomes to form a dual mode contrast agent, which shows T_1 enhancement in the reduced form and also exhibits a CEST effect. Oxidation of divalent $Eu(2.2.2)^{2+}$ to $Eu(2.2.2)^{3+}$ silenced the T_1 enhancement but maintained the CEST effect with similar intensity. Interestingly, the CEST effect was independent from the europium concentration within the liposome, suggesting that the CEST effect is due to the liposome membrane itself rather than the europium compounds within. Detection of both the T_1 enhancement and CEST effect implies that the agent has not responded to an oxidative trigger, but loss of T_1 enhancement indicates
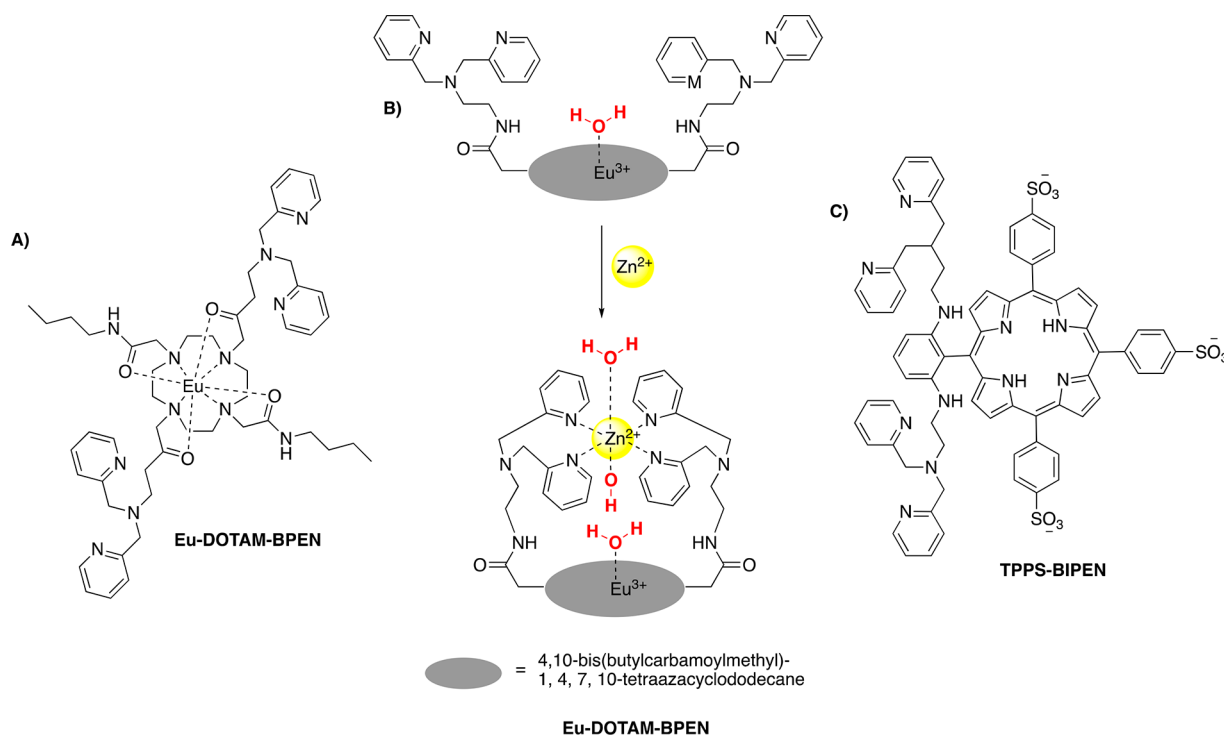
Figure 84. Selected Zn(II) binding MRI contrast agents.[703,704]

irreversible activation by oxidation. The liposomes were kinetically stable for both oxidation states of europium.

Morrow and co-workers reported a triazamacrocyclic cobalt complex with exchangeable protons located on pendant pyrazole groups (Figure 80E).[693] The paramagnetic Co(II) center causes a large shift of these exchangeable protons relative to the water resonance, whereas in the oxidized form with diamagnetic Co(III), these resonances are much closer in frequency to bulk water. The system exhibits a reversible Co(II)/Co(III) redox couple that is tunable over the biologically relevant range from −80 to −280 mV (versus normal hydrogen electrode) by varying the ligand substituents.

6.6. Metal Ion-Responsive Molecular Imaging Agents

Metal ions such as Ca(II), Cu(II), and Zn(II) play an important role in cell signaling. The ability to noninvasively image ion flux would enable studies to elucidate organ function and also to identify pathological states characterized by altered metal ion homeostasis. There are a number of challenges in developing metal ion-responsive contrast agents. In addition to the challenges of sensitivity and appropriate dynamic range that affect all responsive agents, for detecting metal ion flux one requires specificity for the ion of interest and, perhaps more importantly, sufficiently fast reversible binding kinetics to sense metal ion concentration change in real time. For T_1 agents, the strategies of coupling metal binding to modulation of the rotational correlation time or to modulation of the hydration number have been employed. There have also been ion-responsive ParaCEST agents and SPIONs reported in recent years.

6.6.1. Zn(II)-Responsive MR Contrast Agents. The first Zn(II) responsive contrast agents were published by Nagano and co-workers.[696,697] They synthesized a series of Gd-DTPA-bisamide complexes sensitive to Zn(II) ions, and their best candidate is depicted in Figure 82A. In the presence of Zn(II) ions, the authors posit that the chelator undergoes a

geometrical reconfiguration to coordinate Zn(II), which in turn displaces the inner-sphere water molecule. As a consequence, r_1 decreases from 4.8 to 3.4 mM^{-1} s^{-1} after addition of 1 equiv of Zn(II). The binding affinity for Zn(II) was not determined in this study, but notably, this sensor selectively responds to Zn(II) ions over Na(I), K(I), Ca(II), and Mg(II).

Meade and co-workers reported a Gd-DO3A derivative with a pendant iminodiacetate group for zinc binding (Figure 82B).[698,699] Coordination of Zn(II) changes the hydration number for Gd(III) from $q = 0$ to $q = 1$ (i.e., the sensor "turns on" in the presence of zinc with a fairly high r_1 change of 121%). This sensor was selective for Zn(II) over Na(I), K(I), Ca(II), and Mg(II) but also showed some response for Cu(II). In general, it is believed that a simultaneous Cu(II) response does not interfere in in vivo experiments since the Cu(II) concentration is typically much lower in tissue than the Zn(II) concentration. The K_d for Zn(II) is 240 μM, and in vitro MR images showed that zinc concentrations as low as 100 μM could be detected with this agent, which is within the physiologically relevant region. The Zn(II) concentration in vesicles of certain types of glutamatergic neuronal, prostate, and pancreatic cells can reach 300 μM.[571] However, the detection of lower zinc levels in vivo is still desirable.

Esqueda et al. reported the Gd-DOTA-bisamide agent Gd-CP027 that binds up to two equivalents of Zn(II) using pendant N,N-bis(2-pyridyl-methyl) ethylene diamine (BPEN) groups as amide substituents (Figure 83A).[700] In the presence of Zn(II) in a buffer system, Gd-CP027 displays only a modest 20% increase in r_1. However, in the presence of Zn(II) and HSA, a large 165% r_1 change is observed ($r_1 = 6.6$ to 17.4 mM^{-1} s^{-1}). Coordination of Zn(II) to Gd-CP027 enables its binding to a subdomain of HSA, which increases the rotational correlation time of the agent and hence its relaxivity (Figure 83B). In the absence of Zn(II), Gd-CP027 shows no affinity
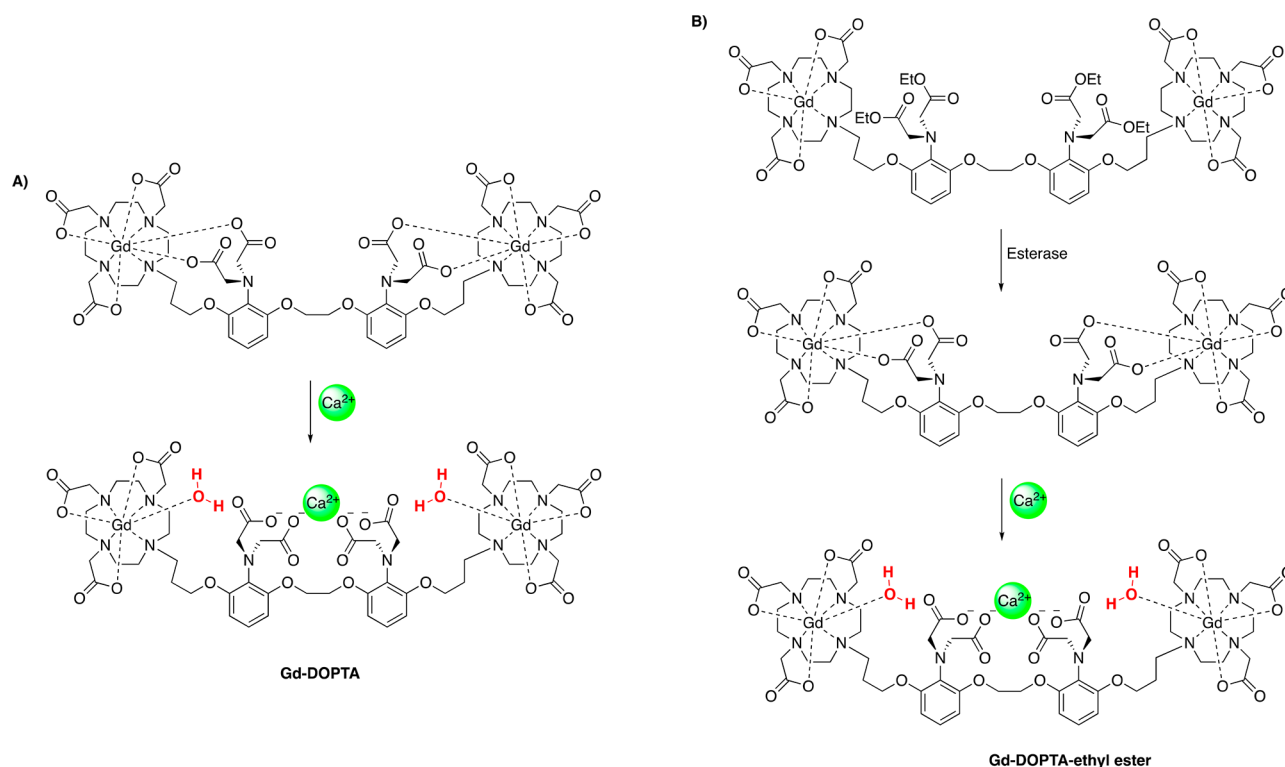
Figure 85. (A) Ca(II)-responsive MRI contrast agent[706,707] and (B) Ca(II)-responsive MRI contrast agent that can discriminate between extra- and intracellular Ca(II) ions.[708]

for HSA. This sensor exhibits sensitivity for Zn(II) ions over Ca(II) and Mg(II) but does respond to Cu(II). The authors demonstrated in in vitro experiments, that in the presence of HSA, zinc concentrations as low as 30 μM could be detected and a remarkably high binding affinity for zinc (K_d = 33.6 nM) was reported. Ultimately, Gd-CP027 was applied in vivo. The authors were able to image the glucose-stimulated Zn(II) secretion in the mouse pancreas or prostate gland.[701,702] The zinc content in prostate cancer tissue is approximately 6-fold decreased in comparison to healthy prostate tissue. Using Gd-CP027, it was feasible to distinguish between healthy and malignant mouse prostate by imaging the differential secretion of Zn(II). As illustrated in Figure 83C, treatment of healthy mice with glucose and Gd-CP027 led to clear contrast enhancement in the healthy mice prostate tissue (bottom). On the other hand, stimulation of prostate tumor-bearing mice with glucose revealed that different stages of tumor development could be discriminated from each other (middle and top) since the zinc concentration decreases with progressing disease.

ParaCEST agents can also be used as Zn(II)-sensitive MR contrast agents. For instance, a Eu-DOTAM derivative equipped with two BPEN units for Zn(II) binding was reported by Sherry and co-workers (Figure 84A).[703] In the absence of Zn(II) ions, the agent shows an intermediate to slow water exchange between the Eu−OH₂ and bulk water molecules. Coordination of Zn(II) ions through the four pendant pyridine units leads to a mononuclear complex close to the europium center. Unexpectedly, the water exchange at the europium center accelerated resulting in disappearance of the CEST signal. The effect was even more dramatic at higher pH (pH 8), suggesting that there is a water ligand also coordinated to Zn(II) that can be partially deprotonated at pH

8 to give Zn−OH. The close proximity of the Zn−OH species to the Eu(III)-bound water molecule is believed to catalyze the prototropic exchange between the Eu(III)-bound water molecule and bulk water (Figure 84B). CEST imaging experiments revealed that the agent is selective for Zn(II) over Ca(II) and Mg(II) ions, and the effective sensitivity range is estimated to be 5 to 120 nM.

Water-soluble Mn(III)-porphyrins were also employed as MRI-based zinc sensors (Figure 84C).[704] Notably, the porphyrin TPPS-BIPEN, Figure 84C, is a fluorescent sensor for Zn(II). When Mn(III) is coordinated by the porphyrin ligand and the complex binds Zn(II), the contrast agent is able to permeate cell membranes making it the first cell permeable MRI sensor for metal ions reported. Due to an unknown mechanism, the T_1 relaxivity decreases from 8.70 to 6.65 mM^{-1} s^{-1} (24%) upon addition of 1 equiv of Zn(II). Interestingly, this trend reverses when the Mn(III)-based agent is treated with Zn(II) ions in a cellular context. Incubation of HEK-293 cells with Mn(III)-porphyrin led to an increase in the T_1 relaxivity in the presence of Zn(II) ions. Additionally, T_2-weighted images of these cells showed also an increase in relaxivity associated with zinc addition. In a follow-up study, the authors reported Zn(II) sensitivity of their contrast agent when it was directly injected into the brain of rats.[705]

6.6.2. Ca(II)-Responsive MR Contrast Agents. Meade and co-workers reported the first Ca(II) ion sensitive contrast agent Gd-DOPTA (Figure 85A).[706,707] Gd-DOPTA consists of two Gd-DO3A units bridged by a modified 1,2-bis(o-aminophenoxy)ethane-N,N,N′,N′-tetraacetic acid (BAPTA) unit, which is known to have specificity for Ca(II) over other metals. In the absence of Ca(II), the anionic carboxylate oxygen donor atoms of the BAPTA unit bind to the

Figure 86. Selected Ca(II) binding MRI contrast agents.[706,707,709,711]

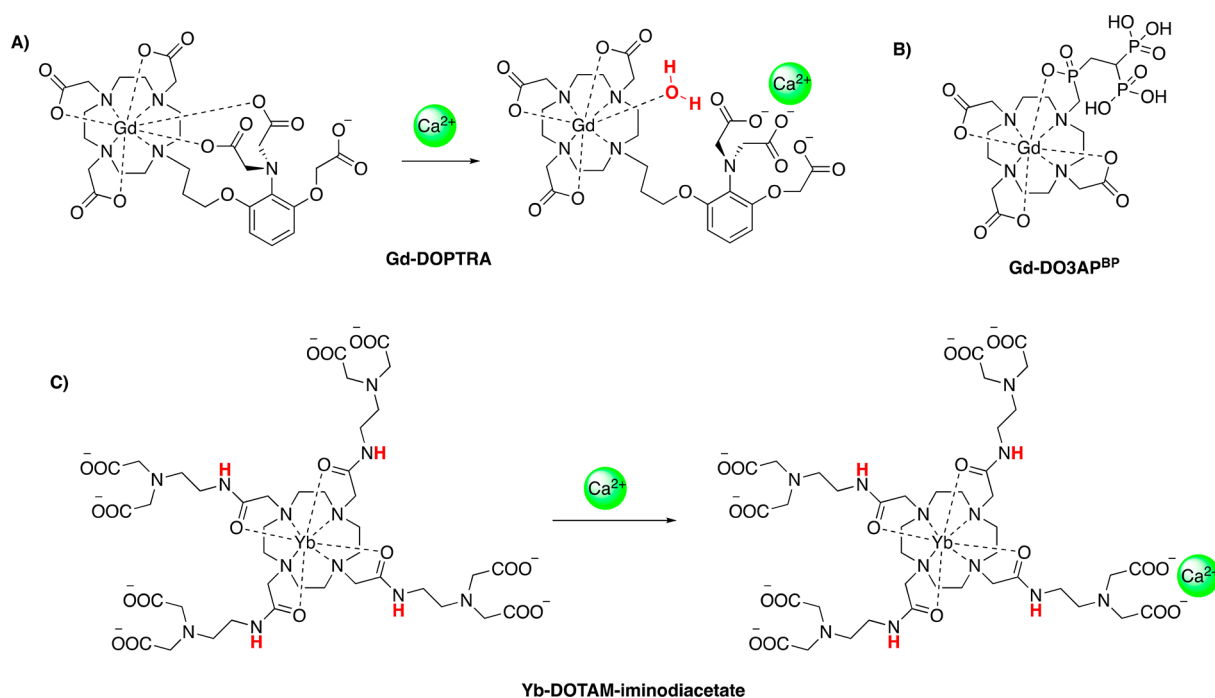gadolinium(III) centers yielding a $q = 0$ complex with $r_1 = 3.26$ mM^{-1} s^{-1}. In the presence of Ca(II), the BAPTA carboxylate groups preferentially coordinate Ca(II), thereby allowing water molecules to coordinate the gadolinium(III) centers, which changes the hydration state per Gd(III) ion from $q = 0$ to $q = 1$. As a result, r_1 increases by 80% to 5.76 mM^{-1} s^{-1}. Gd-DOPTA shows selectivity for Ca(II) over Mg(II) and a binding affinity for calcium of $K_d = 0.96$ μM. In the human body, the intracellular Ca(II) concentration is in the micromolar range while the extracellular Ca(II) concentration is in the millimolar range. Thus, Gd-DOPTA has a MRI response in the intracellular concentration range and a possible application of such an agent is to sense Ca(II) fluctuations in biological settings. This probe was further developed by masking the BAPTA units with ethyl esters to first increase cell labeling and prevent extracellular Ca(II) binding (Figure 85B).[708] Once inside the cell, the ethyl ester groups can be cleaved by the enzyme esterase, thereby unmasking four carboxylates that coordinate to the Gd(III) centers and block access to coordinated water ligands. Subsequent intracellular Ca(II) binding results in an increase in hydration number and facilitates an increase in relaxivity by 66%. This probe design allows for discrimination between extra- and intracellular Ca(II) ions.

Gd-DOPTRA, a Gd(III)-based Ca(II) sensor with the highest "turn-on" response based on a switch in hydration state, was reported by Dhingra et al. (Figure 86A).[709] The agent consists of a Gd-DO3A unit equipped with a pendant calcium-responsive *o*-aminophenol-*N,N,O*-triacetate (APTRA) unit. In the absence of Ca(II)-ions, the APTRA unit can coordinate to the Gd(III) center yielding a $q = 0$ complex. In the presence of Ca(II), the APTRA unit preferably coordinates Ca(II) ions, yielding a $q = 1$ complex resulting in a doubling of r_1 (3.5 to 6.9 mM^{-1} s^{-1}). Gd-DOPTRA shows selectivity for Ca(II) over Mg(II) and Zn(II) and exhibits a binding affinity for calcium in the micromolar range ($K_d = 11$ μM). However, in biological media at 37 °C, r_1 only increased by 25% in the

presence of Ca(II). Presumably, this attenuated response is due to anion binding to the Gd(III) center in the presence of Ca(II) that also blocks water access and dampens r_1.

Kubíček et al. described Gd-DO3AP^{BP}, which is a Gd-DO3A derivative with a pendant biphosphate ligand as a Ca(II) sensor (Figure 86B).[710] Ca(II) binding to the bisphosphonate creates a coordination oligomer that has a slower tumbling rate than the corresponding monomer and, hence, a higher T_1 relaxivity. However, Gd-DO3AP^{BP} is not selective for Ca(II) over Mg(II) or Zn(II). In the presence of ≥3 equiv of either of these ions, r_1 increases by 200 to 500%.

An exemplary ParaCEST agent able to sense Ca(II) is based on a Yb-DOTA-tetraamide chelator with four iminodiacetate arms (Figure 86C).[711] In the absence of Ca(II), a CEST effect is observed for this compound, originating from the slow exchange of the amide protons as well as the Yb−OH$_2$ water ligand. Upon coordination of Ca(II) ions via the pendant iminodiacetate groups, the exchange of the amide protons is slowed down resulting in a marked reduction in the CEST effect. A similar effect is observed in the presence of Mg(II).

Another strategy for sensing Ca(II) ions was proposed by Jasanoff and co-workers.[712,713] These authors developed calmodulin-modified SPIONs for calcium detection using changes in T_2 relaxation. When the calmodulin groups bind Ca(II), this results in an aggregation of the nanoparticles. Particle aggregation is a well-known phenomenon that results in increased r_2. Their best candidate exhibits a r_2 change from 200 to 34 mM^{-1} s^{-1}, which is in a convenient range for intracellular calcium detection (EC$_{50}$ = 1.4 μM). However, the cell membrane impermeability of this agent greatly limits its in vivo application.

Angelovski and co-workers designed a system that combined a change in hydration number with a change in rotational correlation time to amplify Ca(II) sensing.[714] They incorporated an amphiphilic calcium sensor into a liposome bilayer. The sensor consists of a Gd-DO3A chelate coupled to a Ca(II) chelator, which is in turn coupled to a lipophilic alkyl chain
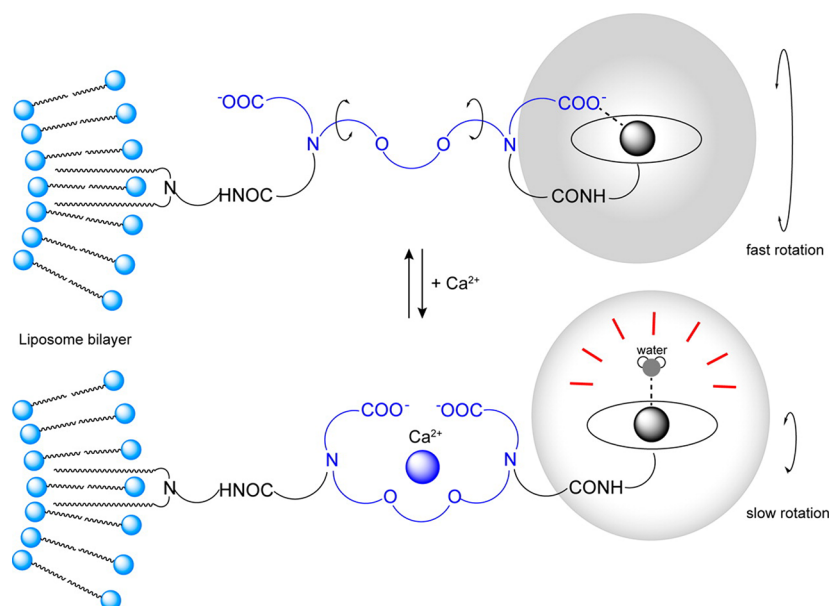
Figure 87. Schematic mechanism that causes the change in T_1 relaxivity in the presence of Ca(II)-ions of a liposomal Ca(II)-responsive Gd(III)-based contrast agent. Reproduced from ref 714. Copyright 2016 American Chemical Society.
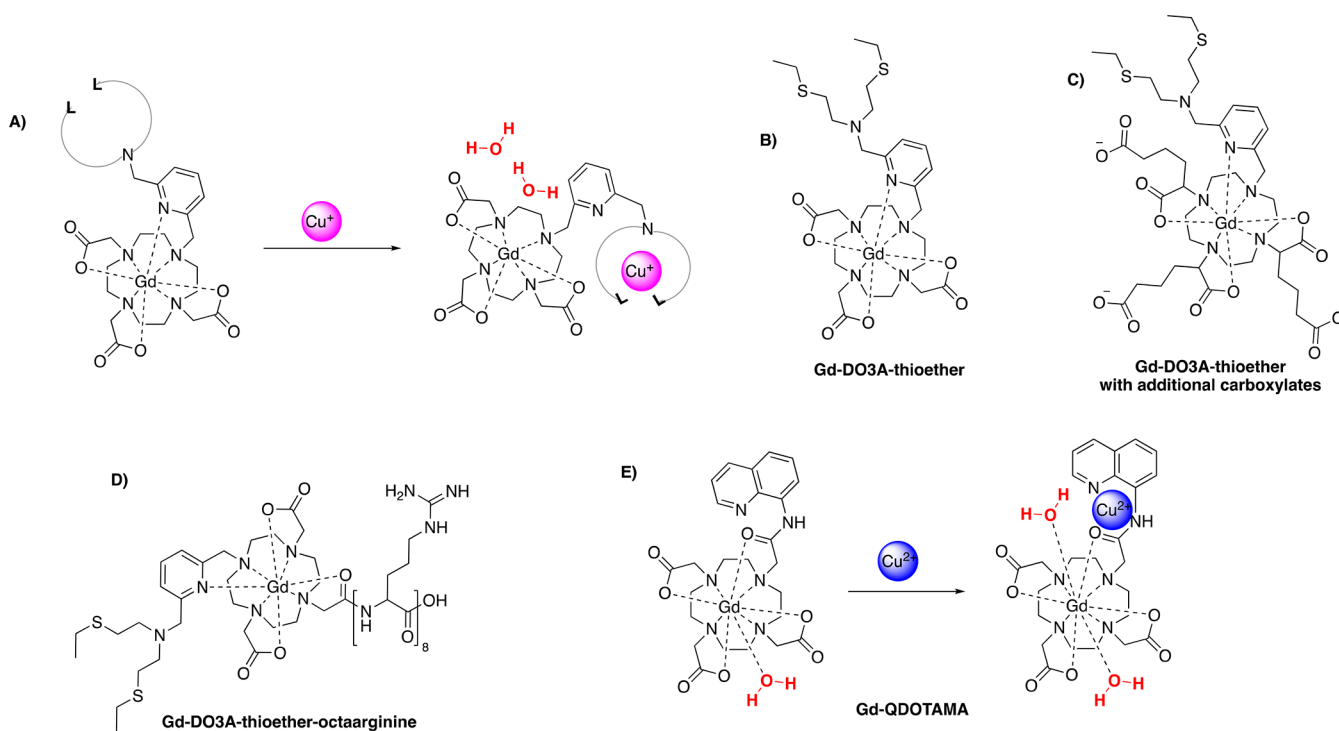
Figure 88. (A) Schematic illustration of a copper binding Gd(III)-based probe that changes its hydration state in the presence of copper ions. (B–E) Selected Cu(I)/Cu(II) binding MRI contrast agents.[716–719]

(Figure 87). The paramagnetic liposome system exhibits r_1 = 7.3 mM^{-1} s^{-1} (15 °C, 20 MHz) in the absence of Ca(II) ions at physiological pH, but after saturation with Ca(II) ions, r_1 increases by a remarkable 400% (r_1 = 38.1 mM^{-1} s^{-1}). This can be explained through additive effects that occur upon Ca(II) binding. Coordination of Ca(II) through the incorporated calcium chelator causes a conformational change within the amphiphilic ligand that, on the one hand, changes the hydration state of the Gd-DO3A unit from $q = 0$ to $q = 1$. At the same time, the fast intramolecular rotation is slowed down, which further enhances r_1 (Figure 87). To the best of

our knowledge, this has been the highest change in T_1 relaxivity for a Ca(II)-responsive Gd(III)-based contrast agent at physiological pH reported so far.

6.6.3. Cu(I)/Cu(II)-Responsive MR contrast agents. Chang and co-workers developed a variety of MRI-based copper(I) sensors.[715,716] The authors utilized Gd-DO3A derivatives coupled to acetate or thioether-rich receptor ligands that are capable of coordinating copper ions. In this molecular framework, the Gd(III) center is shielded from coordinating water molecules in the absence of copper ions. Here a picolyl group coordinates Gd(III) in the absence of

Cu(I) but is displaced by copper binding resulting in coordination of a water ligand to Gd(III) (i.e., the hydration state of the complex changes from $q = 0$ to $q = 1$ or 2) (Figure 88A). For the thioether-tethered Gd-DO3A chelate, that is depicted in Figure 88B, the highest enhancement in r_1 exploiting a hydration state mechanism has been observed after treatment with 1 equiv of Cu(I). The T_1 relaxivity increases by 360% from 1.5 to 6.9 mM^{-1} s^{-1}. Additionally, this sensor shows impressive selectivity for Cu(I) over Na(I), K(I), Ca(II), Mg(II), Fe(II), Fe(III), Cu(II), and Zn(II) and remarkably high affinity for Cu(I) (K_d = 0.26 pM). However, the presence of coordinating anions can compete with the inner-sphere water molecule and affect the relaxivity response to Cu(I) binding. The authors overcame this problem by installation of additional carboxylate groups on the periphery of the molecular scaffold (Figure 88C), a known strategy to reduce the sensitivity to biologically abundant coordinating anions.[717] By maintaining the selectivity and the sensitivity for Cu(I), the relaxivity response to Cu(I) ions was only slightly affected by this modification. In the absence of Cu(I) ions, the contrast agent exhibits a relatively low T_1 relaxivity (2.6 mM^{-1} s^{-1}), whereas addition of Cu(I) triggers a 340% enhancement in r_1 to 11.4 mM^{-1} s^{-1}. As a second modification, the authors conjugated their Cu(I) sensor to an octaarginine peptide (Figure 88D) to enable cellular uptake of the contrast agent.[718] The agent shows a Cu(I)-induced r_1 enhancement of 220% (3.9 to 12.5 mM^{-1} s^{-1}). In vitro experiments demonstrated that this Cu(I) sensor can report on labile copper pools in a disease model where differences in copper accumulation between cells bearing a mutant copper transporter and wildtype cells could be detected.

Chen and co-workers developed Gd-QDOTAMA as a Cu(II) responsive agent that consists of a Gd-DO3A derivative with a pendant quinoline based ligand, chosen to selectively coordinate Cu(II) ions (Figure 88E).[719] Cu(II) coordination provokes a switch in the hydration state of the agent from $q = 1$ to $q = 2$. Upon addition of 1 equiv of Cu(II) ions, r_1 increases from 4.27 to 7.29 mM^{-1} s^{-1} (71%). This agent shows high selectivity for Cu(II) over Na(I), K(I), Ca(II), Mg(II), Fe(II), Fe(III), and Zn(II). The authors estimate the Cu(II) dissociation constant to be K_d = 0.16 nM.

6.7. Other Responsive Molecular Imaging Agents

6.7.1. Neurotransmitter-Responsive MRI Contrast Agents.
Neuroscience, the study of the brain and nervous system, is inspired by the desire to understand the complexity of the brain and behavior. To facilitate its various functions, the brain contains billions of neurons which interact to form circuits and giving rise to a complex network. The major mode for communication between these nerve cells is mediated through chemical neurotransmission.[720,721] Consequently, neuroimaging techniques can provide indispensable insights into the mechanisms of neural functions both in health and disease.[722−724] Such studies may enhance the understanding of physiology and pathophysiology of the brain and, as a consequence, improve the diagnosis and treatment of brain disorders.

Recently, Jasanoff and co-workers developed the first neurotransmitter sensitive MRI contrast agents which are based on advanced molecular engineering techniques (directed evolution[725]) to provide paramagnetic metalloprotein-based molecular MRI probes for neuroimaging.[726,727] In this approach, sophisticated protein engineering gave a para-

magnetic heme iron-containing probe that is selective for the neurotransmitter dopamine. Specific binding of dopamine to a side that is close to the heme iron altered T_1-weighted MRI signals. Using this neurotransmitter sensing technique, the authors were able to quantitatively map neurotransmitter release patterns deep within the living brain.

A crown ether appended Gd(III)-complex capable of sensing amino acid neurotransmitters was reported by Tóth, Angelovski, and co-workers (Figure 89).[728] The complex offers
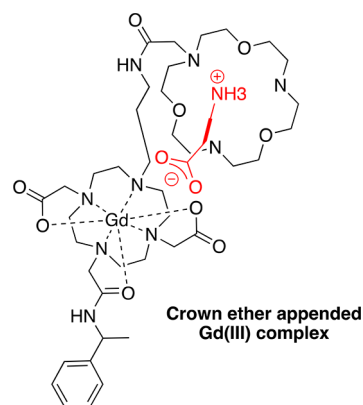
Figure 89. A crown ether appended Gd(III)-complex capable of sensing zwitterionic amino acid neurotransmitters.[728]

ditopic binding for zwitterionic neurotransmitters via interactions (a) between the positively charged and coordinatively unsaturated Gd(III) ion and the carboxylate function and (b) between a pendant triazacrown ether and the amine function of the neurotransmitter. Relaxometric titrations with different neurotransmitters, like γ-aminobutyric acid or glutamate remarkably decreased the T_1 relaxivity of their agent. The T_1 relaxivity change can be attributed to a switch in hydration state from $q = 1.2$ to $q = 0.4$. This complex was successfully employed to monitor neural activity in ex vivo mouse brain slices by MRI.

6.7.2. Temperature-Responsive MRI Contrast Agents.
Recently, noninvasive temperature monitoring with MRI has attracted attention since thermotherapy is rapidly emerging. To this end, Zheng and co-workers developed a thermosensitive microgel based on a manganese porphyrin core incorporated in a cross-linked poly(N-isopropylacrylamide) material (Figure 90).[729] Subtle temperature changes rapidly swell or shrink those microgels (i.e., the volume of the microgel is changed with its lower critical solution temperature) (LCST, 29−33 °C). As the properties of the microgel change, the embedded paramagnetic complexes experience changes in their rotational motion, which in turn influences r_1. Consequently, within a few degrees of temperature variation, an increase in r_1 of 73% could be observed.

Another concept utilizes thermosensitive liposomes that release a Gd-HPDO3A when heated up.[730] As a result, the water-solubility of the Gd(III)-agent is increased, which in turn decreases its T_1 relaxivity.

Since chemical exchange rates are dependent on the temperature, ParaCEST agents have also been used to generate temperature-dependent CEST effects.[605,731−733]

It was also demonstrated that Fe(II) or Co(II)-based ParaSHIFT agents might be promising candidates for MR thermometry applications.[734,735]
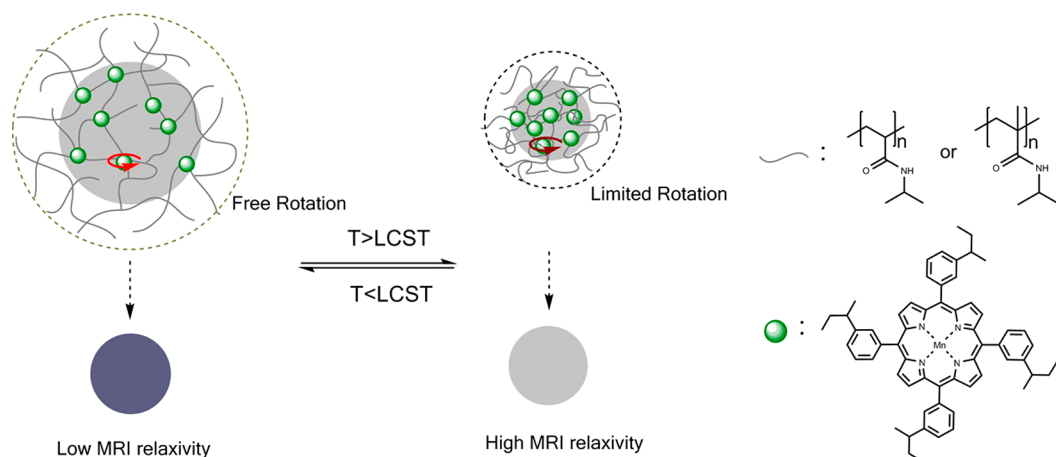
Figure 90. Schematic concept of thermosensitive microgels based on a manganese porphyrin core incorporated in a cross-linked poly(*N*-isopropylacrylamide) material. LCST: lower critical solution temperature 29–33 °C. Reproduced from ref 729. Copyright 2015 American Chemical Society.

6.7.3. Light-Responsive MRI Contrast Agents.

The most prominent example for a light-responsive MRI contrast agent couple is merocyanine-Gd-DO3A/spirooxazine-Gd-DO3A, which is also sensitive to the redox environment and was discussed above (Figure 78A). Following the same mechanism as discussed above, r_1 is decreased after irradiation with visible light at 563 nm and can be increased again by irradiation with UV light, respectively.[670,671]

This concept was further applied for the development of a light-responsive T_2* contrast agent.[736] Louie and co-workers coupled a spyropyran derivative to dextran sulfate coated iron nanoparticles. Light-induced conformational changes of spyropyran between its hydrophopic and hydrophilic isomer led to aggregation or dispersion of the nanoparticles, respectively (Figure 91). Visible light induced aggregation of the particles increased their superparamagnetism and, hence, their T_2* relaxivity.
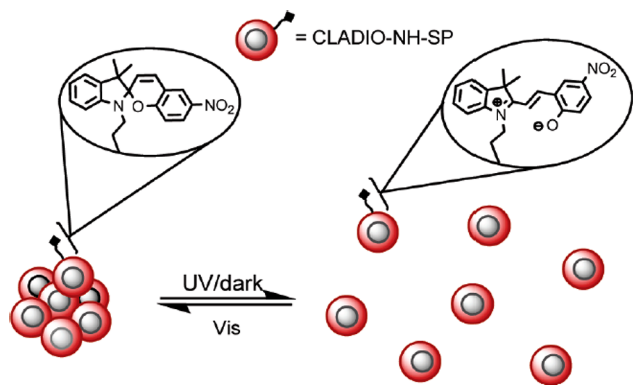
Figure 91. Proposed mechanism of light-induced reversible aggregation of iron oxide nanoparticles coupled to a spyropyran derivative. Reproduced from ref 736. Copyright 2010 American Chemical Society.

6.7.4. DNA-Responsive MRI Contrast Agents.

Detecting specific nucleic acid sequences within the in vitro and in vivo context is extremely challenging using MRI. This is due to the extremely low concentrations of DNA, which is generally far below 1 µM. MRI contrast agents have been designed that are nonspecific to a DNA sequence to be able to track many types of gene delivery systems which can carry a high payload of DNA above the MRI detection threshold. It was shown, that the CEST effect of a polymeric Eu(III)-based ParaCEST agent could be influenced by interaction of the compound with DNA at 1 mM monomer concentration.[737]

In a different approach, magnetite spheres with DNA intercalators were bound to DNA duplexes (0.5 mM base pair concentration) for nucleic acid detection with a T_2* MRI contrast agent.[738] However, the extreme aggregation of the iron oxide nanoparticles reduced the water accessibility and, therefore, the superparamagnetism of the system, so that the expected decrease of T_2* was reversed in this example.

Summaries of the T_1- and CEST activatable probes are listed in Tables 11 and 12, respectively.

7. ACTIVATION AND RETENTION

An effective strategy to overcome major challenges to achieving biochemically targeted or activated MRI contrast is to combine the two approaches. There are multiple advantages to combining activation and retention. For example, off target contrast enhancement can be avoided by developing a nontargeted "pro-agent" that is enzymatically activated to accumulate at a tissue or cell target. Another advantage is that the relatively weak relaxivity changes achieved with most activatable agents can be overcome if the activated agent is accumulated in the aberrant microenvironment after washout of the unactivated agent.

The activation and retention strategy has been applied to image acute inflammation using the myeloperoxidase sensing agent Gd-MPO, comprised of Gd-DTPA with two appended 5-hydroxytryptamines.[739,740] Myeloperoxidase is secreted by activated neutrophils and serves to catalytically amplify the reactivity of reactive oxygen species released during neutrophil burst by converting hydrogen peroxide into electrophilic forms of oxygen such as ferryl heme and hypochlorouos acid. Myeloperoxidase-mediated oxidation of Gd-MPO results in 5-hydroxytryptamine-based radicals that oligomerize to multimeric MPO and form covalent bonds to surface-exposed tyrosines in nearby proteins. Self-oligomerization of Gd-MPO does lead to relaxivity increase at field strengths < 3.0 T but the strong, persistent enhancement that Gd-MPO provides at the inflammatory microenvironment is also due to retention of the oxidized agent. Gd-MPO has been used to image acute

Table 11. Summary of T$_1$-Based Activatable MRI Contrast Agents

responsive MRI probe	stimulus	mechanistic change	r_1 switch (mM^{-1} s^{-1})	% change	ref
Gd-DOTA-4AmP	pH	second sphere effect, τ_m	3.5 to 5.3 (pH 9.5 to 6) at 20 MHz	51% increase	574 and 575
G5-PAMAM dendrimer	pH	second sphere effect, τ_m	10.8 to 24.0 (pH 9.5 to 6) at 20 MHz	122% increase	576
Gd-DOTA-tetramide-hydroxypyridyl	pH	second sphere effect	~5.6 to ~3.1 (pH 8.5 to 6) at 20 MHz	85% decrease	577
Gd-DO3A-sulfonamide	pH	q	~5.4 to 8.0 (pH 7.4 to 6.8) at 65.6 MHz	48% increase	308
Gd-DO3A-p-nitrophenolic arm	pH	q	4.1 to 7.0 (pH 9 to 5) at 20 MHz	71% increase	580
Gd-aminoethyl-DO3A derivatives	pH	q	(pH 9 to 5) at 20 MHz	average: ~100% increase	581 and 582
Gd-DO3A-sulfonamide-Ga-AAZTA	pH	q	3.7 to 10.1 (pH 8.5 to 5) at 20 MHz	150% increase	589
Gd-DO3A-glucuronic acid	β-glucuronidase	q	4.99 to 3.63 (human serum) at 60 MHz	27% decrease	623
Gd-DO3A-ethyl ester	esterase	q	5.7 to 10.5 at 20 MHz	84% increase	624
Gd-DTPA fatty acid complex	lipase	solubilty switch	insoluble active form: 4.7 at 20 MHz	—	625
Gd-DOTA-PEG-peptide	MMP	solubility switch	—	—	626−628
Gd-loaded, protamine-linked liposomes	trypsin	solubilty switch	0.2 to 1.8	800% increase	629
Gd-DTPA with a lysine-masked HSA binding group	TAFI	τ_R	9.8 to 26.5 (37 °C) at 20 MHz	150% increase	630
Gd-DTPA-FPG	β-galactosidase	τ_R	7.6 to 15.5 (37 °C) at 20 MHz	103% increase	631
Gd-DTPA with masked HSA binding group	β-galactosidase	τ_R	3.5 to 5.5 (37 °C) at 20 MHz	57% increase	632
Gd-DTPA-derivative linked to a peptide	legumain	τ_R	27.1 to 73.5 (in cell lysate) at 20 MHz	170% increase	633
Gd-D-DOTA	peroxidase	τ_R	3.75 to 11.5 at 20 MHz	200% increase	635
C-SNAM	caspase-3	τ_R	10.2 to 19.0 at 42.6 MHz	90% increase	640
Mn-polyaminocarboxylates	tyrosinase	L1: release of Mn(II) L3: τ_R	—	—	634
Gd-DO3A-merocyanine	NADH	Q	5.6 to 8.6 at 60 MHz	55% increase	670
Gd-4NO$_2$2MeOSA	hypoxia	q	2.1 to 3.6 at 20 MHz	70% increase	672
Mn(II)-H2qtp1	hydrogen peroxide	q	4.73 to 5.3 at 128 MHz	10% increase	657
Mn(II)-H4qtp2	hydrogen peroxide	q	5.46 to 7.17 at 128 MHz	30% increase	675
Gd-DO3AS-Act	free thiols	q	8.1 to 4.1 at 20 MHz	50% decrease	676
Gd-LC6-SH	free thiols	τ_R	5.3 to 2.33 at 200 MHz	55% decrease	677−679
Gd-SS-liposomes	free thiols/free radicals	τ_R	13.6 to 6.5 s^{-1} mM^{-1} at 20 MHz	50% decrease	681
supramolecular Mn-porphyrine adducts	p(O$_2$)	oxidation	40.8 to 15.2 at 20 MHz	60% decrease	382
Mn-HBET	glutathione/hydrogen peroxide	reduction/oxidation	Mn(II): 2.76 Mn(III): 1.05 at 60 MHz	160% increase/ 60% decrease	686
Mn-JED	L-cysteine/hydrogen peroxide	reduction/oxidation	Mn(II): 3.3 Mn(III): 0.5 at 60 MHz	560% increase/ 80% decrease	689
Gd-DTPA-bisamide derivative	Zn(II)	q	4.8 to 3.4 at 300 MHz	30% decrease	696 and 697
Gd-DO3A-iminodiacetate	Zn(II)	q	2.3−5.1 at 60 MHz	120% increase	698 and 699
Gd-CP027	Zn(II)	τ_R	6.6−17.4 at 23 MHz	165% increase	700
Mn-porphyrin-BPEN	Zn(II)	unknown	8.7 to 6.7 at 200 MHz	24% decrease	704
Gd-DOPTA	Ca(II)	q	3.26−5.76 at 500 MHz	80% increase	706 and 707
Gd-BAPTA-ethyl esters	esterase/Ca(II)	q	7.6 to 12.6 at 60 MHz	66% increase	708
Gd-DOPTRA	Ca(II)	q	3.5 to 6.9 at 400 MHz	97% increase	709
Gd-DO3AP^{BP}	Zn(II), Ca(II), Mg(II)	τ_R	—	200−500% increase	710
Gd(III)-liposomes	Ca(II)	q, τ_R	7.3 to 38.1 at 20 MHz	400% increase	714
Gd-DO3A-thioether	Cu(I)	q	1.5 to 6.9 at 60 MHz	360% increase	715 and 716
Gd-DO3A-thioether-carboxylate	Cu(I)	q	2.6 to 11.4 at 60 MHz	340% increase	717
Gd-DO3A-thioether-octaarginine	Cu(I)	q	3.9 to 12.5 at 60 MHz	220% increase	718
Gd-QDOTAMA	Cu(II)	q	4.3 to 7.3 at 400 MHz	71% increase	719
Gd-DO2A-triazacrown ether	zwitterionic neurotransmitter	q	at 300 MHz	average: 70% decrease	728
Mn-porphyrin microgel	temperature	τ_R	8.4 to 14.5 at 128 MHz	73% increase	729

Table 12. Summary of Activatable CEST Agents

responsive MRI probe	stimulus	ref
dihydrouracil	pH	8
poly-L-lysine	pH	591
iopamidol	pH	449
iopromide	pH	592
iobitridol	pH	590
L-arginine filled liposomes	pH	593
amine-based block copolymers	pH	594
imidazoles	pH	595
Yb-DOTAM-Gly	pH	600
Yb-DOTAM-poly(propylene imine) dendrimers	pH	604
Tm-DOTAM-Gly-Lys	pH	605
Eu-DOTAM-Gly-phenol	pH	606 and 609
Yb-DO3A-oAA	pH	603
Yb-HPDO3A	pH	610
pyridine-Ln-DOTP-butyl (ParaSHIFT)	pH	613
Fe(II)-2-amino-6-picolyl-cyclen	pH	612
DEVD-Tm-DOTA	caspase-3	655
Cbz-GGR-Tm-DOTA	urokinase plasminogen activator	657
Yb-DOTA-β-galactose	β-galactosidase	659
Yb-DO3A-oAA-TML-ester	esterase	661
Yb-DO3A-oAA-TML-Q	DT-diaphorase	661
TM-DO3A-cadaverine	transglutaminase	662
cytosine	cytosine deaminase	663
F5C	cytosine deaminase	663
(LRRASLG)$_8$	protein kinase A	664
(Phe-Arg)-4-amino-2-hydroxybenzoic acid	cathepsin B	665
salicylic acid derivatives	sulfatase or alkaline phosphatase	666 and 667
salicylic acid derivatives	simultaneous detection: esterase and sulfatase	666−668
Yb-DO3A-oAA	NO	691
Eu-DOTAM-N-methylqunolinium	NADH	692
Eu-DOTAM-anthryl	$^1O_2$	201
Eu-DOTAM-nitroxide	hypoxia	184
Gd(III) modified liposomes	reducing environment	695
Eu(2.2.2)-liposomes	oxidation	405
triazamacrocyclic cobalt complex	oxidation/reduction	693
Eu-DOTAM-BPEN	Zn(II)	703
Yb-DOTA-tetraamide-iminodiacetate	Ca(II)/Mg(II)	711
polymeric Eu-DOTAM derivative	DNA	737

cardiovascular inflammation in mouse models of myocardial infarction, stroke, and vasculitis, and in a rabbit model of aneurism.[741−744] Gd-MPO has also been used to image neuroinflammation in a mouse model of multiple sclerosis.[745]

Figure 92 shows Gd-MPO enhanced imaging of myeloperoxidase activity in a mouse model of myocardial infarction. The images in Figure 92 (panels A−C) demonstrates the capability of Gd-MPO to detect differences in myeloperoxidase activity in infarct bearing hearts of wild-type, heterozygous, and homozygous myeloperoxidase knockout mice, respectively. The infarct zone (solid yellow arrows) versus remote myocardium (open yellow block arrows) CNR is correlated tightly with MPO activity, Figure 92D.

The activation and retention strategy was also applied to a EP-2104R-derived agent designed to differentiate active thrombosis from stable clot.[746] The cysteine-disulfide bridge of EP-2104R is key to fibrin affinity, and binding affinity is obviated upon breaking this bridge to form open chain, mixed disulfides. An open chain, mixed disulfide form of EP-2104R was converted back to EP-2104R via action of protein disulfide isomerase (PDI) enzymes which are highly expressed and active on the surface of activated platelets. The mixed disfulfide pro-agent was shown to provide strong enhancement of clotted fibrin in the presence of PDI. No clot enhancement was observed in control samples that did not contain PDI.[746]

Neutrally charged and cell membrane permeant Mn-porphyrin and Mn-PDA agents have been functionalized with acetoxymethyl esters that are cleaved by cytosolic estarases to yield anionic, membrane impermeable carboxylate functionalized complexes.[380,747] These intracellularly activated agents have been considered in cell-labeling applications. For example, the tetra-acetoxymethyl functionalized complex Mn-AMP was used to label mouse embryonic cells. The Mn-AMP-labeled cells remained strongly T1-enhanced as the cells differentiated to cardiomyoctes in vitro.[748] This strategy can ostensibly be extended to image cell populations expressing high levels of myriad other forms of intracellular enzymatic activities.

The activation and retention approach has been applied to develop contrast agents that accumulate in the microenvironments with high activities of matrix metalloprotease (MMP) enzymes.[626−628] These water-soluble agents comprise Gd-DOTA conjugated to PEGylated peptides that are proteolytically cleaved to yield hydrophobic peptides and thus a contrast agent of poor solubility. This approach has been used to image MMP expression in various mouse xenograft models of cancer. For example, an MMP-7 reactive agent was shown to provide strong contrast enhancement of human colon cancer xenografts but strongly attenuated contrast in mice treated
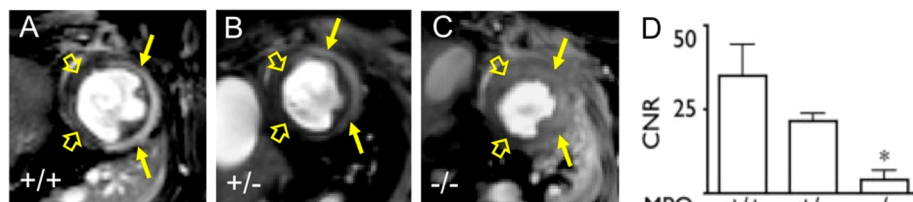
Figure 92. (A−C) T1-weighted images showing short axis views of infarct-bearing hearts of wild-type, heterozygous, and homozygous myeloperoxidase knockout mice, respectively. The myocardial infarction is denoted by the solid yellow arrows, and the remote myocardium is denoted by the open yellow block arrows. (D) Infarct zone vs remote myocardium CNR is tightly correlated to myeloperoxidase activity within the infarction. Reproduced with permission from ref 742. Copyright 2008 Wolters Kluwer Health, Inc.
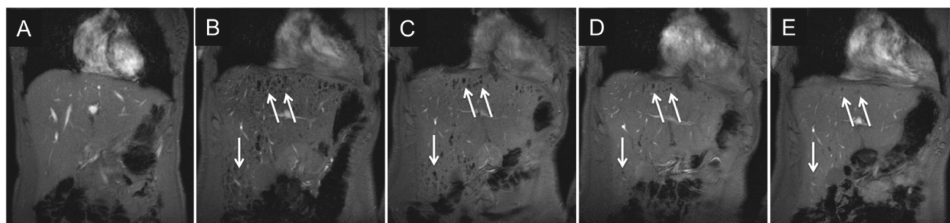
Figure 93. Coronal view of the liver of a Type I diabetes patient receiving implantation of ferucarbotran-labeled pancreatic islets via portal vein injection. (A−E) Images were acquired prior to 1 day, 1 week, 4 weeks, and 28 weeks after transplantation, respectively. The images show that roughly 60% of the engrafted islet do not survive past 1 week after engraftment, but most of the surviving islets persist out past 24 weeks. Reproduced with permission from ref 751. Copyright 2010 Wolters Kluwer Health, Inc.

with MMP inhibitors.[626] In another study, an MMP-2 reactive agent provided strong tumor enhancement in a mouse model of breast cancer.[627] The MMP-2 reactive agent was also capable of differentiating levels of MMP-2 expression between two different mouse models of cancer.[628]

8. CELL TRACKING

A potentially highly impactful application of MRI contrast agents is in cell tracking. Labeling exogenously implanted or endogenously occurring cells with an MRI contrast agent enables noninvasive longitudinal tracking of cell mobility, survival, and differentiation in vivo.

One very promising area for MR cell tracking technology is tracking the fate of implanted cells during transplant or regenerative therapy. For example, ferucarbotran-labeled cells were used to confirm successful transplantation and survival of β-cell containing pancreatic islets in a rat model of Type I diabetes.[749] The islet cells were isolated from healthy rats and were labeled by incubation in ferucarbotran-containing cell culture. The pancreatic islets remained conspicuously hypo-intense for beyond 4 weeks after transplantation. Normal blood sugar levels were obtained in the diabetic rats within 1 week of islet implantation. This technology was extended to clinical trials performed on islet transplantation patients.[750,751] Injection of the contrast agent labeled cells was safe in all patients. Figure 93 shows the liver of a Type I diabetes patient receiving ferucarbotran-labeled pancreatic islet transplant via portal vein injection. Figure 93 (panels A−E) were acquired prior to 1 day, 1 week, 4 weeks, and 28 weeks after transplantation, respectively. The dark spots of signal loss are due to ferucarbotran loaded islets (white arrows). MR cell tracking demonstrates that 60% of the implanted islets do not survive 1 week past engraftment injection, but most of the surviving islets persist out to 24 weeks. The patients in this trial exhibited an increase in C-peptide levels, a biomarker of endogenous insulin production, and 50−80% less insulin was required to achieve near normal blood sugar levels.[751]

Islet transplantation has also been tracked by labeling with perfluorocarbon nanoparticles and F-19 MRI.[752] This direct F-19 detection strategy offers the advantage of quantitative islet tracking with zero background interference.

MR cell tracking is also used to image the homing of immune cells in immunotherapy. In a clinical trial of autologous dendritic cell therapy, immature dendritic cells isolated from the blood were labeled with ferumoxides.[753] Immature dendritic cells are phagocytic and readily internalized the SPIONs. The ferumoxide-labeled dendritic cells were injected into a lymph node and migration to, and accumulation in other lymph nodes was tracked by MRI. MR tracking of the dendritic cells enabled retrospective identification of false

negatives in the clinical trial due to a high rate of mis-injection during intranodular implantation.[753] Immunotherapy cell tracking has also been performed used F-19 MRI. In a clinical trial of stage 4 colorectal cancer immunotherapy, dendritic cells isolated from the patient were combined with lysate of a surgically resected piece of the tumor in order to induce presentation of tumor specific antigens and incubated with perfuorocabon nanoparticles. The F-19 labeled cells were administered intradermally and diminishment of the F-19 signal, due either to cell migration or to cell death and dispersion of the F-19 nanoparticles, was monitored over the course of 24 h.[10]

Immune cells can also be labeled in vivo via a technique called magneto-transfection. Here, vaccine-contrast agent conjugates are injected, which enables visualization of adaptive immune system activation. The process by which antigen-presenting dendritic cells localize in lymph nodes and initiate immune response has been monitored using MRI in a tumor vaccine mouse model following injection of a SPION labeled vaccine.[754]

There are a number of examples where MR cell tracking has been used to monitor the fate of stem cells during cell therapy. In a clinical trial of nerve regeneration in patients suffering traumatic brain injury, autologous neural stem cells isolated from surgically excised tissue where labeled with ferumoxides and reinjected adjacent to the injury and cell migration to the injured tissue was monitored over the course of 3 weeks.[755] In another clinical study, autologous CD34+ marrow stem cells were labeled with magnetic beads. Labeling was achieved by conjugating the magnetic beads to antibodies specific to CD34 antigen. The labeled stem cells were injected intrathecally, and cell migration and accumulation within the lesion was observed over the course of 24 weeks.[756] Cells have also been tracked via labeling with CEST contrast agents. Immortalized mouse skeletal myoblasts were labeled with Eu-HP-DO3A via hypertonic swelling of the cells and used for imaging in a mouse model of cardiac cell therapy.[757] The Eu-HP-DO3A labeled cells implanted in the wall of the left ventricle of the heart provided over 30-fold greater MTR_{asym} than surrounding tissue or unlabeled cells immediately after injection. Cell survival and cell rejection were modeled by implanting cells in both syngeneic and allogeneic mouse models. In the syngeneic mice, the cells provided strong CEST contrast out to 20 days past injection, whereas the cells were rejected and no contrast was observed within 20 days of implantation in the allogenic mice.

Cell tracking has also been used to monitor the dynamics of acute inflammation following tissue injury. The time course of monocyte infiltration into the site of myocardial infarction was visualized using T_1-weighted MRI following injection of Gd-
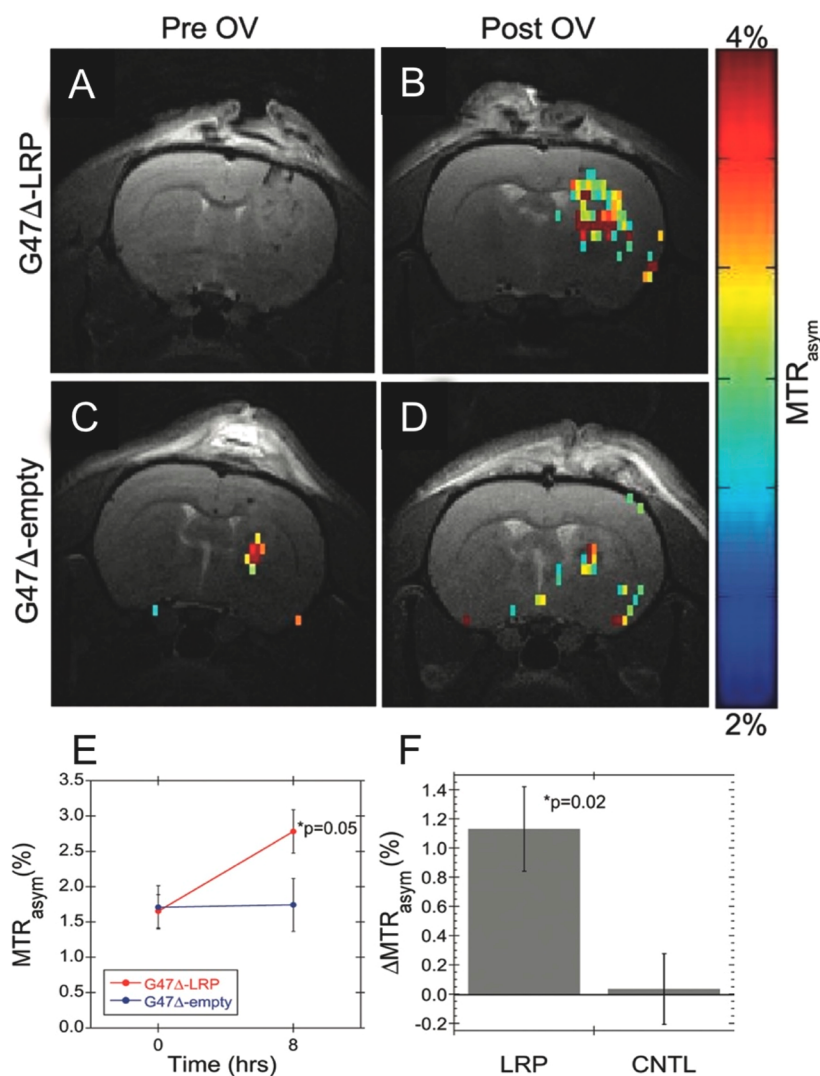
Figure 94. CEST MTR$_{assym}$ maps overlaid with T_2-weighted images of glioma bearing rat brain prior to and 8 h after injection of G47Δ carrying the LRP reporter and LRP empty control virus. (A and B) Images recorded prior to and 8 h after direct intratumoral injection of G47Δ carrying the LRP reporter. (C and D) Images recorded prior to and 8 h after direct intratumoral injection of LRP empty G47Δ. (E) Comparison of MTR$_{assym}$ prior to and 8 h after treatment with virus carrying the LRP reporter gene and LRP empty control. (F) Comparison of ΔMTR$_{assym}$ observed 8 h after treatment with a virus carrying the LRP reporter gene and LRP empty control. Reproduced with permission from ref 761. Copyright 2015 Radiological Society of North America (RSNA).

DTPA loaded liposomes.[554] Here, monocyte labeling was performed in vivo by exploiting the phagocytic nature of monocytes. The time course of R1 enhancement in the infarcted myocardium correlated strongly with ex vivo histologic measures of monocyte infiltration. A similar approach was taken to image monocyte infiltration into tumors in a mouse model using F-19 perfluorocarbon nanoparticles.[758] Here too, the particles were administered intravenously and accumulated in monocytes by endogenous mechanisms. Tumor F-19 signal intensity correlated with histological counting of monocytes. In another study, analogously labeled F-19 monocytes were also used to image inflammation in a rat model of multiple sclerosis.[759] The F-19 signal was used to quantitatively differentiate relative macrophage burden on the spinal cord of MS rats, MS rats receiving daily prophylactic cyclophosphamide treatment (an immunosuppressant), and healthy control rats.

Cells can also be engineered to express reporter genes that provide endogenous MRI contrast. In one proof of concept

study, mice were treated intranasally with adenoviral vector to deliver a reporter gene that results in expression of a ferritin protein engineered to localize in the cytoplasm.[760] Intranasal administration of the reporter gene carrying viral vector resulted in strong T_1-contrast of epithelial olfactory neurons. No contrast enhancement was observed upon treatment with the same vector carrying only a green fluorescent protein reporter gene. In another study, the oncovirus G47Δ, which is currently being evaluated in humans for treatment of progressive glioblastoma, was engineered to carry a lysine-rich protein (LRP) CEST reporter and oncovirus transduction was imaged in a rat model of glioma.[761] Figure 94 (panels A–D) shows CEST MTR$_{assym}$ maps overlaid with T_2-weighted images of the glioma-bearing brain prior to and 8 h after intratumoral injection G47Δ carrying the LRP reporter and LRP empty control virus. A >1% increase in magnetization MTR$_{assym}$ was observed within 8 h, whereas no change in CEST contrast was observed after injection of a LRP-empty control, Figure 94 (panels E and F). LRP expression did not

demonstrate any measurable effect on the efficacy of the oncolytic viral therapy.

There are also reporter genes that do not provide contrast but can lead to expression of receptors that can concentrate exogenously administered contrast agents within the cell or amplify the signal by reaction with activatable MRI contrast agents. Some of these strategies have been described in previous sections. For example, the OATP-seeking agent, Gd-EOB-DTPA, has been used to track the fate of OATP expressing cells in vivo.[526] Transduction of the lacZ operon was confirmed using the β-galactosidase-activated contrast agent.[566] The divalent metal ion transporter (DMT1), which accumulates Mn(II) with high affinity has been used as an MR gene reporter.[762] The DMT1 DNA construct was cloned into a viral vector for transduction into murine glioma cells and intracranially implanted into mice. The resultant DMT1 positive tumors were strongly enhanced in a T_1-weighted scan 24 h after $MnCl_2$ injection, whereas DMT negative control tumors were not T_1 enhanced.

9. CONCLUSIONS

The progress in MRI contrast agents has been mixed. When one of us cowrote a review on the topic in 1999, there had been several contrast agents approved for use in the preceding decade and there were a number of new agents in clinical development. However, in the intervening time very few new agents were approved and many products, like the iron oxide nanoparticles, have been discontinued because of low utilization rates. The lack of a commercially successful new contrast agent has had a chilling effect on the clinical development of new agents. Private investors are reluctant to spend tens of millions of dollars to fund the clinical development of new imaging agents unless they believe that future sales of the agent will be a multiple of that investment. A successful new contrast agent must address a large market size and deliver useful diagnostic information that justifies the cost of the contrast agent and the imaging procedure. A further barrier to commercialization is the difficulty in obtaining proof of concept data in humans. Unlike diagnostic radiopharmaceuticals which are given at microscopic doses, contrast agents are administered in gram quantities necessitating kilo manufacturing and rigorous preclinical safety studies before clinical trials can commence. Together this represents a few million dollars of investment before human studies can begin.

On the other hand, the need for specific molecular information is growing. We are entering into a new era of precision medicine where treatments are tailored to the individual. New powerful, but expensive, therapies are being developed, but many of these therapies are only effective in a subset of patients. Increasingly, noninvasive methods like imaging are being sought to stratify patients to therapies that will benefit them and avoid ineffective and/or costly treatments. In 1999, we reported the first examples of activatable and targeted probes, but now there are numerous examples some of which are well-validated in animal models. Some of the targeted or activatable probes described here may find utility in the context of precision medicine.

Fifteen years ago the safety of the commercial gadolinium-(III) chelates was almost unquestioned. But the advent of NSF and brain deposition has led to increased regulatory scrutiny. We believe that there is a strong need for improved contrast agents that are less retained, provide higher signal, and/or are more specific. It will be interesting to watch this field continue

to evolve as chemists, biologists, physicists, engineers, and physicians continue to innovate.

AUTHOR INFORMATION

Corresponding Author

*E-mail: caravan@nmr.mgh.harvard.edu.

ORCID

Eric M. Gale: 0000-0003-4567-1126
Peter Caravan: 0000-0002-3179-6537

Author Contributions

†J.W. and E.M.G. contributed equally.

Notes

The authors declare the following competing financial interest(s): P.C. and E.M.G. are co-founders of, and hold equity in Reveal Pharmaceuticals which is developing a Mn-based MRI contrast agent. P.C. is a co-founder and holds equity in Collagen Medical LLC and Factor 1A LLC which are pursuing development of collagen-targeted and fibrin-targeted imaging probes. E.M.G. receives consulting income from Collagen Medical. P.C. has received consulting income from Collagen Medical, Guerbet, and Bayer in the last two years. P.C. has research funding from Pfizer, Pliant Therapeutics, and Indalo Therapeutics.

Biographies

Jessica Wahsner is a postdoctoral fellow at the A. A. Martinos Center for Biomedical Imaging, Massachusetts General Hospital and Harvard Medical School. She received both her M.Sc. (2011) and Ph.D. (2015) in chemistry at the Ruhr-University Bochum, Germany, under the mentorship of Prof. Michael Seitz. Receiving a fellowship by the German Research Foundation (DFG), she started her current position as part of Prof. Peter Caravan's group in 2016. Her research interests primarily focus on the development of small molecule PET probes for the molecular imaging of fibrotic disease and of bimodal PET-MR agents for quantitative pH imaging.

Eric M. Gale is an Assistant Professor in Radiology at the A. A. Martinos Center for Biomedical Imaging, Massachusetts General Hospital and Harvard Medical School. He received his B.A. in Chemistry from Rutgers University in 2006 and his Ph.D. in chemistry from the University of Georgia under the mentorship of Todd Harrop, where he synthesized and studied the reactivity of Ni complexes that model the nickel superoxide dismutase active site. He received his postdoctoral training under the mentorship of Peter Caravan between 2012 and 2015, where he primarily focused on studying the chemistry of Mn complexes in the context of MRI. He joined the faculty in 2015. His current research interests center around developing Gd-free alternatives for commercially available contrast agents and on developing redox active transition metal complexes for molecular MR imaging. He is a cofounder of Reveal Pharmaceuticals.

Aurora Rodriguez-Rodriguez was a postdoctoral researcher for two years (2016−2017) at the Athinoula A. Martinos Center for Biomedical Imaging at the Massachusetts General Hospital and Harvard Medical School, working in the group of Prof. Peter Caravan. She received her Bachelor's Degree in Chemistry (2008), her Master's Degree in Environmental and Fundamental Chemistry (2009), and her Ph.D. in Chemistry (2014) from the University of A Coruña (Spain), under the supervision of Prof. María Teresa Rodríguez Blas and Dr. Carlos Platas Iglesias. She was awarded a 12 month postdoctoral fellowship from the Conseil Général du Finistère 29

(France) in 2014 to work in the group ChASaM at the University of Brittany (France) under the mentorship of Prof. Raphaël Tripier and Dr. Véronique Patinec. Her research is focused on the design, synthesis, characterization, and application of new contrast agents for molecular imaging.

Peter Caravan is a native of Bay Roberts, Newfoundland, Canada. He received a B.Sc.(Hons) from Acadia University in Nova Scotia and a Ph.D. in Inorganic Chemistry at the University of British Columbia, where he was a National Sciences and Engineering Research Council (NSERC) postgraduate scholar, under the mentorship of Professor Chris Orvig. He was a NSERC postdoctoral fellow at the Université de Lausanne, Switzerland, where we worked with Professor André Merbach. He then joined Epix Pharmaceuticals in Cambridge, MA, where he worked on the development of targeted MRI contrast agents, including the FDA-approved blood pool agent gadofosveset (MS-325). In 2007, he was recruited to establish a translational molecular imaging lab at the A. A. Martinos Center for Biomedical Imaging at Massachusetts General Hospital and Harvard Medical School. In 2014, he was appointed Co-Director of the Institute for Innovation in Imaging (I3) which focuses on the clinical translation and commercialization of new radiological technologies, including contrast agents. He is a National Institutes of Health funded researcher with a focus on development, application, and clinical translation of novel molecular MRI and PET probes.

REFERENCES

(1) Runge, V. M. Critical Questions Regarding Gadolinium Deposition in the Brain and Body after Injections of the Gadolinium-Based Contrast Agents, Safety, and Clinical Recommendations in Consideration of the EMA's Pharmacovigilance and Risk Assessment Committee Recommendation for Suspension of the Marketing Authorizations for 4 Linear Agents. *Invest. Radiol.* **2017**, *52*, 317−323.

(2) Caravan, P.; Ellison, J. J.; McMurry, T. J.; Lauffer, R. B. Gadolinium(III) Chelates as MRI Contrast Agents: Structure, Dynamics, and Applications. *Chem. Rev.* **1999**, *99*, 2293−2352.

(3) Edelman, R. R.; Hesselink, J. R.; Zlatkin, M. B.; Crues, J. V. *III Clinical Magnetic Resonance Imaging*; Elsevier Health: St. Louis, 2006; Vol. 3.

(4) Prince, M. R.; Zhang, H. L.; Zou, Z. T.; Staron, R. B.; Brill, P. W. Incidence of Immediate Gadolinium Contrast Media Reactions. *AJR, Am. J. Roentgenol.* **2011**, *196*, W138−W143.

(5) Grobner, T. Gadolinium − A Specific Trigger for the Development of Nephrogenic Fibrosing Dermopathy and Nephrogenic Systemic Fibrosis? *Nephrol., Dial., Transplant.* **2006**, *21*, 1104−1108.

(6) Marckmann, P.; Skov, L.; Rossen, K.; Dupont, A.; Damholt, M. B.; Heaf, J. G.; Thomsen, H. S. Nephrogenic Systemic Fibrosis: Suspected Causative Role of Gadodiamide Used for Contrast-Enhanced Magnetic Resonance Imaging. *J. Am. Soc. Nephrol.* **2006**, *17*, 2359−2362.

(7) Kanda, T.; Fukusato, T.; Matsuda, M.; Toyoda, K.; Oba, H.; Kotoku, J.; Haruyama, T.; Kitajima, K.; Furui, S. Gadolinium-Based Contrast Agent Accumulates in the Brain Even in Subjects Without Severe Renal Dysfunction: Evaluation of Autopsy Brain Specimens with Inductively Coupled Plasma Mass Spectroscopy. *Radiology* **2015**, *276*, 228−232.

(8) Ward, K. M.; Balaban, R. S. Determination of pH Using Water Protons and Chemical Exchange Dependent Saturation Transfer (CEST). *Magn. Reson. Med.* **2000**, *44*, 799−802.

(9) Nelson, S. J.; Kurhanewicz, J.; Vigneron, D. B.; Larson, P. E. Z.; Harzstark, A. L.; Ferrone, M.; van Criekinge, M.; Chang, J. W.; Bok, R.; Park, I., et al. Metabolic Imaging of Patients with Prostate Cancer Using Hyperpolarized [13C]pyruvate. *Sci. Transl. Med.* **2013**, *5*, 198ra108 .

(10) Ahrens, E. T.; Helfer, B. M.; O'Hanlon, C. F.; Schirda, C. Clinical Cell Therapy Imaging Using a Perfluorocarbon Tracer and Fluorine-19 MRI. *Magn. Reson. Med.* **2014**, *72*, 1696−1701.

(11) Lohrke, J.; Frenzel, T.; Endrikat, J.; Alves, F. C.; Grist, T. M.; Law, M.; Lee, J. M.; Leiner, T.; Li, K. C.; Nikolaou, K.; et al. 25 Years of Contrast-Enhanced MRI: Developments, Current Challenges and Future Perspectives. *Adv. Ther.* **2016**, *33*, 1−28.

(12) Wang, Y.; Spiller, M.; Caravan, P. Evidence for Weak Protein Binding of Commercial Extracellular Gadolinium Contrast Agents. *Magn. Reson. Med.* **2010**, *63*, 609−616.

(13) FDA (Food and Drug administration). Medical Imaging Drugs Advisory Commitee: Gadolinium Retention after Gadolinium Based Contrast Magnetic Resonance Imaging in Patients with Normal Renal Function (September 2017). https://www.fda.gov/downloads/AdvisoryCommittees/CommitteesMeetingMaterials/Drugs/MedicalImagingDrugsAdvisoryCommittee/UCM572848.pdf (accessed on April 6, 2018).

(14) Runge, V. M. A. Comparison of Two MR Hepatobiliary Gadolinium Chelates: Gd-BOPTA and Gd-EOB-DTPA. *J. Comput. Assist. Tomo.* **1998**, *22*, 643−650.

(15) Aime, S.; Caravan, P. Biodistribution of Gadolinium-Based Contrast Agents, Including Gadolinium Deposition. *J. Magn. Reson. Imaging* **2009**, *30*, 1259−1267.

(16) Lauffer, R. B.; Parmelee, D. J.; Dunham, S. U.; Ouellet, H. S.; Dolan, R. P.; Witte, S.; McMurry, T. J.; Walovitch, R. C. MS-325: Albumin-Targeted Contrast Agent for MR Angiography. *Radiology* **1998**, *207*, 529−538.

(17) Caravan, P.; Cloutier, N. J.; Greenfield, M. T.; McDermid, S. A.; Dunham, S. U.; Bulte, J. W. M.; Amedio, J. C.; Looby, R. J.; Supkowski, R. M.; Horrocks, W. D.; et al. The Interaction of MS-325 with Human Serum Albumin and Its Effect on Proton Relaxation Rates. *J. Am. Chem. Soc.* **2002**, *124*, 3152−3162.

(18) Eldredge, H. B.; Spiller, M.; Chasse, J. M.; Greenwood, M. T.; Caravan, P. Species Dependence on Plasma Protein Binding and Relaxivity of the Gadolinium-Based MRI Contrast Agent MS-325. *Invest. Radiol.* **2006**, *41*, 229−243.

(19) Oliveira, I. S.; Hedgire, S. S.; Li, W.; Ganguli, S.; Prabhakar, A. M. Blood Pool Contrast Agents for Venous Magnetic Resonance Imaging. *Cardiovasc. Diagn. Ther.* **2016**, *6*, 508−518.

(20) Goyen, M. Gadofosveset-Enhanced Magnetic Resonance Angiography. *Vasc. Health Risk Manag.* **2008**, *4*, 1−9.

(21) Goyen, M.; Edelman, M.; Perreault, P.; O'Riordan, E.; Bertoni, H.; Taylor, J.; Siragusa, D.; Sharafuddin, M.; Emile, R.; Mohler, I.; Breger, R.; et al. MR Angiography of Aortoiliac Occlusive Disease: A Phase III Study of the Safety and Effectiveness of the Blood-Pool Contrast Agent MS-325. *Radiology* **2005**, *236*, 825−833.

(22) Paetsch, I.; Huber, M. E.; Bornstedt, A.; Schnackenburg, B.; Boesiger, P.; Stuber, M.; Fleck, E.; Cavagna, F.; Nagel, E. Improved Three-Dimensional Free-Breathing Coronary Magnetic Resonance

Angiography Using Gadocoletic Acid (B-22956) for Intravascular Contrast Enhancement. *J. Magn. Reson. Imaging* **2004**, *20*, 288−293.

(23) Cavagna, F. M.; Lorusso, V.; Anelli, P. L.; Maggioni, F.; de Haen, C. Preclinical Profile and Clinical Potential of Gadocoletic Acid Trisodium Salt (B22956/1), A New Intravascular Contrast Medium for MRI. *Acad. Radiol.* **2002**, *9*, 491−494.

(24) La Noce, A.; Stoelben, S.; Scheffler, K.; Hennig, J.; Lenz, H. M.; La Ferla, R.; Lorusso, V.; Maggioni, F.; Cavagna, F. B22956/1, A New Intravascular Contrast Agent for MRI: First Administration to Humans - Preliminary Results. *Acad. Radiol.* **2002**, *9*, 404−406.

(25) Preda, A.; Novikov, V.; Moglich, M.; Turetschek, K.; Shames, D. M.; Brasch, R. C.; Cavagna, F. M.; Roberts, T. P. L. MRI Monitoring of Avastin (TM) Antiangiogenesis Therapy Using B22956/1, A New Blood Pool Contrast Agent, in an Experimental Model of Human Cancer. *J. Magn. Reson. Imaging* **2004**, *20*, 865−873.

(26) de Haen, C.; Anelli, P. L.; Lorusso, V.; Morisetti, A.; Maggioni, F.; Zheng, J.; Uggeri, F.; Cavagna, F. M. Gadocoletic Acid Trisodium Salt (B22956/1) - A New Blood Pool Magnetic Resonance Contrast Agent with Application in Coronary Angiography. *Invest. Radiol.* **2006**, *41*, 279−291.

(27) Jaspers, K.; Versluis, B.; Leiner, T.; Dijkstra, P.; Oostendorp, M.; van Golde, J. M.; Post, M. J.; Backes, W. H. MR Angiography of Collateral Arteries in a Hind Limb Ischemia Model: Comparison between Blood Pool Agent Gadomer and Small Contrast Agent Gd-DTPA. *PLoS One* **2011**, *6*, e16159 .

(28) Stiriba, S. E.; Frey, H.; Haag, R. Dendritic Polymers in Biomedical Applications: From Potential to Clinical Use in Diagnostics and Therapy. *Angew. Chem., Int. Ed.* **2002**, *41*, 1329−1334.

(29) Herborn, C. U.; Barkhausen, J.; Paetsch, I.; Hunold, P.; Mahler, M.; Shamsi, K.; Nagel, E. Coronary Arteries: Contrast-Enhanced MR Imaging with SH L 643A—Experience in 12 Volunteers. *Radiology* **2003**, *229*, 217−223.

(30) Herborn, C. U.; Schmidt, M.; Bruder, O.; Nagel, E.; Shamsi, K.; Barkhausen, J. MR Coronary Angiography with SH L 643 A: Initial Experience in Patients with Coronary Artery Disease. *Radiology* **2004**, *233*, 567−573.

(31) Port, M.; Corot, C.; Rousseaux, O.; Raynal, I.; Devoldere, L.; Idée, J.-M.; Dencausse, A.; Greneur, S. L.; Simonot, C.; Meyer, D. P792: A Rapid Clearance Blood Pool Agent for Magnetic Resonance Imaging: Preliminary Results. *Magn. Reson. Mater. Phys.* **2001**, *12*, 121−127.

(32) Port, M.; Corot, C.; Raynal, I.; Idee, J.-M.; Dencausse, A.; Lancelot, E.; Meyer, D.; Bonnemain, B.; Lautrou, J. Physicochemical and Biological Evaluation of P792, a Rapid-Clearance Blood-Pool Agent for Magnetic Resonance Imaging. *Invest. Radiol.* **2001**, *36*, 445−454.

(33) Elst, L. V.; Raynal, I.; Port, M.; Tisnès, P.; Muller, R. N. In vitro Relaxometric and Luminescence Characterization of P792 (Gadomelitol, Vistarem®), an Efficient and Rapid Clearance Blood Pool MRI Contrast Agent. *Eur. J. Inorg. Chem.* **2005**, *2005*, 1142−1148.

(34) Gaillard, S.; Kubiak, C.; Stolz, C.; Bonnemain, B.; Chassard, D. Safety and Pharmacokinetics of P792, a New Blood-Pool Agent: Results of Clinical Testing in Nonpatient Volunteers. *Invest. Radiol.* **2002**, *37*, 161−166.

(35) Klein, C.; Nagel, E.; Schnackenburg, B.; Bornstedt, A.; Schalla, S.; Hoffmann, V.; Lehning, A.; Fleck, E. The Intravascular Contrast Agent Clariscan (NC 100150 injection) for 3D MR Coronary Angiography in Patients with Coronary Artery Disease. *Magn. Reson. Mater. Phys.* **2000**, *11*, 65−67.

(36) Kellar, K. E.; Fujii, D. K.; Gunther, W. H. H.; Briley-Sæbø, K.; Bjørnerud, A.; Spiller, M.; Koenig, S. H. NC100150 Injection, A Preparation of Optimized Iron Oxide Nanoparticles for Positive-Contrast MR Angiography. *J. Magn. Reson. Imaging* **2000**, *11*, 488−494.

(37) Wagner, S.; Schnorr, J.; Pilgrimm, H.; Hamm, B.; Taupitz, M. Monomer-Coated Very Small Superparamagnetic Iron Oxide Particles as Contrast Medium for Magnetic Resonance Imaging: Preclinical In Vivo Characterization. *Invest. Radiol.* **2002**, *37*, 167−177.

(38) Wagner, M.; Wagner, S.; Schnorr, J.; Schellenberger, E.; Kivelitz, D.; Krug, L.; Dewey, M.; Laule, M.; Hamm, B.; Taupitz, M. Coronary MR Angiography Using Citrate-Coated Very Small Superparamagnetic Iron Oxide Particles as Blood-Pool Contrast Agent: Initial Experience in Humans. *J. Magn. Reson. Imaging* **2011**, *34*, 816−823.

(39) Jung, C. W.; Jacobs, P. Physical and Chemical Properties of Superparamagnetic Iron Oxide MR Contrast Agents: Ferumoxides, Ferumoxtran, Ferumoxsil. *Magn. Reson. Magn. Reson. Imaging* **1995**, *13*, 661−674.

(40) Weissleder, R.; Elizondo, G.; Wittenberg, J.; Rabito, C. A.; Bengele, H. H.; Josephson, L. Ultrasmall Superparamagnetic Iron Oxide: Characterization of a New Class of Contrast Agents for MR Imaging. *Radiology* **1990**, *175*, 489−493.

(41) Mayo-Smith, W. W.; Saini, S.; Slater, G.; Kaufman, J. A.; Sharma, P.; Hahn, P. F. MR Contrast Material for Vascular Enhancement: Value of Superparamagnetic Iron Oxide. *AJR, Am. J. Roentgenol.* **1996**, *166*, 73−77.

(42) Anzai, Y.; Blackwell, K. E.; Hirschowitz, S. L.; Rogers, J. W.; Sato, Y.; Yuh, W. T.; Runge, V. M.; Morris, M. R.; McLachlan, S. J.; Lufkin, R. B. Initial Clinical Experience with Dextran-Coated Superparamagnetic Iron Oxide for Detection of Lymph Node Metastases in Patients with Head and Neck Cancer. *Radiology* **1994**, *192*, 709−715.

(43) Anzai, Y.; Prince, M. R. Iron Oxide-Enhanced MR Lymphography: The Evaluation of Cervical Lymph Node Metastases in Head and Neck Cancer. *J. Magn. Reson. Imaging* **1997**, *7*, 75−81.

(44) Ahn, S. S.; Kim, M.-J.; Lim, J. S.; Hong, H.-S.; Chung, Y. E.; Choi, J.-Y. Added Value of Gadoxetic Acid−Enhanced Hepatobiliary Phase MR Imaging in the Diagnosis of Hepatocellular Carcinoma. *Radiology* **2010**, *255*, 459−466.

(45) An, S. K.; Lee, J. M.; Suh, K.-S.; Lee, N. J.; Kim, S. H.; Kim, Y. J.; Han, J. K.; Choi, B. I. Gadobenate Dimeglumine-Enhanced Liver MRI as the Sole Preoperative Imaging Technique: A Prospective Study of Living Liver Donors. *AJR, Am. J. Roentgenol.* **2006**, *187*, 1223−1233.

(46) Toft, K. G.; Hustvedt, S. O.; Grant, D.; Martinsen, I.; Gordon, P. B.; Friisk, G. A.; Korsmo, Å. J.; Skotland, T. Metabolism and Pharmacokinetics of MnDPDP in Man. *Acta Radiol.* **1997**, *38*, 677−689.

(47) Wang, Y.-X. J. Superparamagnetic Iron Oxide Based MRI Contrast Agents: Current Status of Clinical Application. *Quant. Imaging Med. Surg.* **2011**, *1*, 35−40.

(48) Clement, O.; Siauve, N.; Cuénod, C.-A.; Frija, G. Liver Imaging With Ferumoxides (Feridex®): Fundamentals, Controversies, and Practical Aspects. *Top. Magn. Reson. Imag.* **1998**, *9*, 167−182.

(49) Reimer, P.; Balzer, T. Ferucarbotran (Resovist): A New Clinically Approved RES-Specific Contrast Agent for Contrast-Enhanced MRI of the Liver: Properties, Clinical Development, and Applications. *Eur. Radiol.* **2003**, *13*, 1266−1276.

(50) Harisinghani, M. G.; Barentsz, J.; Hahn, P. F.; Deserno, W. M.; Tabatabaei, S.; van de Kaa, C. H.; de la Rosette, J.; Weissleder, R. Noninvasive Detection of Clinically Occult Lymph-Node Metastases in Prostate Cancer. *N. Engl. J. Med.* **2003**, *348*, 2491−2499.

(51) Jacobs, K. E.; Behera, D.; Rosenberg, J.; Gold, G.; Moseley, M.; Yeomans, D.; Biswal, S. Oral Manganese as an MRI Contrast Agent for the Detection of Nociceptive Activity. *NMR Biomed.* **2012**, *25*, 563−569.

(52) Arthurs, O. J.; Graves, M. J.; Edwards, A. D.; Joubert, I.; Set, P. A.; Lomas, D. J. Interactive Neonatal Gastrointestinal Magnetic Resonance Imaging Using Fruit Juice as an Oral Contrast Media. *BMC Med. Imaging* **2014**, *14*, 33−41.

(53) Li, K. C. P.; Tart, R. P.; Fitzsimmons, J. R.; Storm, B. L.; Mao, J.; Rolfes, R. J. Barium Sulfate Suspension as a Negative Oral MRI Contrast Agent: In Vitro and Human Optimization Studies. *Magn. Reson. Imaging* **1991**, *9*, 141−150.

(54) Hahn, P. F.; Stark, D. D.; Lewis, J. M.; Saini, S.; Elizondo, G.; Weissleder, R.; Fretz, C. J.; Ferrucci, J. T. First Clinical Trial of a New

Superparamagnetic Iron Oxide for Use as an Oral Gastrointestinal Contrast Agent in MR Imaging. *Radiology* **1990**, *175*, 695−700.

(55) Kaminsky, S.; Laniado, M.; Gogoll, M.; Kornmesser, W.; Clauss, W.; Langer, M.; Claussen, C.; Felix, R. Gadopentetate Dimeglumine as a Bowel Contrast Agent: Safety and Efficacy. *Radiology* **1991**, *178*, 503−508.

(56) Giovagnoni, A.; Fabbri, A.; Maccioni, F. Oral Contrast Agents in MRI of the Gastrointestinal Tract. *Abdom. Imaging* **2002**, *27*, 367−375.

(57) Mosbah, K.; Ruiz-Cabello, J.; Berthezène, Y.; Crémillieux, Y. Aerosols And Gaseous Contrast Agents for Magnetic Resonance Imaging of the Lung. *Contrast Media Mol. Imaging* **2008**, *3*, 173−190.

(58) Pan, D. P. J.; Schmieder, A. H.; Wickline, S. A.; Lanza, G. M. Manganese-Based MRI Contrast Agents: Past, Present, and Future. *Tetrahedron* **2011**, *67*, 8431−8444.

(59) Rohrer, M.; Bauer, H.; Mintorovitch, J.; Requardt, M.; Weinmann, H. J. Comparison of Magnetic Properties of MRI Contrast Media Solutions at Different Magnetic Field Strengths. *Invest. Radiol.* **2005**, *40*, 715−724.

(60) Rooney, W. D.; Johnson, G.; Li, X.; Cohen, E. R.; Kim, S.-g.; Ugurbil, K.; Springer, C. S. Magnetic Field and Tissue Dependencies of Human Brain Longitudinal 1H2O Relaxation in Vivo. *Magn. Reson. Med.* **2007**, *57*, 308−318.

(61) Gahramanov, S.; Muldoon, L. L.; Varallyay, C. G.; Li, X.; Kraemer, D. F.; Fu, R.; Hamilton, B. E.; Rooney, W. D.; Neuwelt, E. A. Pseudoprogression of Glioblastoma after Chemo- and Radiation Therapy: Diagnosis by Using Dynamic Susceptibility-Weighted Contrast-Enhanced Perfusion MR Imaging with Ferumoxytol versus Gadoteridol and Correlation with Survival. *Radiology* **2013**, *266*, 842−852.

(62) De Leõn-Rodríguez, L. M.; Martins, A. F.; Pinho, M. C.; Rofsky, N. M.; Sherry, A. D. Basic MR Relaxation Mechanisms and Contrast Agent Design. *J. Magn. Reson. Imaging* **2015**, *42*, 545−565.

(63) Schellenberger, E. A.; Bogdanov, A., Jr.; Högemann, D.; Tait, J.; Weissleder, R.; Josephson, L. Annexin V − CLIO: A Nanoparticle for Detecting Apoptosis by MRI. *Mol. Imaging* **2002**, *1*, 102−107.

(64) Yeh, T.-c.; Zhang, W.; Ildstad, S. T.; Ho, C. In Vivo Dynamic MRI Tracking of Rat T-Cells Labeled with Superparamagnetic Iron-Oxide Particles. *Magn. Reson. Med.* **1995**, *33*, 200−206.

(65) Na, H. B.; Song, I. C.; Hyeon, T. Inorganic Nanoparticles for MRI Contrast Agents. *Adv. Mater.* **2009**, *21*, 2133−2148.

(66) Bannas, P.; Graumann, O.; Balcerak, P.; Peldschus, K.; Kaul, M. G.; Hohenberg, H.; Haag, F.; Adam, G.; Ittrich, H.; Koch-Nolte, F. Quantitative Magnetic Resonance Imaging of Enzyme Activity on the Cell Surface: In Vitro and In Vivo Monitoring of ADP-Ribosyltransferase 2 on T Cells. *Mol. Imaging* **2010**, *9*, 211−222.

(67) Vogl, T. J.; Hammerstingl, R.; Schwarz, W.; Mack, M. G.; Müller, P. K.; Pegios, W.; Keck, H.; Eibl-Eibesfeldt, A.; Hoelzl, J.; Woessmer, B.; et al. Superparamagnetic Iron Oxide-Enhanced versus Gadolinium-Enhanced MR Imaging for Differential Diagnosis of Focal Liver Lesions. *Radiology* **1996**, *198*, 881−887.

(68) Farrell, B. T.; Hamilton, B. E.; Dósa, E.; Rimely, E.; Nasseri, M.; Gahramanov, S.; Lacy, C. A.; Frenkel, E. P.; Doolittle, N. D.; Jacobs, P. M.; et al. Using Iron Oxide Nanoparticles to Diagnose CNS Inflammatory Diseases and PCNSL. *Neurology* **2013**, *81*, 256−263.

(69) Guivel-Scharen, V.; Sinnwell, T.; Wolff, S. D.; Balaban, R. S. Detection of Proton Chemical Exchange between Metabolites and Water in Biological Tissues. *J. Magn. Reson.* **1998**, *133*, 36−45.

(70) Chan, K. W. Y.; McMahon, M. T.; Kato, Y.; Liu, G.; Bulte, J. W. M.; Bhujwalla, Z. M.; Artemov, D.; Van Zijl, P. C. M. Natural D-Glucose as a Biodegradable MRI Contrast Agent for Detecting Cancer. *Magn. Reson. Med.* **2012**, *68*, 1764−1773.

(71) Walker-Samuel, S.; Ramasawmy, R.; Torrealdea, F.; Rega, M.; Rajkumar, V.; Johnson, S. P.; Richardson, S.; Gonçalves, M.; Parkes, H. G.; Årstad, E.; et al. Vivo Imaging of Glucose Uptake and Metabolism in Tumors. *Nat. Med.* **2013**, *19*, 1067−1072.

(72) Longo, D. L.; Dastrù, W.; Digilio, G.; Keupp, J.; Langereis, S.; Lanzardo, S.; Prestigio, S.; Steinbach, O.; Terreno, E.; Uggeri, F.; et al. Iopamidol as a Responsive MRI-Chemical Exchange Saturation Transfer Contrast Agent for PH Mapping of Kidneys: In Vivo Studies in Mice at 7 T. *Magn. Reson. Med.* **2011**, *65*, 202−211.

(73) Ruiz-Cabello, J.; Barnett, B. P.; Bottomley, P. A.; Bulte, J. W. M. Fluorine (19F) MRS and MRI in Biomedicine. *NMR Biomed.* **2011**, *24*, 114−129.

(74) Díaz-López, R.; Tsapis, N.; Fattal, E. Liquid Perfluorocarbons as Contrast Agents for Ultrasonography and 19F-MRI. *Pharm. Res.* **2010**, *27*, 1−16.

(75) Tirotta, I.; Dichiarante, V.; Pigliacelli, C.; Cavallo, G.; Terraneo, G.; Bombelli, F. B.; Metrangolo, P.; Resnati, G. 19 F Magnetic Resonance Imaging (MRI): From Design of Materials to Clinical Applications. *Chem. Rev.* **2015**, *115*, 1106−1129.

(76) Tanifum, E. A.; Patel, C.; Liaw, M. E.; Pautler, R. G.; Annapragada, A. V. Hydrophilic Fluorinated Molecules for Spectral 19F MRI. *Sci. Rep.* **2018**, *8*, DOI: 10.1038/s41598-018-21178-3.

(77) Aime, S.; Botta, M.; Fasano, M.; Terreno, E.; Kinchesh, P.; Calabi, L.; Paleari, L. A New Ytterbium Chelate as Contrast Agent in Chemical Shift Imaging and Temperature Sensitive Probe for MR Spectroscopy. *Magn. Reson. Med.* **1996**, *35*, 648−651.

(78) Coman, D.; Trubel, H. K.; Hyder, F. Brain Temperature by Biosensor Imaging of Redundant Deviation in Shifts (BIRDS): Comparison between TmDOTP(5−) and TmDOTMA(−). *NMR Biomed.* **2009**, *23*, 277−285.

(79) Hekmatyar, S. K.; Hopewell, P.; Pakin, S. K.; Babsky, A.; Bansal, N. Noninvasive MR Thermometry Using Paramagnetic Lanthanide Complexes of 1,4,7,10-Tetraazacyclododecane-α,α′,α″,α‴-Tetramethyl-1,4,7,10-Tetraacetic Acid (DOTMA4−). *Magn. Reson. Med.* **2005**, *53*, 294−303.

(80) Yang, Y.; Schühle, D. T.; Dai, G.; Alford, J.; Caravan, P. 1H Chemical Shift Magnetic Resonance Imaging Probes with High Sensitivity for Multiplex Imaging. *Contrast Media Mol. Imaging* **2012**, *7*, 276−279.

(81) Mason, K.; Rogers, N. J.; Suturina, E. A.; Kuprov, I.; Aguilar, J. A.; Batsanov, A. S.; Yufit, D. S.; Parker, D. PARASHIFT Probes: Solution NMR and X-ray Structural Studies of Macrocyclic Ytterbium and Yttrium Complexes. *Inorg. Chem.* **2017**, *56*, 4028−4038.

(82) Senanayake, P. K.; Rogers, N. J.; Finney, K. L. N. A.; Harvey, P.; Funk, A. M.; Wilson, J. I.; O'Hogain, D.; Maxwell, R.; Parker, D.; Blamire, A. M. A New Paramagnetically Shifted Imaging Probe for MRI. *Magn. Reson. Med.* **2017**, *77*, 1307−1317.

(83) Chalmers, K. H.; De Luca, E.; Hogg, N. H. M.; Kenwright, A. M.; Kuprov, I.; Parker, D.; Botta, M.; Wilson, J. I.; Blamire, A. M. Design Principles and Theory of Paramagnetic Fluorine-Labelled Lanthanide Complexes as Probes for 19F Magnetic Resonance: A Proof-of-Concept Study. *Chem. - Eur. J.* **2010**, *16*, 134−148.

(84) Chalmers, K. H.; Kenwright, A. M.; Parker, D.; Blamire, A. M. 19F-lanthanide Complexes with Increased Sensitivity for 19F-MRI: Optimization of the MR Acquisition. *Magn. Reson. Med.* **2011**, *66*, 931−936.

(85) Månsson, S.; Johansson, E.; Magnusson, P.; Chai, C.-M.; Hansson, G.; Petersson, J. S.; Ståhlberg, F.; Golman, K. 13C Imaging—A New Diagnostic Platform. *Eur. Radiol.* **2006**, *16*, 57−67.

(86) Golman, K.; Ardenkjaer-Larsen, J. H.; Petersson, J. S.; Mansson, S.; Leunbach, I. Molecular Imaging with Endogenous Substances. *Proc. Natl. Acad. Sci. U. S. A.* **2003**, *100*, 10435−10439.

(87) Mugler, J. P.; Altes, T. A. Hyperpolarized 129Xe MRI of the Human Lung. *J. Magn. Reson. Imaging* **2013**, *37*, 313−331.

(88) van Beek, E. J. R.; Wild, J. M.; Kauczor, H. U.; Schreiber, W.; Mugler, J. P.; de Lange, E. E. Functional MRI of the Lung Using Hyperpolarized 3-Helium Gas. *J. Magn. Reson. Imaging* **2004**, *20*, 540−554.

(89) Roos, J. E.; McAdams, H. P.; Kaushik, S. S.; Driehuys, B. Hyperpolarized Gas MRI: Technique and Applications. *Magn. Reson. Imaging C* **2015**, *23*, 217−229.

(90) Fain, S.; Schiebler, M. L.; McCormack, D. G.; Parraga, G. Imaging of Lung Function Using Hyperpolarized Helium-3 Magnetic Resonance Imaging: Review of Current and Emerging Translational Methods and Applications. *J. Magn. Reson. Imaging* **2010**, *32*, 1398−1408.

(91) Ardenkjaer-Larsen, J. H.; Fridlund, B.; Gram, A.; Hansson, G.; Hansson, L.; Lerche, M. H.; Servin, R.; Thaning, M.; Golman, K. Increase in Signal-to-Noise Ratio of > 10,000 Times in Liquid-State NMR. *Proc. Natl. Acad. Sci. U. S. A.* **2003**, *100*, 10158−10163.

(92) Sinharay, S.; Pagel, M. D. Advances in Magnetic Resonance Imaging Contrast Agents for Biomarker Detection. *Annu. Rev. Anal. Chem.* **2016**, *9*, 95−115.

(93) Bhattacharya, P.; Chekmenev, E. Y.; Perman, W. H.; Harris, K. C.; Lin, A. P.; Norton, V. A.; Tan, C. T.; Ross, B. D.; Weitekamp, D. P. Towards Hyperpolarized 13 C-Succinate Imaging of Brain Cancer. *J. Magn. Reson.* **2007**, *186*, 150−155.

(94) Geraldes, C.; Laurent, S. Classification and Basic Properties of Contrast Agents for Magnetic Resonance Imaging. *Contrast Media Mol. Imaging* **2009**, *4*, 1−23.

(95) Pravdivtsev, A. N.; Yurkovskaya, A. V.; Vieth, H.-M.; Ivanov, K. L. RF-SABRE: A Way to Continuous Spin Hyperpolarization at High Magnetic Fields. *J. Phys. Chem. B* **2015**, *119*, 13619−13629.

(96) Halse, M. E. Perspectives for Hyperpolarisation in Compact NMR. *TrAC, Trends Anal. Chem.* **2016**, *83*, 76−83.

(97) Miyazaki, M.; Akahane, M. Non-Contrast Enhanced MR Angiography: Established Techniques. *J. Magn. Reson. Imaging* **2012**, *35*, 1−19.

(98) Wheaton, A. J.; Miyazaki, M. Non-Contrast Enhanced MR Angiography: Physical Principles. *J. Magn. Reson. Imaging* **2012**, *36*, 286−304.

(99) Chavhan, G. B.; Babyn, P. S.; John, P.; Yoo, S. J.; RIgsby, C. K. Pediatric Body MR Angiography: Principles, Techniques, and Current Status in Body Imaging. *AJR, Am. J. Roentgenol.* **2015**, *205*, 173−184.

(100) de Bazelaire, C. M. J.; Duhamel, G. D.; Rofsky, N. M.; Alsop, D. C. MR Imaging Relaxation Times of Abdominal and Pelvic Tissues Measured in Vivo at 3. 0 T: Preliminary Results 1. *Radiology* **2004**, *230*, 652−659.

(101) Bottomley, P. A.; Hardy, C. J.; Argersinger, R. E.; Allen-Moore, G. A Review of 1h Nuclear Magnetic Resonance Relaxation in Pathology: Are T1 and T2 Diagnostic? *Med. Phys.* **1987**, *14*, 1−37.

(102) Lauffer, R. B. Paramagnetic Metal Complexes as Water Proton Relaxation Agents for NMR Imaging: Theory and Design. *Chem. Rev.* **1987**, *87*, 901−927.

(103) Edelman, R. R.; Micha, J. H., Clinical Magnetic Resonance Imaging. In *Clinical Magnetic Resonance Imaging*, 3rd ed.; Saunders: Philadelphia, 2005.

(104) Bloembergen, N. Spin Relaxation Processes in a Two-Proton System. *Phys. Rev.* **1956**, *104*, 1542−1547.

(105) Solomon, I.; Bloembergen, N. Nuclear Magnetic Interactions in the HF Molecule. *J. Chem. Phys.* **1956**, *25*, 261−266.

(106) Bloembergen, N. Proton Relaxation Times in Paramagnetic Solutions. *J. Chem. Phys.* **1957**, *27*, 572−573.

(107) Bloembergen, N.; Morgan, L. O. Proton Relaxation Times in Paramagnetic Solutions. Effects of Electron Spin Relaxation. *J. Chem. Phys.* **1961**, *34*, 842−850.

(108) Solomon, I. Relaxation Processes in a System of Two Spins. *Phys. Rev.* **1955**, *99*, 559−565.

(109) Caravan, P. Strategies for Increasing the Sensitivity of Gadolinium Based MRI Contrast Agents. *Chem. Soc. Rev.* **2006**, *35*, 512−523.

(110) Laurent, S.; Elst, L. V.; Muller, R. N. Comparative Study of the Physicochemical Properties of Six Clinical Low Molecular Weight Gadolinium Contrast Agents. *Contrast Media Mol. Imaging* **2006**, *1*, 128−137.

(111) Powell, D. H.; Dhubhghaill, O. M. N.; Pubanz, D.; Helm, L.; Lebedev, Y. S.; Schlaepfer, W.; Merbach, A. E. Structural and Dynamic Parameters Obtained from 17O NMR, EPR, and NMRD Studies of Monomeric and Dimeric Gd3+ Complexes of Interest in Magnetic Resonance Imaging: An Integrated and Theoretically Self-Consistent Approach. *J. Am. Chem. Soc.* **1996**, *118*, 9333−9346.

(112) Dumas, S.; Jacques, V.; Sun, W.-C.; Troughton, J. S.; Welch, J. T.; Chasse, J. M.; Schmitt-Willich, H.; Caravan, P. High Relaxivity Magnetic Resonance Imaging Contrast Agents Part 1: Impact of Single Donor Atom Substitution on Relaxivity of Serum Albumin-Bound Gadolinium Complexes. *Invest. Radiol.* **2010**, *45*, 600−612.

(113) Atherton, N. M. *Principles of Electron Spin Resonance*; Ellis Horwood Ltd: New York, 1993.

(114) Bertini, I.; Kowalewski, J.; Luchinat, C.; Nilsson, T.; Parigi, G. Nuclear Spin Relaxation in Paramagnetic Complexes of S = 1: Electron Spin Relaxation Effects. *J. Chem. Phys.* **1999**, *111*, 5795−5807.

(115) Bertini, I.; Luchinat, C.; Parigi, G. *Solution NMR of Paramagnetic Molecules*; Elsevier: Amsterdam, 2001.

(116) Kowalewski, J.; Luchinat, C.; Nilsson, T.; Parigi, G. Nuclear Spin Relaxation in Paramagnetic Systems: Electron Spin Relaxation Effects under Near-Redfield Limit Conditions and Beyond. *J. Phys. Chem. A* **2002**, *106*, 7376−7382.

(117) Kruk, D.; Nilsson, T.; Kowalewski, J. Nuclear Spin Relaxation in Paramagnetic Systems with Zero-Field Splitting and Arbitrary Electron Spin. *Phys. Chem. Chem. Phys.* **2001**, *3*, 4907−4917.

(118) Rubinstein, M.; Luz, Z.; Baram, A. Electronic and Nuclear Relaxation in Solutions of Transition Metal Ions with Spin S = 3/2 and 5/2. *Mol. Phys.* **1971**, *20*, 67−80.

(119) Aime, S.; Fasano, M.; Terreno, E.; Botta, M. Lanthanide(III) Chelates for NMR Biomedical Applications. *Chem. Soc. Rev.* **1998**, *27*, 19−29.

(120) Fries, P. H.; Belorizky, E. Electronic Relaxation of Para-magnetic Metal Ions and NMR Relaxivity in Solution: Critical Analysis of Various Approaches and Application to a Gd(Iii)-Based Contrast Agent. *J. Chem. Phys.* **2005**, *123*, 124510.

(121) Raitsimring, A. M.; Astashkin, A. V.; Poluektov, O. G.; Caravan, P. High Field Pulsed EPR and ENDOR of Gd3+ Complexes in Glassy Solutions. *Appl. Magn. Reson.* **2005**, *28*, 281−295.

(122) Borel, A.; Helm, L.; Merbach, Â. E. Molecular Dynamics Simulations of MRI-Relevant Gd III Chelates: Direct Access to Outer-Sphere Relaxivity. *Chem. - Eur. J.* **2001**, *7*, 600−610.

(123) Boros, E.; Srinivas, R.; Kim, H.-K.; Raitsimring, A. M.; Astashkin, A. V.; Poluektov, O. G.; Niklas, J.; Horning, A. D.; Tidor, B.; Caravan, P. Intramolecular Hydrogen Bonding Restricts Gd−Aqua-Ligand Dynamics. *Angew. Chem., Int. Ed.* **2017**, *56*, 5603−5606.

(124) Caravan, P.; Amedio, J. C., Jr.; Dunham, S. U.; Greenfield, M. T.; Cloutier, N. J.; McDermid, S. A.; Spiller, M.; Zech, S. G.; Looby, R. J.; Raitsimring, A. M.; et al. When are Two Waters Worse Than One? Doubling the Hydration Number of a Gd−DTPA Derivative Decreases Relaxivity. *Chem. - Eur. J.* **2005**, *11*, 5866−5874.

(125) Raitsimring, A. M.; Astashkin, A. V.; Baute, D.; Goldfarb, D.; Poluektov, O. G.; Lowe, M. P.; Zech, S. G.; Caravan, P. Determination of the Hydration Number of Gadolinium(III) Complexes by High-Field Pulsed O-17 ENDOR Spectroscopy. *ChemPhysChem* **2006**, *7*, 1590−1597.

(126) Zech, S. G.; Sun, W. C.; Jacques, V.; Caravan, P.; Astashkin, A. V.; Raitsimring, A. M. Probing the Water Coordination gf Protein-Targeted MRI Contrast Agents by Pulsed ENDOR Spectroscopy. *ChemPhysChem* **2005**, *6*, 2570−2577.

(127) Caravan, P.; Astashkin, A. V.; Raitsimring, A. M. The Gadolinium(III)-Water Hydrogen Distance in MRI Contrast Agents. *Inorg. Chem.* **2003**, *42*, 3972−3974.

(128) Astashkin, A. V.; Raitsimring, A. M.; Caravan, P. Pulsed ENDOR Study Of Water Coordination to Gd3+ Complexes in Orientationally Disordered Systems. *J. Phys. Chem. A* **2004**, *108*, 1990−2001.

(129) Elst, L. V.; Maton, F.; Laurent, S.; Seghi, F.; Chapelle, F.; Muller, R. N. A Multinuclear MR Study of Gd-EOB-DTPA: Comprehensive Preclinical Characterization of an Organ Specific MRI Contrast Agent. *Magn. Reson. Med.* **1997**, *38*, 604−614.

(130) Muller, R. N.; Raduchel, B.; Laurent, S.; Platzek, J.; Pierart, C.; Mareski, P.; Vander Elst, L. Physicochemical Characterization of MS-325, a New Gadolinium Complex, by Multinuclear Relaxometry. *Eur. J. Inorg. Chem.* **1999**, *1999*, 1949−1955.

(131) Polasek, M.; Caravan, P. Is Macrocycle a Synonym for Kinetic Inertness in Gd(III) Complexes? Effect of Coordinating and

Noncoordinating Substituents on Inertness and Relaxivity of Gd(III) Chelates with DO3A-like Ligands. *Inorg. Chem.* **2013**, *52*, 4084−4096.

(132) Benson, M. T.; Saunders, L.; Sommerer, S.; Cundari, T. R. Synthesis, Structure, Computational Studies and Magnetic Properties of a Ten-Coordinate Gadolinium(III) Complex. *Inorg. Chim. Acta* **1997**, *258*, 127−130.

(133) Caravan, P.; Hedlund, T.; Liu, S.; Sjoberg, S.; Orvig, C. Potentiometric, Calorimetric, and Solution NMR Studies of a Tridentate Ligand Which Has a Marked Preference for the Formation of Bis- versus Mono(Ligand) Lanthanide Complexes, and which Exhibits High Selectivity for Heavier Lanthanides. *J. Am. Chem. Soc.* **1995**, *117*, 11230−11238.

(134) Alpoim, M. C.; Urbano, A. M.; Geraldes, C. F. G. C.; Peters, J. A. Determination of the Number of Inner-Sphere Water Molecules in Lanthanide(III) Polyaminocarboxylate Complexes. *J. Chem. Soc., Dalton Trans.* **1992**, *0*, 463−467.

(135) Horrocks, W. D., Jr.; Sudnick, D. R. Lanthanide Ion Probes of Structure in Biology. Laser-Induced Luminescence Decay Constants Provide a Direct Measure of the Number of Metal-Coordinated Water Molecules. *J. Am. Chem. Soc.* **1979**, *101*, 334−340.

(136) Beeby, A.; Clarkson, I. M.; Dickins, R. S.; Faulkner, S.; Parker, D.; Royle, L.; de Sousa, A.; Williams, J. A. G.; Woods, M. Non-Radiative Deactivation of the Excited States of Europium, Terbium and Ytterbium Complexes by Proximate Energy-Matched OH, NH and CH Oscillators: An Improved Luminescence Method for Establishing Solution Hydration States. *J. Chem. Soc., Perkin Trans. 2* **1999**, 493−504.

(137) Supkowski, R. M.; Horrocks, W. D. On the Determination of the Number of Water Molecules, q, Coordinated To Europium(III) Ions In Solution From Luminescence Decay Lifetimes. *Inorg. Chim. Acta* **2002**, *340*, 44−48.

(138) Gale, E. M.; Zhu, J.; Caravan, P. Direct Measurement of the Mn(II) Hydration State in Metal Complexes and Metalloproteinst through 17O NMR Line Widths. *J. Am. Chem. Soc.* **2013**, *135*, 18600−18608.

(139) Caravan, P.; Parigi, G.; Chasse, J. M.; Cloutier, N. J.; Ellison, J. J.; Lauffer, R. B.; Luchinat, C.; McDermid, S. A.; Spiller, M.; McMurry, T. J. Albumin Binding, Relaxivity, and Water Exchange Kinetics of the Diastereoisomers of MS-325, a Gadolinium(III)-Based Magnetic Resonance Angiography Contrast Agent. *Inorg. Chem.* **2007**, *46*, 6632−6639.

(140) Zech, S. G.; Eldredge, H. B.; Lowe, M. P.; Caravan, P. Protein Binding to Lanthanide(III) Complexes Can Reduce the Water Exchange Rate at the Lanthanide. *Inorg. Chem.* **2007**, *46*, 3576−3584.

(141) Zhou, X.; Caravan, P.; Clarkson, R. B.; Westlund, P. O. On the Philosophy of Optimizing Contrast Agents. An Analysis of 1H NMRD Profiles and ESR Lineshapes of the Gd(III) Complex MS-325+HSA. *J. Magn. Reson.* **2004**, *167*, 147−160.

(142) Nair, S. A.; Kolodziej, A. F.; Bhole, G.; Greenfield, M. T.; McMurry, T. J.; Caravan, P. Monovalent and Bivalent Fibrin-Specific MRI Contrast Agents for Detection of Thrombus. *Angew. Chem., Int. Ed.* **2008**, *47*, 4918−4921.

(143) Helm, L.; Merbach, A. E. Inorganic and Bioinorganic Solvent Exchange Mechanisms. *Chem. Rev.* **2005**, *105*, 1923−1960.

(144) Caravan, P.; Farrar, C. T.; Frullano, L.; Uppal, R. Influence of Molecular Parameters and Increasing Magnetic Field Strength on Relaxivity of Gadolinium- and Manganese-Based T1 Contrast Agents. *Contrast Media Mol. Imaging* **2009**, *4*, 89−100.

(145) Aime, S.; Botta, M.; Garda, Z.; Kucera, B. E.; Tircso, G.; Young, V. G.; Woods, M. Properties, Solution State Behavior, and Crystal Structures of Chelates of DOTMA. *Inorg. Chem.* **2011**, *50*, 7955−7965.

(146) Miller, K. J.; Saherwala, A. A.; Webber, B. C.; Wu, Y.; Sherry, A. D.; Woods, M. The Population of SAP and TSAP Isomers in Cyclen-Based Lanthanide (III) Chelates Is Substantially Affected by Solvent. *Inorg. Chem.* **2010**, *49*, 8662−8664.

(147) Tircso, G.; Webber, B. C.; Kucera, B. E.; Young, V. G.; Woods, M. Analysis of the Conformational Behavior and Stability of

(148) Mayer, F.; Platas-Iglesias, C.; Helm, L.; Peters, J. A.; Djanashvili, K. 17O NMR and Density Functional Theory Study of the Dynamics of the Carboxylate Groups in DOTA Complexes of Lanthanides in Aqueous Solution. *Inorg. Chem.* **2012**, *51*, 170−178.

(149) Hermann, P.; Kotek, J.; Kubicek, V.; Lukes, I. Gadolinium (III) Complexes as MRI Contrast Agents: Ligand Design And Properties of the Complexes. *Dalton Trans* **2008**, *23*, 3027−3047.

(150) Howard, J. A. K.; Kenwright, A. M.; Moloney, J. M.; Parker, D.; Port, M.; Navet, M.; Rousseau, O.; Woods, M.; Howard, J. A. K. Structure and Dynamics of all of the Stereoisomers of Europium Complexes of Tetra (Carboxyethyl) Derivatives of Dota: Ring Inversion is Decoupled from Cooperative Arm Rotation in the RRRR and RRRS Isomers. *Chem. Commun.* **1998**, *0*, 1381−1382.

(151) Dunand, F. A.; Dickins, R. S.; Parker, D.; Merbach, A. E. Towards Rational Design of Fast Water-Exchanging Gd (dota-Like) Contrast Agents? Importance of the M/m Ratio. *Chem. - Eur. J.* **2001**, *7*, 5160−5167.

(152) Di Bari, L.; Pintacuda, G.; Salvadori, P. Solution Equilibria in YbDOTMA, a Chiral Analogue of One of the Most Successful Contrast Agents for MRI, GdDOTA. *Eur. J. Inorg. Chem.* **2000**, *2000*, 75−82.

(153) Aime, S.; Botta, M.; Ermondi, G.; Terreno, E.; Anelli, P. L.; Fedeli, F.; Uggeri, F. Relaxometric, Structural, and Dynamic NMR Studies of DOTA-like Ln (III) Complexes (Ln = La, Gd, Ho, Yb) Containing a p-Nitrophenyl Substituent. *Inorg. Chem.* **1996**, *35*, 2726−2736.

(154) Woods, M.; Kovacs, Z.; Zhang, S.; Sherry, A. D. Towards the Rational Design of Magnetic Resonance Imaging Contrast Agents: Isolation of the Two Coordination Isomers of Lanthanide DOTA-Type Complexes. *Angew. Chem., Int. Ed.* **2003**, *42*, 5889−5892.

(155) Woods, M.; Kovacs, Z.; Kiraly, R.; Brucher, E.; Zhang, S.; Sherry, A. D. Solution Dynamics and Stability of Lanthanide (III) (S)-2-(p-Nitrobenzyl)DOTA Complexes. *Inorg. Chem.* **2004**, *43*, 2845−2851.

(156) Ranganathan, R. S.; Pillai, R. K.; Raju, N.; Fan, H.; Nguyen, H.; Tweedle, M. F.; Desreux, J. F.; Jacques, V. Polymethylated DOTA Ligands. 1. Synthesis of Rigidified Ligands and Studies on the Effects of Alkyl Substitution on Acid − Base Properties and Conformational Mobility. *Inorg. Chem.* **2002**, *41*, 6846−6855.

(157) Ranganathan, R. S.; Raju, N.; Fan, H.; Zhang, X.; Tweedle, M. F.; Desreux, J. F.; Jacques, V. Polymethylated DOTA Ligands. 2. Synthesis of Rigidified Lanthanide Chelates and Studies on the Effect of Alkyl Substitution on Conformational Mobility and Relaxivity. *Inorg. Chem.* **2002**, *41*, 6856−6866.

(158) Avecilla, F.; Peters, J. A.; Geraldes, C. F. G. C. X-ray Crystal Structure of a Sodium Salt of [Gd(DOTP)]5-: Implications for Its Second-Sphere Relaxivity and the 23Na NMR Hyperfine Shift Effects of [Tm(DOTP)]5-. *Eur. J. Inorg. Chem.* **2003**, *2003*, 4179−4186.

(159) Rudovsky, J.; Cigler, P.; Kotek, J.; Hermann, P.; Vojtisek, P.; Lukes, I.; Peters, J. A.; Vander Elst, L.; Muller, R. N. Lanthanide(III) Complexes of a Mono (methylphosphonate) Analogue of H(4)dota: The Influence of Protonation of the Phosphonate Moiety on the TSAP/SAP Isomer Ratio and the Water Exchange Rate. *Chem. - Eur. J.* **2005**, *11*, 2373−2384.

(160) Vojtisek, P.; Cigler, P.; Kotek, J.; Rudovsky, J.; Hermann, P.; Lukes, I. Crystal Structures of Lanthanide (III) Complexes with Cyclen Derivative Bearing Three Acetate and One Methylphosphonate Pendants. *Inorg. Chem.* **2005**, *44*, 5591−5599.

(161) Heffern, M. C.; Matosziuk, L. M.; Meade, T. J. Lanthanide Probes for Bioresponsive Imaging. *Chem. Rev.* **2014**, *114*, 4496−4539.

(162) Hwang, L. P.; Freed, J. H. Dynamic Effects of Pair Correlation Functions on Spin Relaxation by Translational Diffusion in Liquids. *J. Chem. Phys.* **1975**, *63*, 4017−4025.

(163) Gueron, M. Nuclear Relaxation in Macromolecules by Paramagnetic Ions: A Novel Mechanism. *J. Magn. Reson.* **1975**, *19*, 58−66.

(164) Caravan, P.; Greenfield, M. T.; Bulte, J. W. Molecular Factors That Determine Curie Spin Relaxation in Dysprosium Complexes. *Magn. Reson. Med.* **2001**, *46*, 917−922.

(165) Tombach, B.; Benner, T.; Reimer, P.; Schuierer, G.; Fallenberg, E. M.; Geens, V.; Wels, T.; Sorensen, A. G. Do Highly Concentrated Gadolinium Chelates Improve MR Brain Perfusion Imaging? Intraindividually Controlled Randomized Crossover Concentration Comparison Study of 0.5 versus 1.0 mol/L Gadobutrol. *Radiology* **2003**, *226*, 880−888.

(166) Choi, J. H.; Nguyen, F. T.; Barone, P. W.; Heller, D. A.; Moll, A. E.; Patel, D.; Boppart, S. A.; Strano, M. S. Multimodal Biomedical Imaging with Asymmetric Single-Walled Carbon Nanotube/Iron Oxide Nanoparticle Complexes. *Nano Lett.* **2007**, *7*, 861−867.

(167) Pereira, G. A.; Peters, J. A.; Paz, F. A. A.; Geraldes, C. F. G. C.; Rocha, J. Evaluation of [Ln(H2cmp)(H2O)] Metal Organic Framework Materials for Potential Application as Magnetic Resonance Imaging Contrast Agents. *Inorg. Chem.* **2010**, *49*, 2969−2974.

(168) Vold, R. L.; Daniel, E. S.; Chan, S. O. Magnetic Resonance Measurements of Proton Exchange in Aqueous Urea. *J. Am. Chem. Soc.* **1970**, *92*, 6771−6776.

(169) Granot, J.; Fiat, D. Effect of Chemical Exchange on the Transverse Relaxation Rate of Nuclei in Solution Containing Paramagnetic Ions. *J. Magn. Reson.* **1974**, *15*, 540−548.

(170) Sherry, A. D.; Wu, Y. The Importance of Water Exchange Rates in the Design of Responsive Agents for MRI. *Curr. Opin. Chem. Biol.* **2013**, *17*, 167−174.

(171) Hancu, I.; Dixon, W. T.; Woods, M.; Vinogradov, E.; Sherry, A. D.; Lenkinski, R. E. CEST and PARACEST MR Contrast Agents. *Acta Radiol.* **2010**, *51*, 910−923.

(172) Huinink, H. P.; Sanders, H. M. H. F.; Erich, S. J. F.; Nicolay, K.; Strijkers, G. J.; Merkx, M.; Adan, O. C. G. High-Resolution NMR Imaging of Paramagnetic Liposomes Targeted to a Functionalized Surface. *Magn. Reson. Med.* **2008**, *59*, 1282−1286.

(173) Soesbe, T. C.; Wu, Y.; Dean Sherry, A. Advantages of Paramagnetic Chemical Exchange Saturation Transfer (CEST) Complexes Having Slow to Intermediate Water Exchange Properties as Responsive MRI Agents. *NMR Biomed.* **2013**, *26*, 829−838.

(174) Morrow, J. R.; Tóth, É. Magnetic Resonance Imaging Contrast Agents. *Inorg. Chem.* **2017**, *56*, 6029−6034.

(175) Vinogradov, E.; Sherry, A. D.; Lenkinski, R. E. CEST: From Basic Principles to Applications, Challenges and Opportunities. *J. Magn. Reson.* **2013**, *229*, 155−172.

(176) van Zijl, P. C. M.; Yadav, N. Chemical Exchange Saturation Transfer (CEST): What is in a Name and What isn't? *Magn. Reson. Med.* **2011**, *65*, 927−948.

(177) Yang, X.; Yadav, N. N.; Song, X.; Ray Banerjee, S.; Edelman, H.; Minn, I.; van Zijl, P. C. M.; Pomper, M. G.; McMahon, M. T. Tuning Phenols with Intra-Molecular Bond Shifted HYdrogens (IM-SHY) as diaCEST MRI Contrast Agents. *Chem. - Eur. J.* **2014**, *20*, 15824−15832.

(178) Zhou, J.; Zijl, P. C. M. v. Chemical Exchange Saturation Transfer Imaging and Spectroscopy. *Prog. Nucl. Magn. Reson. Spectrosc.* **2006**, *48*, 109−136.

(179) Wu, B.; Warnock, G.; Zaiss, M.; Lin, C.; Chen, M.; Zhou, Z.; Mu, L.; Nanz, D.; Tuura, R.; Delso, G. An Overview of CEST MRI for Non-MR Physicists. *EJNMMI Phys.* **2016**, *3*, 19−40.

(180) Liu, G.; Song, X.; Chan, K. W. Y.; Mcmahon, M. T. Nuts and Bolts of Chemical Exchange Saturation Transfer MRI. *NMR Biomed.* **2013**, *26*, 810−828.

(181) Li, Y.; Chen, H.; Xu, J.; Yadav, N. N.; Chan, K. W. Y.; Luo, L.; McMahon, M. T.; Vogelstein, B.; van Zijl, P. C. M.; Zhou, S.; et al. CEST Theranostics: Label-Free MR Imaging of Anticancer Drugs. *Oncotarget* **2016**, *7*, 6369−6378.

(182) Dula, A. N.; Smith, S. A.; Gore, J. C. Application of Chemical Exchange Saturation Transfer (CEST) MRI for Endogenous Contrast at 7 T. *J. Neuroimaging* **2013**, *23*, 526−532.

(183) Bryant, L. H., Jr.; Hodges, M. W.; Bryant, R. G. Test of Electron Delocalization Effects on Water-Proton Spin-Lattice Relaxation by Bromination of [Tetrakis(4-sulfonatopheny)porphine]-manganese. *Inorg. Chem.* **1999**, *38*, 1002−1005.

(184) Ratnakar, S. J.; Soesbe, T. C.; Lumata, L. L.; Do, Q. N.; Viswanathan, S.; Lin, C.-Y.; Sherry, A. D.; Kovacs, Z. Modulation of CEST Images in Vivo by T1 Relaxation: A New Approach in the Design of Responsive PARACEST Agents. *J. Am. Chem. Soc.* **2013**, *135*, 14904−14907.

(185) Hingorani, D. V.; Yoo, B.; Bernstein, A. S.; Pagel, M. D. Detecting Enzyme Activities with Exogenous MRI Contrast Agents. *Chem. - Eur. J.* **2014**, *20*, 9840−9850.

(186) Dorazio, S. J.; Olatunde, A. O.; Tsitovich, P. B.; Morrow, J. R. Comparison of Divalent Transition Metal Ion ParaCEST MRI Contrast Agents. *JBIC, J. Biol. Inorg. Chem.* **2014**, *19*, 191−205.

(187) Stevens, T. K.; Palaniappan, K. K.; Ramirez, R. M.; Francis, M. B.; Wemmer, D. E.; Pines, A. HyperCEST Detection of a 129Xe-Based Contrast Agent Composed of Cryptophane-A Molecular Cages on a Bacteriophage Scaffold. *Magn. Reson. Med.* **2013**, *69*, 1245−1252.

(188) Zaiss, M.; Schnurr, M.; Bachert, P. Analytical Solution for the Depolarization of Hyperpolarized Nuclei by Chemical Exchange Saturation Transfer Between Free and Encapsulated Xenon (HyperCEST). *J. Chem. Phys.* **2012**, *136*, 144106.

(189) Jones, K. M.; Pollard, A. C.; Pagel, M. D. Clinical Applications of Chemical Exchange Saturation Transfer (CEST) MRI. *J. Magn. Reson. Imaging* **2018**, *47*, 11−27.

(190) Castelli, D. D.; Longo, D.; Aime, S.; Terreno, E. Nanoparticle-Based Chemical Exchange Saturation Transfer (CEST) Agents. *NMR Biomed.* **2013**, *26*, 839−849.

(191) Walker, T. G.; Happer, W. Spin-Exchange Optical Pumping of Noble-Gas Nuclei. *Rev. Mod. Phys.* **1997**, *69*, 629−642.

(192) Wei, Q.; Seward, G. K.; Hill, P. A.; Patton, B.; Dimitrov, I. E.; Kuzma, N. N.; Dmochowski, I. J. Designing 129Xe NMR Biosensors for Matrix Metalloproteinase Detection. *J. Am. Chem. Soc.* **2006**, *128*, 13274−13283.

(193) Schröder, L.; Lowery, T. J.; Hilty, C.; Wemmer, D. E.; Pines, A. Molecular Imaging Using a Targeted Magnetic Resonance Hyperpolarized Biosensor. *Science* **2006**, *314*, 446−449.

(194) Chambers, J. M.; Hill, P. A.; Aaron, J. A.; Han, Z.; Christianson, D. W.; Kuzma, N. N.; Dmochowski, I. J. Cryptophane Xenon-129 Nuclear Magnetic Resonance Biosensors Targeting Human Carbonic Anhydrase. *J. Am. Chem. Soc.* **2009**, *131*, 563−569.

(195) Rose, H. M.; Witte, C.; Rossella, F.; Klippel, S.; Freund, C.; Schroder, L. Development of an Antibody-Based, Modular Biosensor for 129Xe NMR Molecular Imaging of Cells at Nanomolar Concentrations. *Proc. Natl. Acad. Sci. U. S. A.* **2014**, *111*, 11697−11702.

(196) Schilling, F.; Schroder, L.; Palaniappan, K. K.; Zapf, S.; Wemmer, D. E.; Pines, A. MRI Thermometry Based on Encapsulated Hyperpolarized Xenon. *ChemPhysChem* **2010**, *11*, 3529−3533.

(197) Wang, Y.; Dmochowski, I. J. An Expanded Palette of Xenon-129 NMR Biosensors. *Acc. Chem. Res.* **2016**, *49*, 2179−2187.

(198) Fernando, W. S.; Martins, A. F.; Zhao, P.; Wu, Y.; Kiefer, G. E.; Platas-Iglesias, C.; Sherry, A. D. Breaking the Barrier to Slow Water Exchange Rates for Optimal Magnetic Resonance Detection of ParaCEST Agents. *Inorg. Chem.* **2016**, *55*, 3007−3014.

(199) Zhang, S.; Michaudet, L.; Burgess, S.; Sherry, A. D. The Amide Protons of an Ytterbium(III) Dota Tetraamide Complex Act as Efficient Antennae for Transfer of Magnetization to Bulk Water. *Angew. Chem., Int. Ed.* **2002**, *41*, 1919−1921.

(200) Woods, M.; Woessner, D. E.; Sherry, A. D. Paramagnetic lanthanide Complexes as PARACEST Agents for Medical Imaging. *Chem. Soc. Rev.* **2006**, *35*, 500−511.

(201) Song, B.; Wu, Y.; Yu, M.; Zhao, P.; Zhou, C.; Kiefer, G. E.; Sherry, A. D. A Europium(III)-Based PARACEST Agent for Sensing Singlet Oxygen by MRI. *Dalton Trans* **2013**, *42*, 8066−8069.

(202) Zhang, S. R.; Merritt, M.; Woessner, D. E.; Lenkinski, R. E.; Sherry, A. D. PARACEST Agents: Modulating MRI Contrast via Water Proton Exchange. *Acc. Chem. Res.* **2003**, *36*, 783−790.

(203) Cacheris, W. P.; Quay, S. C.; Rocklage, S. M. The Relationship Between Thermodynamics and the Toxicity of Gadolinium Complexes. *Magn. Reson. Imaging* **1990**, *8*, 467–481.

(204) Kumar, K.; Chang, C. A.; Tweedle, M. F. Equilibrium and Kinetic Studies of Lanthanide Complexes of Macrocyclic Polyamino Carboxylates. *Inorg. Chem.* **1993**, *32*, 587–593.

(205) Sherry, A. D.; Caravan, P.; Lenkinski, R. E. Primer on Gadolinium Chemistry. *J. Magn. Reson. Imaging* **2009**, *30*, 1240–1248.

(206) Schühle, D. T.; Caravan, P. Metal-Based MRI Contrast Agents. In *Comprehensive Inorganic Chemistry II*, 2nd ed.; Poeppelmeier, K., Ed.; Elsevier: Amsterdam, 2013.

(207) Smith, R. M.; Martell, A. E. Critical Stability Constants, Enthalpies and Entropies for the Formation of Metal Complexes of Aminopolycarboxylic Acids and Carboxylic Acids. *Sci. Total Environ.* **1987**, *64*, 125–147.

(208) Port, M.; Idée, J.-M.; Medina, C.; Robic, C.; Sabatou, M.; Corot, C. Efficiency, Thermodynamic and Kinetic Stability of Marketed Gadolinium Chelates and Their Possible Clinical Consequences: A Critical Review. *BioMetals* **2008**, *21*, 469–490.

(209) Schmitt-Willich, H.; Brehm, M.; Ewers, C. L. J.; Michl, G.; Müller-Fahrnow, A.; Petrov, O.; Platzek, J.; Radüchel, B.; Sülzle, D. Synthesis and Physicochemical Characterization of a New Gadolinium Chelate: The Liver-Specific Magnetic Resonance Imaging Contrast Agent Gd-EOB-DTPA. *Inorg. Chem.* **1999**, *38*, 1134–1144.

(210) Caravan, P.; Comuzzi, C.; Crooks, W.; McMurry, T. J.; Choppin, G. R.; Woulfe, S. R. Thermodynamic Stability and Kinetic Inertness of MS-325, a New Blood Pool Agent for Magnetic Resonance Imaging. *Inorg. Chem.* **2001**, *40*, 2170–2176.

(211) Cacheris, W. P.; Nickle, S. K.; Sherry, A. D. Thermodynamic Study Of Lanthanide Complexes of 1,4,7-Triazacyclononane-N,N′,N″-Triacetic Acid (NOTA) and 1,4,7,10-Tetraazacyclododecane-N,N′,N″,N‴-Tetraacetic Acid (DOTA). *Inorg. Chem.* **1987**, *26*, 958–960.

(212) Bellin, M. F.; Vasile, M.; Morel-Precetti, S. Currently Used Non-Specific Extracellular MR Contrast Media. *Eur. Radiol.* **2003**, *13*, 2688–2698.

(213) Sieber, M. A.; Pietsch, H.; Walter, J.; Haider, W.; Frenzel, T.; Weinmann, H.-J. A Preclinical Study to Investigate the Development of Nephrogenic Systemic Fibrosis: A Possible Role for Gadolinium-Based Contrast Media. *Invest. Radiol.* **2008**, *43*, 65–75.

(214) Sieber, M. A.; Lengsfeld, P.; Frenzel, T.; Golfier, S.; Schmitt-Willich, H.; Siegmund, F.; Walter, J.; Weinmann, H.-J.; Pietsch, H. Preclinical Investigation to Compare Different Gadolinium-Based Contrast Agents Regarding Their Propensity to Release Gadolinium In Vivo and to Trigger Nephrogenic Systemic Fibrosis-Like Lesions. *Eur. Radiol.* **2008**, *18*, 2164–2173.

(215) Wedeking, P.; Kumar, K.; Tweedle, M. F. Dissociation of Gadolinium Chelates in Mice: Relationship to Chemical Characteristics. *Magn. Reson. Imaging* **1992**, *10*, 641–648.

(216) Tweedle, M. F.; Wedeking, P.; Kumar, K. Biodistribution of Radiolabeled, Formulated Gadopentetate, Gadoteridol, Gadoterate, and Gadodiamide in Mice and Rats. *Invest. Radiol.* **1995**, *30*, 372–380.

(217) Laurent, S.; Elst, L. V.; Copoix, F.; Muller, R. N. Stability of MRI Paramagnetic Contrast Media: A Proton Relaxometric Protocol for Transmetallation Assessment. *Invest. Radiol.* **2001**, *36*, 115–122.

(218) Frenzel, T.; Lengsfeld, P.; Schirmer, H.; Hutter, J.; Weinmann, H. J. Stability of Gadolinium-Based Magnetic Resonance Imaging Contrast Agents in Human Serum at 37 Degrees C. *Invest. Radiol.* **2008**, *43*, 817–828.

(219) Do, Q. N.; Ratnakar, J. S.; Kovacs, Z.; Tircso, G.; Krisztian Kalman, F.; Baranyai, Z.; Brucher, E.; Toth, I. Chapter 1 General Synthetic and Physical Methods. In *Contrast Agents for MRI: Experimental Methods*; The Royal Society of Chemistry, 2018.

(220) Palinkas, Z.; Baranyai, Z.; Brucher, E.; Rozsa, B. Kinetics of the Exchange Reactions between Gd(DTPA)(2-), Gd(BOPTA)(2-), and Gd(DTPA-BMA) Complexes, Used As MRI Contrast Agents,

and the Triethylenetetraamine-Hexaacetate Ligand. *Inorg. Chem.* **2011**, *50*, 3471–3478.

(221) Pasha, A.; Tircsó, G.; Benyó, E. T.; Brücher, E.; Sherry, A. D. Synthesis and Characterization of DOTA-(amide)4 Derivatives: Equilibrium and Kinetic Behavior of Their Lanthanide(III) Complexes. *Eur. J. Inorg. Chem.* **2007**, *2007*, 4340–4349.

(222) Wang, X.; Jin, T.; Comblin, V.; Lopez-Mut, A.; Merciny, E.; Desreux, J. F. A Kinetic Investigation of the Lanthanide DOTA Chelates. Stability and Rates of Formation and of Dissociation of a Macrocyclic Gadolinium(III) Polyaza Polycarboxylic MRI Contrast Agent. *Inorg. Chem.* **1992**, *31*, 1095–1099.

(223) Tóth, É.; Király, R.; Platzek, J.; Radüchel, B.; Brücher, E. Equilibrium and Kinetic Studies on Complexes of 10-[2,3-dihydroxy-(1-hydroxymethyl)-propyl]-1,4,7,10-tetraazacyclododecane-1,4,7-triacetate. *Inorg. Chim. Acta* **1996**, *249*, 191–199.

(224) Sieber, M. A.; Steger-Hartmann, T.; Lengsfeld, P.; Pietsch, H. Gadolinium-Based Contrast Agents and NSF: Evidence From Animal Experience. *J. Magn. Reson. Imaging* **2009**, *30*, 1268–1276.

(225) Idée, J. M.; Port, M.; Robic, C.; Medina, C.; Sabatou, M.; Corot, C. Role of Thermodynamic and Kinetic Parameters in Gadolinium Chelate Stability. *J. Magn. Reson. Imaging* **2009**, *30*, 1249–1258.

(226) Fretellier, N.; Idée, J.-M.; Dencausse, A.; Karroum, O.; Guerret, S.; Poveda, N.; Jestin, G.; Factor, C.; Raynal, I.; Zamia, P.; et al. Comparative In Vivo Dissociation of Gadolinium Chelates in Renally Impaired Rats: A Relaxometry Study. *Invest. Radiol.* **2011**, *46*, 292–300.

(227) Filippi, M.; Rovaris, M.; Capra, R.; Gasperini, C.; Yousry, T. A.; Sormani, M. P.; Prandini, F.; Horsfield, M. A.; Martinelli, V.; Bastianello, S.; et al. A Multi-Centre Longitudinal Study Comparing the Sensitivity of Monthly MRI after Standard and Triple Dose Gadolinium-DTPA for Monitoring Disease Activity in Multiple Sclerosis - Implications for Phase II Clinical Trials. *Brain* **1998**, *121*, 2011–2020.

(228) Schuhmann-Giampieri, G.; Krestin, G. Pharmacokinetics of Gd-DTPA in Patients with Chronic Renal Failure. *Invest. Radiol.* **1991**, *26*, 975–979.

(229) Joffe, P.; Thomsen, H. S.; Meusel, M. Pharmacokinetics of Gadodiamide Injection in Patients with Severe Renal Insufficiency and Patients Undergoing Hemodialysis or Continuous Ambulatory Peritoneal Dialysis. *Acad. Radiol.* **1998**, *5*, 491–502.

(230) Tombach, B.; Bremer, C.; Reimer, P.; Schaefer, R. M.; Ebert, W.; Geens, V.; Heindel, W. Pharmacokinetics of 1M Gadobutrol in Patients with Chronic Renal Failure. *Invest. Radiol.* **2000**, *35*, 35–40.

(231) Weinmann, H. J.; Laniado, M.; Mutzel, W. Pharmacokinetics of GdDTPA/dimeglumine after Intravenous Injection into Healthy Volunteers. *Physiol. Chem. Phys. Med. NMR* **1984**, *16*, 167–172.

(232) Van Wagoner, M.; O'Toole, M.; Worah, D.; Leese, P. T.; Quay, S. C. A Phase I Clinical Trial with Gadodiamide Injection, a Nonionic Magnetic Resonance Imaging Enhancement Agent. *Invest. Radiol.* **1991**, *26*, 980–986.

(233) McLachlan, S. J.; Eaton, S.; De Simone, D. N. Pharmacokinetic Behavior of Gadoteridol Injection. *Invest. Radiol.* **1992**, *27*, S16.

(234) Van Wagoner, M.; Worah, D. Gadodiamide injection. First Human Experience with the Nonionic Magnetic Resonance Imaging Enhancement Agent. *Invest. Radiol.* **1993**, *28*, S44–S48.

(235) Swan, S. K.; Baker, J. F.; Free, R.; Tucker, R. M.; Barron, B.; Barr, R.; Seltzer, S.; Gazelle, G. S.; Maravilla, K. R.; Barr, W.; et al. Pharmacokinetics, Safety, and Tolerability of Gadoversetamide Injection (OptiMARK) in Subjects with Central Nervous System or Liver Pathology and Varying Degrees of Renal Function. *J. Magn. Reson. Imaging* **1999**, *9*, 317–321.

(236) Baker, J. F.; Kratz, L. C.; Stevens, G. R.; Wible, J. H., Jr. Pharmacokinetics and Safety of the MRI Contrast Agent Gadoversetamide Injection (OptiMARK) in Healthy Pediatric Subjects. *Invest. Radiol.* **2004**, *39*, 334–339.

(237) *Assessment Report for Gadolinium-Containing Contrast Agents*, Proc.No. EMEA/H/A-31/1097; European Medicines Agency, 2010.

(238) *Gadolinium-Based Contrast Agents and Nephrogenic Systemic Fibrosis FDA Briefing Document*; Advisory Committee, 2009.

(239) Yang, L.; Krefting, I.; Gorovets, A.; Marzella, L.; Kaiser, J.; Boucher, R.; Rieves, D. Nephrogenic Systemic Fibrosis and Class Labeling of Gadolinium-Based Contrast Agents by the Food and Drug Administration. *Radiology* 2012, 265, 248−253.

(240) *ACR Manual on Contrast Media v10.1*; American College of Radiology, 2015.

(241) Kanda, T.; Kawaguchi, H. Hyperintense Dentate Nucleas and Globus Pallidus on Unenhanced T1-Weighted MR Images are Associated with Gadolinium-Based Contrast Media. *Neuroradiology* 2013, 55, 1268−1269.

(242) Kanda, T.; ishii, K.; Kawaguchi, H.; Kitajima, K.; Takenaka, D. High Signal Intensity in the Dentate Nucleus and Globus Pallidus on Unenhanced T1-Weighted MR Images: Relationship with Increasing Cumulative Dose of a Gadolinium-Based Contrast Material. *Radiology* 2014, 270, 834−841.

(243) Kanda, T.; Osawa, M.; Oba, H.; Toyoda, K.; Kotoku, J.; Haruyama, T.; Takeshita, K.; Furui, S. High Signal Intensity in Dentate Nucleus on Unenhanced T1-Weighted MR Images: Association with Linear versus Macrocyclic Gadolinium Chelate Administration. *Radiology* 2015, 275, 803−809.

(244) Zhang, Y.; Cao, Y.; Shih, G. L.; Hecht, E. M.; Prince, M. R. Extent of Signal Hyperintensity on Unenhanced T1-Weighted Brain MR Images after More than 35 Administrations of Linear Gadolinium-Based Contrast Agents. *Radiology* 2017, 282, 516−525.

(245) Stojanov, D. A.; Aracki-Trenkic, A.; Vojinovic, S.; Benedeto-Stojanov, D.; Ljubisavljevic, S. Increasing Signal Intensity within the Dentate Nucleus and Globus Pallidus on Unenhanced T1W Magnetic Resonance Images in Patients with Relapsing-Remitting Multiple Sclerosis: Correlation with Cumulative Dose of a Macrocyclic Gadolinium-Based Contrast Agent, Gadobutrol. *Eur. Radiol.* 2016, 26, 807−815.

(246) Splendiani, A.; Perri, M.; Marsecano, C.; Vellucci, V.; Michelini, G.; Barile, A.; Di Cesare, E. Effects of Serial Macrocyclic-Based Contrast Materials Gadoterate Meglumine and Gadobutrol Administrations on Gadolinium-Related Dentate Nuclei Signal Increases in Unenhanced T1-Weighted Brain: A Retrospective Study in 158 Multiple Sclerosis (MS) Patients. *Radiol. Med.* 2018, 123, 125−134.

(247) Radbruch, A.; Weberling, L. D.; Kieslich, P. J.; Hepp, J.; Kickingereder, P.; Wick, W.; Schlemmer, H. P.; Bendszus, M. High-Signal Intensity in the Dentate Nucleus and Globus Pallidus on Unenhanced T1-Weighted Images Evaluation of the Macrocyclic Gadolinium-Based Contrast Agent Gadobutrol. *Invest. Radiol.* 2015, 50, 805−810.

(248) Gibby, W. A.; Gibby, K. A.; Gibby, W. A. Comparison of Gd DTPA-BMA (Omniscan) versus GdHP-DO3A (ProHance) Retention in Human Bone Tissue by Inductively Coupled Plasma Atomic Emission Spectroscopy. *Invest. Radiol.* 2004, 39, 138−142.

(249) Murata, N.; Gonzalez-Cuyar, L. F.; Murata, K.; Fligner, C.; Dills, R.; Hippe, D.; Maravilla, K. R. Macrocyclic and Other Non−Group 1 Gadolinium Contrast Agents Deposit Low Levels of Gadolinium in Brain and Bone Tissue Preliminary Results From 9 Patients With Normal Renal Function. *Invest. Radiol.* 2016, 51, 447−453.

(250) Lord, M. L.; Chettle, D. R.; Grafe, J. L.; Noseworthy, M. D.; McNeill, F. E. Observed Deposition of Gadolinium in Bone Using a New Noninvasive in Vivo Biomedical Device: Results of a Small Pilot Feasibility Study. *Radiology* 2018, 287, 96−103.

(251) Maximova, N.; Gregori, M.; Zennaro, F.; Sonzogni, A.; Simeone, R.; Zanon, D. Hepatic Gadolinium Deposition and Reversibility after Contrast Agent-Enhanced MR Imaging of Pediatric Hematopoietic Stem Cell Transplant Recipients. *Radiology* 2016, 281, 418−426.

(252) George, S. J.; Webb, S. M.; Abraham, J. L.; Cramer, S. P. Synchrotron X-Ray Analyses Demonstrate Phosphate-Bound Gadolinium in Skin in Nephrogenic Systemic Fibrosis. *Br. J. Dermatol.* 2010, 163, 1077−1081.

(253) Birka, M.; Wentker, K. S.; Lusmoller, E.; Arheilger, B.; Wehe, C. A.; Sperling, M.; Stadler, R.; Karst, U. Diagnosis of Nephrogenic Systemic Fibrosis by means of Elemental Bioimaging and Speciation Analysis. *Anal. Chem.* 2015, 87, 3321−3328.

(254) Frenzel, T.; Apte, C.; Jost, G.; Schockel, L.; Lohrke, J.; Pietsch, H. Quantification and Assessment of the Chemical Form of Residual Gadolinium in the Brain After Repeated Administration of Gadolinium-Based Contrast Agents Comparative Study in Rats. *Invest. Radiol.* 2017, 52, 396−404.

(255) Gianolio, E.; Bardini, P.; Arena, F.; Stefania, R.; Di Gregorio, E.; Iani, R.; Aime, S. Gadolinium Retention in the Rat Brain: Assessment of the Amounts of Insoluble Gadolinium-containing Species and Intact Gadolinium Complexes after Repeated Administration of Gadolinium-Based Contrast Agents. *Radiology* 2017, 285, 839−849.

(256) Rees, J. A.; Deblonde, G. J. P.; An, D. D.; Ansoborlo, C.; Gauny, S. S.; Abergel, R. J. Evaluating the Potential of Chelation Therapy to Prevent and Treat Gadolinium Deposition from MRI Contrast Agents. *Sci. Rep.* 2018, 8, DOI: 10.1038/s41598-018-22511-6.

(257) Burke, L. M. B.; Ramalho, M.; AlObaidy, M.; Chang, E.; Jay, M.; Semelka, R. C. Self-Reported Gadolinium Toxicity: A Survey of Patients with Chronic Symptoms. *Magn. Reson. Imaging* 2016, 34, 1078−1080.

(258) Semelka, R. C.; Commander, C.; Jay, M.; Burke, L. M. B.; Ramalho, M. Presumed Gadolinium Toxicity in Subjects With Normal Renal Function: A Report of 4 Cases. *Invest. Radiol.* 2016, 51, 661−665.

(259) Semelka, R. C.; Ramalho, J.; Vakharia, A.; AlObaidy, M.; Burke, L. M.; Jay, M.; Ramalho, M. Gadolinium Deposition Disease: Initial Description of a Disease That Has Been Around for a While. *Magn. Reson. Imaging* 2016, 34, 1383−1390.

(260) Dos Santos Ferreira, D.; Jesus de Oliveira Pinto, B. L.; Kumar, V.; Cardoso, V. N.; Fernandes, S. O.; Souza, C. M.; Cassali, G. D.; Moore, A.; Sosnovik, D. E.; Farrar, C. T.; et al. Evaluation of Antitumor Activity and Cardiac Toxicity of a Bone-Targeted PH-Sensitive Liposomal Formulation in a Bone Metastasis Tumor Model in Mice. *Nanomedicine* 2017, 13, 1693−1701.

(261) *Gadolinium-Based Contrast Agents & Nephrogenic Systemic Fibrosis FDA Briefing Document*; FDA Advisory Committee, 2015.

(262) Desogere, P.; Tapias, L. F.; Hariri, L. P.; Rotile, N. J.; Rietz, T. A.; Probst, C. K.; Blasi, F.; Day, H.; Mino-Kenudson, M.; Weinreb, P., et al. Type I Collagen-Targeted PET Probe for Pulmonary Fibrosis Detection and Staging in Preclinical Models. *Sci. Transl. Med.* 2017, 9, eaaf4696.

(263) United States Renal Data System, 2016. *USRDS Annual Data Report Vol. 1: Chronic Kidney Disease in the United States*; National Institutes of Health, National Institue of Diabetes Digestive and Kidney Diseases: Bethesda, MD, 2016.

(264) United States Renal Data System, 2013. *USRDS Annual Data Report: Atlas of Chronic Kidney Disease and End-Stage Renal Disease in The United States*; National Institutes of Health, National Institute of Diabetes, Digestive and Kidney Diseases: Bethesda, MD, 2013.

(265) Daly, C. Is Early Chronic Kidney Disease an Important Risk Factor for Cardiovascular Disease? A Background Paper Prepared for the UK Consensus Conference on Early Chronic Kidney Disease. *Nephrol., Dial., Transplant.* 2007, 22, ix19−ix25.

(266) Solomon, R. J.; Natarajan, M. K.; Doucet, S.; Sharma, S. K.; Staniloae, C. S.; Katholi, R. E.; Gelormini, J. L.; Labinaz, M.; Moreyra, A. E. Cardiac Angiography in Renally Impaired Patients (CARE) Study: A Randomized Double-Blind Trial of Contrast-Induced Nephropathy in Patients with Chronic Kidney Disease. *Circulation* 2007, 115, 3189−3196.

(267) FDA Orders Stricter Warnings for Ferumoxytol (Feraheme). Medscape Medical News, www.medscape.com/viewarticle/842309 (accessed on April 5, 2018).

(268) Wang, C. L.; Graham, D. J.; Kane, R. C.; Xie, D. Q.; Wernecke, M.; Levenson, M.; MaCurdy, T. E.; Houstoun, M.; Ryan, Q.; Wong, S.; et al. Comparative Risk of Anaphylactic Reactions

Associated With Intravenous Iron Products. *JAMA-J. Am. Med. Assoc.* **2015**, *314*, 2062–2068.

(269) Wedeking, P.; Sotak, C. H.; Telser, J.; Kumar, K.; Chang, C. A.; Tweedle, M. F. Quantitative Dependence of MR Signal Intensity on Tissue Concentration of Gd(HP-DO3A) in the Nephrectomized Rat. *Magn. Reson. Imaging* **1992**, *10*, 97–108.

(270) Werner, E. J.; Datta, A.; Jocher, C. J.; Raymond, K. N. High-Relaxivity MRI Contrast Agents: Where Coordination Chemistry Meets Medical Imaging. *Angew. Chem., Int. Ed.* **2008**, *47*, 8568–8580.

(271) Siriwardena-Mahanama, B. N.; Allen, M. J. Strategies for Optimizing Water-Exchange Rates of Lanthanide-Based Contrast Agents for Magnetic Resonance Imaging. *Molecules* **2013**, *18*, 9352–9381.

(272) Supkowski, R. M.; Horrocks, W. D. Displacement of Inner-Sphere Water Molecules from Eu3+ Analogues of Gd3+ MRI Contrast Agents by Carbonate and Phosphate Anions: Dissociation Constants from Luminescence Data in the Rapid-Exchange Limit. *Inorg. Chem.* **1999**, *38*, 5616–5619.

(273) Kim, W. D.; Kiefer, G. E.; Maton, F.; McMillan, K.; Muller, R. N.; Sherry, A. D. Relaxometry, Luminescence Measurement, Electrophoresis, and Animal Biodistribution of Lanthanide(III) Complexes of Some Polyaza Macrocyclic Acetates Containing Pyridine. *Inorg. Chem.* **1995**, *34*, 2233–2243.

(274) Aime, S.; Botta, M.; Geninatti Crich, S.; Giovenzana, G. B.; Jommi, G.; Pagliarin, R.; Sisti, M. Synthesis and NMR Studies of Three Pyridine-Containing Triaza Macrocyclic Triacetate Ligands and Their Complexes with Lanthanide Ions. *Inorg. Chem.* **1997**, *36*, 2992–3000.

(275) Port, M.; Raynal, I.; Vander Elst, L.; Muller, R. N.; Dioury, F.; Ferroud, C.; Guy, A. Impact of Rigidification on Relaxometric Properties of a Tricyclic Tetraazatriacetic Gadolinium Chelate. *Contrast Media Mol. Imaging* **2006**, *1*, 121–127.

(276) Tircsó, G.; Benyó, E. T.; Suh, E. H.; Jurek, P.; Kiefer, G. E.; Sherry, A. D.; Kovács, Z. (S)-5-(p-Nitrobenzyl)-PCTA, a Promising Bifunctional Ligand with Advantageous Metal Ion Complexation Kinetics. *Bioconjugate Chem.* **2009**, *20*, 565–575.

(277) Brücher, E.; Tircsó, G.; Baranyai, Z.; Kovács, Z.; Sherry, A. D. Stability and Toxicity of Contrast Agents. In *The Chemistry of Contrast Agents in Medical Magnetic Resonance Imaging*, Merbach, A., Helm, L., Tóth, É., Eds.; John Wiley & Sons, Ltd., 2013.

(278) Aime, S.; Calabi, L.; Cavallotti, C.; Gianolio, E.; Giovenzana, G. B.; Losi, P.; Maiocchi, A.; Palmisano, G.; Sisti, M. [Gd-AAZTA]-: A New Structural Entry for an Improved Generation of MRI Contrast Agents. *Inorg. Chem.* **2004**, *43*, 7588–7590.

(279) Elemento, E. M.; Parker, D.; Aime, S.; Gianolio, E.; Lattuada, L. Variation of Water Exchange Dynamics with Ligand Structure and Stereochemistry in Lanthanide Complexes Based on 1,4-Diazepine Derivatives. *Org. Biomol. Chem.* **2009**, *7*, 1120–1131.

(280) Gugliotta, G.; Botta, M.; Giovenzana, G. B.; Tei, L. Fast and Easy Access to Efficient Bifunctional Chelators for MRI Applications. *Bioorg. Med. Chem. Lett.* **2009**, *19*, 3442–3444.

(281) Gale, E. M.; Kenton, N.; Caravan, P. [Gd(CyPic3A)(H2O)-2]-: a Stable, Bis(Aquated) and High-Relaxivity Gd(III) Complex. *Chem. Commun.* **2013**, *49*, 8060–8062.

(282) Messeri, D.; Lowe, M. P.; Parker, D.; Botta, M. A Stable, High Relaxivity, Diaqua Gadolinium Complex that Suppresses Anion and Protein Binding. *Chem. Commun.* **2001**, *0*, 2742–2743.

(283) Datta, A.; Raymond, K. N. Gd−Hydroxypyridinone (HOPO)-Based High-Relaxivity Magnetic Resonance Imaging (MRI) Contrast Agents. *Acc. Chem. Res.* **2009**, *42*, 938–947.

(284) Thompson, M. K.; Botta, M.; Nicolle, G.; Helm, L.; Aime, S.; Merbach, A. E.; Raymond, K. N. A Highly Stable Gadolinium Complex with a Fast, Associative Mechanism of Water Exchange. *J. Am. Chem. Soc.* **2003**, *125*, 14274–14275.

(285) Thompson, M. K.; Misselwitz, B.; Tso, L. S.; Doble, D. M. J.; Schmitt-Willich, H.; Raymond, K. N. In Vivo Evaluation of Gadolinium Hydroxypyridonate Chelates: Initial Experience as Contrast Media in Magnetic Resonance Imaging. *J. Med. Chem.* **2005**, *48*, 3874–3877.

(286) Werner, E. J.; Avedano, S.; Botta, M.; Hay, B. P.; Moore, E. G.; Aime, S.; Raymond, K. N. Highly Soluble Tris-hydroxypyridonate Gd(III) Complexes with Increased Hydration Number, Fast Water Exchange, Slow Electronic Relaxation, and High Relaxivity. *J. Am. Chem. Soc.* **2007**, *129*, 1870–1871.

(287) Hajela, S.; Botta, M.; Giraudo, S.; Xu, J.; Raymond, K. N.; Aime, S. A Tris-hydroxymethyl-Substituted Derivative of Gd-TREN-Me-3,2-HOPO: An MRI Relaxation Agent with Improved Efficiency. *J. Am. Chem. Soc.* **2000**, *122*, 11228–11229.

(288) Fries, P.; Müller, A.; Seidel, R.; Robert, P.; Denda, G.; Menger, M. D.; Schneider, G.; Buecker, A. P03277—A New Approach to Achieve High-Contrast Enhancement: Initial Results of an Experimental Extracellular Gadolinium-Based Magnetic Resonance Contrast Agent. *Invest. Radiol.* **2015**, *50*, 835–842.

(289) Helm, L.; Morrow, J. R.; Bond, C. J.; Carniato, F.; Botta, M.; Braun, M.; Baranyai, Z.; Pujales-Paradela, R.; Regueiro-Figueroa, M.; Esteban-Gomez, D., et al. Gadolinium-Based Contrast Agents. In *Contrast Agents for MRI: Experimental Methods*; The Royal Society of Chemistry, 2018; Chapter 2.

(290) Frullano, L.; Caravan, P. Strategies for the Preparation of Bifunctional Gadolinium(III) Chelators. *Curr. Org. Synth.* **2011**, *8*, 535–565.

(291) Villaraza, A. J. L.; Bumb, A.; Brechbiel, M. W. Macromolecules, Dendrimers, and Nanomaterials in Magnetic Resonance Imaging: The Interplay between Size, Function, and Pharmacokinetics. *Chem. Rev.* **2010**, *110*, 2921–2959.

(292) Venditto, V. J.; Regino, C. A. S.; Brechbiel, M. W. PAMAM Dendrimer Based Macromolecules as Improved Contrast Agents. *Mol. Pharmaceutics* **2005**, *2*, 302–311.

(293) Aime, S.; Castelli, D. D.; Crich, S. G.; Gianolio, E.; Terreno, E. Pushing the Sensitivity Envelope of Lanthanide-Based Magnetic Resonance Imaging (MRI) Contrast Agents for Molecular Imaging Applications. *Acc. Chem. Res.* **2009**, *42*, 822–831.

(294) Lauffer, R. B.; Brady, T. J. Preparation and Water Relaxation Properties of Proteins Labeled with Paramagnetic Metal Chelates. *Magn. Reson. Imaging* **1985**, *3*, 11–16.

(295) Schmiedl, U.; Ogan, M.; Paajanen, H.; Marotti, M.; Crooks, L. E.; Brito, A. C.; Brasch, R. C. Albumin Labeled with Gd-DTPA as an Intravascular, Blood Pool-Enhancing Agent for MR Imaging: Biodistribution and Imaging Studies. *Radiology* **1987**, *162*, 205–210.

(296) Ogan, M. D.; Schmiedl, U.; Moseley, M. E.; Grodd, W.; Paajanen, H.; Brasch, R. C. Albumin Labeled with Gd-DTPA: An Intravascular Contrast-Enhancing Agent for Magnetic Resonance Blood Pool Imaging: Preparation and Characterization. *Invest. Radiol.* **1987**, *22*, 665–671.

(297) Spanoghe, M.; Lanens, D.; Dommisse, R.; Van der Linden, A.; Alderweireldt, F. Proton Relaxation Enhancement by means of Serum Albumin and Poly-L-lysine Labeled with DTPA-Gd3+: Relaxivities as a Function of Molecular Weight and Conjugation Efficiency. *Magn. Reson. Imaging* **1992**, *10*, 913–917.

(298) Schuhmann-Giampieri, G.; Schmitt-Willich, H.; Frenzel, T.; Press, W.-R.; Weinmann, H.-J. In Vivo and In Vitro Evaluation of Gd-DTPA-Polylysine as a Macromolecular Contrast Agent for Magnetic Resonance Imaging. *Invest. Radiol.* **1991**, *26*, 969–974.

(299) Caravan, P.; Greenwood, J. M.; Welch, J. T.; Franklin, S. J. Gadolinium-Binding Helix-Turn-Helix Peptides: DNA-Dependent MRI Contrast Agents. *Chem. Commun.* **2003**, *0*, 2574–2575.

(300) Xue, S.; Qiao, J.; Jiang, J.; Hubbard, K.; White, N.; Wei, L.; Li, S.; Liu, Z. R.; Yang, J. J. Design of ProCAs (Protein-Based Gd3+ MRI Contrast Agents) with High Dose Efficiency and Capability for Molecular Imaging of Cancer Biomarkers. *Med. Res. Rev.* **2014**, *34*, 1070–1099.

(301) Yang, J. J.; Yang, J.; Wei, L.; Zurkiya, O.; Yang, W.; Li, S.; Zou, J.; Zhou, Y.; Maniccia, A. L. W.; Mao, H.; et al. Rational Design of Protein-Based MRI Contrast Agents. *J. Am. Chem. Soc.* **2008**, *130*, 9260–9267.

(302) Wei, L.; Li, S.; Yang, J.; Ye, Y.; Zou, J.; Wang, L.; Long, R.; Zurkiya, O.; Zhao, T.; Johnson, J.; et al. Protein-Based MRI Contrast

Agents for Molecular Imaging of Prostate Cancer. *Mol. Imaging Biol.* **2011**, *13*, 416−423.

(303) Xue, S.; Yang, H.; Qiao, J.; Pu, F.; Jiang, J.; Hubbard, K.; Hekmatyar, K.; Langley, J.; Salarian, M.; Long, R. C.; et al. Protein MRI Contrast Agent with Unprecedented Metal Selectivity and Sensitivity for Liver Cancer Imaging. *Proc. Natl. Acad. Sci. U. S. A.* **2015**, *112*, 6607−6612.

(304) Casali, C.; Janier, M.; Canet, E.; Obadia, J. F.; Benderbous, S.; Corot, C.; Revel, D. Evaluation of Gd-DOTA-Labeled Dextran Polymer as an Intravascular MR Contrast Agent for Myocardial Perfusion. *Acad. Radiol.* **1998**, *5*, 214−218.

(305) Dwek, R. *Nuclear Magnetic Resonance in Biochemistry: Applications To Enzyme Systems*; Clarendon Press, 1973.

(306) Dunand, F. A.; Aime, S.; Merbach, A. E. First 17O NMR Observation of Coordinated Water on Both Isomers of [Eu (DOTAM)(H2O)] 3+: A Direct Access to Water Exchange and its Role in the Isomerization. *J. Am. Chem. Soc.* **2000**, *122*, 1506−1512.

(307) Dunand, F. A.; Borel, A.; Merbach, A. E. How Does Internal Motion Influence the Relaxation of the Water Protons in LnIIIDOTA-like Complexes? *J. Am. Chem. Soc.* **2002**, *124*, 710−716.

(308) Lowe, M. P.; Parker, D.; Reany, O.; Aime, S.; Botta, M.; Castellano, G.; Gianolio, E.; Pagliarin, R. pH-Dependent Modulation of Relaxivity and Luminescence in Macrocyclic Gadolinium and Europium Complexes Based on Reversible Intramolecular Sulfona-mide Ligation. *J. Am. Chem. Soc.* **2001**, *123*, 7601−7609.

(309) Dumas, S.; Jacques, V.; Sun, W.-C.; Troughton, J. S.; Welch, J. T.; Chasse, J. M.; Schmitt-Willich, H.; Caravan, P. High Relaxivity MRI Contrast Agents Part 1: Impact of Single Donor Atom Substitution on Relaxivity of Serum Albumin-Bound Gadolinium Complexes. *Invest. Radiol.* **2010**, *45*, 600−612.

(310) Jacques, V.; Dumas, S.; Sun, W.-C.; Troughton, J. S.; Greenfield, M. T.; Caravan, P. High Relaxivity MRI Contrast Agents Part 2: Optimization of Inner- and Second-Sphere Relaxivity. *Invest. Radiol.* **2010**, *45*, 613−624.

(311) Rudovský, J.; Botta, M.; Hermann, P.; Hardcastle, K. I.; Lukeš, I.; Aime, S. PAMAM Dendrimeric Conjugates with a Gd−DOTA Phosphinate Derivative and Their Adducts with Polyaminoacids: The Interplay of Global Motion, Internal Rotation, and Fast Water Exchange. *Bioconjugate Chem.* **2006**, *17*, 975−987.

(312) Nicolle, G. M.; Tóth, É.; Eisenwiener, K.-P.; Mäcke, H. R.; Merbach, A. E. From Monomers to Micelles: Investigation of the Parameters Influencing Proton Relaxivity. *JBIC, J. Biol. Inorg. Chem.* **2002**, *7*, 757−769.

(313) Carniato, F.; Tei, L.; Dastru, W.; Marchese, L.; Botta, M. Relaxivity Modulation in Gd-Functionalised Mesoporous Silicas. *Chem. Commun.* **2009**, *0*, 1246−1248.

(314) Yerly, F.; Borel, A.; Helm, L.; Merbach, A. E. MD Simulations of Acyclic and Macrocyclic Gd3+-Based MRI Contrast Agents: Influence of the Internal Mobility on Water Proton Relaxivity. *Chem. - Eur. J.* **2003**, *9*, 5468−5480.

(315) Lipari, G.; Szabo, A. Model-Free Approach to the Interpretation of Nuclear Magnetic Resonance Relaxation in Macro-molecules. 1. Theory and Range of Validity. *J. Am. Chem. Soc.* **1982**, *104*, 4546−4559.

(316) Port, M.; Meyer, D.; Bonnemain, B.; Corot, C.; Schaefer, M.; Rousseaux, O.; Simonot, C.; Bourrinet, P.; Benderbous, S.; Dencausse, A.; et al. P760 and P775: MRI Contrast Agents Characterized by New Pharmacokinetic Properties. *Magn. Reson. Mater. Phys.* **1999**, *8*, 172−176.

(317) Fulton, D. A.; O'Halloran, M.; Parker, D.; Senanayake, K.; Botta, M.; Aime, S. Efficient Relaxivity Enhancement in Dendritic Gadolinium Complexes: Effective Motional Coupling in Medium Molecular Weight Conjugates. *Chem. Commun.* **2005**, *0*, 474−476.

(318) Jacques, V.; Desreux, J. F. New Classes of MRI Contrast Agents. In *Contrast Agents I: Magnetic Resonance Imaging*, Krause, W., Ed.; Springer: Berlin, 2002.

(319) Livramento, J. B.; Tóth, É.; Sour, A.; Borel, A.; Merbach, A. E.; Ruloff, R. High Relaxivity Confined to a Small Molecular Space: A

Metallostar-Based, Potential MRI Contrast Agent. *Angew. Chem., Int. Ed.* **2005**, *44*, 1480−1484.

(320) Livramento, J. B.; Weidensteiner, C.; Prata, M. I. M.; Allegrini, P. R.; Geraldes, C. F. G. C.; Helm, L.; Kneuer, R.; Merbach, A. E.; Santos, A. C.; Schmidt, P.; et al. First In Vivo MRI Assessment of a Self-Assembled Metallostar Compound Endowed with a Remarkable High Field Relaxivity. *Contrast Media Mol. Imaging* **2006**, *1*, 30−39.

(321) Zhang, Z.; Greenfield, M. T.; Spiller, M.; McMurry, T. J.; Lauffer, R. B.; Caravan, P. Multilocus Binding Increases the Relaxivity of Protein-Bound MRI Contrast Agents. *Angew. Chem., Int. Ed.* **2005**, *44*, 6766−6769.

(322) Kielar, F.; Tei, L.; Terreno, E.; Botta, M. Large Relaxivity Enhancement of Paramagnetic Lipid Nanoparticles by Restricting the Local Motions of the Gd(III) Chelates. *J. Am. Chem. Soc.* **2010**, *132*, 7836−7837.

(323) Filippi, M.; Remotti, D.; Botta, M.; Terreno, E.; Tei, L. GdDOTAGA(C18)2: An Efficient Amphiphilic Gd(III) Chelate for the Preparation of Self-Assembled High Relaxivity MRI Nanoprobes. *Chem. Commun.* **2015**, *51*, 17455−17458.

(324) Boros, E.; Polasek, M.; Zhang, Z.; Caravan, P. Gd(DOTAla): A Single Amino Acid Gd-complex as a Modular Tool for High Relaxivity MR Contrast Agent Development. *J. Am. Chem. Soc.* **2012**, *134*, 19858−19868.

(325) Paris, J.; Gameiro, C.; Humblet, V.; Mohapatra, P. K.; Jacques, V.; Desreux, J. F. Auto-Assembling of Ditopic Macrocyclic Lanthanide Chelates with Transition-Metal Ions. Rigid Multimetallic High Relaxivity Contrast Agents for Magnetic Resonance Imaging. *Inorg. Chem.* **2006**, *45*, 5092−5102.

(326) Song, Y.; Kohlmeir, E. K.; Meade, T. J. Synthesis of Multimeric MR Contrast Agents for Cellular Imaging. *J. Am. Chem. Soc.* **2008**, *130*, 6662−6663.

(327) Pierre, V. C.; Botta, M.; Aime, S.; Raymond, K. N. Fe(III)-Templated Gd(III) Self-AssembliesA New Route toward Macro-molecular MRI Contrast Agents. *J. Am. Chem. Soc.* **2006**, *128*, 9272−9273.

(328) Mastarone, D. J.; Harrison, V. S. R.; Eckermann, A. L.; Parigi, G.; Luchinat, C.; Meade, T. J. A Modular System for the Synthesis of Multiplexed Magnetic Resonance Probes. *J. Am. Chem. Soc.* **2011**, *133*, 5329−5337.

(329) Livramento, J. B.; Sour, A.; Borel, A.; Merbach, A. E.; Tóth, É. A Starburst-Shaped Heterometallic Compound Incorporating Six Densely Packed Gd3+ Ions. *Chem. - Eur. J.* **2006**, *12*, 989−1003.

(330) Fulton, D. A.; Elemento, E. M.; Aime, S.; Chaabane, L.; Botta, M.; Parker, D. Glycoconjugates of Gadolinium Complexes for MRI Applications. *Chem. Commun.* **2006**, *0*, 1064−1066.

(331) Troughton, J. S.; Greenfield, M. T.; Greenwood, J. M.; Dumas, S.; Wiethoff, A. J.; Wang, J.; Spiller, M.; McMurry, T. J.; Caravan, P. Synthesis and Evaluation of a High Relaxivity Manganese(II)-Based MRI Contrast Agent. *Inorg. Chem.* **2004**, *43*, 6313−6323.

(332) Aime, S.; Anelli, P. L.; Botta, M.; Brocchetta, M.; Canton, S.; Fedeli, F.; Gianolio, E.; Terreno, E. Relaxometric Evaluation of Novel Manganese(II) Complexes for Application as Contrast Agents in Magnetic Resonance Imaging. *JBIC, J. Biol. Inorg. Chem.* **2002**, *7*, 58−67.

(333) Cheng, W.; Ganesh, T.; Martinez, F.; Lam, J.; Yoon, H.; Macgregor, R. B.; Scholl, T. J.; Cheng, H.-L. M.; Zhang, X.-a. Binding of a Dimeric Manganese Porphyrin to Serum Albumin: Towards a Gadolinium-Free Blood-Pool T 1 MRI Contrast Agent. *JBIC, J. Biol. Inorg. Chem.* **2014**, *19*, 229−235.

(334) Zhu, J.; Gale, E. M.; Atanasova, I.; Rietz, T. A.; Caravan, P. Hexameric MnII Dendrimer as MRI Contrast Agent. *Chem. - Eur. J.* **2014**, *20*, 14507−14513.

(335) Tóth, É.; Pubanz, D.; Vauthey, S.; Helm, L.; Merbach, A. E. The Role of Water Exchange in Attaining Maximum Relaxivities for Dendrimeric MRI Contrast Agents. *Chem. - Eur. J.* **1996**, *2*, 1607−1615.

(336) Toth, E.; Burai, L.; Brucher, E.; Merbach, A. E. Tuning Water-Exchange Rates on (carboxymethyl)iminobis(ethylenenitrilo)-

tetraacetate (dtpa)-type Gadolinium(III) Complexes. *J. Chem. Soc., Dalton Trans.* **1997**, 1587–1594.

(337) Laus, S.; Ruloff, R.; Tóth, É.; Merbach, A. E. GdIII Complexes with Fast Water Exchange and High Thermodynamic Stability: Potential Building Blocks for High-Relaxivity MRI Contrast Agents. *Chem. - Eur. J.* **2003**, 9, 3555–3566.

(338) Jaszberenyi, Z.; Sour, A.; Toth, E.; Benmelouka, M.; Merbach, A. E. Fine-Tuning Water Exchange on GdIII Poly(Amino Carboxylates) by Modulation of Steric Crowding. *Dalton Trans* **2005**, 0, 2713–2719.

(339) Boros, E.; Gale, E. M.; Caravan, P. MR Imaging Probes: Design and Applications. *Dalton Trans* **2015**, 44, 4804–4818.

(340) Rudovsky, J.; Kotek, J.; Hermann, P.; Lukes, I.; Mainero, V.; Aime, S. Synthesis of a Bifunctional Monophosphinic Acid DOTA Analogue Ligand and its Lanthanide(III) Complexes. A Gadolinium-(III) Complex Endowed with an Optimal Water Exchange Rate for MRI Applications. *Org. Biomol. Chem.* **2005**, 3, 112–117.

(341) Polasek, M.; Rudovsky, J.; Hermann, P.; Lukes, I.; Elst, L. V.; Muller, R. N. Lanthanide(III) Complexes of a Pyridine N-Cxide Analogue of DOTA: Exclusive M Isomer Formation Induced by a Six-Membered Chelate Ring. *Chem. Commun.* **2004**, 0, 2602–2603.

(342) Boros, E.; Karimi, S.; Kenton, N.; Helm, L.; Caravan, P. Gd(DOTAlaP): Exploring the Boundaries of Fast Water Exchange in Gadolinium-Based Magnetic Resonance Imaging Contrast Agents. *Inorg. Chem.* **2014**, 53, 6985–6994.

(343) Bruckman, M. A.; Yu, X.; Steinmetz, N. F. Engineering Gd-Loaded Nanoparticles to Enhance MRI Sensitivity via T_1 Shortening. *Nanotechnology* **2013**, 24, 462001–462020.

(344) Huang, C.-H.; Tsourkas, A. Gd-Based Macromolecules and Nanoparticles as Magnetic Resonance Contrast Agents for Molecular Imaging. *Curr. Top. Med. Chem.* **2013**, 13, 411–421.

(345) Yang, C.-T.; Padmanabhan, P.; Gulyas, B. Z. Gadolinium(iii) Based Nanoparticles for T1-Weighted Magnetic Resonance Imaging Probes. *RSC Adv.* **2016**, 6, 60945–60966.

(346) Nicolay, K.; Strijkers, G.; Grüll, H. Gd-Containing Nanoparticles as MRI Contrast Agents. In *The Chemistry of Contrast Agents in Medical Magnetic Resonance Imaging*; Merbach, A., Helm, L., Tóth, É., Eds.; John Wiley & Sons, Ltd., 2013.

(347) Sitharaman, B.; Wilson, L. J. Gadofullerenes and Gadonanotubes: A New Paradigm for High-Performance Magnetic Resonance Imaging Contrast Agent Probes. *J. Biomed. Nanotechnol.* **2007**, 3, 342–352.

(348) Sitharaman, B.; Kissell, K. R.; Hartman, K. B.; Tran, L. A.; Baikalov, A.; Rusakova, I.; Sun, Y.; Khant, H. A.; Ludtke, S. J.; Chiu, W.; et al. Superparamagnetic Gadonanotubes are High-Performance MRI Contrast Agents. *Chem. Commun.* **2005**, 0, 3915–3917.

(349) Manus, L. M.; Mastarone, D. J.; Waters, E. A.; Zhang, X.-Q.; Schultz-Sikma, E. A.; MacRenaris, K. W.; Ho, D.; Meade, T. J. Gd(III)-Nanodiamond Conjugates for MRI Contrast Enhancement. *Nano Lett.* **2010**, 10, 484–489.

(350) Wartenberg, N.; Fries, P.; Raccurt, O.; Guillermo, A.; Imbert, D.; Mazzanti, M. A Gadolinium Complex Confined in Silica Nanoparticles as a Highly Efficient T1/T2MRI Contrast Agent. *Chem. - Eur. J.* **2013**, 19, 6980–6983.

(351) Courant, T.; Roullin, V. G.; Cadiou, C.; Callewaert, M.; Andry, M. C.; Portefaix, C.; Hoeffel, C.; de Goltstein, M. C.; Port, M.; Laurent, S.; et al. Hydrogels Incorporating GdDOTA: Towards Highly Efficient Dual T1/T2MRI Contrast Agents. *Angew. Chem., Int. Ed.* **2012**, 51, 9119–9122.

(352) Balogh, E.; Tripier, R.; Fouskova, P.; Reviriego, F.; Handel, H.; Toth, E. Monopropionate Analogues of DOTA4- and DTPA5-: Kinetics of Formation and Dissociation of their Lanthanide(III) Complexes. *Dalton Trans* **2007**, 3572–3581.

(353) Clarke, E. T.; Martell, A. E. Stabilities of Trivalent Metal Ion Complexes of the Tetraacetate Derivatives of 12-, 13- and 14-Membered Tetraazamacrocycles. *Inorg. Chim. Acta* **1991**, 190, 37–46.

(354) Balogh, E.; Tripier, R.; Ruloff, R.; Toth, E. Kinetics of Formation and Dissociation of Lanthanide(III) Complexes with the

13-Membered Macrocyclic Ligand TRITA4. *Dalton Trans* **2005**, 1058–1065.

(355) Pálinkás, Z.; Roca-Sabio, A.; Mato-Iglesias, M.; Esteban-Gómez, D.; Platas-Iglesias, C.; de Blas, A.; Rodríguez-Blas, T.; Tóth, É. Stability, Water Exchange, and Anion Binding Studies on Lanthanide(III) Complexes with a Macrocyclic Ligand Based on 1,7-Diaza-12-crown-4: Extremely Fast Water Exchange on the Gd3+ Complex. *Inorg. Chem.* **2009**, 48, 8878–8889.

(356) Tircsó, G.; Regueiro-Figueroa, M.; Nagy, V.; Garda, Z.; Garai, T.; Kálmán, F. K.; Esteban-Gómez, D.; Tóth, É.; Platas-Iglesias, C. Approaching the Kinetic Inertness of Macrocyclic Gadolinium(III)-Based MRI Contrast Agents with Highly Rigid Open-Chain Derivatives. *Chem. - Eur. J.* **2016**, 22, 896–901.

(357) Rodríguez-Rodríguez, A.; Esteban-Gómez, D.; Tripier, R.; Tircsó, G.; Garda, Z.; Tóth, I.; de Blas, A.; Rodríguez-Blas, T.; Platas-Iglesias, C. Lanthanide(III) Complexes with a Reinforced Cyclam Ligand Show Unprecedented Kinetic Inertness. *J. Am. Chem. Soc.* **2014**, 136, 17954–17957.

(358) Dai, L.; Jones, C. M.; Chan, W. T. K.; Pham, T. A.; Ling, X.; Gale, E. M.; Rotile, N. J.; Tai, W. C.-S.; Anderson, C. J.; Caravan, P., et al. Chiral DOTA Chelators as an Improved Platform for Biomedical Imaging and Therapy Applications. *Nat. Commun.* **2018**, 9, DOI: 10.1038/s41467-018-03315-8.

(359) Bolskar, R. D. Gadofullerene MRI Contrast Agents. *Nanomedicine* **2008**, 3, 201–213.

(360) Chen, Z.; Ma, L.; Liu, Y.; Chen, C. Applications of Functionalized Fullerenes in Tumor Theranostics. *Theranostics* **2012**, 2, 238–250.

(361) Aihara, J.-i. Kinetic Stability of Metallofullerenes as Predicted by the Bond Resonance Energy Model. *Phys. Chem. Chem. Phys.* **2001**, 3, 1427–1431.

(362) Drahoš, B.; Lukeš, I.; Tóth, E. Mn(II) Complexes as Potential Contrast Agents for MRI. *Eur. J. Inorg. Chem.* **2012**, 2012, 1975–1986.

(363) Kálmán, F. K.; Tircsó, G. Kinetic Inertness of the Mn Complexes Formed with AAZTA and Some Open-Chain EDTA Derivatives. *Inorg. Chem.* **2012**, 51, 10065–10067.

(364) Rolla, G. A.; Platas-Iglesias, C.; Botta, M.; Tei, L.; Helm, L. 1H and 17O NMR Relaxometric and Computational Study on Macrocyclic Mn(II) Complexes. *Inorg. Chem.* **2013**, 52, 3268–3279.

(365) Drahoš, B.; Pniok, M.; Havlíčková, J.; Kotek, J.; Císařová, I.; Hermann, P.; Lukeš, I.; Tóth, E. Mn2+ Complexes of 1-oxa-4,7-Diazacyclononane Based Ligands with Acetic, Phosphonic, and Phosphinic Acid Pendant Arms: Stability and Relaxation Studies. *Dalton Trans* **2011**, 40, 10131–10146.

(366) Drahoš, B.; Kotek, J.; Císařová, I.; Hermann, P.; Helm, L.; Lukeš, I.; Tóth, E. Mn2+ Complexes with 12-member Pyridine Based Macrocycles Bearing Carboxylate or Phosphonate Pendant Arm: Crystallographic, Thermodynamic, Kinetic, Redox and 1H/ 17O Relaxation Studies. *Inorg. Chem.* **2011**, 50, 12785–12801.

(367) Drahoš, B.; Kotek, J.; Hermann, P.; Lukeš, I.; Tóth, E. Mn2+ Complexes with Pyridine Containing 15-Membered Macrocycles: Thermodynamic, Kinetic, Crystallographic and 1H/ 17O Relaxation Studies. *Inorg. Chem.* **2010**, 49, 3224–3238.

(368) Tei, L.; Gugliotta, G.; Fekete, M.; Kálmán, F. K.; Botta, M. Mn(II) Complexes of Novel Hexadentate AAZTA-like Chelators: A Solution Thermodynamics and Relaxometric Study. *Dalton Trans* **2011**, 40, 2025–2032.

(369) Su, H.; Wu, C.; Zhu, J.; Miao, T.; Wang, D.; Xia, C.; Zhao, X.; Gong, Q.; Song, B.; Ai, H. Rigid Mn(II) Chelate as Efficient MRI Contrast Agent for Vascular Imaging. *Dalton Trans* **2012**, 41, 14480–14483.

(370) Rocklage, S. M.; Cacheris, W. P.; Quay, S. C.; Hahn, F. E.; Raymond, K. N. Manganese(II) N,N'-dipyrodoxylethelynediamine-N,N'-diacetate 5,5'-bis(phosphate). Synthesis and Characterization of a Paramagnetic Chelate for Magnetic Resonance Imaging Enhancement. *Inorg. Chem.* **1989**, 28, 477–485.

(371) Gale, E. M.; Mukherjee, S.; Liu, C.; Loving, G. S.; Caravan, P. Structure-Redox-Relaxivity Relationships for Redox Responsive

Manganese-Based Magnetic Resonance Imaging Probes. *Inorg. Chem.* **2014**, *53*, 10748−10761.

(372) Bianchi, A.; Calabi, L.; Giorgi, C.; Losi, P.; Mariani, P.; Palano, D.; Paoli, P.; Rossi, P.; Valtancoli, B. Thermodynamic and Structural Aspects of Manganese(II) Complexes with Polyaminopolycarboxylic Ligands Based upon 1,4,7,10- tetraazacyclododecane (cyclen). Crystal Structure of Dimeric [MnL]2−2CH3OH Containing the New Ligand 1,4,7,10-Tetraaza- Cyclododecane-1,4-Diacetate. *J. Chem. Soc., Dalton Trans.* **2001**, *0*, 917−922.

(373) Cortes, S.; Brücher, E.; Geraldes, C. F. G. C.; Sherry, A. D. Potentiometry and NMR Studies of 1,5,9-Triazacyclododecane-N,N',N''-Triacetic Acid and its Metal Ion Complexes. *Inorg. Chem.* **1990**, *29*, 5−9.

(374) Drahoš, B.; Kubíček, V.; Bonnet, C. S.; Hermann, P.; Lukeš, I.; Tóth, E. Dissociation kinetics of Mn²⁺ complexes of NOTA and DOTA. *Dalton Trans* **2011**, *40*, 1945−1951.

(375) de Sá, A.; Bonnet, C. S.; Geraldes, C. F. G. C.; Tóth, É.; Ferreira, P. M. T.; André, J. P. Thermodynamic Stability and Relaxation Studies of Small, Triaza-Macrocyclic Mn(II) Chelates. *Dalton Trans* **2013**, *42*, 4522−4532.

(376) Balogh, E.; He, Z.; Hsieh, W.; Liu, S.; Tóth, E. Dinuclear Complexes Formed with the Triazacyclononane Derivative ENOTA4-: High-Pressure 17O NMR Evidence of an Associative Water Exchange on [Mn(II)2(ENOTA)(H2O)2]. *Inorg. Chem.* **2007**, *46*, 238−250.

(377) Gale, E. M.; Atanasova, I.; Blasi, F.; Ay, I.; Caravan, P. A Manganese Alternative to Gadolinium for MRI Contrast. *J. Am. Chem. Soc.* **2015**, *137*, 15548−15557.

(378) Gale, E. M.; Wey, H. Y.; Ramsay, I.; Yen, Y. F.; Sosnovik, D.; Caravan, P. A Manganese-Based Alternative to Gadolinium: Contrast Enhanced MR Angiography, Pharmacokinetics, and Metabolism. *Radiology* **2018**, *286*, 865−872.

(379) Koenig, S. H.; Brown, R. D., III; Spiller, M. The Anamolous Relaxivity of Mn3+(TPPS4). *Magn. Reson. Med.* **1987**, *4*, 252−260.

(380) Barandov, A.; Bartelle, B. B.; Gonzalez, B. A.; White, W. L.; Lippard, S. J.; Jasanoff, A. Membrane-Permeable Mn(III) Complexes for Molecular Magnetic Resonance Imaging of Intracellular Targets. *J. Am. Chem. Soc.* **2016**, *138*, 5483−5486.

(381) Dees, A.; Zahl, A.; Puchta, R.; van Eikema Hommes, N. J. R.; Heinemann, F. W.; Ivanović-Burmazović, I. Water Exchange on Seven-Coordinate Mn(II) Complexes with Macrocyclic Pentadentate Ligands: Insight in the Mechanism of Mn(II) SOD Mimetics. *Inorg. Chem.* **2007**, *46*, 2459−2470.

(382) Aime, S.; Botta, M.; Gianolio, E.; Terreno, E. A p(O2)-Responsive MRI Contrast Agent Based on the Redox Switch of Manganese(II/III) − Porphyrin Complexes. *Angew. Chem., Int. Ed.* **2000**, *39*, 747−750.

(383) Cheng, H. L. M.; Haedicke, I. E.; Cheng, W. R.; Nofiele, J. T.; Zhang, X. A. Gadolinium-Free T-1 Contrast Agents for MRI: Tunable Pharmacokinetics of a New Class of Manganese Porphyrins. *J. Magn. Reson. Imaging* **2014**, *40*, 1474−1480.

(384) Cheng, W.; Haedicke, I. E.; Nofiele, J.; Martinez, F.; Beera, K.; Scholl, T. J.; Cheng, H.-L. M.; Zhang, X.-a. Complementary Strategies for Developing Gd-Free High-Field T1MRI Contrast Agents Based on Mn(III) Porphyrins. *J. Med. Chem.* **2014**, *57*, 516−520.

(385) Cheng, W.; Ganesh, T.; Martinez, F.; Lam, J.; Yoon, H.; Macgregor, R. B.; Scholl, T. J.; Cheng, H.-L. M.; Zhang, X.-a. Binding of a Dimeric Manganese Porphyrin to Serum Albumin: Towards a Gadolinium-Free Blood-Pool T-1 MRI Contrast Agent. *JBIC, J. Biol. Inorg. Chem.* **2014**, *19*, 229−235.

(386) Schmiedl, U. P.; Nelson, J. A.; Starr, F. L.; Schmidt, R. Hepatic Contrast-Enhancing Properties of Manganese-Mesoporphyrin and Manganese-TPPS4. A Comparative Magnetic Resonance Imaging Study in Rats. *Invest. Radiol.* **1992**, *27*, 536−542.

(387) Schmiedl, U. P.; Nelson, J. A.; Robinson, D. H.; Michalson, A.; Starr, F.; Frenzel, T.; Ebert, W.; Schumanngiampieri-Giampier, G. Pharmaceutical Properties, Biodistribution, and Imaging Characteristics of Manganese-Mesoporphyrin. A Potential Hepatobiliary

Contrast Agent for Magnetic Resonance Imaging. *Invest. Radiol.* **1993**, *28*, 925−932.

(388) Zhang, Z.; He, R.; Yan, K.; Guo, Q. N.; Lu, Y. G.; Wang, X. X.; Lei, H.; Li, Z. Y. Synthesis and In Vitro and In Vivo Evaluation of Manganese(III) Porphyrin-Dextran as a Novel MRI Contrast Agent. *Bioorg. Med. Chem. Lett.* **2009**, *19*, 6675−6678.

(389) Boehm-Sturm, P.; Haeckel, A.; Hauptmann, R.; Mueller, S.; Kuhl, C. K.; Schellenberger, E. A. Low-Molecular-Weight Iron Chelates May Be an Alternative to Gadolinium-Based Contrast Agents for T1-Weighted Contrast-Enhanced MR Imaging. *Radiology* **2018**, *286*, 537−546.

(390) Lauffer, R. B.; Greif, W. L.; Stark, D. D.; Vincent, A. C.; Saini, S.; Wedeen, V. J.; Brady, T. J. Iron-EHPG as an Hepatobilliary MR Contrast Agent: Initial Imaging and Biodistribution Studies. *J. Comput. Assist. Tomogr.* **1985**, *9*, 431−438.

(391) Larsen, S. K.; Jenkins, B. G.; Memon, N. G.; Lauffer, R. B. Structure-Affinity Relationships in the Binding of Unsubstituted Iron Phenolate Complexes to Human Serum Albumin. Molecular Structure of Iron(III) N, N'-bis(2-hydroxybenzyl)ethylenediamine-N,N'-diacetate. *Inorg. Chem.* **1990**, *29*, 1147−1152.

(392) Jenkins, B. G.; Armstrong, E.; Lauffer, R. B. Site-Specific Water Proton Relaxation Enhancement of Iron(III) Chelates Noncovalently Bound to Human Serum Albumin. *Magn. Reson. Med.* **1991**, *17*, 164−178.

(393) Touti, F.; Singh, A. K.; Maurin, P.; Canaple, L.; Beuf, O.; Samarut, J.; Hasserodt, J. An Electroneutral Macrocyclic Iron(II) Complex That Enhances MRI Contrast in Vivo. *J. Med. Chem.* **2011**, *54*, 4274−4278.

(394) Wang, J.; Gondrand, C.; Touti, F.; Hasserodt, J. A Pair of Highly Biotolerated Diamagnetic and Paramagnetic Iron(II) Complexes Displaying Electroneutrality. *Dalton Trans* **2015**, *44*, 15391−15395.

(395) Caravan, P.; Tóth, E.; Rockenbauer, A.; Merbach, A. E. Nuclear and Electronic Relaxation of Eu2+(aq): An Extremely Labile Aqua Ion. *J. Am. Chem. Soc.* **1999**, *121*, 10403−10409.

(396) Caravan, P.; Merbach, A. E. An Extreme Water Exchange Rate: The Europium(II) Aqua Ion. *Chem. Commun.* **1997**, *0*, 2147−2148.

(397) Seibig, S.; Toth, E.; Merbach, A. E. Unexpected Differences in the Dynamics and in the Nuclear and Electronic Relaxation Properties of the Isoelectronic Eu-II(DTPA)(H2O) (3-) and Gd-III(DTPA)-(H2O) (2-) complexes (DTPA = diethylenetriamine pentaacetate). *J. Am. Chem. Soc.* **2000**, *122*, 5822−5830.

(398) Burai, L.; Toth, E.; Seibig, S.; Scopelliti, R.; Merbach, A. E. High-Pressure NMR Kinetics, Part 95 - Solution and Solid-State Characterization of Eu-II Chelates: A Possible Route Towards Redox Responsive MRI Contrast Agents. *Chem. - Eur. J.* **2000**, *6*, 3761−3770.

(399) Burai, L.; Scopelliti, R.; Toth, E. Eu-II-Cryptate with Optimal Water Exchange and Electronic Relaxation: A Synthon for Potential pO(2) Responsive Macromolecular MRI Contrast Agents. *Chem. Commun.* **2002**, *0*, 2366−2367.

(400) Gamage, N. D. H.; Mei, Y. J.; Garcia, J.; Allen, M. J. Oxidatively Stable, Aqueous Europium(II) Complexes through Steric and Electronic Manipulation of Cryptand Coordination Chemistry. *Angew. Chem., Int. Ed.* **2010**, *49*, 8923−8925.

(401) Garcia, J.; Kuda-Wedagedara, A. N. W.; Allen, M. J. Physical Properties of Eu2+-Containing Cryptates as Contrast Agents for Ultrahigh-Field Magnetic Resonance Imaging. *Eur. J. Inorg. Chem.* **2012**, *2012*, 2135−2140.

(402) Kuda-Wedagedara, A. N. W.; Allen, M. J. Enhancing Magnetic Resonance Imaging with Contrast Agents for Ultra-High Field Strengths. *Analyst* **2014**, *139*, 4401−4410.

(403) Garcia, J.; Neelavalli, J.; Haacke, E. M.; Allen, M. J. Eu-II-Containing Cryptates as Contrast Agents for Ultra-High Field Strength Magnetic Resonance Imaging. *Chem. Commun.* **2011**, *47*, 12858−12860.

(404) Laurent, S.; Vander Elst, L.; Henoumont, C.; Muller, R. N. How to Measure the Transmetallation of a Gadolinium Complex. *Contrast Media Mol. Imaging* **2010**, *5*, 305−308.

(405) Ekanger, L. A.; Ali, M. M.; Allen, M. J. Oxidation-Responsive Eu2+/3+-Liposomal Contrast Agent for Dual-Mode Magnetic Resonance Imaging. *Chem. Commun.* **2014**, *50*, 14835−14838.

(406) Ekanger, L. A.; Polin, L. A.; Shen, Y.; Haacke, E. M.; Martin, P. D.; Allen, M. J. A EuII-Containing Cryptate as aRedoxSensor in Magnetic ResonanceImaging of Living Tissue. *Angew. Chem., Int. Ed.* **2015**, *54*, 14398−14401.

(407) Basal, L. A.; Yan, Y.; Shen, Y. M.; Haacke, E. M.; Mehrmohammadi, M.; Allen, M. J. Oxidation-Responsive, Eu-II/III-Based, Multimodal Contrast Agent for Magnetic Resonance and Photoacoustic Imaging. *ACS Omega* **2017**, *2*, 800−805.

(408) Ekanger, L. A.; Polin, L. A.; Shen, Y. M.; Haacke, E. M.; Allen, M. J. Evaluation of Eu-II-Based Positive Contrast Enhancement after Intravenous, Intraperitoneal, and Subcutaneous Injections. *Contrast Media Mol. Imaging* **2016**, *11*, 299−303.

(409) Ekanger, L. A.; Basal, L. A.; Allen, M. J. The Role of Coordination Environment and pH in Tuning the Oxidation Rate of Europium(II). *Chem. - Eur. J.* **2017**, *23*, 1145−1150.

(410) Lenora, C. U.; Carniato, F.; Shen, Y. M.; Latif, Z.; Haacke, E. M.; Martin, P. D.; Botta, M.; Allen, M. J. Structural Features of Europium(II)-Containing Cryptates That Influence Relaxivity. *Chem. - Eur. J.* **2017**, *23*, 15404−15414.

(411) Lovin, J.; Wesbey, G.; Engelstad, B.; Brasch, R.; Sosnovsky, G.; Moseley, M.; McNamara, M.; Ehman, R. Structure-Relaxivity Relationships for Piperidine Nitroxide Spin Labels - MRI Contrast Agents. *Invest. Radiol.* **1984**, *19*, 24−24.

(412) Vallet, P.; Vanhaverbeke, Y.; Bonnet, P. A.; Subra, G.; Chapat, J. P.; Muller, R. N. Relaxivity Enhancement of Low Molecular Weight Nitroxide Stable Free Radicals: Importance of Structure and Medium. *Magn. Reson. Med.* **1994**, *32*, 11−15.

(413) Winalski, C. S.; Shortkroff, S.; Mulkern, R. V.; Schneider, E.; Rosen, G. M. Magnetic Resonance Relaxivity of Dendrimer-Linked Nitroxides. *Magn. Reson. Med.* **2002**, *48*, 965−972.

(414) Emoto, M. C.; Yamada, K.; Yamato, M.; Fujii, H. G. Novel Ascorbic Acid-Resistive Nitroxide in a Lipid Emulsion: An Efficient Brain Imaging Contrast Agent for MRI of small rodents. *Neurosci. Lett.* **2013**, *546*, 11−15.

(415) Bye, N.; Hutt, O. E.; Hinton, T. M.; Acharya, D. P.; Waddington, L. J.; Moffat, B. A.; Wright, D. K.; Wang, H. X.; Mulet, X.; Muir, B. W. Nitroxide-Loaded Hexosomes Provide MRI Contrast in Vivo. *Langmuir* **2014**, *30*, 8898−8906.

(416) Hyodo, F.; Matsumoto, K.; Matsumoto, A.; Mitchell, J. B.; Krishna, M. C. Probing The Intracellular Redox Status of Tumors with Magnetic Resonance Imaging and Redox-Sensitive Contrast Agents. *Cancer Res.* **2006**, *66*, 9921−9928.

(417) Davis, R. M.; Matsumoto, S.; Bernardo, M.; Sowers, A.; Matsumoto, K. I.; Krishna, M. C.; Mitchell, J. B. Magnetic Resonance Imaging of Organic Contrast Agents in Mice: Capturing the Whole-Body Redox Landscape. *Free Radical Biol. Med.* **2011**, *50*, 459−468.

(418) Bakalova, R.; Zhelev, Z.; Aoki, I.; Saga, T. Tissue Redox Activity as a Hallmark of Carcinogenesis: From Early to Terminal Stages of Cancer. *Clin. Cancer Res.* **2013**, *19*, 2503−2517.

(419) Zhelev, Z.; Aoki, I.; Gadjeva, V.; Nikolova, B.; Bakalova, R.; Saga, T. Tissue Redox Activity as a Sensing Platform for Imaging of Cancer Based on Nitroxide Redox Cycle. *Eur. J. Cancer* **2013**, *49*, 1467−1578.

(420) Zhelev, Z.; Bakalova, R.; Aoki, I.; Lazarova, D.; Saga, T. Imaging of Superoxide Generation in the Dopaminergic Area of the Brain in Parkinson's Disease, Using Mito-TEMPO. *ACS Chem. Neurosci.* **2013**, *4*, 1439−1445.

(421) Vianello, F.; Momo, F.; Scarpa, M.; Rigo, A. Kinetics of Nitroxide Spin Label Removal in Biological Systems: An In Vitro And In Vivo ESR Study. *Magn. Reson. Imaging* **1995**, *13*, 219−226.

(422) Rajca, A.; Wang, Y.; Boska, M.; Paletta, J. T.; Olankitwanit, A.; Swanson, M. A.; Mitchell, D. G.; Eaton, S. S.; Eaton, G. R.; Rajca, S. Organic Radical Contrast Agents for Magnetic Resonance Imaging. *J. Am. Chem. Soc.* **2012**, *134*, 15724−15727.

(423) Nguyen, H. V. T.; Chen, Q. X.; Paletta, J. T.; Harvey, P.; Jiang, Y.; Zhang, H.; Boska, M. D.; Ottaviani, M. F.; Jasanoff, A.; Rajca, A.; et al. Nitroxide-Based Macromolecular Contrast Agents with Unprecedented Transverse Relaxivity and Stability for Magnetic Resonance Imaging of Tumors. *ACS Cent. Sci.* **2017**, *3*, 800−811.

(424) Weissleder, R.; Stark, D. D.; Engelstad, B. L.; Bacon, B. R.; Compton, C. C.; White, D. L.; Jacobs, P.; Lewis, J. Superparamagnetic Iron Oxide: Pharmacokinetics and Toxicity. *AJR, Am. J. Roentgenol.* **1989**, *152*, 167−173.

(425) Chouly, C.; Pouliquen, D.; Lucet, I.; Jeune, J. J.; Jallet, P. Development of Superparamagnetic Nanoparticles for MRI: Effect of Particle Size, Charge and Surface Nature on Biodistribution. *J. Microencapsulation* **1996**, *13*, 245−255.

(426) Gale, E. M.; Caravan, P.; Rao, A. G.; McDonald, R. J.; Winfeld, M.; Fleck, R. J.; Gee, M. S. Gadolinium-Based Contrast Agents in Pediatric Magnetic Resonance Imaging. *Pediatr. Radiol.* **2017**, *47*, 507−521.

(427) Reimer, P.; Muller, M.; Marx, C.; Wiedermann, D.; Muller, R.; Rummeny, E. J.; Ebert, W.; Shamsi, K.; Peters, P. E. T1 Effects of a Bolus-Injectable Superparamagnetic Iron Oxide, SH U 555 A: Dependence on Field Strength and Plasma Concentration Preliminary Clinical Experience with Dynamic T1-Weighted MR Imaging. *Radiology* **1998**, *209*, 831−836.

(428) Heesakkers, R. A. M.; Jager, G. J.; Hövels, A. M.; de Hoop, B.; van den Bosch, H. C. M.; Raat, F.; Witjes, J. A.; Mulders, P. F. A.; van der Kaa, C. H.; Barentsz, J. O. Prostate Cancer: Detection of Lymph Node Metastases Outside the Routine Surgical Area with Ferumox-tran-10 - Enhanced MR Imaging. *Radiology* **2009**, *251*, 408−414.

(429) Weissleder, R.; Nahrendorf, M.; Pittet, M. J. Imaging Macrophages with Nanoparticles. *Nat. Mater.* **2014**, *13*, 125−138.

(430) Corot, C.; Petry, K. G.; Trivedi, R.; Saleh, A.; Jonkmanns, C.; Le Bas, J. F.; Blezer, E.; Rausch, M.; Brochet, B.; Foster-Gareau, P.; et al. Macrophage Imaging in Central Nervous System and in Carotid Atherosclerotic Plaque Using Ultrasmall Superparamagnetic Iron Oxide in Magnetic Resonance Imaging. *Invest. Radiol.* **2004**, *39*, 619−625.

(431) Neuwelt, A.; Sidhu, N.; Hu, C. A. A.; Mlady, G.; Eberhardt, S. C.; Sillerud, L. O. Iron-Based Superparamagnetic Nanoparticle Contrast Agents for MRI of Infection and Inflammation. *AJR, Am. J. Roentgenol.* **2015**, *204*, W302−W313.

(432) Kooi, M. E.; Cappendijk, V. C.; Cleutjens, K. B.; Kessels, A. G.; Kitslaar, P. J.; Borgers, M.; Frederik, P. M.; Daemen, M. J.; van Engelshoven, J. M. Accumulation of Ultrasmall Superparamagnetic Particles of Iron Oxide in Human Atherosclerotic Plaques can be Detected by In Vivo Magnetic Resonance Imaging. *Circulation* **2003**, *107*, 2453−2458.

(433) Schmitz, S. A.; Taupitz, M.; Wagner, S.; Wolf, K. J.; Beyersdorff, D.; Hamm, B. Magnetic resonance imaging of atherosclerotic plaques using superparamagnetic iron oxide particles. *J. Magn. Reson. Imaging* **2001**, *14*, 355−361.

(434) Schmitz, S. A.; Taupitz, M.; Wagner, S.; Wolf, K. J.; Beyersdorff, D.; Hamm, B. Magnetic Resonance Imaging of Atherosclerotic Plaques Using Superparamagnetic Iron Oxide Particles. *J. Magn. Reson. Imaging* **2001**, *14*, 355−361.

(435) Saleh, A.; Schroeter, M.; Ringelstein, A.; Hartung, H. P.; Siebler, M.; Modder, U.; Jander, S. Iron Oxide Particle-Enhanced MRI Suggests Variability of Brain Inflammation at Early Stages after Ischemic Stroke. *Stroke* **2007**, *38*, 2733−2737.

(436) Nighoghossian, N.; Wiart, M.; Cakmak, S.; Berthezene, Y.; Derex, L.; Cho, T. H.; Nemoz, C.; Chapuis, F.; Tisserand, G. L.; Pialat, J. B.; et al. Inflammatory Response after Ischemic Stroke - A USPIO-Enhanced MRI Study in Patients. *Stroke* **2007**, *38*, 303−307.

(437) Alam, S. R.; Shah, A. S. V.; Richards, J.; Lang, N. N.; Barnes, G.; Joshi, N.; MacGillivray, T.; McKillop, G.; Mirsadraee, S.; Payne, J.; et al. Ultrasmall Superparamagnetic Particles of Iron Oxide in Patients With Acute Myocardial Infarction Early Clinical Experience. *Circ. Cardiovasc. Imaging* **2012**, *5*, 559−565.

(438) Bashir, M. R.; Bhatti, L.; Marin, D.; Nelson, R. C. Emerging Applications for Ferumoxytol as a Contrast Agent in MRI. *J. Magn. Reson. Imaging* 2015, *41*, 884–898.

(439) Stabi, K. L.; Bendz, L. M. Ferumoxytol Use as an Intravenous Contrast Agent for Magnetic Resonance Angiography. *Ann. Pharmacother.* 2011, *45*, 1571–1575.

(440) Bashir, M. R.; Jaffe, T. A.; Brennan, T. V.; Patel, U. D.; Ellis, M. J. Renal Transplant Imaging Using Magnetic Resonance Angiography With a Nonnephrotoxic Contrast Agent. *Transplantation* 2013, *96*, 91–96.

(441) Sigovan, M.; Gasper, W.; Alley, H. F.; Owens, C. D.; Saloner, D. USPIO-Enhanced MR Angiography of Arteriovenous Fistulas in Patients with Renal Failure. *Radiology* 2012, *265*, 584–590.

(442) Hansch, A.; Betge, S.; Poehlmann, G.; Neumann, S.; Baltzer, P.; Pfeil, A.; Waginger, M.; Boettcher, J.; Kaiser, W. A.; Wolf, G.; et al. Combined Magnetic Resonance Imaging of Deep Venous Thrombosis and Pulmonary Arteries after a Single Injection of a Blood Pool Contrast Agent. *Eur. Radiol.* 2011, *21*, 318–325.

(443) Thompson, E. M.; Guillaume, D. J.; Dósa, E.; Li, X.; Nazemi, K. J.; Gahramanov, S.; Hamilton, B. E.; Neuwelt, E. A. Dual Contrast Perfusion MRI in a Single Imaging Session for Assessment of Pediatric Brain Tumors. *J. Neuro-Oncol.* 2012, *109*, 105–114.

(444) Wei, H.; Bruns, O. T.; Kaul, M. G.; Hansen, E. C.; Barch, M.; Wisniowska, A.; Chen, O.; Chen, Y.; Li, N.; Okada, S.; et al. Exceedingly Small Iron Oxide Nanoparticles as Positive MRI Contrast Agents. *Proc. Natl. Acad. Sci. U. S. A.* 2017, *114*, 2325–2330.

(445) Bernd, H.; De Kerviler, E.; Gaillard, S.; Bonnemain, B. Safety and Tolerability of Ultrasmall Superparamagnetic Iron Oxide Contrast Agent Comprehensive Analysis of a Clinical Development Program. *Invest. Radiol.* 2009, *44*, 336–342.

(446) Schiller, B.; Bhat, P.; Sharma, A. Safety and Effectiveness of Ferumoxytol in Hemodialysis Patients at 3 Dialysis Chains in the United States Over a 12-Month Period. *Clin. Ther.* 2014, *36*, 70–83.

(447) Unterweger, H.; Janko, C.; Schwarz, M.; Dezsi, L.; Urbanics, R.; Matuszak, J.; Orfi, E.; Fulop, T.; Bauerle, T.; Szebeni, J.; et al. Non-Immunogenic Dextran-Coated Superparamagnetic Iron Oxide Nanoparticles: A Biocompatible, Size-Tunable Contrast Agent for Magnetic Resonance Imaging. *Int. J. Nanomed.* 2017, *12*, 5223–5238.

(448) Singh, N.; Jenkins, G. J. S.; Asadi, R.; Doak, S. H. Potential Toxicity of Superparamagnetic Iron Oxide Nanoparticles (SPION). *Nano Rev.* 2010, *1*, 5358–5372.

(449) Aime, S.; Calabi, L.; Biondi, L.; De Miranda, M.; Ghelli, S.; Paleari, L.; Rebaudengo, C.; Terreno, E. Iopamidol: Exploring the Potential Use of a Well-Established X-ray Contrast Agent for MRI. *Magn. Reson. Med.* 2005, *53*, 830–834.

(450) Anemone, A.; Consolino, L.; Longo, D. L. MRI-CEST Assessment of Tumour Perfusion Using X-ray Iodinated Agents: Comparison with a Conventional Gd-Based Agent. *Eur. Radiol.* 2017, *27*, 2170–2179.

(451) Ratnakar, S. J.; Woods, M.; Lubag, A. J. M.; Kovács, Z.; Sherry, A. D. Modulation of Water Exchange in Europium(III) DOTA-Tetraamide Complexes Via Electronic Substituent Effects. *J. Am. Chem. Soc.* 2008, *130*, 6–7.

(452) Woods, M.; Pasha, A.; Zhao, P. Y.; Tircso, G.; Chowdhury, S.; Kiefer, G.; Woessner, D. E.; Sherry, A. D. Investigations into Whole Water, Prototropic and Amide Proton Exchange in Lanthanide(III) DOTA-Tetraamide Chelates. *Dalton Trans* 2011, *40*, 6759–6764.

(453) Sherry, A. D.; Woods, M. Chemical Exchange Saturation Transfer Contrast Agents for Magnetic Resonance Imaging. *Annu. Rev. Biomed. Eng.* 2008, *10*, 391–411.

(454) Dorazio, S. J.; Olatunde, A. O.; Spernyak, J. A.; Morrow, J. R. CoCEST: Cobalt(II) Amide-Appended ParaCEST MRI Contrast Agents. *Chem. Commun.* 2013, *49*, 10025–10027.

(455) Dorazio, S. J.; Tsitovich, P. B.; Siters, K. E.; Spernyak, J. A.; Morrow, J. R. Iron(II) PARACEST MRI Contrast Agents. *J. Am. Chem. Soc.* 2011, *133*, 14154–14156.

(456) Nwe, K.; Andolina, C. M.; Huang, C. H.; Morrow, J. R. PARACEST Properties of a Dinuclear Neodymium(III) Complex Bound to DNA or Carbonate. *Bioconjugate Chem.* 2009, *20*, 1375–1382.

(457) Olatunde, A. O.; Bond, C. J.; Dorazio, S. J.; Cox, J. M.; Benedict, J. B.; Daddario, M. D.; Spernyak, J. A.; Morrow, J. R. Six, Seven or Eight Coordinate Fe-II, Co-II or Ni-II Complexes of Amide-Appended Tetraazamacrocycles for ParaCEST Thermometry. *Chem. - Eur. J.* 2015, *21*, 18290–18300.

(458) Olatunde, A. O.; Dorazio, S. J.; Spernyak, J. A.; Morrow, J. R. The NiCEST Approach: Nickel(II) ParaCEST MRI Contrast Agents. *J. Am. Chem. Soc.* 2012, *134*, 18503–18505.

(459) Du, K.; Harris, T. D. A Cu-2(II) Paramagnetic Chemical Exchange Saturation Transfer Contrast Agent Enabled by Magnetic Exchange Coupling. *J. Am. Chem. Soc.* 2016, *138*, 7804–7807.

(460) Ali, M. M.; Woods, M.; Suh, E. H.; Kovacs, Z.; Tircso, G.; Zhao, P. Y.; Kodibagkar, V. D.; Sherry, A. D. Albumin-Binding PARACEST Agents. *JBIC, J. Biol. Inorg. Chem.* 2007, *12*, 855–865.

(461) Pasha, A.; Lin, M.; Tircso, G.; Rostollan, C. L.; Woods, M.; Kiefer, G. E.; Sherry, A. D.; Sun, X. Synthesis and Evaluation of Lanthanide Ion DOTA-Tetraamide Complexes Bearing Peripheral Hydroxyl Groups. *JBIC, J. Biol. Inorg. Chem.* 2009, *14*, 421–438.

(462) Vymazal, J.; Spuentrup, E.; Cardenas-Molina, G.; Wiethoff, A. J.; Hartmann, M. G.; Caravan, P.; Parsons, E. C., Jr. Thrombus Imaging with Fibrin-Specific Gadolinium-Based MR Contrast Agent EP-2104R. *Invest. Radiol.* 2009, *44*, 697–704.

(463) Spuentrup, E.; Botnar, R. M.; Wiethoff, A. J.; Ibrahim, T.; Kelle, S.; Katoh, M.; Ozgun, M.; Nagel, E.; Vymazal, J.; Graham, P. B.; et al. MR Imaging of Thrombi Using EP-2104R, a Fibrin-Specific Contrast Agent: Initial Results in Patients. *Eur. Radiol.* 2008, *18*, 1995–2005.

(464) Kolodziej, A. F.; Nair, S. A.; Graham, P.; McMurry, T. J.; Ladner, R. C.; Wescott, C.; Sexton, D. J.; Caravan, P. Fibrin Specific Peptides Derived by Phage Display: Characterization of Peptides and Conjugates for Imaging. *Bioconjugate Chem.* 2012, *23*, 548–556.

(465) Kolodziej, A. F.; Zhang, Z.; Overoye-Chan, K.; Jacques, V.; Caravan, P. Peptide Optimization and Conjugation Strategies in the Development of Molecularly Targeted Magnetic Resonance Imaging Contrast Agents. *Methods Mol. Biol.* 2014, *1088*, 185–211.

(466) Overoye-Chan, K.; Koerner, S.; Looby, R. J.; Kolodziej, A. F.; Zech, S. G.; Deng, Q.; Chasse, J. M.; McMurry, T. J.; Caravan, P. EP-2104R: a Fibrin-Specific Gadolinium-Based MRI Contrast Agent for Detection of Thrombus. *J. Am. Chem. Soc.* 2008, *130*, 6025–6039.

(467) Zhang, Z.; Kolodziej, A. F.; Qi, J.; Nair, S. A.; Wang, X.; Case, A. W.; Greenfield, M. T.; Graham, P. B.; McMurry, T. J.; Caravan, P. Effect of Peptide-Chelate Architecture on Metabolic Stability of Peptide-Based MRI Contrast Agents. *New J. Chem.* 2010, *34*, 611–616.

(468) Uppal, R.; Ay, I.; Dai, G.; Kim, Y. R.; Sorensen, A. G.; Caravan, P. Molecular MRI of Intracranial Thrombus in a Rat Ischemic Stroke Model. *Stroke* 2010, *41*, 1271–1277.

(469) Uppal, R.; Medarova, Z.; Farrar, C. T.; Dai, G.; Moore, A.; Caravan, P. Molecular Imaging of Fibrin in a Breast Cancer Xenograft Mouse Model. *Invest. Radiol.* 2012, *47*, 553–558.

(470) Winter, P. M.; Caruthers, S. D.; Yu, X.; Song, S. K.; Chen, J.; Miller, B.; Bulte, J. W.; Robertson, J. D.; Gaffney, P. J.; Wickline, S. A.; et al. Improved Molecular Imaging Contrast Agent for Detection of Human Thrombus. *Magn. Reson. Med.* 2003, *50*, 411–416.

(471) Flacke, S.; Fischer, S.; Scott, M. J.; Fuhrhop, R. J.; Allen, J. S.; McLean, M.; Winter, P.; Sicard, G. A.; Gaffney, P. J.; Wickline, S. A.; et al. Novel MRI Contrast Agent for Molecular Imaging of Fibrin Implications for Detecting Vulnerable Plaques. *Circulation* 2001, *104*, 1280–1285.

(472) Yu, X.; Song, S. K.; Chen, J.; Scott, M. J.; Fuhrhop, R. J.; Hall, C. S.; Gaffney, P. J.; Wickline, S. A.; Lanza, G. M. High-Resolution MRI Characterization of Human Thrombus Using a Novel Fibrin-Targeted Paramagnetic Nanoparticle Contrast Agent. *Magn. Reson. Med.* 2000, *44*, 867–872.

(473) Temme, S.; Grapentin, C.; Quast, C.; Jacoby, C.; Grandoch, M.; Ding, Z.; Owenier, C.; Mayenfels, F.; Fischer, J. W.; Schubert, R.; et al. Noninvasive Imaging of Early Venous Thrombosis by 19F

Magnetic Resonance Imaging With Targeted Perfluorocarbon Nanoemulsions. *Circulation* **2015**, *131*, 1405−1414.

(474) Caravan, P. Protein-Targeted Gadolinium-Based Magnetic Resonance Imaging (MRI) Contrast Agents: Design and Mechanism of Action. *Acc. Chem. Res.* **2009**, *42*, 851−862.

(475) Caravan, P.; Comuzzi, C.; Crooks, W.; McMurry, T. J.; Choppin, G. R.; Woulfe, S. R. Thermodynamic Stability and Kinetic Inertness of the MS-325, a new Blood Pool Agents for Magnetic Resonance Imaging. *Inorg. Chem.* **2001**, *40*, 2170−2176.

(476) McMurry, T. J.; Parmelee, D. J.; Sajiki, H.; Scott, D. M.; Oullet, H. S.; Walovitch, R. C.; Tyeklár, Z.; Dumas, S.; Bernard, P.; Nadler, S.; et al. The Effect of a Phosphodiester Linking Group on Albumin Binding, Blood Half-Life, and Relaxivity of Intravascular Diethylenetriaminepentaacetato Aquo Gadolinium(III) MRI Contrast Agents. *J. Med. Chem.* **2002**, *45*, 3465−3474.

(477) Herborn, C. U.; Lauenstein, T. C.; Vogt, F. M.; Lauffer, R. B.; Debatin, J. F.; Ruehm, S. G. Interstitial MR Lymphography with MS-325: Characterization of Normal and Tumor-Invaded Lymph Nodes in a Rabbit Model. *AJR, Am. J. Roentgenol.* **2002**, *179*, 1567−1572.

(478) Montesi, S.; Rao, R.; Liang, L.; Caravan, P.; Sharma, A.; Digumarthy, S.; Seethamraju, R.; Tager, A. M. Use Of Gadofosveset-Enhanced Lung Mri To Assess Ongoing Lung Injury In Fibrotic Interstitial Lung Disease. *Am. J. Resp. Crit. Care* **2017**, *195*, A6417.

(479) Lorusso, V.; Pascolo, L.; Fernetti, C.; Visigalli, M.; Anelli, P.; Tiribelli, C. Vitro and In Vivo Hepatic Transport of the Magnetic Resonance Imaging Contrast Agent B22956/1: Role of MRP Proteins. *Biochem. Biophys. Res. Commun.* **2002**, *293*, 100−105.

(480) Boschi, F.; Marzola, P.; Sandri, M.; Nicolato, E.; Galie, M.; Fiorini, S.; Merigo, F.; Lorusso, V.; Chaabane, L.; Sbarbati, A. Tumor Microvasculature Observed Using Different Contrast Agents: A Comparison Between Gd-DTPA-Albumin and B-22956/1 in an Experimental Model of Mammary Carcinoma. *MAGMA* **2008**, *21*, 169−176.

(481) Ramponi, S.; Rebaudengo, C.; Cabella, C.; Grotti, A.; Vultaggio, S.; Aime, S.; Morisetti, A.; Lorusso, V. Contrast-Enhanced MRI of Murine Sponge Model for Progressive Angiogensis Assessed with Gadoteridol(ProHance) and Gadocoletic Acid Trisodium salt(B22956/1). *J. Magn. Reson. Imaging* **2008**, *27*, 872−880.

(482) Gianolio, E.; Cabella, C.; Serra, S. C.; Valbusa, G.; Arena, F.; Maiocchi, A.; Miragoli, L.; Tedoldi, F.; Uggeri, F.; Visigalli, M.; et al. B25716/1: A Novel Albumin-Binding Gd-AAZTA MRI Contrast Agent with Improved Properties in Tumor Imaging. *JBIC, J. Biol. Inorg. Chem.* **2014**, *19*, 715−726.

(483) Boros, E.; Caravan, P. Structure-Relaxivity Relationships of Serum Albumin Targeted MRI Probes Based on a Single Amino Acid Gd Complex. *J. Med. Chem.* **2013**, *56*, 1782−1786.

(484) Caravan, P.; Zhang, Z. Structure - relaxivity relationships among Targeted MR contrast agents. *Eur. J. Inorg. Chem.* **2012**, *2012*, 1916−1923.

(485) Iki, N.; Boros, E.; Nakamura, M.; Baba, R.; Caravan, P. Gd3TCAS2: An Aquated Gd(3+)-Thiacalix[4]arene Sandwich Cluster with Extremely Slow Ligand Substitution Kinetics. *Inorg. Chem.* **2016**, *55*, 4000−4005.

(486) Boros, E.; Caravan, P. Probing the Structure-Relaxivity Relationship of Bis-Hydrated Gd(DOTAla) Derivatives. *Inorg. Chem.* **2015**, *54*, 2403−2410.

(487) Moriggi, L.; Yaseen, M. A.; Helm, L.; Caravan, P. Serum Albumin Targeted, pH-Dependent Magnetic Resonance Relaxation Agents. *Chem. - Eur. J.* **2012**, *18*, 3675−3686.

(488) Jung, K. H.; Kim, H. K.; Park, J. A.; Nam, K. S.; Lee, G. H.; Chang, Y.; Kim, T. J. Gd Complexes of DO3A-(Biphenyl-2,2′-bisamides) Conjugates as MRI Blood-Pool Contrast Agents. *ACS Med. Chem. Lett.* **2012**, *3*, 1003−1007.

(489) Jung, K. H.; Kim, H. K.; Lee, G. H.; Kang, D. S.; Park, J. A.; Kim, K. M.; Chang, Y. M.; Kim, T. J. Gd Complexes of Macrocyclic Diethylenetriaminepentaacetic Acid (DTPA) Biphenyl-2,2′-bisamides as Strong Blood-Pool Magnetic Resonance Imaging Contrast Agents. *J. Med. Chem.* **2011**, *54*, 5385−5394.

(490) Caravan, P.; Das, B.; Dumas, S.; Epstein, F. H.; Helm, P. A.; Jacques, V.; Koerner, S.; Kolodziej, A.; Shen, L.; Sun, W. C.; et al. Collagen-Targeted MRI Contrast Agent for Molecular Imaging of Fibrosis. *Angew. Chem., Int. Ed.* **2007**, *46*, 8171−8173.

(491) Spuentrup, E.; Ruhl, K. M.; Botnar, R. M.; Wiethoff, A. J.; Buhl, A.; Jacques, V.; Greenfield, M. T.; Krombach, G. A.; Günther, R. W.; Vangel, M. G.; et al. Molecular Magnetic Resonance Imaging of Myocardial Perfusion with EP-3600, a Collagen-Specific Contrast Agent. *Circulation* **2009**, *119*, 1768−1775.

(492) Farrar, C. T.; Gale, E. M.; Kennan, R.; Ramsay, I.; Masia, R.; Arora, G.; Looby, K.; Wei, L.; Kalpathy-Cramer, J.; Bunzel, M. M.; et al. CM-101: Type I Collagen-Targeted MR Imaging Probe for Detection of Liver Fibrosis. *Radiology* **2018**, *287*, 581−589.

(493) Zhu, B.; Wei, L.; Rotile, N.; Day, H.; Rietz, T.; Farrar, C. T.; Lauwers, G. Y.; Tanabe, K. K.; Rosen, B.; Fuchs, B. C.; et al. Combined Magnetic Resonance Elastography and Collagen Molecular Magnetic Resonance Imaging Accurately Stage Liver Fibrosis in a Rat Model. *Hepatology* **2017**, *65*, 1015−1025.

(494) Farrar, C. T.; DePeralta, D. K.; Day, H.; Rietz, T. A.; Wei, L.; Lauwers, G. Y.; Keil, B.; Subramaniam, A.; Sinskey, A. J.; Tanabe, K. K.; et al. 3D Molecular MR imaging of Liver Fibrosis and Response to Rapamycin Therapy in a Bile Duct Ligation Rat Model. *J. Hepatol.* **2015**, *63*, 689−696.

(495) Helm, P. A.; Caravan, P.; French, B. A.; Jacques, V.; Shen, L.; Xu, Y.; Beyers, R. J.; Roy, R. J.; Kramer, C. M.; Epstein, F. H. Postinfarction Myocardial Scarring in Mice: Molecular MR Imaging with Use of a Collagen-targeting Contrast Agent. *Radiology* **2008**, *247*, 788−796.

(496) Polasek, M.; Yang, Y.; Schuhle, D. T.; Yaseen, M. A.; Kim, Y. R.; Sung, Y. S.; Guimaraes, A. R.; Caravan, P. Molecular MR Imaging of Fibrosis in a Mouse Model of Pancreatic Cancer. *Sci. Rep.* **2017**, *7*, DOI: 10.1038/s41598-017-08838-6.

(497) Caravan, P.; Yang, Y.; Zachariah, R.; Schmitt, A.; Mino-Kenudson, M.; Chen, H. H.; Sosnovik, D. E.; Dai, G.; Fuchs, B. C.; Lanuti, M. Molecular Magnetic Resonance Imaging of Pulmonary Fibrosis in Mice. *Am. J. Respir. Cell Mol. Biol.* **2013**, *49*, 1120−1126.

(498) Waghorn, P. A.; Oliveira, B. L.; Jones, C. M.; Tager, A. M.; Caravan, P. High Sensitivity HPLC Method for Determination of the Allysine Concentration in Tissue by Use of a Naphthol Derivative. *J. Chromatogr. B: Anal. Technol. Biomed. Life Sci.* **2017**, *1064*, 7−13.

(499) Chen, H. H.; Waghorn, P. A.; Wei, L.; Tapias, L. F.; Schuhle, D. T.; Rotile, N. J.; Jones, C. M.; Looby, R. J.; Zhao, G.; Elliott, J. M., et al. Molecular Imaging of Oxidized Collagen Quantifies Pulmonary and Hepatic Fibrogenesis. *JCI Insight* **2017**, *2*, DOI: 10.1172/jci.insight.91506.

(500) Waghorn, P. A.; Jones, C. M.; Rotile, N. J.; Koerner, S. K.; Ferreira, D. S.; Chen, H. H.; Probst, C. K.; Tager, A. M.; Caravan, P. Molecular Magnetic Resonance Imaging of Lung Fibrogenesis with an Oxyamine-Based Probe. *Angew. Chem., Int. Ed.* **2017**, *56*, 9825−9828.

(501) Pilch, J.; Brown, D. M.; Komatsu, M.; Jarvinen, T. A. H.; Yang, M.; Peters, D.; Hoffman, R. M.; Ruoslahti, E. Peptides Selected for Binding to Clotted Plasma Accumulate in Tumor Stroma and Wounds. *Proc. Natl. Acad. Sci. U. S. A.* **2006**, *103*, 2800−2804.

(502) Ye, F. R.; Jeong, E. K.; Jia, Z. J.; Yang, T. X.; Parker, D.; Lu, Z. R. A Peptide Targeted Contrast Agent Specific to Fibrin-Fibronectin Complexes for Cancer Molecular Imaging with MRI. *Bioconjugate Chem.* **2008**, *19*, 2300−2303.

(503) Simberg, D.; Duza, T.; Park, J. H.; Essler, M.; Pilch, J.; Zhang, L. L.; Derfus, A. M.; Yang, M.; Hoffman, R. M.; Bhatia, S.; et al. Biomimetic Amplification of Nanoparticle Homing to Tumors. *Proc. Natl. Acad. Sci. U. S. A.* **2007**, *104*, 932−936.

(504) Zhou, Z. X.; Wu, X. M.; Kresak, A.; Griswold, M.; Lu, Z. R. Peptide Targeted Tripod Macrocyclic Gd(III) Chelates For Cancer Molecular MRI. *Biomaterials* **2013**, *34*, 7683−7693.

(505) Zhou, Z. X.; Qutaish, M.; Han, Z.; Schur, R. M.; Liu, Y. Q.; Wilson, D. L.; Lu, Z. R. MRI Detection of Breast Cancer Micrometastases with a Fibronectin-Targeting Contrast Agent. *Nat. Commun.* **2015**, *6*, DOI: 10.1038/ncomms8984.

(506) Tan, M. Q.; Burden-Gulley, S. M.; Li, W.; Wu, X. M.; Lindner, D.; Brady-Kalnay, S. M.; Gulani, V.; Lu, Z. R. MR Molecular Imaging of Prostate Cancer with a Peptide-Targeted Contrast Agent in a Mouse Orthotopic Prostate Cancer Model. *Pharm. Res.* **2012**, *29*, 953−960.

(507) Botnar, R. M.; Wiethoff, A. J.; Ebersberger, U.; Lacerda, S.; Blume, U.; Warley, A.; Jansen, C. H. P.; Onthank, D. C.; Cesati, R. R.; Rezavi, R.; et al. In Vivo Assessment of Aortic Aneurysm Wall Integrity Using Elastin-Specific Molecular Magnetic Resonance Imaging. *Circ. Cardiovasc. Imaging* **2014**, *7*, 679−689.

(508) Phinikaridou, A.; Andia, M. E.; Indermuehle, A.; Onthank, D. C.; Cesati, R. R.; Smith, A.; Robinson, S. P.; Saha, P.; Botnar, R. M. Vascular Remodeling and Plaque Vulnerability in a Rabbit Model of Atherosclerosis: Comparison of Delayed Enhancement MR Imaging with an Elastin-Specific Contrast Agent and Unenhanced Black-Blood MR Imaging. *Radiology* **2014**, *271*, 390−399.

(509) Wildgruber, M.; Bielicki, I.; Aichler, M.; Kosanke, K.; Feuchtinger, A.; Settles, M.; Onthank, D. C.; Cesati, R. R.; Robinson, S. P.; Huber, A. M.; et al. Assessment of Myocardial Infarction and Postinfarction Scar Remodeling With an Elastin-Specific Magnetic Resonance Agent. *Circ. Cardiovasc. Imaging* **2014**, *7*, 321−329.

(510) Protti, A.; Lavin, B.; Dong, X.; Lorrio, S.; Robinson, S.; Onthank, D. C.; Shah, A. M.; Botnar, R. M. Assessment of Myocardial Remodeling Using an Elastin/ Tropoelastin Specific Agent with High Field Magnetic Resonance Imaging (MRI). *J. Am. Heart Assoc.* **2015**, *4*, DOI: 10.1161/JAHA.115.001851.

(511) Frullano, L.; Zhu, J. Q.; Wang, C. N.; Wu, C. Y.; Miller, R. H.; Wang, Y. M. Myelin Imaging Compound (MIC) Enhanced Magnetic Resonance Imaging of Myelination. *J. Med. Chem.* **2012**, *55*, 94−105.

(512) Frullano, L.; Wang, C. N.; Miller, R. H.; Wang, Y. M. A Myelin-Specific Contrast Agent for Magnetic Resonance Imaging of Myelination. *J. Am. Chem. Soc.* **2011**, *133*, 1611−1613.

(513) Wang, C. N.; Popescu, D. C.; Wu, C. Y.; Zhu, J. Q.; Macklin, W.; Wang, Y. M. In Situ Fluorescence Imaging of Myelination. *J. Histochem. Cytochem.* **2010**, *58*, 611−621.

(514) Poduslo, J. F.; Wengenack, T. M.; Curran, G. L.; Wisniewski, T.; Sigurdsson, E. M.; Macura, S. I.; Borowski, B. J.; Jack, C. R. Molecular Targeting Of Alzheimer's Amyloid Plaques for Contrast-Enhanced Magnetic Resonance Imaging. *Neurobiol. Dis.* **2002**, *11*, 315−329.

(515) Poduslo, J. F.; Curran, G. L. Polyamine Modification Increases the Permeability of Proteins at the Blood-Nerve and Blood-Brain Barriers. *J. Neurochem.* **1996**, *66*, 1599−1609.

(516) Wadghiri, Y. Z.; Li, J. L.; Wang, J. H.; Hoang, D. M.; Sun, Y. J.; Xu, H.; Tsui, W.; Li, Y. S.; Boutajangout, A.; Wang, A., et al. Detection of Amyloid Plaques Targeted by Bifunctional USPIO in Alzheimer's Disease Transgenic Mice Using Magnetic Resonance Microimaging. *PLoS One* **2013**, *8*, e57097.

(517) Sigurdsson, E. M.; Wadghiri, Y. Z.; Mosconi, L.; Blind, J. A.; Knudsen, E.; Asuni, A.; Scholtzova, H.; Tsui, W. H.; Li, Y.; Sadowski, M.; et al. A Non-Toxic Ligand for Voxel-Based MRI Analysis of Plaques in AD Transgenic Mice. *Neurobiol. Aging* **2008**, *29*, 836−847.

(518) Martins, A. F.; Dias, D. M.; Morfin, J.-F.; Lacerda, S.; Laurents, D. V.; Toth, E.; Geraldes, C. F. G. C. Interaction of PiB-Derivative Metal Complexes with Beta-Amyloid Peptides: Selective Recognition of the Aggregated Forms. *Chem. - Eur. J.* **2015**, *21*, 5413−5422.

(519) Martins, A. F.; Morfin, J. F.; Geraldes, C.; Toth, E. Gd3+ Complexes Conjugated to Pittsburgh Compound B: Potential MRI Markers of Beta-Amyloid Plaques. *JBIC, J. Biol. Inorg. Chem.* **2014**, *19*, 281−295.

(520) Sillerud, L. O.; Solberg, N. O.; Chamberlain, R.; Orlando, R. A.; Heidrich, J. E.; Brown, D. C.; Brady, C. I.; Vander Jagt, T. A.; Garwood, M.; Vander Jagt, D. L. SPION-Enhanced Magnetic Resonance Imaging of Alzheimer's Disease Plaques in A beta PP/ PS-1 Transgenic Mouse Brain. *J. Alzheimer's Dis.* **2013**, *34*, 349−365.

(521) Van Montfoort, J. E.; Stieger, B.; Meijer, D. K. F.; Weinmann, H. J.; Meier, P. J.; Fattinger, K. E. Hepatic Uptake of the Magnetic Resonance Imaging Contrast Agent Gadoxetate by the Organic Anion Transporting Polypeptide Oatp1. *J. Pharmacol. Exp. Ther.* **1999**, *290*, 153−157.

(522) Junqiang, L.; Yinzhong, W.; Li, Z.; Shunlin, G.; Xiaohui, W.; Yanan, Z.; Kehu, Y. Gadoxetic Acid Disodium (Gd-EOBDTPA)-Enhanced Magnetic Resonance Imaging for the Detection of Hepatocellular Carcinoma: a Meta-Analysis. *J. Magn. Reson. Imaging* **2014**, *39*, 1079−1087.

(523) de Haen, C.; La Ferla, R.; Maggioni, F. Gadobenate Dimeglumine 0.5 M Solution for Injection (MultiHance) as Contrast Agent for Magnetic Resonance Imaging of the Liver: Mechanistic Studies in Animals. *J. Comput. Assist. Tomo.* **1999**, *23*, S169−S179.

(524) Purysko, A. S.; Remer, E. M.; Coppa, C. P.; Obuchowski, N. A.; Schneider, E.; Veniero, J. C. Characteristics and Distinguishing Features of Hepatocellular Adenoma and Focal Nodular Hyperplasia on Gadoxetate Disodium-Enhanced MRI. *AJR, Am. J. Roentgenol.* **2012**, *198*, 115−123.

(525) Islam, M. K.; Kim, S.; Kim, H. K.; Park, S.; Lee, G. H.; Kang, H. J.; Jung, J. C.; Park, J. S.; Kim, T. J.; Chang, Y. Manganese Complex of Ethylenediaminetetraacetic Acid (EDTA)-Benzothiazole Aniline (BTA) Conjugate as a Potential Liver-Targeting MRI Contrast Agent. *J. Med. Chem.* **2017**, *60*, 2993−3001.

(526) Patrick, P. S.; Hammersley, J.; Loizou, L.; Kettunen, M. I.; Rodrigues, T. B.; Hu, D. E.; Tee, S. S.; Hesketh, R.; Lyons, S. K.; Soloviev, D.; et al. Dual-Modality Gene Reporter for In Vivo Imaging. *Proc. Natl. Acad. Sci. U. S. A.* **2014**, *111*, 415−420.

(527) Xu, X.; Yadav, N. N.; Knutsson, L.; Hua, J.; Kalyani, R.; Hall, E.; Laterra, J.; Blakeley, J.; Strowd, R.; Pomper, M.; et al. Dynamic Glucose-Enhanced (DGE) MRI: Translation to Human Scanning and First Results in Glioma Patients. *Tomography* **2015**, *1*, 105−114.

(528) Rivlin, M.; Tsarfaty, I.; Navon, G. Functional Molecular Imaging of Tumors by Chemical Exchange Saturation Transfer MRI of 3-O-Methyl-D-Glucose. *Magn. Reson. Med.* **2014**, *72*, 1375−1380.

(529) Rivlin, M.; Navon, G. Glucosamine and N-Acetyl Glucosamine as New CEST MRI Agents for Molecular Imaging of Tumors. *Sci. Rep.* **2016**, *6*, DOI: 10.1038/srep32648.

(530) Rivlin, M.; Horev, J.; Tsarfaty, I.; Navon, G. Molecular Imaging of Tumors and Metastases Using Chemical Exchange Saturation Transfer (CEST) MRI. *Sci. Rep.* **2013**, *3*, DOI: 10.1038/srep03045.

(531) Paech, D.; Schuenke, P.; Koehler, C.; Windschuh, J.; Mundiyanapurath, S.; Bickelhaupt, S.; Bonekamp, D.; Baumer, P.; Bachert, P.; Ladd, M. E.; et al. T1 rho- Weighted Dynamic Glucose-Enhanced MR Imaging in the Human Brain. *Radiology* **2017**, *285*, 914−922.

(532) Kresse, M.; Wagner, S.; Pfefferer, D.; Lawaczeck, R.; Elste, V.; Semmler, W. Targeting of Ultrasmall Superparamagnetic Iron Oxide (USPIO) Particles to Tumor Cells In Vivo by Using Transferrin Receptor Pathways. *Magn. Reson. Med.* **1998**, *40*, 236−242.

(533) Hwang, D. W.; Ko, H. Y.; Lee, J. H.; Kang, H.; Ryu, S. H.; Song, I. C.; Lee, D. S.; Kim, S. A Nucleolin-Targeted Multimodal Nanoparticle Imaging Probe for Tracking Cancer Cells Using an Aptamer. *J. Nucl. Med.* **2010**, *51*, 98−105.

(534) Anderson, S. A.; Rader, R. K.; Westlin, W. F.; Null, C.; Jackson, D.; Lanza, C. M.; Wickline, S. A.; Kotyk, J. J. Magnetic Resonance Contrast Enhancement of Neovasculature with alpha(v)-beta(3)-Targeted Nanoparticles. *Magn. Reson. Med.* **2000**, *44*, 433−439.

(535) Chen, K.; Xie, J.; Xu, H. Y.; Behera, D.; Michalski, M. H.; Biswal, S.; Wang, A.; Chen, X. Y. Triblock Copolymer Coated Iron Oxide Nanoparticle Conjugate for Tumor Integrin Targeting. *Biomaterials* **2009**, *30*, 6912−6919.

(536) Zhang, C. F.; Jugold, M.; Woenne, E. C.; Lammers, T.; Morgenstern, B.; Mueller, M. M.; Zentgraf, H.; Bock, M.; Eisenhut, M.; Semmler, W.; et al. Specific Targeting of Tumor Angiogenesis by RGD-conjugated Ultrasmall Sperparamagnetic Iron Oxide Particles Using a Clinical 1.5-T Magnetic Resonance Scanner. *Cancer Res.* **2007**, *67*, 1555−1562.

(537) Liu, Y. J.; Yang, Y.; Zhang, C. F. A Concise Review of Magnetic Resonance Molecular Imaging of Tumor Angiogenesis by Targeting Integrin Alpha v Beta 3 with Magnetic Probes. *Int. J. Nanomed.* **2013**, *8*, 1083−1093.

(538) Crich, S. G.; Terreno, E.; Aime, S. Nano-sized and Other Improved Reporters for Magnetic Resonance Imaging Of Angiogenesis. *Adv. Drug Delivery Rev.* **2017**, *119*, 61−72.

(539) Kalber, T. L.; Kamaly, N.; So, P. W.; Pugh, J. A.; Bunch, J.; McLeod, C. W.; Jorgensen, M. R.; Miller, A. D.; Bell, J. D. A Low Molecular Weight Folate Receptor Targeted Contrast Agent for Magnetic Resonance Tumor Imaging. *Mol. Imaging Biol.* **2011**, *13*, 653−662.

(540) Corot, C.; Robert, P.; Lancelot, E.; Prigent, P.; Ballet, S.; Guilbert, I.; Raynaud, J. S.; Raynal, I.; Port, M. Tumor Imaging Using P866, a High-Relaxivity Gadolinium Chelate Designed for Folate Receptor Targeting. *Magn. Reson. Med.* **2008**, *60*, 1337−1346.

(541) Wang, Z. J.; Boddington, S.; Wendland, M.; Meier, R.; Corot, C.; Daldrup-Link, H. MR Imaging of Ovarian Tumors Using Folate-Receptor-Targeted Contrast Agents. *Pediatr. Radiol.* **2008**, *38*, 529−537.

(542) Konda, S. D.; Aref, M.; Brechbiel, M.; Wiener, E. C. Development of a Tumor-targeting MR Contrast Agent Using the High-Affinity Folate Receptor - Work in Progress. *Invest. Radiol.* **2000**, *35*, 50−57.

(543) Konda, S. D.; Wang, S.; Brechbiel, M.; Wiener, E. C. Biodistribution of a Gd-153-Folate Dendrimer, Generation = 4, in Mice with Folate-Receptor Positive and Negative Ovarian Tumor Xenografts. *Invest. Radiol.* **2002**, *37*, 199−204.

(544) Ding, N.; Lu, Y.; Lee, R. J.; Yang, C.; Huang, L.; Liu, J.; Xiang, G. Y. Folate Receptor-Targeted Fluorescent Paramagnetic Bimodal Liposomes for Tumor Imaging. *Int. J. Nanomed.* **2011**, *6*, 2513−2520.

(545) Kamaly, N.; Kalber, T.; Thanou, M.; Bell, J. D.; Miller, A. D. Folate Receptor Targeted Bimodal Liposomes for Tumor Magnetic Resonance Imaging. *Bioconjugate Chem.* **2009**, *20*, 648−655.

(546) Nakamura, T.; Kawano, K.; Shiraishi, K.; Yokoyama, M.; Maitani, Y. Folate-Targeted Gadolinium-Lipid-Based Nanoparticles as a Bimodal Contrast Agent for Tumor Fluorescent and Magnetic Resonance Imaging. *Biol. Pharm. Bull.* **2014**, *37*, 521−527.

(547) Sideratou, Z.; Tsiourvas, D.; Theodossiou, T.; Fardis, M.; Paleos, C. M. Synthesis and Characterization of Multifunctional Hyperbranched Polyesters as Prospective Contrast Agents for Targeted MRI. *Bioorg. Med. Chem. Lett.* **2010**, *20*, 4177−4181.

(548) McAteer, M. A.; Mankia, K.; Ruparelia, N.; Jefferson, A.; Nugent, H. B.; Stork, L. A.; Channon, K. M.; Schneider, J. E.; Choudhury, R. P. A Leukocyte-Mimetic Magnetic Resonance Imaging Contrast Agent Homes Rapidly to Activated Endothelium and Tracks With Atherosclerotic Lesion Macrophage Content. *Arterioscler., Thromb., Vasc. Biol.* **2012**, *32*, 1427−1435.

(549) Fournier, A. P.; Quenault, A.; Marinez de Lizarrondo, S.; Gauberti, M.; Defer, G.; Vivien, D.; Docagne, F.; Macrez, R. Prediction of Disease Activity in Models of Multiple Sclerosis by Molecular Magnetic Resonance Imaging of P-selectin. *Proc. Natl. Acad. Sci. U. S. A.* **2017**, *114*, 6116−6121.

(550) Boutry, S.; Laurent, S.; Vander Elst, L.; Muller, R. N. Specific E-selectin Targeting with a Superparamagnetic MRI Contrast Agent. *Contrast Media Mol. Imaging* **2006**, *1*, 15−22.

(551) Laurent, S.; Vander Elst, L.; Fu, Y. J.; Muller, R. N. Synthesis and Physicochemical Characterization of Gd-DTPA-B(sLe(x))A, a New MRI Contrast Agent Targeted to Inflammation. *Bioconjugate Chem.* **2004**, *15*, 99−103.

(552) Boutry, S.; Burtea, C.; Laurent, S.; Toubeau, G.; Vander Elst, L.; Muller, R. N. Magnetic Resonance Imaging of Inflammation with a Specific Selectin-Targeted Contrast Agent. *Magn. Reson. Med.* **2005**, *53*, 800−807.

(553) Yancy, A. D.; Olzinski, A. R.; Hu, T. C.; Lenhard, S. C.; Aravindhan, K.; Gruver, S. M.; Jacobs, P. M.; Willette, R. N.; Jucker, B. M. Differential Uptake of ferumoxtran-10 and ferumoxytol, Ultrasmall Superparamagnetic Iron Oxide Contrast Agents in Rabbit: Critical Determinants of Atherosclerotic Plaque Labeling. *J. Magn. Reson. Imaging* **2005**, *21*, 432−442.

(554) Naresh, N. K.; Xu, Y.; Klibanov, A. L.; Vandsburger, M. H.; Meyer, C. H.; Leor, J.; Kramer, C. M.; French, B. A.; Epstein, F. H. Monocyte and/or Macrophage Infiltration of Heart after Myocardial Infarction: MR Imaging by Using T1-shortening Liposomes1. *Radiology* **2012**, *264*, 428−435.

(555) Jacoby, C.; Borg, N.; Heusch, P.; Sauter, M.; Bönner, F.; Kandolf, R.; Klingel, K.; Schrader, J.; Flögel, U. Visualization of Immune Cell Infiltration in Experimental Viral Myocarditis by 19F MRI In Vivo. *MAGMA* **2014**, *27*, 101−106.

(556) Bönner, F.; Merx, M. W.; Klingel, K.; Begovatz, P.; Flögel, U.; Sager, M.; Temme, S.; Jacoby, C.; Ravesh, M. S.; Grapentin, C.; et al. Monocyte Imaging Aftermyocardial Infarction with 19FMRI at 3 T: A Pilot Study in Explanted Porcine Hearts. *Eur. Heart J. Cardiovasc. Imaging* **2015**, *16*, 612−620.

(557) Bönner, F.; Jacoby, C.; Temme, S.; Borg, N.; Ding, Z.; Schrader, J.; Flögel, U. Multifunctional MR Monitoring of the Healing Process after Myocardial Infarction. *Basic Res. Cardiol.* **2014**, *109*, 430−445.

(558) Krishnan, A. S.; Neves, A. A.; de Backer, M. M.; Hu, D. E.; Davletov, B.; Kettunen, M. I.; Brindle, K. M. Detection of Cell Death in Tumors by Using MR Imaging and a Gadolinium-Based Targeted Contrast Agent. *Radiology* **2008**, *246*, 854−862.

(559) van Tilborg, G. A. F.; Mulder, W. J. M.; Deckers, N.; Storm, G.; Reutelingsperger, C. P. M.; Strijkers, G. J.; Nicolay, K. Annexin A5-Functionalized Bimodal Lipid-Based Contrast Agents for the Detection of Apoptosis. *Bioconjugate Chem.* **2006**, *17*, 741−749.

(560) van Tilborg, G. A. F.; Vucic, E.; Strijkers, G. J.; Cormode, D. P.; Mani, V.; Skajaa, T.; Reutelingsperger, C. P. M.; Fayad, Z. A.; Mulder, W. J. M.; Nicolay, K. Annexin A5-Functionalized Bimodal Nanoparticles for MRI and Fluorescence Imaging of Atherosclerotic Plaques. *Bioconjugate Chem.* **2010**, *21*, 1794−1803.

(561) Sosnovik, D. E.; Schellenberger, E. A.; Nahrendorf, M.; Novikov, M. S.; Matsui, T.; Dai, G.; Reynolds, F.; Grazette, L.; Rosenzweig, A.; Weissleder, R.; et al. Magnetic Resonance Imaging of Cardiomyocyte Apoptosis with a Novel Magneto-Optical Nanoparticle. *Magn. Reson. Med.* **2005**, *54*, 718−724.

(562) Huang, S.; Chen, H. H.; Yuan, H.; Dai, G.; Schühle, D. T.; Mekkaoui, C.; Ngoy, S.; Liao, R.; Caravan, P.; Josephson, L.; et al. Molecular MRI of Actue Necrosis with a Novel DNA-Binding Gadolinium Chelate: Kinetics of Cell Death and Clearance in Infarcted Myocardium. *Circ. Cardiovasc. Imaging* **2011**, *4*, 729−737.

(563) Moats, R. A.; Fraser, S. E.; Meade, T. J. A "Smart" Magnetic Resonance Imaging Agent That Reports on Specific Enzymatic Activity. *Angew. Chem., Int. Ed. Engl.* **1997**, *36*, 726−728.

(564) Serebriiskii, I. G.; Golemis, E. A. Uses of lacZ to Study Gene Function: Evaluation of β-Galactosidase Assays Employed in the Yeast Two-Hybrid System. *Anal. Biochem.* **2000**, *285*, 1−15.

(565) Nolan, G. P.; Fiering, S.; Nicolas, J. F.; Herzenberg, L. A. Fluorescence-activated Cell Analysis and Sorting of Viable Mammalian Cells Based on Beta-d-galactosidase Activity after Transduction of Escherichia coli lacZ. *Proc. Natl. Acad. Sci. U. S. A.* **1988**, *85*, 2603−2607.

(566) Louie, A. Y.; Hüber, M. M.; Ahrens, E. T.; Rothbächer, U.; Moats, R.; Jacobs, R. E.; Fraser, S. E.; Meade, T. J. In Vivo Visualization of Gene Expression Using Magentic Resonance Imaging. *Nat. Biotechnol.* **2000**, *18*, 321−325.

(567) Hingorani, D. V.; Bernstein, A. S.; Pagel, M. D. A Review of Responsive MRI Contrast Agents: 2005−2014. Contrast Media. *Contrast Media Mol. Imaging* **2015**, *10*, 245−265.

(568) Tu, C.; Osborne, E. A.; Louie, A. Y. Activatable T 1 and T 2 Magnetic Resonance Imaging Contrast Agents. *Ann. Biomed. Eng.* **2011**, *39*, 1335−1348.

(569) Louie, A. MRI Biosensors: A Short Primer. *J. Magn. Reson. Imaging* **2013**, *38*, 530−539.

(570) Do, Q. N.; Ratnakar, J. S.; Kovács, Z.; Sherry, A. D. Redox- and Hypoxia-Responsive MRI Contrast Agents. *ChemMedChem* **2014**, *9*, 1116−1129.

(571) Que, E. L.; Chang, C. J. Responsive Magnetic Resonance Imaging Contrast Agents as Chemical Sensors for Metals in Biology and Medicine. *Chem. Soc. Rev.* **2010**, *39*, 51−60.

(572) Davies, G.-L.; Kramberger, I.; Davis, J. J. Environmentally Responsive MRI Contrast Agents. *Chem. Commun.* **2013**, *49*, 9704−9721.

(573) Pérez-Mayoral, E.; Negri, V.; Soler-Padrós, J.; Cerdán, S.; Ballesteros, P. Chemistry of Paramagnetic and Diamagnetic Contrast Agents for Magnetic Resonance Imaging and Spectroscopy. *Eur. J. Radiol.* **2008**, *67*, 453−458.

(574) Zhang, S.; Wu, K.; Sherry, A. D. A Novel pH-Sensitive MRI Contrast Agent. *Angew. Chem., Int. Ed.* **1999**, *38*, 3192−3194.

(575) Kálmán, F. K.; Woods, M.; Caravan, P.; Jurek, P.; Spiller, M.; Tircsó, G.; Király, R.; Brücher, E.; Sherry, A. D. Potentiometric and Relaxometric Properties of a Gadolinium-Based MRI Contrast Agent for Sensing Tissue pH. *Inorg. Chem.* **2007**, *46*, 5260−5270.

(576) Ali, M. M.; Woods, M.; Caravan, P.; Opina, A. C. L.; Spiller, M.; Fettinger, J. C.; Sherry, A. D. Synthesis and Relaxometric Studies of a Dendrimer-Based pH-Responsive MRI Contrast Agent. *Chem. - Eur. J.* **2008**, *14*, 7250−7258.

(577) Woods, M.; Zhang, S.; Ebron, V. H.; Sherry, A. D. pH-Sensitive Modulation of the Second Hydration Sphere in Lanthanide-(III) Tetraamide−DOTA Complexes: A Novel Approach to Smart MR Contrast Media. *Chem. - Eur. J.* **2003**, *9*, 4634−4640.

(578) Bruce, J. I.; Dickins, R. S.; Govenlock, L. J.; Gunnlaugsson, T.; Lopinski, S.; Lowe, M. P.; Parker, D.; Peacock, R. D.; Perry, J. J. B.; Aime, S.; et al. The Selectivity of Reversible Oxy-Anion Binding in Aqueous Solution at a Chiral Europium and Terbium Center: Signaling of Carbonate Chelation by Changes in the Form and Circular Polarization of Luminescence Emission. *J. Am. Chem. Soc.* **2000**, *122*, 9674−9684.

(579) Aime, S.; Gianolio, E.; Terreno, E.; Giovenzana, G. B.; Pagliarin, R.; Sisti, M.; Palmisano, G.; Botta, M.; Lowe, M. P.; Parker, D. Ternary Gd(III)L-HSA Adducts: Evidence for the Replacement of Inner-Sphere Water Molecules by Coordinating Groups of the Protein. Implications for the Design of Contrast Agents for MRI. *JBIC, J. Biol. Inorg. Chem.* **2000**, *5*, 488−497.

(580) Woods, M.; Kiefer, G. E.; Bott, S.; Castillo-Muzquiz, A.; Eshelbrenner, C.; Michaudet, L.; McMillan, K.; Mudigunda, S. D. K.; Ogrin, D.; Tircsó, G.; et al. Synthesis, Relaxometric and Photophysical Properties of a New pH-Responsive MRI Contrast Agent: The Effect of Other Ligating Groups on Dissociation of a p-Nitrophenolic Pendant Arm. *J. Am. Chem. Soc.* **2004**, *126*, 9248−9256.

(581) Giovenzana, G. B.; Negri, R.; Rolla, G. A.; Tei, L. Gd-Aminoethyl-DO3A Complexes: A Novel Class of pH-Sensitive MRI Contrast Agents. *Eur. J. Inorg. Chem.* **2012**, *2012*, 2035−2039.

(582) Baranyai, Z.; Rolla, G. A.; Negri, R.; Forgács, A.; Giovenzana, G. B.; Tei, L. Comprehensive Evaluation of the Physicochemical Properties of LnIII Complexes of Aminoethyl-DO3A as pH-Responsive T1-MRI Contrast Agents. *Chem. - Eur. J.* **2014**, *20*, 2933−2944.

(583) Raghunand, N.; Howison, C.; Sherry, A. D.; Zhang, S.; Gillies, R. J. Renal and Systemic pH Imaging by Contrast-Enhanced MRI. *Magn. Reson. Med.* **2003**, *49*, 249−257.

(584) Garcia-Martin, M. L.; Martinez, G. V.; Raghunand, N.; Sherry, A. D.; Zhang, S.; Gillies, R. J. High resolution pHe Imaging of Rat Glioma using pH-dependent Relaxivity. *Magn. Reson. Med.* **2006**, *55*, 309−315.

(585) Martinez, G. V.; Zhang, X.; García-Martín, M. L.; Morse, D. L.; Woods, M.; Sherry, A. D.; Gillies, R. J. Imaging the Extracellular pH of Tumors by MRI after Injection of a Single Cocktail of T1 and T2 Contrast Agents. *NMR Biomed.* **2011**, *24*, 1380−1391.

(586) Aime, S.; Fedeli, F.; Sanino, A.; Terreno, E. A R2/R1 Ratiometric Procedure for a Concentration-Independent, pH-Responsive, Gd(III)-Based MRI Agent. *J. Am. Chem. Soc.* **2006**, *128*, 11326−11327.

(587) Frullano, L.; Catana, C.; Benner, T.; Sherry, A. D.; Caravan, P. Bimodal MR−PET Agent for Quantitative pH Imaging. *Angew. Chem., Int. Ed.* **2010**, *49*, 2382−2384.

(588) Gianolio, E.; Maciocco, L.; Imperio, D.; Giovenzana, G. B.; Simonelli, F.; Abbas, K.; Bisi, G.; Aime, S. Dual MRI-SPECT Agent for pH-Mapping. *Chem. Commun.* **2011**, *47*, 1539−1541.

(589) Vologdin, N.; Rolla, G. A.; Botta, M.; Tei, L. Orthogonal Synthesis of a Heterodimeric Ligand for the Development of the GdIII-GaIII ditopic Complex as a Potential pH-sensitive MRI/PET Probe. *Org. Biomol. Chem.* **2013**, *11*, 1683−1690.

(590) Longo, D. L.; Sun, P. Z.; Consolino, L.; Michelotti, F. C.; Uggeri, F.; Aime, S. A General MRI-CEST Ratiometric Approach for pH Imaging: Demonstration of in Vivo pH Mapping with Iobitridol. *J. Am. Chem. Soc.* **2014**, *136*, 14333−14336.

(591) McMahon, M. T.; Gilad, A. A.; Zhou, J.; Sun, P. Z.; Bulte, J. W. M.; van Zijl, P. C. M. Quantifying Exchange Rates in Chemical Exchange Saturation Transfer Agents Using the Saturation Time and Saturation Power Dependencies of the Magnetization Transfer Effect on the Magnetic Resonance Imaging Signal (QUEST and QUESP): Ph Calibration for Poly-L-lysine and a Starburst Dendrimer. *Magn. Reson. Med.* **2006**, *55*, 836−847.

(592) Chen, L. Q.; Howison, C. M.; Jeffery, J. J.; Robey, I. F.; Kuo, P. H.; Pagel, M. D. Evaluations of Extracellular pH within In Vivo Tumors using AcidoCEST MRI. *Magn. Reson. Med.* **2014**, *72*, 1408−1417.

(593) Chan, K. W. Y.; Liu, G.; Song, X.; Kim, H.; Yu, T.; Arifin, D. R.; Gilad, A. A.; Hanes, J.; Walczak, P.; van Zijl, P. C. M.; et al. MRI-detectable pH Nanosensors Incorporated into Hydrogels for In Vivo Sensing of Transplanted-Cell Viability. *Nat. Mater.* **2013**, *12*, 268−275.

(594) Zhang, S.; Zhou, K.; Huang, G.; Takahashi, M.; Dean Sherry, A.; Gao, J. A Novel Class of Polymeric pH-responsive MRI CEST Agents. *Chem. Commun.* **2013**, *49*, 6418−6420.

(595) Yang, X.; Song, X.; Ray Banerjee, S.; Li, Y.; Byun, Y.; Liu, G.; Bhujwalla, Z. M.; Pomper, M. G.; McMahon, M. T. Developing Imidazoles as CEST MRI pH Sensors. *Contrast Media Mol. Imaging* **2016**, *11*, 304−312.

(596) Longo, D. L.; Busato, A.; Lanzardo, S.; Antico, F.; Aime, S. Imaging the pH Evolution of an Acute Kidney Injury Model by Means of Iopamidol, a MRI-CEST pH-responsive Contrast Agent. *Magn. Reson. Med.* **2013**, *70*, 859−864.

(597) Longo, D. L.; Bartoli, A.; Consolino, L.; Bardini, P.; Arena, F.; Schwaiger, M.; Aime, S. In Vivo Imaging of Tumor Metabolism and Acidosis by Combining PET and MRI-CEST pH Imaging. *Cancer Res.* **2016**, *76*, 6463−6470.

(598) Napolitano, R.; Soesbe, T. C.; De León-Rodríguez, L. M.; Sherry, A. D.; Udugamasooriya, D. G. On-Bead Combinatorial Synthesis and Imaging of Chemical Exchange Saturation Transfer Magnetic Resonance Imaging Agents To Identify Factors That Influence Water Exchange. *J. Am. Chem. Soc.* **2011**, *133*, 13023−13030.

(599) Singh, J.; Rustagi, V.; Zhang, S.; Sherry, A. D.; Udugamasooriya, D. G. On-Bead Combinatorial Synthesis and Imaging of Europium(III)-Based ParaCEST Agents Aids in Identification of Chemical Features that Enhance CEST Sensitivity. *Magn. Reson. Chem.* **2017**, *55*, 747−753.

(600) Aime, S.; Barge, A.; Delli Castelli, D.; Fedeli, F.; Mortillaro, A.; Nielsen, F. U.; Terreno, E. Paramagnetic Lanthanide(III) Complexes as pH-sensitive Chemical Exchange Saturation Transfer (CEST) Contrast Agents for MRI Applications. *Magn. Reson. Med.* **2002**, *47*, 639−648.

(601) Terreno, E. P.; Castelli, D. D. P.; Cravotto, G. P.; Milone, L. P.; Aime, S. P. Ln(III)-DOTAMGly Complexes: A Versatile Series to Assess the Determinants of the Efficacy of Paramagnetic Chemical Exchange Saturation Transfer Agents for Magnetic Resonance Imaging Applications. *Invest. Radiol.* **2004**, *39*, 235−243.

(602) Aime, S.; Delli Castelli, D.; Terreno, E. Novel pH-Reporter MRI Contrast Agents. *Angew. Chem., Int. Ed.* **2002**, *41*, 4334−4336.

(603) Liu, G.; Li, Y.; Sheth, V. R.; Pagel, M. D. Imaging in Vivo Extracellular pH with a Single Paramagnetic Chemical Exchange Saturation Transfer Magnetic Resonance Imaging Contrast Agent. *Mol. Imaging* **2012**, *11*, 47−57.

(604) Pikkemaat, J. A.; Wegh, R. T.; Lamerichs, R.; van de Molengraaf, R. A.; Langereis, S.; Burdinski, D.; Raymond, A. Y. F.; Janssen, H. M.; de Waal, B. F. M.; Willard, N. P.; et al. Dendritic PARACEST Contrast Agents for Magnetic Resonance Imaging. *Contrast Media Mol. Imaging* **2007**, *2*, 229−239.

(605) McVicar, N.; Li, A. X.; Suchý, M.; Hudson, R. H. E.; Menon, R. S.; Bartha, R. Simultaneous In Vivo pH and Temperature Mapping Using a PARACEST-MRI Contrast Agent. *Magn. Reson. Med.* **2013**, *70*, 1016−1025.

(606) Wu, Y.; Soesbe, T. C.; Kiefer, G. E.; Zhao, P.; Sherry, A. D. A Responsive Europium(III) Chelate That Provides a Direct Readout of pH by MRI. *J. Am. Chem. Soc.* **2010**, *132*, 14002−14003.

(607) Sheth, V. R.; Liu, G.; Li, Y.; Pagel, M. D. Improved pH Measurements with a Single PARACEST MRI Contrast Agent. *Contrast Media Mol. Imaging* **2012**, *7*, 26−34.

(608) Sheth, V. R.; Li, Y.; Chen, L. Q.; Howison, C. M.; Flask, C. A.; Pagel, M. D. Measuring In Vivo Tumor pHe with CEST-FISP MRI. *Magn. Reson. Med.* **2012**, *67*, 760−768.

(609) Wu, Y.; Zhang, S.; Soesbe, T. C.; Yu, J.; Vinogradov, E.; Lenkinski, R. E.; Sherry, A. D. pH Imaging of Mouse Kidneys In Vivo Using a Frequency-Dependent ParaCEST Agent. *Magn. Reson. Med.* **2016**, *75*, 2432−2441.

(610) Delli Castelli, D.; Terreno, E.; Aime, S. YbIII-HPDO3A: A Dual pH- and Temperature-Responsive CEST Agent. *Angew. Chem., Int. Ed.* **2011**, *50*, 1798−1800.

(611) Delli Castelli, D.; Ferrauto, G.; Cutrin, J. C.; Terreno, E.; Aime, S. In Vivo Maps of Extracellular pH in Murine Melanoma by CEST−MRI. *Magn. Reson. Med.* **2014**, *71*, 326−332.

(612) Tsitovich, P. B.; Cox, J. M.; Spernyak, J. A.; Morrow, J. R. Gear Up for a pH Shift: A Responsive Iron(II) 2-Amino-6-picolyl-Appended Macrocyclic paraCEST Agent That Protonates at a Pendent Group. *Inorg. Chem.* **2016**, *55*, 12001−12010.

(613) Finney, K.-L. N. A.; Harnden, A. C.; Rogers, N. J.; Senanayake, P. K.; Blamire, A. M.; O'Hogain, D.; Parker, D. Simultaneous Triple Imaging with Two PARASHIFT Probes: Encoding Anatomical, pH and Temperature Information using Magnetic Resonance Shift Imaging. *Chem. - Eur. J.* **2017**, *23*, 7976−7989.

(614) Okada, S.; Mizukami, S.; Kikuchi, K. Application of a Stimuli-Responsive Polymer to the Development of Novel MRI Probes. *ChemBioChem* **2010**, *11*, 785−787.

(615) Okada, S.; Mizukami, S.; Kikuchi, K. Switchable MRI Contrast Agents Based on Morphological Changes of pH-responsive Polymers. *Bioorg. Med. Chem.* **2012**, *20*, 769−774.

(616) Kim, K. S.; Park, W.; Hu, J.; Bae, Y. H.; Na, K. A Cancer-Recognizable MRI Contrast Agents Using pH-responsive Polymeric Micelle. *Biomaterials* **2014**, *35*, 337−343.

(617) Torres, E.; Mainini, F.; Napolitano, R.; Fedeli, F.; Cavalli, R.; Aime, S.; Terreno, E. Improved Paramagnetic Liposomes for MRI Visualization of pH Triggered Release. *J. Controlled Release* **2011**, *154*, 196−202.

(618) Kim, T.; Cho, E. J.; Chae, Y.; Kim, M.; Oh, A.; Jin, J.; Lee, E. S.; Baik, H.; Haam, S.; Suh, J. S.; et al. Urchin-Shaped Manganese Oxide Nanoparticles as pH-Responsive Activatable T1 Contrast Agents for Magnetic Resonance Imaging. *Angew. Chem., Int. Ed.* **2011**, *50*, 10589−10593.

(619) Chen, Y.; Yin, Q.; Ji, X.; Zhang, S.; Chen, H.; Zheng, Y.; Sun, Y.; Qu, H.; Wang, Z.; Li, Y.; et al. Manganese Oxide-Based Multifunctionalized Mesoporous Silica Nanoparticles for pH-responsive MRI, Ultrasonography and Circumvention of MDR in Cancer Cells. *Biomaterials* **2012**, *33*, 7126−7137.

(620) Mi, P.; Kokuryo, D.; Cabral, H.; Wu, H.; Terada, Y.; Saga, T.; Aoki, I.; Nishiyama, N.; Kataoka, K. A pH-Activatable Nanoparticle with Signal-Amplification Capabilities for Non-Invasive Imaging of Tumour Malignancy. *Nat. Nanotechnol.* **2016**, *11*, 724−730.

(621) Lin, C.-W.; Tseng, S. J.; Kempson, I. M.; Yang, S.-C.; Hong, T.-M.; Yang, P.-C. Extracellular Delivery of Modified Oligonucleotide and Superparamagnetic Iron Oxide Nanoparticles from a Degradable

Hydrogel Triggered by Tumor Acidosis. *Biomaterials* **2013**, *34*, 4387−4393.

(622) Gao, G. H.; Im, G. H.; Kim, M. S.; Lee, J. W.; Yang, J.; Jeon, H.; Lee, J. H.; Lee, D. S. Magnetite-Nanoparticle-Encapsulated pH-Responsive Polymeric Micelle as an MRI Probe for Detecting Acidic Pathologic Areas. *Small* **2010**, *6*, 1201−1204.

(623) Duimstra, J. A.; Femia, F. J.; Meade, T. J. A Gadolinium Chelate for Detection of β-Glucuronidase: A Self-Immolative Approach. *J. Am. Chem. Soc.* **2005**, *127*, 12847−12855.

(624) Giardiello, M.; Lowe, M. P.; Botta, M. An Esterase-Activated Magnetic Resonance Contrast Agent. *Chem. Commun.* **2007**, *0*, 4044−4046.

(625) Himmelreich, U.; Aime, S.; Hieronymus, T.; Justicia, C.; Uggeri, F.; Zenke, M.; Hoehn, M. A Responsive MRI Contrast Agent to Monitor Functional Cell Status. *NeuroImage* **2006**, *32*, 1142−1149.

(626) Lepage, M.; Dow, W. C.; Melchior, M.; You, Y.; Fingleton, B.; Quarles, C. C.; Pepin, C.; Gore, J. C.; Matrisian, L. M.; McIntyre, J. O. Noninvasive Detection of Matrix Metalloproteinase Activity In Vivo using a Novel Magnetic Resonance Imaging Contrast Agent with a Solubility Switch. *Mol. Imaging* **2007**, *6*, 393−403.

(627) Lebel, R.; Jastrzębska, B.; Therriault, H.; Cournoyer, M.-M.; McIntyre, J. O.; Escher, E.; Neugebauer, W.; Paquette, B.; Lepage, M. Novel Solubility-Switchable MRI Agent Allows the Noninvasive Detection of Matrix Metalloproteinase-2 Activity In Vivo in a Mouse Model. *Magn. Reson. Med.* **2008**, *60*, 1056−1065.

(628) Jastrzębska, B.; Lebel, R.; Therriault, H.; McIntyre, J. O.; Escher, E.; Guérin, B.; Paquette, B.; Neugebauer, W. A.; Lepage, M. New Enzyme-Activated Solubility-Switchable Contrast Agent for Magnetic Resonance Imaging: From Synthesis to in Vivo Imaging. *J. Med. Chem.* **2009**, *52*, 1576−1581.

(629) Figueiredo, S.; Moreira, J. N.; Geraldes, C. F. G. C.; Aime, S.; Terreno, E. Supramolecular Protamine/Gd-loaded Liposomes Adducts as Relaxometric Protease Responsive Probes. *Bioorg. Med. Chem.* **2011**, *19*, 1131−1135.

(630) Nivorozhkin, A. L.; Kolodziej, A. F.; Caravan, P.; Greenfield, M. T.; Lauffer, R. B.; McMurry, T. J. Enzyme-Activated Gd3+ Magnetic Resonance Imaging Contrast Agents with a Prominent Receptor-Induced Magnetization Enhancement. *Angew. Chem., Int. Ed.* **2001**, *40*, 2903−2906.

(631) Chang, Y.-T.; Cheng, C.-M.; Su, Y.-Z.; Lee, W.-T.; Hsu, J.-S.; Liu, G.-C.; Cheng, T.-L.; Wang, Y.-M. Synthesis and Characterization of a New Bioactivated Paramagnetic Gadolinium(III) Complex [Gd(DOTA-FPG)(H2O)] for Tracing Gene Expression. *Bioconjugate Chem.* **2007**, *18*, 1716−1727.

(632) Hanaoka, K.; Kikuchi, K.; Terai, T.; Komatsu, T.; Nagano, T. A Gd3+-Based Magnetic Resonance Imaging Contrast Agent Sensitive to β-Galactosidase Activity Utilizing a Receptor-Induced Magnetization Enhancement (RIME) Phenomenon. *Chem. - Eur. J.* **2008**, *14*, 987−995.

(633) Chen, Y.-J.; Wu, S.-C.; Chen, C.-Y.; Tzou, S.-C.; Cheng, T.-L.; Huang, Y.-F.; Yuan, S.-S.; Wang, Y.-M. Peptide-Based MRI Contrast Agent and Near-Infrared Fluorescent Probe for Intratumoral Legumain Detection. *Biomaterials* **2014**, *35*, 304−315.

(634) Rolla, G. A.; Tei, L.; Fekete, M.; Arena, F.; Gianolio, E.; Botta, M. Responsive Mn(II) Complexes for Potential Applications in Diagnostic Magnetic Resonance Imaging. *Bioorg. Med. Chem.* **2011**, *19*, 1115−1122.

(635) Bogdanov, A., Jr.; Matuszewski, L.; Bremer, C.; Petrovsky, A.; Weissleder, R. Oligomerization of Paramagnetic Substrates Result in Signal Amplification and Can be Used for MR Imaging of Molecular Targets. *Mol. Imaging* **2002**, *1*, 16−23.

(636) Querol, M.; Chen, J. W.; Weissleder, R.; Bogdanov, A. DTPA-bisamide-Based MR Sensor Agents for Peroxidase Imaging. *Org. Lett.* **2005**, *7*, 1719−1722.

(637) Querol, M.; Bennett, D. G.; Sotak, C.; Kang, H. W.; Bogdanov, A. A Paramagnetic Contrast Agent for Detecting Tyrosinase Activity. *ChemBioChem* **2007**, *8*, 1637−1641.

(638) Shiftan, L.; Israely, T.; Cohen, M.; Frydman, V.; Dafni, H.; Stern, R.; Neeman, M. Magnetic Resonance Imaging Visualization of

Hyaluronidase in Ovarian Carcinoma. *Cancer Res.* **2005**, *65*, 10316−10323.

(639) Shiftan, L.; Neeman, M. Kinetic Analysis of Hyaluronidase Activity Using a Bioactive MRI Contrast Agent. *Contrast Media Mol. Imaging* **2006**, *1*, 106−112.

(640) Nejadnik, H.; Ye, D.; Lenkov, O. D.; Donig, J. S.; Martin, J. E.; Castillo, R.; Derugin, N.; Sennino, B.; Rao, J.; Daldrup-Link, H. Magnetic Resonance Imaging of Stem Cell Apoptosis in Arthritic Joints with a Caspase Activatable Contrast Agent. *ACS Nano* **2015**, *9*, 1150−1160.

(641) Abu-Qare, A. W.; Abou-Donia, M. B. Biomarkers of Apoptosis: Release of Cytochrome c, Activation of Caspase-3, Induction of 8-hydroxy-2'-deoxyguanosine, Increased 3-nitrotyrosine, and Alteration of p53 Gene. *J. Toxicol. Environ. Health, Part B* **2001**, *4*, 313−332.

(642) Ye, D.; Shuhendler, A. J.; Pandit, P.; Brewer, K. D.; Tee, S. S.; Cui, L.; Tikhomirov, G.; Rutt, B.; Rao, J. Caspase-responsive Smart gadolinium-Based Contrast Agent for Magnetic Resonance Imaging of Drug-Induced Apoptosis. *Chem. Sci.* **2014**, *5*, 3845−3852.

(643) Shuhendler, A. J.; Ye, D.; Brewer, K. D.; Bazalova-Carter, M.; Lee, K.-H.; Kempen, P.; Dane Wittrup, K.; Graves, E. E.; Rutt, B.; Rao, J. Molecular Magnetic Resonance Imaging of Tumor Response to Therapy. *Sci. Rep.* **2015**, *5*, DOI: 10.1038/srep14759.

(644) Granot, D.; Shapiro, E. M. Release Activation of Iron Oxide Nanoparticles: (REACTION) A Novel Environmentally Sensitive MRI Paradigm. *Magn. Reson. Med.* **2011**, *65*, 1253−1259.

(645) Matsumura, S.; Aoki, I.; Saga, T.; Shiba, K. A Tumor-Environment-Responsive Nanocarrier That Evolves Its Surface Properties upon Sensing Matrix Metalloproteinase-2 and Initiates Agglomeration to Enhance T2 Relaxivity for Magnetic Resonance Imaging. *Mol. Pharmaceutics* **2011**, *8*, 1970−1974.

(646) Schellenberger, E.; Rudloff, F.; Warmuth, C.; Taupitz, M.; Hamm, B.; Schnorr, J. Protease-Specific Nanosensors for Magnetic Resonance Imaging. *Bioconjugate Chem.* **2008**, *19*, 2440−2445.

(647) Perez, J. M.; Simeone, F. J.; Tsourkas, A.; Josephson, L.; Weissleder, R. Peroxidase Substrate Nanosensors for MR Imaging. *Nano Lett.* **2004**, *4*, 119−122.

(648) Perez, J. M.; Josephson, L.; O'Loughlin, T.; Högemann, D.; Weissleder, R. Magnetic Relaxation Switches Capable of Sensing Molecular Interactions. *Nat. Biotechnol.* **2002**, *20*, 816−820.

(649) Zhao, M.; Josephson, L.; Tang, Y.; Weissleder, R. Magnetic Sensors for Protease Assays. *Angew. Chem.* **2003**, *115*, 1413−1416.

(650) Yu, S. S.; Scherer, R. L.; Ortega, R. A.; Bell, C. S.; O'Neil, C. P.; Hubbell, J. A.; Giorgio, T. D. Enzymatic- and Temperature-Sensitive Controlled Release of Ultrasmall Superparamagnetic Iron Oxides (USPIOs). *J. Nanobiotechnol.* **2011**, *9*, 51.

(651) Mizukami, S.; Takikawa, R.; Sugihara, F.; Hori, Y.; Tochio, H.; Wälchli, M.; Shirakawa, M.; Kikuchi, K. Paramagnetic Relaxation-Based 19F MRI Probe To Detect Protease Activity. *J. Am. Chem. Soc.* **2008**, *130*, 794−795.

(652) Mizukami, S.; Takikawa, R.; Sugihara, F.; Shirakawa, M.; Kikuchi, K. Dual-Function Probe to Detect Protease Activity for Fluorescence Measurement and 19F MRI. *Angew. Chem., Int. Ed.* **2009**, *48*, 3641−3643.

(653) Matsushita, H.; Mizukami, S.; Mori, Y.; Sugihara, F.; Shirakawa, M.; Yoshioka, Y.; Kikuchi, K. 19F MRI Monitoring of Gene Expression in Living Cells through Cell-Surface β-Lactamase Activity. *ChemBioChem* **2012**, *13*, 1579−1583.

(654) Mizukami, S.; Matsushita, H.; Takikawa, R.; Sugihara, F.; Shirakawa, M.; Kikuchi, K. 19F MRI Detection of [small beta]-galactosidase Activity for Imaging of Gene Expression. *Chem. Sci.* **2011**, *2*, 1151−1155.

(655) Yoo, B.; Pagel, M. D. A PARACEST MRI Contrast Agent To Detect Enzyme Activity. *J. Am. Chem. Soc.* **2006**, *128*, 14032−14033.

(656) Yoo, B.; Raam, M. S.; Rosenblum, R. M.; Pagel, M. D. Enzyme-responsive PARACEST MRI Contrast Agents: A New Biomedical Imaging Approach for Studies of the Proteasome. *Contrast Media Mol. Imaging* **2007**, *2*, 189−198.

(657) Yoo, B.; Sheth, V. R.; Howison, C. M.; Douglas, M. J. K.; Pineda, C. T.; Maine, E. A.; Baker, A. F.; Pagel, M. D. Detection of In Vivo Enzyme Activity with CatalyCEST MRI. *Magn. Reson. Med.* **2014**, *71*, 1221−1230.

(658) Suchy, M.; Ta, R.; Li, A. X.; Wojciechowski, F.; Pasternak, S. H.; Bartha, R.; Hudson, R. H. E. A Paramagnetic Chemical Exchange-Based MRI Probe Metabolized by Cathepsin D: Design, Synthesis and Cellular Uptake Studies. *Org. Biomol. Chem.* **2010**, *8*, 2560−2566.

(659) Chauvin, T.; Durand, P.; Bernier, M.; Meudal, H.; Doan, B.-T.; Noury, F.; Badet, B.; Beloeil, J.-C.; Tóth, É. Detection of Enzymatic Activity by PARACEST MRI: A General Approach to Target a Large Variety of Enzymes. *Angew. Chem., Int. Ed.* **2008**, *47*, 4370−4372.

(660) Li, Y.; Sheth, V. R.; Liu, G.; Pagel, M. D. A Self-Calibrating PARACEST MRI Contrast Agent That Detects Esterase Enzyme Activity. *Contrast Media Mol. Imaging* **2010**, *6*, 219−228.

(661) Daryaei, I.; Jones, K. M.; Pagel, M. D. Detection of DT-diaphorase Enzyme with a ParaCEST MRI Contrast Agent. *Chem. - Eur. J.* **2017**, *23*, 6514−6517.

(662) Hingorani, D. V.; Randtke, E. A.; Pagel, M. D. A CatalyCEST MRI Contrast Agent That Detects the Enzyme-Catalyzed Creation of a Covalent Bond. *J. Am. Chem. Soc.* **2013**, *135*, 6396−6398.

(663) Liu, G.; Liang, Y.; Bar-Shir, A.; Chan, K. W. Y.; Galpoththawela, C. S.; Bernard, S. M.; Tse, T.; Yadav, N. N.; Walczak, P.; McMahon, M. T.; et al. Monitoring Enzyme Activity Using a Diamagnetic Chemical Exchange Saturation Transfer Magnetic Resonance Imaging Contrast Agent. *J. Am. Chem. Soc.* **2011**, *133*, 16326−16329.

(664) Airan, R. D.; Bar-Shir, A.; Liu, G.; Pelled, G.; McMahon, M. T.; van Zijl, P. C. M.; Bulte, J. W. M.; Gilad, A. A. MRI Biosensor for Protein Kinase A Encoded By a Single Synthetic Gene. *Magn. Reson. Med.* **2012**, *68*, 1919−1923.

(665) Hingorani, D. V.; Montano, L. A.; Randtke, E. A.; Lee, Y. S.; Cárdenas-Rodríguez, J.; Pagel, M. D. A Single Diamagnetic CatalyCEST MRI Contrast Agent That Detects Cathepsin B Enzyme Activity by Using a Ratio of Two CEST Signals. *Contrast Media Mol. Imaging* **2016**, *11*, 130−138.

(666) Sinharay, S.; Fernández-Cuervo, G.; Acfalle, J. P.; Pagel, M. D. Detection of Sulfatase Enzyme Activity with a CatalyCEST MRI Contrast Agent. *Chem. - Eur. J.* **2016**, *22*, 6491−6495.

(667) Daryaei, I.; Mohammadebrahim Ghaffari, M.; Jones, K. M.; Pagel, M. D. Detection of Alkaline Phosphatase Enzyme Activity with a CatalyCEST MRI Biosensor. *ACS Sens* **2016**, *1*, 857−861.

(668) Fernández-Cuervo, G.; Sinharay, S.; Pagel, M. D. A CatalyCEST MRI Contrast Agent that Can Simultaneously Detect Two Enzyme Activities. *ChemBioChem* **2016**, *17*, 383−387.

(669) Sinharay, S.; Randtke, E. A.; Jones, K. M.; Howison, C. M.; Chambers, S. K.; Kobayashi, H.; Pagel, M. D. Noninvasive Detection of Enzyme Activity in Tumor Models of Human Ovarian Cancer Using CatalyCEST MRI. *Magn. Reson. Med.* **2017**, *77*, 2005−2014.

(670) Tu, C.; Osborne, E. A.; Louie, A. Y. Synthesis and Characterization of a Redox- and Light-sensitive MRI Contrast Agent. *Tetrahedron* **2009**, *65*, 1241−1246.

(671) Tu, C.; Nagao, R.; Louie, A. Y. Multimodal Magnetic-Resonance/Optical-Imaging Contrast Agent Sensitive to NADH. *Angew. Chem., Int. Ed.* **2009**, *48*, 6547−6551.

(672) Iwaki, S.; Hanaoka, K.; Piao, W.; Komatsu, T.; Ueno, T.; Terai, T.; Nagano, T. Development of Hypoxia-sensitive Gd3+-Based MRI Contrast Agents. *Bioorg. Med. Chem. Lett.* **2012**, *22*, 2798−2802.

(673) Yu, M.; Beyers, R. J.; Gorden, J. D.; Cross, J. N.; Goldsmith, C. R. A Magnetic Resonance Imaging Contrast Agent Capable of Detecting Hydrogen Peroxide. *Inorg. Chem.* **2012**, *51*, 9153−9155.

(674) Yu, M.; Ambrose, S. L.; Whaley, Z. L.; Fan, S.; Gorden, J. D.; Beyers, R. J.; Schwartz, D. D.; Goldsmith, C. R. A Mononuclear Manganese(II) Complex Demonstrates a Strategy To Simultaneously Image and Treat Oxidative Stress. *J. Am. Chem. Soc.* **2014**, *136*, 12836−12839.

(675) Yu, M.; Ward, M. B.; Franke, A.; Ambrose, S. L.; Whaley, Z. L.; Bradford, T. M.; Gorden, J. D.; Beyers, R. J.; Cattley, R. C.;

Ivanović-Burmazović, I.; et al. Adding a Second Quinol to a Redox-Responsive MRI Contrast Agent Improves Its Relaxivity Response to H2O2. *Inorg. Chem.* **2017**, *56*, 2812−2826.

(676) Carrera, C.; Digilio, G.; Baroni, S.; Burgio, D.; Consol, S.; Fedeli, F.; Longo, D.; Mortillaro, A.; Aime, S. Synthesis and Characterization of a Gd(III) Based Contrast Agent Responsive to Thiol Containing Compounds. *Dalton Trans* **2007**, *0*, 4980−4987.

(677) Raghunand, N.; Jagadish, B.; Trouard, T. P.; Galons, J.-P.; Gillies, R. J.; Mash, E. A. Redox-sensitive Contrast Agents for MRI Based on Reversible Binding of Thiols to Serum Albumin. *Magn. Reson. Med.* **2006**, *55*, 1272−1280.

(678) Jagadish, B.; Guntle, G. P.; Zhao, D.; Gokhale, V.; Ozumerzifon, T. J.; Ahad, A. M.; Mash, E. A.; Raghunand, N. Redox-active Magnetic Resonance Imaging Contrast Agents: Studies with Thiol-bearing 1,4,7,10-Tetraazacyclododecane-1,4,7,10-tetracetic Acid Derivatives. *J. Med. Chem.* **2012**, *55*, 10378−10386.

(679) Raghunand, N.; Guntle, G. P.; Gokhale, V.; Nichol, G. S.; Mash, E. A.; Jagadish, B. Design, Synthesis, and Evaluation of 1,4,7,10-Tetraazacyclododecane-1,4,7-triacetic Acid Derived, Redox-Sensitive Contrast Agents for Magnetic Resonance Imaging. *J. Med. Chem.* **2010**, *53*, 6747−6757.

(680) Guntle, G. P.; Jagadish, B.; Mash, E. A.; Powis, G.; Dorr, R. T.; Raghunand, N. Tumor Xenograft Response to Redox-Active Therapies Assessed by Magnetic Resonance Imaging Using a Thiol-Bearing DOTA Complex of Gadolinium. *Transl. Oncol.* **2012**, *5*, 190−199.

(681) Gløgård, C.; Stensrud, G.; Aime, S. Novel Radical-Responsive MRI Contrast Agent Based on Paramagnetic Liposomes. *Magn. Reson. Chem.* **2003**, *41*, 585−588.

(682) Furmanski, P.; Longley, C. Metalloporphyrin Enhancement of Magnetic Resonance Imaging of Human Tumor Xenografts in Nude Mice. *Cancer Res.* **1988**, *48*, 4604−4610.

(683) Fiel, R. J.; Musser, D. A.; Mark, E. H.; Mazurchuk, R.; Alletto, J. J. A Comparative Study of Manganese Meso-Sulfonatophenyl Porphyrins: Contrast-Enhancing Agents for Tumors. *Magn. Reson. Imaging* **1990**, *8*, 255−259.

(684) Ogan, M.; Revel, D.; Brasch, R. Metalloporphyrin Contrast Enhancement of Tumors in Magnetic Resonance Imaging A Study of Human Carcinoma, Lymphoma, and Fibrosarcoma in Mice. *Invest. Radiol.* **1987**, *22*, 822−828.

(685) Fiel, R. J.; Button, T. M.; Gilani, S.; Mark, E. H.; Musser, D. A.; Henkelman, R. M.; Bronskill, M. J.; van Heteren, J. G. Proton Relaxation Enhancement by Manganese(III)TPPS4 in a Model Tumor System. *Magn. Reson. Imaging* **1987**, *5*, 149−156.

(686) Loving, G. S.; Mukherjee, S.; Caravan, P. Redox-Activated Manganese-Based MR Contrast Agent. *J. Am. Chem. Soc.* **2013**, *135*, 4620−4623.

(687) Hamm, R. E.; Suwyn, M. A. Preparation and Characterization of Some Aminopolycarboxylate Complexes of Manganese(III). *Inorg. Chem.* **1967**, *6*, 139−142.

(688) Frost, A. E.; Freedman, H. H.; Westerback, S. J.; Martell, A. E. Chelating Tendencies of N,N'-Ethylenebis- [2-(0-hydroxyphenyl)]-glycine. *J. Am. Chem. Soc.* **1958**, *80*, 530−536.

(689) Gale, E. M.; Jones, C. M.; Ramsay, I.; Farrar, C. T.; Caravan, P. A Janus Chelator Enables Biochemically Responsive MRI Contrast with Exceptional Dynamic Range. *J. Am. Chem. Soc.* **2016**, *138*, 15861−15864.

(690) Di Gregorio, E.; Ferrauto, G.; Gianolio, E.; Lanzardo, S.; Carrera, C.; Fedeli, F.; Aime, S. An MRI Method To Map Tumor Hypoxia Using Red Blood Cells Loaded with a pO2-Responsive Gd-Agent. *ACS Nano* **2015**, *9*, 8239−8248.

(691) Liu, G.; Li, Y.; Pagel, M. D. Design and Characterization of a New Irreversible Responsive PARACEST MRI Contrast Agent That Detects Nitric Oxide. *Magn. Reson. Med.* **2007**, *58*, 1249−1256.

(692) Ratnakar, S. J.; Viswanathan, S.; Kovacs, Z.; Jindal, A. K.; Green, K. N.; Sherry, A. D. Europium(III) DOTA-tetraamide Complexes as Redox-Active MRI Sensors. *J. Am. Chem. Soc.* **2012**, *134*, 5798−5800.

(693) Tsitovich, P. B.; Spernyak, J. A.; Morrow, J. R. A Redox-Activated MRI Contrast Agent that Switches Between Paramagnetic and Diamagnetic States. *Angew. Chem., Int. Ed.* **2013**, *52*, 13997−14000.

(694) Aime, S.; Delli Castelli, D.; Terreno, E. Highly Sensitive MRI Chemical Exchange Saturation Transfer Agents Using Liposomes. *Angew. Chem., Int. Ed.* **2005**, *44*, 5513−5515.

(695) Terreno, E.; Boffa, C.; Menchise, V.; Fedeli, F.; Carrera, C.; Castelli, D. D.; Digilio, G.; Aime, S. Gadolinium-doped LipoCEST Agents: A Potential Novel Class of Dual 1H-MRI Probes. *Chem. Commun.* **2011**, *47*, 4667−4669.

(696) Hanaoka, K.; Kikuchi, K.; Urano, Y.; Nagano, T. Selective Sensing of Zinc Ions with a Novel Magnetic Resonance Imaging Contrast Agent. *J. Chem. Soc., Perkin Trans.* **2001**, *2*, 1840−1843.

(697) Hanaoka, K.; Kikuchi, K.; Urano, Y.; Narazaki, M.; Yokawa, T.; Sakamoto, S.; Yamaguchi, K.; Nagano, T. Design and Synthesis of a Novel Magnetic Resonance Imaging Contrast Agent for Selective Sensing of Zinc Ion. *Chem. Biol.* **2002**, *9*, 1027−1032.

(698) Major, J. L.; Parigi, G.; Luchinat, C.; Meade, T. J. The Synthesis and In Vitro Testing of a Zinc-activated MRI Contrast Agent. *Proc. Natl. Acad. Sci. U. S. A.* **2007**, *104*, 13881−13886.

(699) Major, J. L.; Boiteau, R. M.; Meade, T. J. Mechanisms of ZnII-Activated Magnetic Resonance Imaging Agents. *Inorg. Chem.* **2008**, *47*, 10788−10795.

(700) Esqueda, A. C.; López, J. A.; Andreu-de-Riquer, G.; Alvarado-Monzón, J. C.; Ratnakar, J.; Lubag, A. J. M.; Sherry, A. D.; De León-Rodríguez, L. M. A New Gadolinium-Based MRI Zinc Sensor. *J. Am. Chem. Soc.* **2009**, *131*, 11387−11391.

(701) Lubag, A. J. M.; De Leon-Rodriguez, L. M.; Burgess, S. C.; Sherry, A. D. Noninvasive MRI of β-cell Function Using a Zn2+-responsive Contrast Agent. *Proc. Natl. Acad. Sci. U. S. A.* **2011**, *108*, 18400−18405.

(702) Clavijo Jordan, M. V.; Lo, S.-T.; Chen, S.; Preihs, C.; Chirayil, S.; Zhang, S.; Kapur, P.; Li, W.-H.; De Leon-Rodriguez, L. M.; Lubag, A. J. M.; et al. Zinc-sensitive MRI Contrast Agent Detects Differential Release of Zn(II) Ions from the Healthy vs. Malignant Mouse Prostate. *Proc. Natl. Acad. Sci. U. S. A.* **2016**, *113*, E5464−E5471.

(703) Trokowski, R.; Ren, J.; Kálmán, F. K.; Sherry, A. D. Selective Sensing of Zinc Ions with a PARACEST Contrast Agent. *Angew. Chem., Int. Ed.* **2005**, *44*, 6920−6923.

(704) Zhang, X.-a.; Lovejoy, K. S.; Jasanoff, A.; Lippard, S. J. Water-Soluble Porphyrins as a Dual-Function Molecular Imaging Platform for MRI and Fluorescence Zinc Sensing. *Proc. Natl. Acad. Sci. U. S. A.* **2007**, *104*, 10780−10785.

(705) Lee, T.; Zhang, X.-a.; Dhar, S.; Faas, H.; Lippard, S. J.; Jasanoff, A. In Vivo Imaging with a Cell-Permeable Porphyrin-Based MRI Contrast Agent. *Chem. Biol.* **2010**, *17*, 665−673.

(706) Li, W.-h.; Fraser, S. E.; Meade, T. J. A Calcium-Sensitive Magnetic Resonance Imaging Contrast Agent. *J. Am. Chem. Soc.* **1999**, *121*, 1413−1414.

(707) Li, W.-h.; Parigi, G.; Fragai, M.; Luchinat, C.; Meade, T. J. Mechanistic Studies of a Calcium-Dependent MRI Contrast Agent. *Inorg. Chem.* **2002**, *41*, 4018−4024.

(708) MacRenaris, K. W.; Ma, Z.; Krueger, R. L.; Carney, C. E.; Meade, T. J. Cell-Permeable Esterase-Activated Ca(II)-Sensitive MRI Contrast Agent. *Bioconjugate Chem.* **2016**, *27*, 465−473.

(709) Dhingra, K.; Maier, M. E.; Beyerlein, M.; Angelovski, G.; Logothetis, N. K. Synthesis and Characterization of a Smart Contrast Agent Sensitive to Calcium. *Chem. Commun.* **2008**, *0*, 3444−3446.

(710) Kubíček, V.; Vitha, T.; Kotek, J.; Hermann, P.; Vander Elst, L.; Muller, R. N.; Lukeš, I.; Peters, J. A. Towards MRI Contrast Agents Responsive to Ca(II) and Mg(II) Ions: Metal-Induced Oligomerization of Dota−Bisphosphonate Conjugates. *Contrast Media Mol. Imaging* **2010**, *5*, 294−296.

(711) Angelovski, G.; Chauvin, T.; Pohmann, R.; Logothetis, N. K.; Tóth, É. Calcium-responsive Paramagnetic CEST Agents. *Bioorg. Med. Chem.* **2011**, *19*, 1097−1105.

(712) Atanasijevic, T.; Shusteff, M.; Fam, P.; Jasanoff, A. Calcium-sensitive MRI Contrast Agents Based on Superparamagnetic Iron

Oxide Nanoparticles and Calmodulin. *Proc. Natl. Acad. Sci. U. S. A.* 2006, 103, 14707−14712.

(713) Atanasijevic, T.; Jasanoff, A. Preparation of Iron Oxide-Based Calcium Sensors for MRI. *Nat. Protoc.* 2007, 2, 2582−2589.

(714) Garello, F.; Vibhute, S.; Gündüz, S.; Logothetis, N. K.; Terreno, E.; Angelovski, G. Innovative Design of Ca-Sensitive Paramagnetic Liposomes Results in an Unprecedented Increase in Longitudinal Relaxivity. *Biomacromolecules* 2016, 17, 1303−1311.

(715) Que, E. L.; Chang, C. J. A Smart Magnetic Resonance Contrast Agent for Selective Copper Sensing. *J. Am. Chem. Soc.* 2006, 128, 15942−15943.

(716) Que, E. L.; Gianolio, E.; Baker, S. L.; Wong, A. P.; Aime, S.; Chang, C. J. Copper-Responsive Magnetic Resonance Imaging Contrast Agents. *J. Am. Chem. Soc.* 2009, 131, 8527−8536.

(717) Que, E. L.; Gianolio, E.; Baker, S. L.; Aime, S.; Chang, C. J. A Copper-activated Magnetic Resonance Imaging Contrast Agent with Improved Turn-On Relaxivity Response and Anion Compatibility. *Dalton Trans* 2010, 39, 469−476.

(718) Que, E. L.; New, E. J.; Chang, C. J. A Cell-Permeable Gadolinium Contrast Agent for Magnetic Resonance Imaging of Copper in a Menkes Disease Model. *Chem. Sci.* 2012, 3, 1829−1834.

(719) Li, W.-S.; Luo, J.; Chen, Z.-N. A Gadolinium(III) Complex with 8-Amidequinoline Based Ligand as Copper(II) Ion Responsive Contrast Agent. *Dalton Trans* 2011, 40, 484−488.

(720) De-Miguel, F. F.; Fuxe, K. Extrasynaptic Neurotransmission as a Way of Modulating Neuronal Functions. *Front. Physiol.* 2012, 3, DOI: 10.3389/fphys.2012.00016.

(721) Hyman, S. E. Neurotransmitters. *Curr. Biol.* 2005, 15, R154−R158.

(722) Devor, A.; Bandettini, P. A.; Boas, D. A.; Bower, J. M.; Buxton, R. B.; Cohen, L. B.; Dale, A. M.; Einevoll, G. T.; Fox, P. T.; Franceschini, M. A.; et al. The Challenge of Connecting the Dots in the B.R.A.I.N. *Neuron* 2013, 80, 270−274.

(723) Klohs, J.; Rudin, M. Unveiling Molecular Events in the Brain by Noninvasive Imaging. *Neuroscientist* 2011, 17, 539−559.

(724) Badgaiyan, R. D. Neurotransmitter Imaging: Basic Concepts and Future Perspectives. *Curr. Med. Imaging Rev.* 2011, 7, 98−103.

(725) Bloom, J. D.; Meyer, M. M.; Meinhold, P.; Otey, C. R.; MacMillan, D.; Arnold, F. H. Evolving Strategies for Enzyme Engineering. *Curr. Opin. Struct. Biol.* 2005, 15, 447−452.

(726) Lee, T.; Cai, L. X.; Lelyveld, V. S.; Hai, A.; Jasanoff, A. Molecular-Level Functional Magnetic Resonance Imaging of Dopaminergic Signaling. *Science* 2014, 344, 533−535.

(727) Shapiro, M. G.; Westmeyer, G. G.; Romero, P. A.; Szablowski, J. O.; Küster, B.; Shah, A.; Otey, C. R.; Langer, R.; Arnold, F. H.; Jasanoff, A. Directed Evolution of a Magnetic Resonance Imaging Contrast Agent for Noninvasive Imaging of Dopamine. *Nat. Biotechnol.* 2010, 28, 264−270.

(728) Oukhatar, F.; Même, S.; Même, W.; Szeremeta, F.; Logothetis, N. K.; Angelovski, G.; Tóth, É. MRI Sensing of Neurotransmitters with a Crown Ether Appended Gd3+ Complex. *ACS Chem. Neurosci.* 2015, 6, 219−225.

(729) Zheng, X.; Qian, J.; Tang, F.; Wang, Z.; Cao, C.; Zhong, K. Microgel-Based Thermosensitive MRI Contrast Agent. *ACS Macro Lett.* 2015, 4, 431−435.

(730) de Smet, M.; Langereis, S.; den Bosch, S. v.; Grüll, H. Temperature-sensitive Liposomes for Doxorubicin Delivery under MRI Guidance. *J. Controlled Release* 2010, 143, 120−127.

(731) Zhang, S.; Malloy, C. R.; Sherry, A. D. MRI Thermometry Based on PARACEST Agents. *J. Am. Chem. Soc.* 2005, 127, 17572−17573.

(732) Li, A. X.; Wojciechowski, F.; Suchy, M.; Jones, C. K.; Hudson, R. H. E.; Menon, R. S.; Bartha, R. A Sensitive PARACEST Contrast Agent for Temperature MRI: Eu3+-DOTAM-glycine (Gly)-phenylalanine (Phe). *Magn. Reson. Med.* 2008, 59, 374−381.

(733) Stevens, T. K.; Milne, M.; Elmehriki, A. A. H.; Suchý, M.; Bartha, R.; Hudson, R. H. E. A DOTAM-Based ParaCEST Agent Favoring TSAP Geometry for Enhanced Amide Proton Chemical Shift Dispersion and Temperature Sensitivity. *Contrast Media Mol. Imaging* 2013, 8, 289−292.

(734) Tsitovich, P. B.; Cox, J. M.; Benedict, J. B.; Morrow, J. R. Six-coordinate Iron(II) and Cobalt(II) ParaSHIFT Agents for Measuring Temperature by Magnetic Resonance Spectroscopy. *Inorg. Chem.* 2016, 55, 700−716.

(735) Tsitovich, P. B.; Tittiris, T. Y.; Cox, J. M.; Benedict, J. B.; Morrow, J. R. Fe(II) and Co(II) N-methylated CYCLEN Complexes as ParaSHIFT Agents with Large Temperature Dependent Shifts. *Dalton Trans* 2018, 47, 916−924.

(736) Osborne, E. A.; Jarrett, B. R.; Tu, C.; Louie, A. Y. Modulation of T2 Relaxation Time by Light-Induced, Reversible Aggregation of Magnetic Nanoparticles. *J. Am. Chem. Soc.* 2010, 132, 5934−5935.

(737) Wu, Y.; Carney, C. E.; Denton, M.; Hart, E.; Zhao, P.; Streblow, D. N.; Sherry, A. D.; Woods, M. Polymeric PARACEST MRI Contrast Agents as Potential Reporters for Gene Therapy. *Org. Biomol. Chem.* 2010, 8, 5333−5338.

(738) Smolensky, E. D.; Peterson, K. L.; Weitz, E. A.; Lewandowski, C.; Pierre, V. C. Magnetoluminescent Light Switches − Dual Modality in DNA Detection. *J. Am. Chem. Soc.* 2013, 135, 8966−8972.

(739) Rodríguez, E.; Nilges, M.; Weissleder, R.; Chen, J. W. Activatable Magnetic Resonance Imaging Agents for Myeloperoxidase Sensing: Mechanism of Activation, Stability, and Toxicity. *J. Am. Chem. Soc.* 2010, 132, 168−177.

(740) Shazeeb, M. S.; Xie, Y.; Gupta, S.; Bogdanov, A. A., Jr. A Novel Paramagnetic Substrate for Detecting Myeloperoxidase Activity In Vivo. *Mol. Imaging* 2012, 11, 433−443.

(741) Su, H. S.; Nahrendorf, M.; Panizzi, P.; Breckwoldt, M. O.; Rodriguez, E.; Iwamoto, Y.; Aikawa, E.; Weissleder, R.; Chen, J. W. Vasculitis: Molecular Imaging by Targeting the Inflammatory Enzyme Myeloperoxidase. *Radiology* 2012, 262, 181−190.

(742) Nahrendorf, M.; Sosnovik, D.; Chen, J. W.; Panizzi, P.; Figueiredo, J.-L.; Aikawa, E.; Libby, P.; Swirski, F. K.; Weissleder, R. Activatable Magnetic Resonance Imaging Agent Reports Myeloperoxidase Activity in Healing Infarcts and Noninvasively Detects the Antiinflammatory Effects of Atorvastatin on Ischemia-Reperfusion Injury. *Circulation* 2008, 117, 1153−1169.

(743) Breckwoldt, M. O.; Chen, J. W.; Stangenberg, L.; Aikawa, E.; Rodriguez, E.; Qiu, S.; Moskowitz, M. A.; Weissleder, R. Tracking the Inflammatory Response in Stroke In Vivo by Sensing the Enzyme Myeloperoxidase. *Proc. Natl. Acad. Sci. U. S. A.* 2008, 105, 18584−18589.

(744) DeLeo, M. J., III; Gounis, M. J.; Hong, B.; Ford, J. C.; Wakhloo, A. K.; Bogdanov, A. A., Jr. Carotid Artery Brain Aneurysm Model: In Vivo Molecular Enzyme-Specific MR Imaging of Active Inflammation in a Pilot Study. *Radiology* 2009, 252, 696−703.

(745) Forghani, R.; Wojtkiewicz, G. R.; Zhang, Y. N.; Seeburg, D.; Bautz, B. R. M.; Pulli, B.; Milewski, A. R.; Atkinson, W. L.; Iwamoto, Y.; Zhang, E. R.; et al. Demyelinating Diseases: Myeloperoxidase as an Imaging Biomarker and Therapeutic Target. *Radiology* 2012, 263, 451−460.

(746) Loving, G. S.; Caravan, P. Activation and Retention: A Magnetic Resonance Probe for the Detection of Acute Thrombosis. *Angew. Chem., Int. Ed.* 2014, 53, 1140−1143.

(747) Haedicke, I. E.; Li, T.; Zhu, Y. L. K.; Martinez, F.; Hamilton, A. M.; Murrell, D. H.; Nofiele, J. T.; Cheng, H. L. M.; Scholl, T. J.; Foster, P. J.; et al. An Enzyme-Activatable and Cell-Permeable Mn-III Porphyrin as a Highly Efficient T-1 MRI Contrast Agent for Cell Labeling. *Chem. Sci.* 2016, 7, 4308−4317.

(748) Loai, S.; Haedicke, I.; Mirzaei, Z.; Simmons, C. A.; Zhang, X.; Cheng, H. L. Positive-Contrast Cellular MRI of Embryonic Stem Cells for Tissue Regeneration Using a Highly Efficient T-1 MRI Contrast Agent. *J. Magn. Reson. Imaging* 2016, 44, 1456−1463.

(749) Jirak, D.; Kriz, J.; Herynek, V.; Andersson, B.; Girman, P.; Burian, M.; Saudek, F.; Hajek, M. MRI of Transplanted Pancreatic Islets. *Magn. Reson. Med.* 2004, 52, 1228−1233.

(750) Toso, C.; Vallee, J.-P.; Morel, P.; Ris, F.; Demuylder-Mischler, S.; Lepetit-Coiffe, M.; Marangon, N.; Saudek, F.; Shapiro, A. M. J.;

Bosco, D.; et al. Clinical Magnetic Resonance Imaging of Pancreatic Islet Grafts after Iron Nanoparticle Labeling. *Am. J. Transplant.* **2008**, *8*, 701−706.

(751) Saudek, F.; Jirák, D.; Girman, P.; Herynek, V.; Dezortová, M.; Kříž, J.; Peregrin, J.; Berková, Z.; Zacharovová, K.; Hájek, M. Magnetic Resonance Imaging of Pancreatic Islets Transplanted Into the Liver in Humans. *Transplantation* **2010**, *90*, 1602−1606.

(752) Barnett, B. P.; Ruiz-Cabello, J.; Hota, P.; Ouwerkerk, R.; Shamblott, M. J.; Lauzon, C.; Walczak, P.; Gilson, W. D.; Chacko, V. P.; Kraitchman, D. L.; et al. Use of Perfluorocarbon Nanoparticles for Non-Invasive Multimodal Cell Tracking of Human Pancreatic Islets. *Contrast Media Mol. Imaging* **2011**, *6*, 251−259.

(753) de Vries, I. J. M.; Lesterhuis, W. J.; Barentsz, J. O.; Verdijk, P.; van Krieken, J. H.; Boerman, O. C.; Oyen, W. J. G.; Bonenkamp, J. J.; Boezeman, J. B.; Adema, G. J.; et al. Magnetic Resonance Tracking of Dendritic Cells in Melanoma Patients for Monitoring of Cellular Therapy. *Nat. Biotechnol.* **2005**, *23*, 1407−1413.

(754) Long, C. M.; van Laarhoven, H. W. M.; Bulte, J. W. M.; Levitsky, H. I. Magnetovaccination as a Novel Method to Assess and Quantify Dendritic Cell Tumor Antigen Capture and Delivery to Lymph Nodes. *Cancer Res.* **2009**, *69*, 3180−3187.

(755) Zhu, J. H.; Zhou, L. F.; XingWu, F. G. Tracking Neural Stem Cells in Patients with Brain Trauma. *N. Engl. J. Med.* **2006**, *355*, 2376−2378.

(756) Callera, F.; de Melo, C. M. T. P. Magnetic Resonance Tracking of Magnetically Labeled Autologous Bone Marrow CD34(+) Cells Transplanted into the Spinal Cord via Lumbar Puncture Technique in Patients with Chronic Spinal Cord Injury: CD34(+) Cells' Migration into the Injured Site. *Stem Cells Dev.* **2007**, *16*, 461−466.

(757) Pumphrey, A. L.; Ye, S. J.; Yang, Z. S.; Simkin, J.; Gensel, J. C.; Abdel-Latif, A.; Vandsburger, M. H. Cardiac Chemical Exchange Saturation Transfer MR Imaging Tracking of Cell Survival or Rejection in Mouse Models of Cell Therapy. *Radiology* **2017**, *282*, 131−138.

(758) Khurana, A.; Chapelin, F.; Xu, H. Y.; Acevedo, J. R.; Molinolo, A.; Nguyen, Q.; Ahrens, E. T. Visualization of Macrophage Recruitment in Head and Neck Carcinoma Model Using Fluorine-19 Magnetic Resonance Imaging. *Magn. Reson. Med.* **2018**, *79*, 1972−1980.

(759) Zhong, J.; Narsinh, K.; Morel, P. A.; Xu, H. Y.; Ahrens, E. T. In Vivo Quantification of Inflammation in Experimental Autoimmune Encephalomyelitis Rats Using Fluorine-19 Magnetic Resonance Imaging Reveals Immune Cell Recruitment outside the Nervous System. *PLoS One* **2015**, *10*, e0140238.

(760) Iordanova, B.; Hitchens, T. K.; Robison, C. S.; Ahrens, E. T. Engineered Mitochondrial Ferritin as a Magnetic Resonance Imaging Reporter in Mouse Olfactory Epithelium. *PLoS One* **2013**, *8*, e72720.

(761) Farrar, C. T.; Buhrman, J. S.; Liu, G.; Kleijn, A.; Lamfers, M. L.; McMahon, M. T.; Gilad, A. A.; Fulci, G. Establishing the Lysine-rich Protein CEST Reporter Gene as a CEST MR Imaging Detector for Oncolytic Virotherapy. *Radiology* **2015**, *275*, 746−754.

(762) Bartelle, B. B.; Szulc, K. U.; Suero-Abreu, G. A.; Rodriguez, J. J.; Turnbull, D. H. Divalent Metal Transporter, DMT1: A Novel MRI Reporter Protein. *Magn. Reson. Med.* **2013**, *70*, 842−850.